Improving the spacer-concrete interface for durable structures

Fadhilah Muslim

Department of Civil and Environmental Engineering

Imperial College London

June 2018

A thesis submitted in fulfilment of the requirements for the degree of

Doctor of Philosophy and Diploma of Imperial College London

Declaration

I hereby declare that this thesis is my own work carried out in the Concrete Durability Group, Department of Civil and Environmental Engineering, Imperial College London. Any information obtained from the work of others, whether published or unpublished, is acknowledged by reference to the sources. This thesis has not been submitted in any form to any other academic institutions for any degree, diploma, certificate or other qualification.

The copyright of this thesis rests with the author and is made available under a Creative Commons Attribution Non-Commercial No Derivatives licence. Researchers are free to copy, distribute or transmit the thesis on the condition that they attribute it, that they do not use it for commercial purposes and that they do not alter, transform or build upon it. For any reuse or redistribution, researchers must make clear to others the licence terms of this work.

London, 13th June 2018

Fadhilah Muslim

Abstract

Spacers are important devices in reinforced concrete that are used to support reinforcing steel during concreting in order to achieve the required cover. They are placed at every meter length or less of steel reinforcement and left permanently in the structure. However, very few studies have been carried out on the effect of spacers on the performance of concrete.

This work aims to develop a better understanding of the influence of spacers on the microstructure and long-term durability of concrete structures. The work also aims to develop methods to enhance bonding and mechanical interlocking of spacers with concrete.

Extensive experimental testing was performed. Concrete samples containing a range of commercially available spacers (plastic or cementitious) were prepared with different binder types including Portland cement CEM I and CEM I blended with silica fume, fly ash or ground granulated blast-furnace slag. Samples containing horizontal or vertical spacers were prepared, cured in a fog room (100% RH, 21°C) for various periods before bond strength measurement. Samples were also conditioned at 75% RH, 21°C or in a 50°C oven for microstructure analysis and transport testing such as oxygen diffusion, oxygen permeation, water absorption, electrical conduction, chloride penetration, and fluorescent epoxy impregnation. Finally, a large number of prefabricated modified cementitious spacers were prepared with a range of mix compositions and surface textures and then cast into concrete for splitting tensile strength and transport testing.

Results showed that the inclusion of spacer in reinforced concrete produces a weak, porous and micro-cracked interface regardless of whether the spacer was cast for horizontal or vertical reinforcement. This lowers the resistance of concrete to ingress of aggressive agents. Cross-sections of fluorescence epoxy impregnated samples images under UV light showed a preferential transport along the spacer-concrete interface. Higher penetration of chloride ions was also detected along the interface compared to the bulk paste farther away from the spacer and to the control sample without a spacer. The extent of the effect of spacer depends on the spacer type and binders used, and drying regime.

Modifying the spacer surface textures has a clear effect on increasing their interlocking with concrete, and this leads to a significant improvement in the bond strength of the spacer-concrete interface by up to 133%. This was found to decrease the tendency for cracking at the spacer-concrete interface due to differential volume changes, thus leading to a significant decrease in pressure-induced flow. The effect of surface texture on the overall strength of spacer-concrete interface and transport properties is dependent on the roughness, shape, and orientation of the spacer surface texture.

The implications of the findings from this study on the durability of concrete structures are discussed. Finally, recommendations on other possible methods to improve both bond strength and durability of the spacer-concrete interface are presented.

Acknowledgement

In the name of Allah, the most Merciful and Beneficent.

Alhamdullilah, all praises to Allah, the Almighty, the greatest of all for giving me the opportunity, strength, determination, and his blessings to complete this thesis.

This thesis not only represents my research work but also marks an incredible journey that I have gone through since mid-June 2014 in the Concrete Durability Group, Department of Civil and Environmental Engineering, Imperial College London. It has been a journey full of learning and pleasurable experiences, new friendships and unique opportunities. I would not have been able to make it through to the end of my PhD without the support and help from the remarkable individuals below.

First and foremost, I would like to express my deepest appreciation to my supervisors, Dr Hong Wong and Professor Nick Buenfeld for their continuous supervision and support throughout my PhD study. Dr Wong has guided me with his patience and tremendous knowledge. I have truly learnt a lot from him. It was a pleasure to be given the opportunities to co-supervise with him both undergraduate and MSc students in their final projects and to help as a graduate teaching assistant (GTA) in his Reinforced Concrete Design and Structural Mechanics modules, both of which were very rewarding experiences. I could not have asked for a better supervisor for my PhD study.

This thesis would not have been possible without the financial support from the Indonesian Endowment Fund for Education (LPDP), covering my tuition fees for the first three years, writing up fees, living allowance in London for 48 months, book allowance, a return ticket between London and Jakarta as well as funding for my research. I would also like to thank the financial support provided by the Imperial College Trust Fund which enabled me to present my work at the 16th Euroseminar on Microscopy Applied to Building Materials held in Les Diablerets, Switzerland in May 2017.

I praise the enormous help given by Andrew Morris in the laboratory throughout these years. I can never forget how he called me the ‘Women of Engineering’ and ‘Chief of Engineers’ when we cast concrete together in the lab. His sense of humour had always made my day in the lab full of laughter and smiles. Behind the scene, the eight undergraduate and MSc students assisted

me with my experiments and data collection: Marwa El-Fassi and Guanghan Cheng for their help with transport testing in Chapter 4, Joshua Agbede and Zheng Gu for their help with transport testing in Chapter 5, Xianyi Yu and Evangelos Pastras for their help with epoxy impregnation in Chapter 6, Richard Man and Quentin Chiu for their help with tensile strength testing in Chapter 7. I truly appreciate their help. Thanks also go to Professor Chris Cheeseman, who examined my early stage and late stage assessments and provided me with invaluable advice.

I would also like thank the postgraduate administrators, Fionnuala Ni Dhonnabhain and Sarah Willis, for helping me with administrative issues related to my PhD. Fionnuala also provided me with an opportunity to work as a GTA responsible for lecture room preparation every morning, which also encouraged me to become a morning person as the job required me to arrive at the college by 7.45am every day! It will be an unforgettable experience in my life. My thanks are also extended to other departmental staffs: Louise Green, Tina Mikellides and Anna Hikel, and the staff in the central library, student hub, ICT services, graduate schools, international office and Centre for Academic English for their assistance throughout my PhD.

In my daily work, I am grateful to a number of colleagues whom I have been fortunate enough to share an office with over the years, and special thanks go to my best friend at Imperial College: Dr Marcus Yio, for his technical advice on the operation of Laser scanning confocal microscopy, daily lunch breaks, holiday, endless discussions and above all his friendship and moral support during my PhD. His willingness to give his time so generously has been very much appreciated. I would also like to thank Alalea Kia and Dr Fatmawati Abdul Wahid who have made my time in the office so enjoyable and pleasant, and Xi Chen and Kai Zhang for their support during my writing up period. I would like to thank Monika Mac, Dr Sukina Alzyoud, Young Han Shin, and Dr Zhigen Wu, who welcomed me and provided me with help during my first six months at Imperial College.

I am also grateful to be able to develop friendship and share my morning days with Qili Fang, Abobakr Elwakeel and Adeleke Soyemi, other PhD students at this Department, whom I worked with every morning to set up the lecture rooms. Also, thanks are extended to Dr Aliyyah Masjuki for sharing her PhD ups and downs with me during her PhD.

I am also appreciative of the motivation and friendship I received from some of my Indonesian friends at Imperial College London. They are Aldyla Raditya, Vanya Valindria, Wahyu Meka, Vani Virdyawan, Andri Setiawan, Ratri Wulandari, Ari Dwijayanti, Renard Xaviero, Joko Pebrianto, Hendarto, Husni Rois Ali, Nur Ahmadi, Agung Santoso, Amanda Larasati and Emma

Bangun. I would also like to thank all my Indonesian flatmates: Rosi Destiani, Faldo Maldini, Farid Nurrahman, Alfan Prasekal, Elzafira Felaza, Dorothy Ferrary and Hilda Mulu, whom I have shared my flat with in Lewisham since July 2014.

Special thanks go to Aishah Praswoto for her continued friendship since our master studies together in Paris. I have learnt a lot of things from her. I also wish to acknowledge my friendship with my lovely best friend ever, Amanah Ramadiah, with whom I have shared my room since October 2017. Thank you for taking care of me during the very tough writing period of this thesis. Both Aishah and Amanah are my true friends ever. Thank you both for all the memories and your kindness.

Last but certainly not least, I would like to thank my family for their unconditional love, continued encouragement and faith in me. My parents, Dr Muslim Tawakal SH, MPd and Dra. Rosliani Rauf SH, MA have unconditionally supported every decision I have made in my life and have always reminded me of God while I am far away from them. They have been a source of love and energy ever since. My sisters and brother, Istianah Muslim, Kamalia Muslim and Fuadi Farhan Muslim have always been my source of happiness. I love them all from the deepest of my heart and I wish them a healthy and happy life. I would also like to extend my gratitude to my extended family, of whom there are too many to mention!

This thesis is dedicated to my parents, for they are the most important people to me.

Notation

Abbreviations

Aft	Alumina ferric oxide or ettringite
Al	Aluminium
Al_2O_3	Aluminium oxide
AU	Airy unit
BSE	Backscattered electron
C-S-H	Calcium silicate hydrate
$Ca(OH)_2$ or CH	Calcium hydroxide or portlandite
CaO	Calcium oxide
C_3A	Tricalcium aluminate
C_4AF	Tetracalcium aluminoferrite
C_3S	Tricalcium silicate
C_2S	Dicalcium silicate
Cl^-	Chloride ion
CO_2	Carbon dioxide
CEM I	Portland cement
CEM II	Portland-composite cement
CS	Cementitious spacer
EDM	Euclidean Distance Mapping
FA	Fly ash
Fe_2O_3	Ferric Oxide
GGBS	Ground granulated blast-furnace slag
ITZ	Interfacial transition zone
K_2O	Potassium oxide
LOI	Loss on ignition
LSCM	Laser scanning confocal microscopy
MIP	Mercury intrusion porosimetry
µXRF	Micro X-ray Fluorescence
MgO	Magnesium oxide
MK	Metakaolin

MSA	Maximum size aggregate
NaCl	Sodium chloride
OPC	Ordinary Portland cement
PMT	Photomultiplier tube
PS	Plastic spacer
PVA	Polyvinyl alcohol
Rh	Rhodium
RH	Relative humidity
SBR	Styrene-Butadiene-Rubber
SCI	Steel-concrete interface
SCMs	Supplementary cementitious materials
SEM	Scanning electron microscopy
S.E.	Standard error
SF	Silica fume
SiC	Silicon carbide
SiO_2	Silicon dioxide
SO_3	Sulphur trioxide
SSD	Surface dry condition
UHPFC	Ultra-high-performance fibre concrete
UV	Ultraviolet
w/b	Water binder ratio
w/c	Water cement ratio
XRD	X-ray diffraction

Greek letters

φ	Accessible porosity (%)
ρ	Density of concrete (kg/m^3)
ρ_w	Density of water (kg/m^3)
ρ^*	Density of fluid (kg/m^3)
Ø	Diameter (mm)
η	Dynamic viscosity of the fluid (Ns/m^2)
σ_e	Electrical conductivity (S/mm)
η_g	Gas viscosity coefficient (Ns/m^2)

β	Klinkenberg constant (N/m^2)
π	Phi
σ	Standard deviation

Roman letters

a	Fitting constant
A	Cross-sectional area of sample (m^2)
A_0	Projected surface area (m^2)
A_t	Total area covered the projected surface areas (m^2)
A_T	Total surface area following the shape of the dimples
C_1	Mean concentration of oxygen in the nitrogen stream at 1 bar (m^3/m^3)
C_2	Concentration of oxygen in the oxygen stream at 1 bar (m^3/m^3)
C_A	Concentration of oxygen (mol/m^3)
C_s	Chloride ion concentration of the sample at the surface which is in contact with the chloride solution
$C(x,t)$	Chloride penetration at a depth x (mm) at time t (seconds)
d	Sample thickness (m)
D	Non-steady state apparent diffusion coefficient (m^2/s)
erf	Error function which can be found in many mathematical tables
f_t	Tensile splitting strength (MPa)
F	Maximum applied load (N)
G_0	Percentage of oxygen in the initial nitrogen stream
G_1	Percentage of oxygen in outflow stream
h	Profile depth (mm)
H	Height of sample (mm)
i	Cumulative absorbed water per unit area of the inflow face (g/m^2)
J_A	Oxygen transport rate (kg/m^{2}s)
k_g	Gas permeability coefficient (m^2)
k_{int}	Intrinsic permeability coefficient (m^2)
l	Length of dimple (mm)
m_D	Mass of sample at preconditioned state (g)
m_{SSD}	Mass of sample at vacuum saturated-surface dry condition (g)

L	Length of sample (mm)
N	Number of dimple
P_1	Pressure of oxygen stream (bar)
P_2	Pressure difference between the oxygen and nitrogen stream (bar)
P_1^*	Absolute pressure on the inlet face (N/m^2)
P_2^*	Absolute pressure on the outlet face (N/m^2)
P_m	Mean inlet and outlet gas pressures (N/m^2)
ΔP	Pressure gradient (N/m^3)
Q	Oxygen diffusion rate at 1 bar (m^3/s)
Q^*	Oxygen permeation rate (m^3/s)
r	Surface roughness
R_1	Flow rate of nitrogen stream (mL/min)
R_2	Flow rate of oxygen stream (mL/min)
R	Measured electrical resistance (Ω)
R^2	Square-root
S	Sorptivity coefficient ($g/m^2min^{0.5}$)
t	Elapsed time (min)
$t_{exposure}$	Length of exposure to the chloride solution (seconds)
T_d	Texture density (%)
U	Voltage drop across the sample (V)
V	Sample volume (m^3)
Δw	Weight difference (g)
w	Width of dimple (mm)
W	Width of sample (mm)
x	Distance (m)

Table of contents

Declaration **2**

Abstract **3**

Acknowledgement **4**

Notation **7**

Table of contents **11**

List of tables **15**

List of figures **16**

Chapter 1 Introduction **24**

1.1 Research background 24

1.2 Objectives and scope 26

1.3 Thesis outline 26

Chapter 2 Literature review **28**

2.1 Interfaces in reinforced concrete 28

2.1.1 Aggregate-cement paste interface 28

2.1.2 Steel-concrete interface 31

2.1.3 New-to-old concrete interface 33

2.2 Effect of interfaces on bond strength 35

2.2.1 Aggregate-paste bond strength 35

2.2.2 Steel-concrete bond strength 35

2.2.3 New-to-old concrete bond strength 37

2.3 Effect of interfaces on mass transport properties 39

2.4 Reinforcement spacers 42

2.4.1 Background 42

2.4.2 Definitions and categories 44

2.4.3 Fixing and applications of spacers 46

2.4.4 Effect of spacers on properties of concrete 50

2.5 Summary 56

Chapter 3 Methodology 58
3.1 Materials 58
3.2 Spacers 59
3.4 Mass transport properties 62
3.3.1 Oxygen diffusion 62
3.3.2 Oxygen permeation 65
3.3.3 Water absorption 69
3.3.5 Accessible porosity 71
3.3.6 Electrical conduction 72
3.3.7 Chloride penetration 73
3.5 Fluorescent epoxy impregnation 79
3.6 Summary 82
Chapter 4 Combined effects of vertical reinforcement spacers and segregation on transport properties of concrete 83
4.1 Introduction 83
4.2 Experimental 84
4.2.1 Materials and mixture proportion 84
4.2.2 Experimental setup 86
4.2.3 Mixing, curing and conditioning 88
4.2.4 Image analysis to estimate segregation 94
4.2.5 Transport properties 96
4.3 Results 97
4.3.1 Segregation profile 97
4.3.2 Water sorptivity 99
4.3.3 Electrical conductivity 104
4.3.4 Sample porosity 104
4.3.6 Relationship between aggregate content, spacers and transport properties 107
4.4 Discussion 109
4.5 Conclusions 113
Chapter 5 Influence of SCMs on transport properties of concrete containing spacers 114
5.1 Introduction 114
5.2 Experimental 115

5.2.1 Materials and mixture proportions....115
5.2.2 Experimental setup....116
5.2.3 Sample mixing and curing....118
5.2.4 Sample conditioning....120
5.2.5 Transport properties measurement....123
5.3 Results....125
5.3.1 Transport properties after conditioning at 75% RH, 21°C....125
5.3.2 Accessible porosity from vacuum saturation....128
5.3.3 Transport properties after oven-drying at 50°C....128
5.4 Discussion....131
5.5 Conclusions....135
Chapter 6 Microstructure and chloride profile of spacer-concrete interface containing SCMs....136
6.1 Introduction....136
6.2 Experimental....137
6.2.1 Samples....137
6.2.2 Fluorescent epoxy impregnation....138
6.2.3 Sample preparation for microscopy....139
6.2.4 Laser scanning confocal microscopy....142
6.2.5 Quantitative image analysis....145
6.2.6 Chloride penetration....147
6.3 Results....150
6.3.1 Epoxy impregnation depth....150
6.3.2 Porosity of the spacer-concrete interface....155
6.3.3 Chloride penetration profile....159
6.4 Discussion....161
6.5 Conclusions....162
Chapter 7 Influence of surface texture on the spacer-concrete bond strength .. 163
7.1 Introduction....163
7.2 Experimental....165
7.2.1 Materials and mixture proportions....165
7.2.2 Producing surface texture on prefabricated spacers....166
7.2.3 Sample preparation....174

7.2.4 Splitting tensile strength test 178
7.3 Results 180
7.3.1 Prefabricated spacer properties 180
7.3.2 Bond strength of spacer-concrete interface 181
7.3.3 Relationship between curing ages, surface parameters and interface bond strength 186
7.3.4 Failure mode of prefabricated spacer-concrete interface 189
7.4 Discussion 193
7.5 Conclusions 195
Chapter 8 Influence of surface texture on transport properties 196
8.1 Introduction 196
8.2 Experimental 197
8.2.1 Materials and mixture proportions 197
8.2.2 Sample preparation 198
8.2.3 Transport measurements 199
8.3 Results and discussion 201
8.3.1 Oxygen diffusivity, oxygen permeability, and water sorptivity 201
8.3.2 Epoxy impregnation depth 207
8.3.3 Relationship between interface bond strength, surface texture parameters and transport properties 211
8.4 Conclusions 216
Chapter 9 Conclusions 217
Chapter 10 Implications and recommendations 222
10.1 Implications 222
10.2 Recommendations for future research 224
References 226
Appendices 238
Appendix I - Interface bond strength between spacer and concrete cured for 1 and 7 days 238
Appendix II - Failure mode of spacer-concrete interface 239
Appendix III - Publications arising from this research 245

List of tables

Table 2.1 Key literature on the effects of aggregate-paste ITZ on transport properties, arranged in chronological order. 39

Table 2.2 Key literature of the effects of steel-concrete interface on corrosion, arranged in chronological order. 40

Table 2.3 Key literature of the effects of new-to-old concrete interface on transport properties, arranged in chronological order. 41

Table 2.4 Summary of various codes of practice on spacer classification and placement. 43

Table 3.1 Specific gravity at saturated and surface dry condition (SSD), moisture condition and absorption values of the aggregates used. 59

Table 3.2 Properties of commercial spacers used in this study. 61

Table 3.3 Optimal operating conditions of the μXRF for chloride analysis 78

Table 4.1 Concrete mix proportion used in this chapter 85

Table 4.2 Compaction factors 90

Table 5.1 Oxide compositions and properties of cementitious materials used 116

Table 5.2 Mix proportions. 116

Table 5.4 Measured density of hardened concrete samples at 24 hours after demoulding 120

Table 7.1 Selected references on methods for improving interface bond strength for concrete repairs. 164

Table 7.2 Mix proportion of the mortar and concrete used in this chapter. 166

Table 7.3 Operating conditions of the LSCM for surface texture analysis. 167

Table 7.4 Dimensions of prefabricated spacer surface texture (units in mm). 173

Table 7.5 Shape, profile depth and various of surface texture parameters investigated. 174

Table 7.6 Density and compressive strength of prefabricated spacers. 181

Table 7.7 Splitting tensile test results 192

Table 8.1 Mix proportion for the prefabricated spacer and concrete used in this chapter. 197

List of figures

Figure 2.1 Schematic showing the formation of ITZ between aggregate and cement paste (Kjellsen et al., 1998).....29

Figure 2.2 Model of the ITZ between cement paste and aggregate particle (Zimbelmann, 1985). 30

Figure 2.3 Schematic illustration of the steel-concrete interface. *Red dashed lines* indicate preferential pathways for chloride ingress; *blue dots* represent adsorbed water (Angst et al., 2017). 32

Figure 2.4 Typical of microstructural gradients of (a) CH (Portlandite) and (b) porosity at the steel-concrete interface (Angst et al., 2017, Horne et al., 2007). 33

Figure 2.5 Schematic showing proposed microstructure of the old-new concrete interface. The second layer defined as a boundary between fresh and old concrete is the weakest layer of the interfacial zone (Xie et al., 2002).....34

Figure 2.6 Defects at the steel-concrete interface (Soylev and Francois, 2003). 37

Figure 2.7 Schematic of various test methods to determine interface bond strength (Beushausen and Alexander, 2008). 39

Figure 2.8 Types of spacers as classified according to BS 7973-1. Brackets refer to the load category of the spacer (L = Light; N = Normal; H = Heavy; C = Chairs).....46

Figure 2.9 Spacers for (a) bottom and (b) top reinforcements in slabs according to BS 7973-2 (dimension in millimetres). 47

Figure 2.10 Spacers for beams according to BS 7973-2 (dimensions in millimetres). 48

Figure 2.11 Spacers for columns according to BS 7973-2 (dimensions in millimetres). 49

Figure 2.12 Spacer causing corrosion on a reinforcing bar after 10 years weathering (Levitt and Herbert, 1970). 51

Figure 2.13 Spalling at the location of plastic spacer (Levitt and Herbert, 1970). 51

Figure 2.14 Reinforced concrete cubes containing embedded plastic spacer (a) and concrete block spacer (b) after over two years in an aggressive seawater environment (Society, 1981). 52

Figure 2.15 Inadequate quality of concrete spacers (Kenai and Bahar, 2003).....53

Figure 2.16 Corrosion occurring adjacent to plastic spacer (Rostam, 2005). 53

Figure 2.17 Preferential ingress of de-icing salts at the location of plastic spacers causing severe local corrosion in columns of road bridges in a marine environment (Poulsen and Mejlbro, 2010).....54

Figure 2.18 Spacer still attached to reinforcement after the concrete had been removed with no sign of corrosion (Shaw, 2008).....55

Figure 2.19 Typical example of corrosion occurring at the spacer-concrete interface (Tang and Utgenannt, 2009). Spacer location marked with a red circle. 55

Figure 2.20 Backscattered electron micrographs showing a porous and cracked spacer-concrete interface that facilitates penetration of external aggressive species causing degradation (Alzyoud et al., 2016). 56

Figure 3.1 Particle size distribution of sand and gravel.....59

Figure 3.2 Commercially-available spacers used in this study. 60

Figure 3.3 Diffusion test cell. 64

Figure 3.4 Schematic of the oxygen diffusivity test set-up (Wong et al., 2006a). 64

Figure 3.5 A typical kg vs 1/Pm plot for Klinkenberg correction. Sample is concrete at w/c 0.4. 66

Figure 3.6 Permeation test cell.....68

Figure 3.7 Schematic of the oxygen permeability test set-up (Wong et al., 2006a).....68

Figure 3.8 Example of water absorption test set-up; and (b) Schematic diagram of sorptivity test (Hall, 1989). 70

Figure 3.9 Typical plot of cumulative water absorption against square-root of time for concrete. 70

Figure 3.10 Vacuum saturation equipment.....72

Figure 3.11 Electrical conductivity test set-up.....73

Figure 3.12 Schematic of electrical conduction test set-up. 73

Figure 3.13 Chloride penetration test setup. 75

Figure 3.14 Freeze drying chamber.....75

Figure 3.15 Orbis Micro X-ray Fluorescence (μXRF) spectrometer. 77

Figure 3.16 Schematic diagram showing the main components of the ORBIS PC micro x-ray fluorescence (μ-XRF) bench-top analyzer (Source: EDAX AMETEK Inc.). 77

Figure 3.17 Set-up for fluorescent epoxy impregnation. 80

Figure 3.18 Procedure of epoxy impregnation.....80

Figure 3.19 Illustration of impregnation cell during experiment. 81

Figure 3.20 Setup for fluorescence imaging; A sample was placed directly under the camera at a distance of 150 mm between the sample and camera, and a distance of 50 mm between the sample and UV lamp. 82

Figure 4.1 Spacers used in this chapter. 84

Figure 4.2 Slump tests showing the improvement in workability of the fresh concrete with added superplasticiser. 85

Figure 4.3 Schematic diagrams showing: a) cast column *L80 x W90 x 400H*; b) cross section of column parallel to A-side showing the position of spacers and Ø12mm rebar and; c) samples extracted from column for transport tests (front and side view). 86

Figure 4.4 Set-up for casting column samples (front and side view of formwork).....87

Figure 4.5 Top view of column samples cast in a specially fabricated wooden mould with dimensions 80 mm depth, 90 mm width and 400 mm height after 24 hours of curing.....88

Figure 4.6 Illustration of the compaction process. 89

Figure 4.7 Samples during compaction process. Spacers placed at near the top samples remain in the right position. 89

Figure 4.8 Initial trials showing aggregate distribution on the cross-sections of cylindrical samples prepared at different levels of vibration.....90

Figure 4.9 Surface defects occurred due to inadequate release agent oil on mould. 91

Figure 4.10 Schematic diagram showing the top and bottom samples extracted for transport testing. Dimensions in millimetres. 92

Figure 4.11 Cross-section of rectangular samples extracted from column with cementitious (left) and plastic spacers (right) for transport testing. 93

Figure 4.12 Sample designation. 93

Figure 4.13 Example of image analysis showing segmented coarse aggregate particles on cross-sections taken at different heights (Sample is C2-PS). 95

Figure 4.14 Diagram of test set-up for the water absorption test. 96

Figure 4.15 Segregation profiles of samples compacted according to regime C1 and C2. ..97

Figure 4.16 Area distribution of aggregate particles measured from cut-surfaces at different heights. 98

Figure 4.17 Comparison between aggregate size distribution measured using sieve analysis method (solid line) and image analysis technique (dashed line). 99

Figure 4.18 Effect of spacer type and position on water sorptivity for compaction regime (a) C1 and (b) C2. Samples were conditioned at 75% RH, 21°C. 100

Figure 4.19 Effect of oven-drying at 50°C on the measured water sorptivity for compaction regime (a) C1 and (b) C2. 101

Figure 4.20 Typical plots of cumulative water absorption against square-root of time after conditioning at: (a) 75% RH, 21°C; (b) 50°C (Compaction regime C1). 102

Figure 4.21 (a) Fine cracks appearing on the base of samples containing plastic spacers conditioned at 50°C. (b) Crack widths were measured using a stereo microscope SZX9. .103

Figure 4.22 Effect of spacer type and position on electrical conductivity for compaction regime (a) C1 and (b) C2. Samples were conditioned at 75% RH, 21ºC then vacuum saturated prior to measurement.....104

Figure 4.23 Effect of spacer type and position on sample porosity for compaction regime (a) C1 and (b) C2. Samples were conditioned at 75% RH, 21°C then vacuum saturated prior to measurement.....105

Figure 4.24 Effect of oven-drying at 50°C on sample porosity for compaction regime (a) C1 and (b) C2. 106

Figure 4.25 Correlation between sample porosity and transport properties: (a) Water sorptivity; (b) Electrical conductivity. 108

Figure 4.26 Correlation between sample porosity and aggregate fraction. Showing that porosity increased with decreasing aggregate fraction. Solid and dashed circles indicate the C1- bottom and top samples respectively. 108

Figure 4.27 Effect of segregation and spacers on transport properties. Solid and dashed circles indicate the C1- bottom and top samples respectively. 109

Figure 4.28 Cross-section of samples extracted from column with plastic (top) and cementitious spacers (bottom) showing a porous interface underneath the spacer due to trapped bleed water. 111

Figure 5.1 Dimensions of the 'A' clip plastic spacer and cementitious spacer used in this chapter. 115

Figure 5.2 Experimental setup for casting cylindrical samples of 100 mm diameter and 50 mm height. 117

Figure 5.3 Materials used for casting concrete samples. 118

Figure 5.4 Compacted samples surrounded by wet hessian.....119

Figure 5.5 Conditioning box containing saturated NaCl to maintain relative humidity at ~75%. 121

Figure 5.6 Change in mass for 120d-samples subjected to conditioning at 75% RH, 21°C.. 122

Figure 5.7 Change in mass of samples subjected to conditioning at 50°C oven. 123

Figure 5.8 Typical plots of cumulative water absorption against square-root of time for 3d-samples containing 8% SF after conditioning at 75% RH, 21ºC.....124

Figure 5.9 Effect of spacers on a) oxygen diffusivity, b) oxygen permeability, c) water sorptivity, and d) electrical conductivity after conditioning at 75%RH, 21°C. 127

Figure 5.10 Accessible porosity after vacuum saturation. 128

Figure 5.11 Effect of spacers on (a) oxygen diffusivity, (b) oxygen permeability, and (c) water sorptivity after conditioning in a 50°C oven. 130

Figure 5.12 Effect of oven drying on sample porosity (28d-samples). 130

Figure 5.13 Cracks appearing on the surface of samples containing plastic spacer after conditioning at 50°C. 134

Figure 5.14 Illustration of the location of cracks on samples containing plastic spacer. ...134

Figure 6.1 Schematic illustration of cylindrical sample containing a cementitious spacer. 137

Figure 6.2 Sample designation. 138

Figure 6.3 a) Set-up of the vacuum epoxy impregnation kit; b) Pressure chamber. 140

Figure 6.4 Schematic of the extraction of a block sample for imaging. Drawing not to scale. 141

Figure 6.5 Grinding and polishing machine. 141

Figure 6.6 Olympus BX-51 petrographic microscope. 142

Figure 6.7 Epoxy impregnated and flat polished block samples ready for imaging. 142

Figure 6.8 Leica TCS SP5 laser scanning confocal microscope. 143

Figure 6.9 Schematic of LSCM. 144

Figure 6.10 Screenshot of Fiji/ImageJ, showing a LSCM image and its corresponding brightness histogram obtained when the brightness and contrast settings was set at optimum. The sample is FA-PS-120d. 145

Figure 6.11 Measuring porosity gradient at spacer-concrete interface using EDM. Sample is FA-CS-3d. 146

Figure 6.12 Quantifying porosity distribution at the cementitious spacer-concrete interface using brightness histograms of the pore and paste distance maps. 147

Figure 6.13 Change in mass of samples containing silica fume subjected to freeze drying. 148

Figure 6.14 Cross-sections of samples with plastic spacer (top) and cementitious spacer (bottom) showing the locations of µXRF spot analysis (red dots) for chloride profiling. 149

Figure 6.15 Close-up of the spacer-concrete interface showing the analysed µXRF spot (red dot) and fine debonding cracks at the interface. 150

Figure 6.16 Fluorescence images showing the extent of epoxy penetration on 3d-samples containing SF imaged under UV light after conditioning at 75% RH, 21°C (left) and at 50°C (right). 151

Figure 6.17 Fluorescence images showing the extent of epoxy penetration on 3d-samples containing FA imaged under UV light with different conditioning regime after conditioning at 75% RH, 21°C (left) and at 50°C (right). 152

Figure 6.18 Fluorescence images showing the extent of epoxy penetration on 3d-samples containing GGBS imaged under UV light with different conditioning regime after conditioning at 75% RH, 21°C (left) and at 50°C (right). 153

Figure 6.19 Effect of spacers, conditioning regime and SCM on the maximum depth of epoxy impregnation. 154

Figure 6.20 Examples of LSCM images showing (a) cementitious spacer-concrete interface and (b) plastic spacer-concrete interface. Samples are FA – 3d. 155

Figure 6.21 Average porosity distribution from the spacer-concrete interface for samples containing cementitious and plastic spacers. Samples were dried in a 40ºC oven for seven days prior to impregnation. 156

Figure 6.22 BSE image showing microstructure of the cementitious spacer-concrete interface at 500x magnification (field of view 415 x 553 μm). Sample is FA-CS-3d. 158

Figure 6.23 BSE image showing microstructure of the plastic spacer-concrete interface at 500x magnification (field of view 415 x 553 μm). Sample is FA-PS-3d. 158

Figure 6.24 Chloride penetration profiles for 28d-samples containing silica fume: (a) Conditioned at 75%RH, 21°C, vacuum saturated with water and then exposed to salt solution for 12 months; (b) Conditioned at 50°C oven and exposed to salt solution for 4 months 160

Figure 7.1 Aluminium plates for producing prefabricated spacers with various surface textures. 168

Figure 7.2 Examples of 3D surface texture plots. 169

Figure 7.3 Poor surface quality due to hydrogen gas released from the reaction between aluminium plate and alkalis from Portland cement. 170

Figure 7.4 Silicone moulds used for producing various surface texture.....171

Figure 7.5 Illustration of surface texture parameters used for calculating roughness and texture density 172

Figure 7.6 Flow chart summarising the sample preparation and testing methodology. ...175

Figure 7.7 Mould assembly for preparing prefabricated spacers with modified surface texture. 175

Figure 7.8 Fresh mortar and concrete mixes. 176

Figure 7.9 Prefabricated cementitious spacers with various surface textures. 176

Figure 7.10 Set-up for casting concrete against prefabricated spacers. 177

Figure 7.11 Example of prefabricated mortar spacer-concrete sample with different interface characteristics after 24hr of casting (Left: CO; right: HS). 177

Figure 7.12 Schematic diagram of splitting tensile strength test for prefabricated spacer-concrete interface. 179

Figure 7.13 Splitting tensile strength set-up. 180

Figure 7.14 Splitting tensile strength of prefabricated mortar and concrete spacers. 181

Figure 7.15 Development of prefabricated mortar spacer-concrete bond strength with age for various interface surface textures. 182

Figure 7.16 Development of prefabricated concrete spacer-concrete bond strength with age for various interface surface textures. 182

Figure 7.17 Relationship between bond strength and surface roughness (Cured for 28d). 183

Figure 7.18 Relationship between bond strength and texture density (samples were cured for 28d). 183

Figure 7.19 Entrapped air voids (circled) at the prefabricated spacer-concrete interface (Top: RL texture; Bottom: PY texture). 184

Figure 7.20 Relationship between bond strength and profile depth. (Samples were cured for 28d). 185

Figure 7.21 The direction of the grooves on the GV and GH textures relative to loading direction has an effect on failure mode and bond strength. 185

Figure 7.22 Relationship between surface texture parameters, curing ages and interface bond strength of samples with prefabricated concrete spacer. 187

Figure 7.23 Relationship between surface texture parameters, curing ages and interface bond strength of samples with prefabricated mortar spacer. 188

Figure 7.24 Schematic of failure mode at the prefabricated spacer-concrete interface: (a) ID only; (b) ID and FS; (c) ID and FC. 189

Figure 7.25 Example of a split prefabricated spacer-concrete interface showing failure by combined debonding and fracturing. 190

Figure 7.26 Typical failure (interface debonding) at the prefabricated spacer-concrete interface for the control sample (flat interface). 191

Figure 7.27 Typical failure at the prefabricated spacer-concrete interface after curing for 1d (top), 7d (middle), and 28d (bottom). Sample contains prefabricated spacer with square texture (SQ). 191

Figure 7.28 Comparison of failure interface between (a) Prefabricated mortar spacer-concrete and (b) Prefabricated concrete spacer-concrete. 193

Figure 8.1 Cured cylindrical sample containing half-spacer and half-concrete. 198

Figure 8.2 Change in mass of samples subjected to 50°C. 199

Figure 8.3 Transport test cell showing a sample with textured spacer-concrete interface. 200

Figure 8.4 Effect of spacer surface texture on mass transport properties of samples after drying at 50°C 202

Figure 8.5 Normalised oxygen diffusivity, oxygen permeability and water sorptivity showing the substantial reduction in permeability for samples with textured spacers. 203

Figure 8.6 Sample with GV texture showing groves parallel to the flow direction of gas/water during transport testing. 203

Figure 8.7 Entrapped air voids at the prefabricated spacer-concrete interface. 205

Figure 8.8 Entrapped air content at the prefabricated spacer-concrete interface measured using image analysis. 206

Figure 8.9 Accessible porosity of prefabricated spacer-concrete composite samples of various interface textures. 207

Figure 8.10 Relationship between total accessible porosity and air void fraction measured at prefabricated spacer-concrete interface.....207

Figure 8.11 Maximum intrusion depth of fluorescent epoxy at the prefabricated spacer-concrete interface.....208

Figure 8.12 Cross-sections of fluorescence images showing the extent of epoxy penetration at the prefabricated spacer-concrete interface. All samples contain half-concrete spacer and half-concrete (Red boxes show prefabricated spacer-concrete interface).....210

Figure 8.13 Relationship between interface bond strength and transport properties for samples with various textured spacer-concrete interface.....212

Figure 8.14 Relationship between interface bond strength and accessible porosity for samples with various textured spacer-concrete interface.....213

Figure 8.15 Relationship between transport properties and surface texture parameters for samples with various textured spacer-concrete interface.....214

Figure 8.16 Relationship between accessible porosity and transport properties.....215

Chapter 1

Introduction

1.1 Research background

Concrete, a composite material consisting mainly of Portland cement, water, and aggregates, is by far the most commonly used man-made construction material on earth. It is strong under compression, versatile, relatively cheap, and suitable for a wide range of construction applications. Current production of concrete is well over 1 m^3/year for every person on earth, and this is the most used material in the world after water and it will continue to rise. Because of the vast amounts of concrete used, it is estimated that the cement industry contributes about 5-7% global man-made CO_2, making it the second largest industrial source of carbon emission after the steel industry (Worrell et al., 2001, Summerbell et al., 2016, Naucler and Enkvist, 2009, Tanaka and Stigson, 2009, Flatt et al., 2012).

However, concrete structures can gradually degrade when subjected to various exposure environments. The most common degradation mechanism affecting concrete structures is corrosion of embedded steel reinforcement. Other forms of degradation mechanisms include frost damage, sulphate attack, alkali-aggregate reaction and leaching. These are caused by ingress or movement of water and dissolved aggressive agents such as oxygen, chlorides, carbon dioxide, sulphates, or acids into concrete via its porous microstructure. Therefore, the transport properties of concrete, i.e. the resistance of concrete against different transport mechanisms such as diffusion, permeation and capillary suction play a major role in determining long-term durability.

Degradation of concrete structures leads to problems such as cracking, spalling, reduction in steel reinforcement area, strength reduction, and loss of functionality. Premature degradation of concrete is a major problem worldwide with huge economic, environmental and societal impacts. As such, research on understanding factors influencing degradation mechanisms and developing methods to enhance the durability of concrete is of significance importance.

Concrete cover is the distance between the steel reinforcement and the outer surface of the concrete (BS EN 1992-1-1:2004+A1:2014). It acts to protect the reinforcement from the

external environment by providing a physical barrier against ingress of harmful substances during the service life of the concrete structure. It is a fundamental design parameter and plays an important role to ensure the long-term performance of concrete structures. An adequate cover of good quality concrete and sufficient thickness is essential to ensure durability, and in particular, to protect steel reinforcement against the corrosion (Rostam, 1996, Subramanian and Geetha, 1997).

Reinforcement spacers are important devices in reinforced concrete that are used to support reinforcing steel during concreting in order to achieve the required concrete cover. Spacers are generally made of cementitious material, plastic or steel wire (BS 7973-1:2001). Design standards and codes of practice for concrete structures require a spacer to be located at every meter (or less), or as otherwise necessary, along the length of reinforcing bars to ensure that the bars remain in place during concreting and left permanently in the structure (BS 7973-2:2001). Therefore, spacers are an essential component of reinforced concrete. Although it seems small and inconsequential, a typical concrete structure can contain thousands of spacers. Despite the obvious importance of spacers, very little fundamental research has been carried out on the influence of spacers on the long-term durability of concrete structures.

Recent research at the Concrete Durability Group, Imperial College London found that cementitious spacers, plastic spacers and wire chairs can have negative effects on the microstructure of the surrounding concrete, which in turn increases the mass transport properties of concrete (Alzyoud et al., 2016). It was found that the presence of spacers produces a micro-cracked and highly porous interface, which lowers the resistance of concrete to ingress of aggressive agents causing degradation. Earlier studies by Society (1981) and Vik (2002) also suggested that there might be a poor bond between spacers and concrete and that this is likely to encourage corrosion, although no experimental evidence was provided. The study by Tang and Utgenannt (2009) also suggested that the presence of spacers may lead to chloride ions penetrating concrete due to the poor interface between concrete and spacers, thus accelerating corrosion initiation. Possible causes for the inferior spacer-concrete interface include poor bonding, differential volume changes (shrinkage, thermal movements) causing cracking and high porosity at the interface due to micro-bleeding or poor particle packing effects. The inadequate quality of spacers used in construction as investigated by Kenai and Bahar (2003) is also considered to be a factor contributing to concrete deterioration.

Despite some evidence showing the negative effects of spacers in concrete by providing easy access of aggressive agents through the spacer itself or the spacer-concrete interface, very little fundamental and systematic research has been undertaken to address this problem. To the best

of our knowledge, research in how to improve spacer design to enhance the microstructure and the durability of the spacer-concrete interface is lacking. These are the critical issues that the present work seeks to redress.

1.2 Objectives and scope

This thesis aims to develop a better understanding of the influence of reinforcement spacers on the microstructure and mass transport properties of concrete structures. The work also aims to develop methods to enhance the bonding and mechanical interlocking between a spacer and concrete, thereby reducing the penetration of deleterious species along the interface.

These will be achieved by:

- Understanding the effects of vertically cast spacers and segregation on mass transport properties;
- Investigating the potential of using supplementary cementitious materials (SCMs) to improve the spacer-concrete interface;
- Re-engineering the spacer surface texture to enhance mechanical interlocking with concrete as well as its resistance to transport processes.

1.3 Thesis outline

The thesis consists of ten chapters. Chapter 1 introduces the research background, objectives and scope of the study. Chapter 2 reviews the different types of interface characteristics in reinforced concrete, such as the interface between aggregate and cement paste, between steel reinforcement and concrete, and between old and new concrete (e.g. in patch repair). It also provides a critical literature review of reinforcement spacers and their effects on the microstructure and durability of concrete. Chapter 3 gives the detail of materials and equipment used in this study including the experimental approach and the detailed test procedures. The main findings are then presented in Chapters 4, 5, 6, 7 and 8.

Most studies to date have concentrated on the properties of concrete containing spacers that support horizontal reinforcement. However, it is suspected that the use of spacers for vertical reinforcement would have induced greater impact on the microstructure and mass transport properties. This is due to bleeding and segregation that inevitably occur in fresh concrete. Understanding and quantifying these were the focus of Chapter 4.

A range of methods to enhance the interface between a spacer and concrete was then investigated. Chapters 5 and 6 present the influence of supplementary cementitious materials (SCMs) such as silica fume (SF), fly ash (FA) and ground granulated blast-furnace slag (GGBS) as a partial replacement of Portland cement CEM I on microstructure and transport properties of concrete containing reinforcement spacers respectively. It is well-known that the incorporation of SCMs can improve the properties of concrete via a filler effect and pozzolanic reaction. The focus of Chapters 5 and 6 is to establish whether this can be used to mitigate the negative effect of spacers.

Chapter 7 deals with another approach to enhance the interface bond strength between a spacer and concrete by optimising the surface texture of spacers. Cementitious spacers with a range of surface textures were prepared. A splitting tensile test was carried out to ascertain if the engineered surface texture and enlarged contact surface area can improve adhesion and achieve a better mechanical interlocking with concrete. The influence of spacer composition on the interface properties was also discussed.

Chapter 8 investigates the influence of spacer surface texture on the transport properties. This is to establish whether the surface texture can also improve the resistance of concrete to penetration of gas and liquids. The pore structure at the spacer-concrete interface was studied using fluorescent epoxy impregnation method and quantitative image analysis.

Finally, the main findings from this thesis are summarised in Chapter 9. The implications of these findings and recommendations for further work are given in Chapter 10.

Chapter 2

Literature review

This chapter reviews the literature on the topics relevant to the scope of this thesis. Very little fundamental knowledge and research about the interface between a spacer and concrete exist. Therefore, the review will first focus on the characteristics of other interfaces in reinforced concrete including those between: a) aggregate particles and cement paste, i.e. the interfacial transition zone (ITZ); b) steel reinforcing bars and concrete; and c) old and new concrete (repair materials). The microstructural characteristics and mechanical properties of these interfacial zones and their influence on the durability of concrete are presented. This is followed by a review of the types and applications of spacers, including standards and codes of practice. Findings from previous studies on the influence of spacers on properties and durability of concrete are also discussed. Other topics relevant to this study will be reviewed and presented in the following chapters as appropriate.

2.1 Interfaces in reinforced concrete

The existence of interfaces in concrete was first investigated by Jacques Farran in 1956 as mentioned in the RILEM report "Interfacial transition zone in concrete" Farran (1996). It was known as "transition aureole" between aggregate and cement paste, and hereafter referred to as the interfacial transition zone (ITZ). Since then, many studies have been conducted to understand the nature and characteristics of the ITZ in concrete as well as its influence on concrete properties, even today. Other types of interfaces also exist, and the relevant ones are reviewed in the following sections.

2.1.1 Aggregate-cement paste interface

Formation mechanism and microstructure

According to Scrivener et al. (2004), the ITZ between aggregate particles and cement paste is a particularly important interface in reinforced concrete. This refers to the cement paste region adjacent to every aggregate particle surface, which has a microstructure that is disrupted by the

presence of the aggregate itself. Zimbelmann (1987) and Bentur and Odler (1996) found that the formation of the ITZ is mainly influenced by micro-bleeding and wall effects. Bleeding occurs when the mix water separates from other denser constituents and accumulate on the surface of aggregate particles or becomes trapped under aggregate particles. In contrast, the wall effect refers to the difficulty of packing small particles close to the surfaces of larger particles. In concrete, cement particles are unable to effectively fill the space adjacent to aggregate particles. Both effects create a high-water content and low cement content, therefore an effectively larger water/cement ratio in the vicinity of the aggregate surface compared to the "bulk" paste region farther away. Thus, the ITZ tends to be a highly porous zone that contains less anhydrous cement content, but rich in $Ca(OH)_2$ due to preferential precipitation. Apart from bleeding and wall effects, the higher porosity at the ITZ is also caused by the one-sided growth effect, as proposed by Garboczi and Bentz (1991). In the bulk paste region farther away from the aggregate surface, hydration products are able grow into from all directions. But very near the aggregate surface, there is no growth from the direction of the aggregate since the aggregate is non-reactive, therefore the space-filling resulting from hydration is less prominent at the ITZ. The main mechanisms forming the ITZ are shown in Figure 2.1.

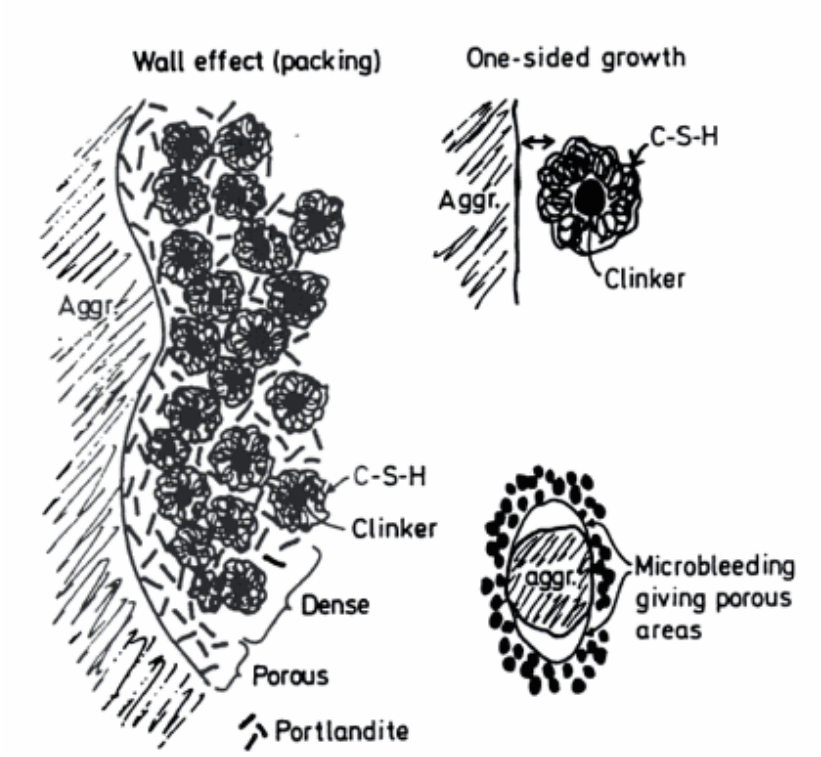

Figure 2.1 Schematic showing the formation of ITZ between aggregate and cement paste (Kjellsen et al., 1998).

Although the mechanisms forming the ITZ are approximately the same, the thickness of the ITZ is not uniformly exhibited in different concrete mixes and even within the same concrete mix. Studies have shown that the ITZ thickness varies between different aggregate particles and on different parts of the same aggregate. It also depends on the cement type and size, w/c ratio and the aggregate size used (Monteiro et al., 1985b, Breton et al., 1992a). Several techniques have been used to examine and to quantitatively characterise the ITZ. These include scanning electron microscope in the backscattered electron (BSE) imaging mode (Scrivener et al., 1988, Diamond, 2004, Diamond and Huang, 2001), mercury intrusion porosimetry (MIP) (Snyder et al., 1992), X-ray diffraction (XRD) (Tasong et al., 1999, Gao et al., 2005a), laser scanning confocal microscopy (LSCM) (Zampini et al., 1995), and nanoindentation testing (Mondal et al., 2008).

For example, Hoshino (1989) found ITZ widths ranging from approximately 10 to 100μm, with the highest porosity forming near the bottom surface of aggregate particles and the lowest porosity near the top surface, relative to casting direction. Ollivier et al. (1995) and Scrivener et al. (2004) estimated the effective ITZ thickness to be approximately 20 to 50μm, with the major difference in characteristics from the bulk paste occurring within the first 20μm from the aggregate particle. This is the region where the microstructure and hydration products formed are significantly different from the bulk cement paste. The microstructure of the ITZ as illustrated by Zimbelmann (1985) is shown in Figure 2.2.

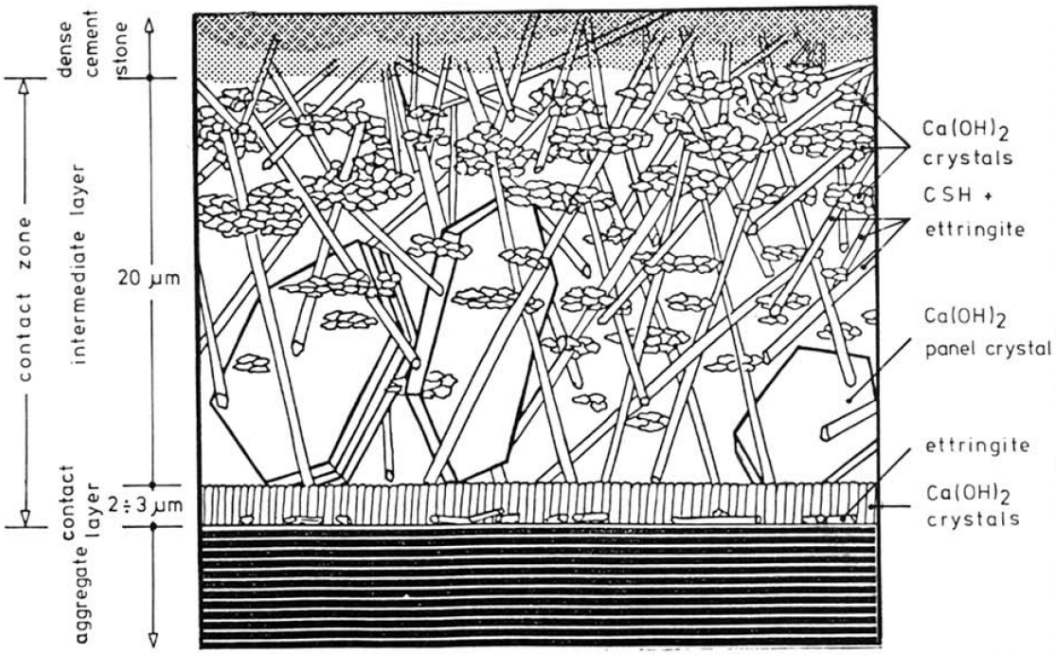

Figure 2.2 Model of the ITZ between cement paste and aggregate particle (Zimbelmann, 1985).

Influence of mineral admixtures

Generally, the use of ultrafine reactive supplementary cementitious materials to replace Portland cement will improve particle packing and hence the characteristics of the ITZ. For example, Cheng-yi and Feldman (1985); Bentur and Cohen (1987); Scrivener et al. (1988); Cohen et al. (1994) showed that by incorporating silica fume in the mortar mix, the microstructure of the ITZ becomes much denser and homogeneous, without the presence of large CH precipitates. The level of porosity at the ITZ becomes similar to that of the bulk paste, thereby improving the paste-aggregate bond. Bentz and Garboczi (1991) also found that the inclusion of fly ash in the mix reduces the volume fraction of CH and increases the amount of the total C-S-H at the ITZ, relative to that present in the bulk paste. Larbi (1993) described that addition of silica fume, fly ash, metakaolin or blast furnace slag in mortar mixes modifies the interface to become denser with no CH crystals.

2.1.2 Steel-concrete interface

Formation mechanism and microstructure

It is well-established that concrete is strong in compression, but weak in tension. Therefore, steel reinforcement is embedded in structural concrete to form a composite material i.e. reinforced concrete, that can withstand not only compression, but also bending and tension. The presence of steel leads to the formation of an interfacial zone between steel and concrete. Similar to the aggregate-cement paste interface, the steel-concrete interface plays an important role in determining the performance of reinforced concrete. The formation mechanism and microstructure of the steel-concrete interface are considered to be similar to that of the aggregate-paste ITZ in terms of porosity and portlandite distribution, which is primarily attributed to the inefficient packing of cement particles due to a wall-effect (Khalaf and Page, 1979, Monteiro et al., 1985a, Yue and Shuguang, 2001, Horne et al., 2007).

However, differences between the aggregate-paste interface and the steel-concrete interface have been noted. For example, Otsuki et al. (1998) noted that gaps tend to form at the steel-concrete interface as a result of vibration. It was observed that the vibration can lead to higher local water content and inefficient packing around the steel. Khayat (1998) explained that the voids formed under horizontal rebar were due to bleeding, aggregate segregation, or surface settlement (bulk shrinkage) of fresh concrete. Fresh concrete consists of an unstable dispersion of cement paste and aggregate. When the bleeding water rises towards the upper concrete

surface, some of the bleed water can become trapped under various obstacles for example steel reinforcement. It causes an increase in the local w/c ratio under the rebar, thus increasing the porosity. The settlement of aggregates at the same time can also lead to a minute separation between the lower portions of reinforcement and concrete leaving an air void. A study by Horne et al. (2007) also observed that the underside of horizontal rebars had gaps or much higher porosity, and no CH within the first 40µm compared to the topside and around vertical rebar as shown in Figure 2.4. A recent review paper by Angst et al. (2017) presented a schematic illustration to describe the characteristics of the steel-concrete interface (Figure 2.3).

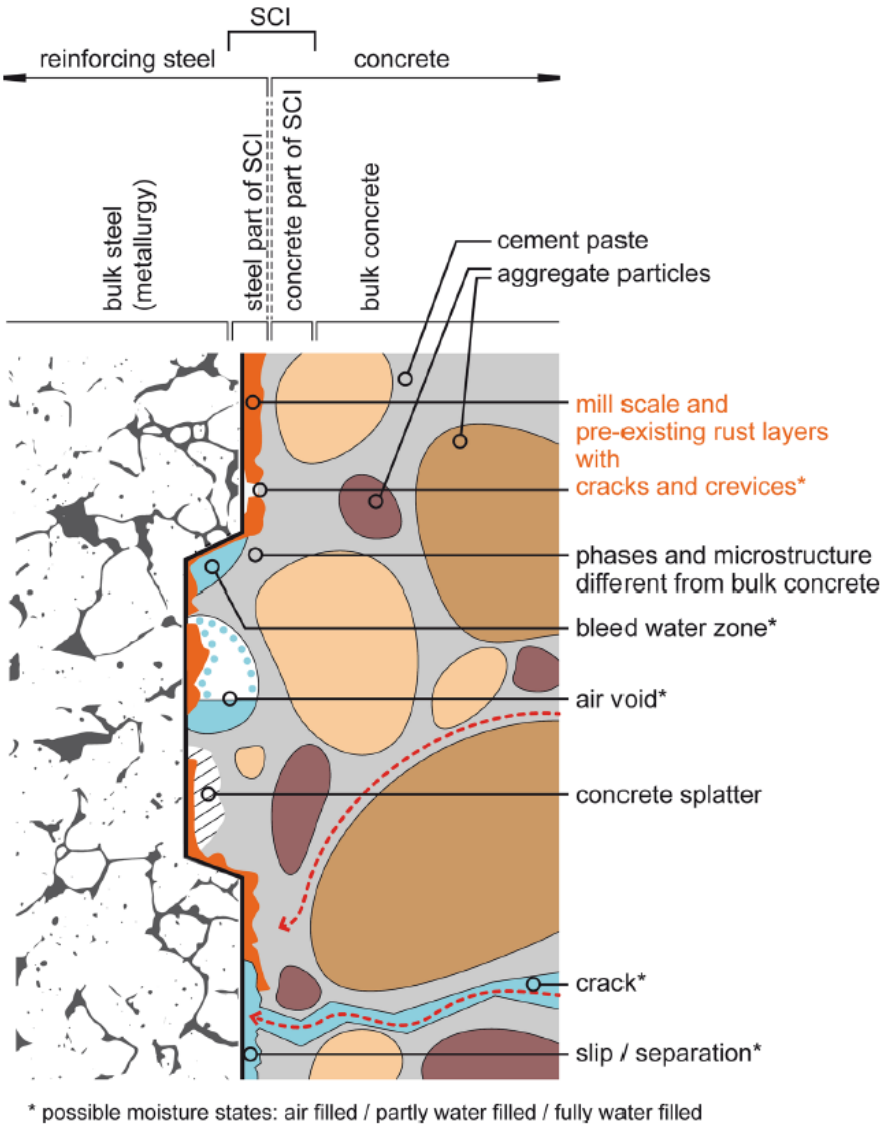

Figure 2.3 **Schematic illustration of the steel-concrete interface. *Red dashed lines* indicate preferential pathways for chloride ingress; *blue dots* represent adsorbed water (Angst et al., 2017).**

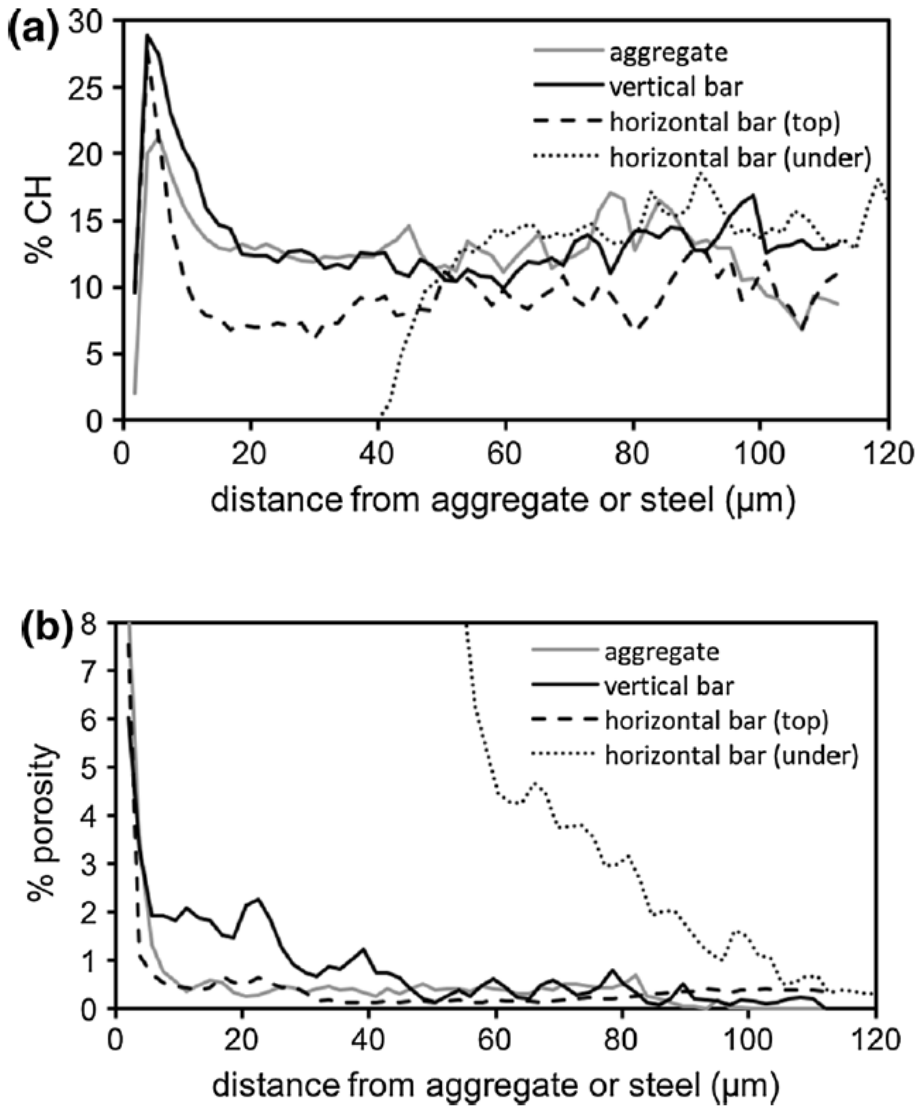

Figure 2.4 Typical of microstructural gradients of (a) CH (Portlandite) and (b) porosity at the steel-concrete interface (Angst et al., 2017, Horne et al., 2007).

2.1.3 New-to-old concrete interface

Formation mechanism and microstructure

An interface forms when new concrete is cast against old concrete. Such interfaces are common in construction, for example: between two different concrete elements, concrete overlays used for repair and strengthening of concrete members or composite members consisting of precast elements. According to Pigeon and Saucier (1992), Carles-Gibergues et al. (1993b) and Delagrave et al. (1997), the interface between the old (substrate) and the new concrete (repair material) displays similar characteristics to the interface between aggregate and cement paste. This has been attributed to the wall-effect that creates a weak link in the repaired material.

Further studies by Momayez et al. (2004) and Lukovic et al. (2014) observed that the weak link leads to a high probability of cracking.

Xie et al. (2002) proposed a model of the interfacial microstructure between new and old concrete. This is shown in Figure 2.5. The first layer located on the old concrete surface is called a penetration layer. This mainly consists of C-S-H and some amount of Aft (ettringite) or $Ca(OH)_2$ (portlandite) and is assumed to have no harmful influence on interface bond strength. The second layer was defined as a boundary between fresh and old concrete, also known as the strongly-affected layer. This layer is not only rich in $Ca(OH)_2$ and needle-shaped ettringite (Aft) crystals, but also contains a large number of voids and cracks. This layer is the weakest layer of the interfacial zone. The third layer is known as the weakly-affected layer, which is located within the new concrete. It has a similar microstructure as the new concrete but less C-S-H, therefore, is stronger than the second layer. The thickness of this layer depends on the nature of the new concrete and bonding agent.

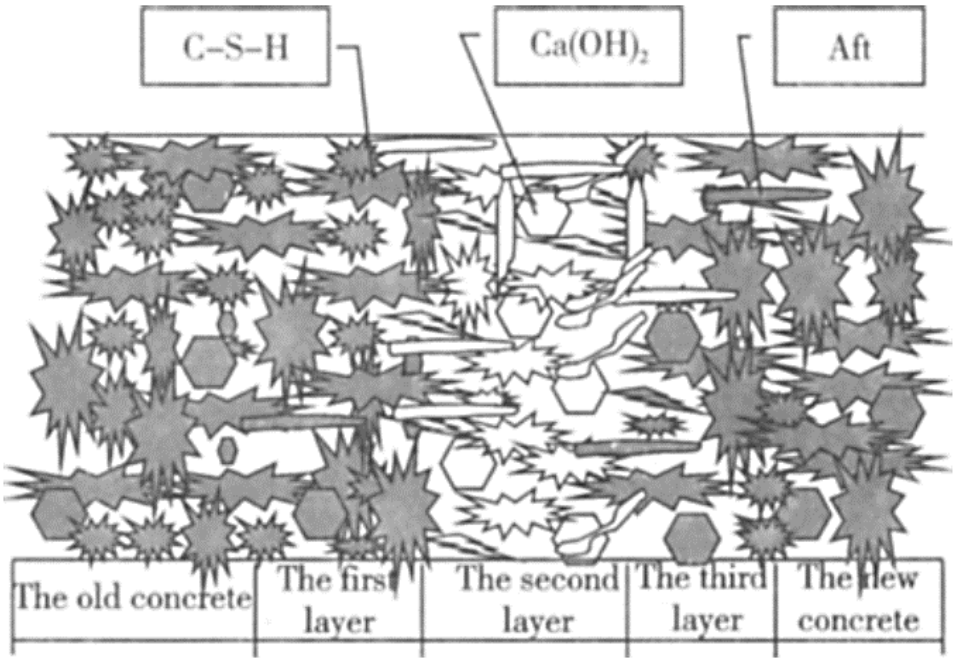

Figure 2.5 Schematic showing proposed microstructure of the old-new concrete interface. The second layer defined as a boundary between fresh and old concrete is the weakest layer of the interfacial zone (Xie et al., 2002).

2.2 Effect of interfaces on bond strength

Bond strength is a generic term used to describe the quality of the bond between two systems, for example between aggregate and cement paste, steel and concrete, and substrate and new concrete. It is measured by the stress required to separate the bonded layers from each other. The bond characteristics of each interface are discussed below.

2.2.1 Aggregate-paste bond strength

The ITZ is generally considered a weak link in concrete influencing its mechanical performance and is responsible for limiting some of the basic strength properties of concrete. This is because the bond strength between the aggregate-cement paste ITZ is much lower than the strength of either the aggregate particles or cement paste. Hsu and Slate (1963) investigated four types of rock (sandstone, granite, New York limestone, Indiana limestone) containing different moisture contents to investigate the tensile bond strength between the aggregate and cement paste. Three different surface roughness (naturally-fractured, saw-cut, and polished surface) were used for each rock. They observed that the cement paste-aggregate tensile bond strength was about 41 to 91% of the paste bond strength depending on the type and surface roughness of the aggregate and w/c ratio. A rougher surface and lower w/c ratio produced higher bond strengths. Bentur and Cohen (1987) showed that by using silica fume, an increase in concrete strength in the order of 25-30% over plain cement concrete can be achieved, without any corresponding strength increase in the paste sample. Pink and Beaudoin (1993) also found that the aggregate-paste bond strength depends on the thickness of the water layer on the aggregate surface and w/c ratio. Therefore, decreasing the thickness of the water layer at the beginning of the mixing and w/c ratio are two effective ways to increase bond strength. However, this finding was based on numerical simulations only and no experiments were performed to prove this argument.

2.2.2 Steel-concrete bond strength

The bond between steel and concrete is very important in reinforced concrete structures because without any bond, the steel is completely ineffective and does not contribute to the flexural resistance of the structure. The bond depends on chemical adhesion, steel-concrete friction, and the hardened concrete properties. The microstructural characteristics of the interface between steel and concrete also greatly affects the interface bond strength. Soylev and Francois (2003) and Castel et al. (2006) investigated the presence of defects (e.g. voids) at the underside of the horizontal rebar as shown in Figure 2.6. The authors found that such defects decrease the bond strength between the rebar and concrete.

As described in Section 2.1, the inclusion of supplementary cementitious materials such as silica fume in concrete can also reduce both the porosity and thickness of the interfacial zone and hence increase the pull-out strength between steel and concrete (Gjorv et al., 1990). This is due to a decrease in the amount of bleed water accumulating at the interface during casting and the amount of CH deposits, as well as densification of the interface because of the pozzolanic reaction between CH and SF. Li et al. (1998) conducted a study on the enhancement of steel-concrete bond properties. Several methods were investigated including matrix modification by adding 1 or 2% (by weight of cement) of polyvinyl alcohol (PVA) powder into the concrete mix and surface modifications by coating the steel surface with cement, cement plus silica fume, and cement plus PVA. The mechanical properties of the interface were evaluated by push-out tests, microhardness measurement and scanning electron microscopy (SEM). The results showed that such treatment methods reduced the porosity at the interface and increased the interfacial micro hardness. However, no explanation was provided for this.

Surface treatments such as sand-blasting, water immersion, and ozone treatment have also been found to improve mechanical interlocking between steel and concrete, thus enhancing the interface (Chung, 2001). Sand-blasting results in roughening and cleaning the steel surface by removing rust and other contaminants on the surface. Water immersion involves immersing the steel in water at room temperature for two days leading to the formation of a black oxide layer on the steel surface. Ozone treatment involves exposing the steel to ozone gas for 20 minutes at 160°C, followed by drying at high-temperature (110°C) for another 50 minutes. This causes the formation of a dark grey oxide layer on the surface. The results showed that all the treatments increased bond strength, however ozone treatment produced the highest bond strength compared to sand-blasting and water immersion.

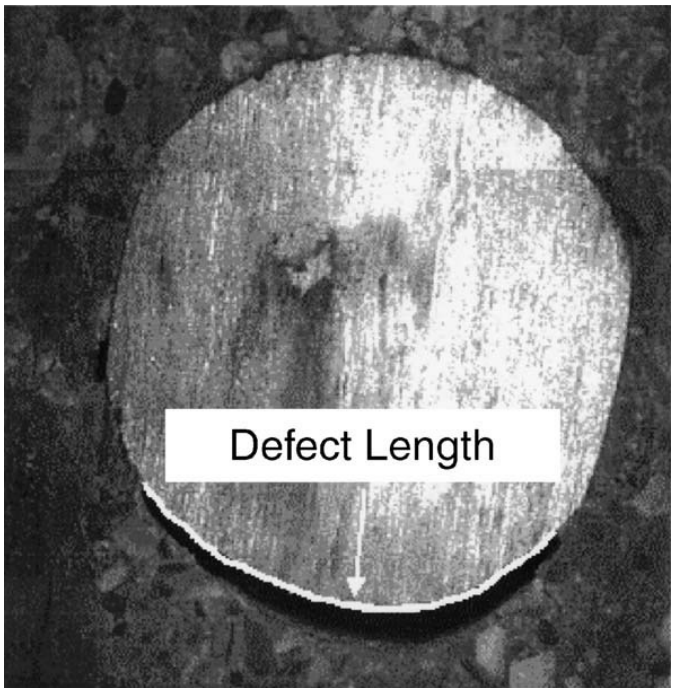

Figure 2.6 Defects at the steel-concrete interface (Soylev and Francois, 2003).

2.2.3 New-to-old concrete bond strength

According to Emberson and Mays (1990), repair materials for concrete structures can be categorised into three groups: resinous materials (i.e. epoxy mortar), polymer modified cementitious materials (i.e. SBR modified), and conventional cementitious materials (i.e. OPC/sand mortar). Conventional cementitious materials such as mortars and concretes are often used, and they are considered to be the best option as repair materials because of the compatibility with the damaged concrete. Also, they are easy to be applied, placed and cured, and are cost-effective.

A successful repair is considered to be achieved when the repaired concrete shows uniform performance and behaves as a monolithic system with the substrate (old concrete). There are two crucial criteria for achieving reliable performance and durability of the repair. The repair material should be compatible with the concrete substrate in terms of the physical, chemical and electrochemical properties, and have sufficient bond strength to enable uniform transfer of stresses (Morgan, 1996, Emmons and Vaysburd, 1994).

British Standard (BS EN 1504-10:2017) defines bond as the adhesion of the applied repair material to the old concrete (concrete substrate). There are two main parameters that affect bond strength and its development at the interface between the new and old concrete. These are adhesion force and moisture transport. Adhesion force covers at least three types of bond:

chemical bond which is the result of chemical reactions that occur between the old and new concrete, mechanical bond which is related to the interpenetration of the new concrete into the roughness and porosity of the old concrete resulting in mechanical interlocking, and a physical bond associated with the Van der Waals and surface tension forces (Courard, 2000). Moisture transport is driven by the difference in the moisture content between new and old concrete. Water will move from areas of higher concentration to areas of lower concentration. In other words, unsaturated old concrete will absorb the water from fresh concrete by capillary suction. The absorption rate of the old concrete is influenced by its initial moisture content and surface porosity.

The interface bond strength is influenced by at least three factors: (i) the properties of the old concrete and its surface (moisture content and roughness); (ii) the properties of the new concrete and its ability to adhere to the old concrete; and (iii) environmental conditions. A number of studies have been carried out on understanding the factors affecting the bond strength. These have included substrate surface roughness (Morgan, 1996, Julio et al., 2004, Beushausen and Alexander, 2008, Santos and Julio, 2011, Tayeh et al., 2013), substrate moisture content (Wall and Shrive, 1988, Morgan, 1996, Carles-Gibergues et al., 1993a, Geissert et al., 1999), and the properties of substrate concrete and repair materials (Wall and Shrive, 1988, Carles-Gibergues et al., 1993a, Li et al., 2001, Hassan et al., 2001, Julio et al., 2006, Beushausen and Alexander, 2008, Santos and Julio, 2011, Tayeh et al., 2013). Among these, the surface roughness is considered to be the primary factor contributing to bond strength.

A range of tests has been developed in the laboratory to evaluate bond strength (Beushausen and Alexander, 2008, Momayez et al., 2004). They are divided into several categories. The first category is based on applying tensile stress, either via a pull-off test (Figure 2.7a), direct tension, and tensile splitting (Figure 2.7b). The most commonly used test methods under this category are the tensile pull-off test and the splitting test. In the tensile splitting test, a prism or circular or square cross-section is placed under longitudinal compressive loading (Figure 2.7b). Tensile stresses cause failure and split the specimen into two halves. A further explanation on this test is provided in Chapter 7. The second category is based on applying shear stress and is referred to as a direct shear method. This consists of L-shaped and direct shear tests (Figure 2.7c). The third category is based on the combination of shear and compression. The slant shear test is the most widely used test in this category (Figure 2.7d). The slant shear test uses a square prism, or a cylindrical sample made of two identical halves bonded at 30° and tested under axial compression, as seen in Figure 2.7d. During loading, the interface is under compressive and shear stresses.

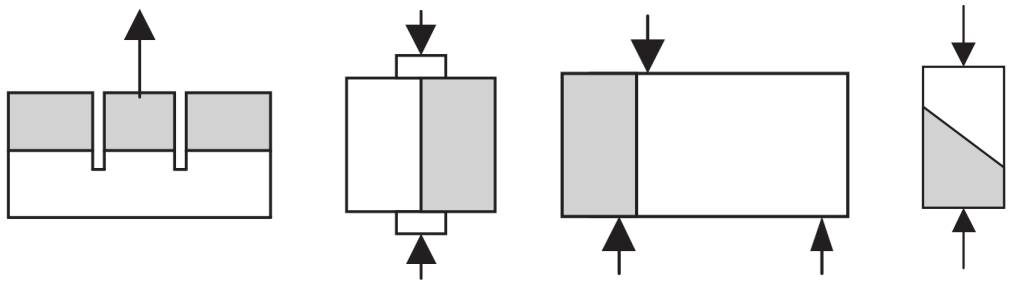

(a) Pull-off test (b) Splitting-tensile test (c) Direct shear test (d) Slant shear test

Figure 2.7 **Schematic of various test methods to determine interface bond strength (Beushausen and Alexander, 2008).**

2.3 Effect of interfaces on mass transport properties

Achieving an adequate interfacial bond between various constituents is a critical requirement for durable reinforced concrete. As reviewed in the previous sections, interfaces are highly porous and considered to be a weak link in reinforced concrete. Consequently, cracks tend to form within this zone, providing a direct path for the ingress of aggressive agents into concrete. A summary of the main studies on the effect of interfaces on mass transport properties published since 2000 is presented in Tables 2.1 to 2.3.

Table 2.1 Key literature on the effects of aggregate-paste ITZ on transport properties, arranged in chronological order.

Reference	Sample details	Transport properties	Summary finding
(Shane et al., 2000)	OPC with 0.4 w/c, silica sand content 0-50% vol.	Electrical conductivity from time of mixing up to 32 days, using impedance spectroscopy	The presence of ITZ did not affect the global electrical conductivity of mortar. However, there were significant differences in conductivity between ITZ and the bulk paste. These were most significant when the hydration degree was between 0.5 and 0.8.
(Asbridge et al., 2001)	OPC and OPC/10% MK mortars at w/c 0.35 and 0.40, with silica glass bead (1–1.25 mm diameter) as sand at 0 55% vol.	Chloride diffusion was monitored under both steady- and non-steady-state condition on 3 mm thick disc	Non-steady-state chloride diffusivity of OPC mortar increased with sand content; a sharp rise was observed at sand vol. fraction above 35%. Steady-state diffusivity of mortars incorporating MK did not vary significantly with sand vol. fraction, suggesting an improved ITZ.
(Princigallo et al., 2003)	Concrete at w/c 0.37, 10% SF and total aggregate of 0-75% vol. Max	Electrical conductivity tested at early ages of 10 min up	Results showed that the existence of a percolating pathway through the ITZ

	aggregate size: 16 mm.	to 5 days after mixing.	when the aggregate exceeded 60% vol. fraction.
(Wong et al., 2009)	Cement paste, mortars and concrete at w/c 0.3 and 0.5, binder type: CEM I and CEM II with 8% SF, total aggregate of 0-70%.	Oxygen diffusivity, oxygen permeability, water sorptivity	The ITZ may contain a higher local transport property than the bulk paste, but its effect on the overall transport property is small. This is because the effects of total porosity, tortuosity, and presence of cracks outweigh the effect of ITZ.
(Jiang et al., 2016)	Cement mortar with rod-shaped aggregates at w/c 0.55 and river sand of 10% volume fraction.	Water vapor diffusivity was measured by the penetration rate of water vapor through thin slide of specimens.	Results showed that polishing the aggregate surface increases the diffusivity significantly.

Table 2.2 Key literature of the effects of steel-concrete interface on corrosion, arranged in chronological order.

Reference	Sample details	Test methods	Summary finding
(Soylev and Francois, 2003)	Samples containing Ø10 mm steel rebar were immersed in the 35 g/l NaCl solution for 1 week and kept in room conditions for 4 weeks (wet/dry cycle). A total of cycle is 55 weeks.	Corrosion was measured by polarisation resistance at the end of each steel and corroded surface area.	Presence of porous interface enhances the corrosion of reinforcing steel due to lack of chemical (passivation) and physical protection supplied by dense concrete.
(Nasser et al., 2010)	110 x 220 mm cylinder specimens containing Ø12 mm ribbed bars	Macrocell corrosion	Defects at the steel-concrete interface (air void or gap) significantly increases the microcell driving potential and the galvanic corrosion current.
(Zhang et al., 2011)	Concretes contained Ø12 mm horizontal ribbed steel bar at different levels were subjected to wetting/crying cycles in salt water.	Polarisation resistance was performed to monitor steel corrosion during ageing up to 55 weeks.	Presence of interfacial defects (air voids) significantly increases the corrosion rate. The corrosion pattern observed along the steel-concrete interface was affected by the void.

Table 2.3 Key literature of the effects of new-to-old concrete interface on transport properties, arranged in chronological order.

Reference	Sample details	Transport properties	Summary finding
(Misra et al., 2001)	Old concrete at w/c 0.4, 0.5 and 0.6 was cured in water for two weeks. The top surface was shot blasted. 50 mm thick new concrete was placed on it and cured for four weeks at 20°C. The effect of applying the cement slurry at the interface was investigated.	Air permeability on 50 mm thickness sample and 300 mm x 125 mm cut surface area.	Very small differences in air permeability were observed between interface with a cement slurry coat and control, or between interfaces with a poor bond and good bond.
(Tayeh et al., 2012)	Old concrete: Normal concrete and new concrete: UHPFC. Old concrete was cured in water for 3 days. Composite samples were steam cured for 48h at 90°C, 100% RH, subsequently cured in water for 7 and 28 days.	Gas and water permeability on 40 mm thick, 50 mm diameter discs.	Gas and water mostly passed through the old-concrete with little or no influence of the interfacial zone.
(Guang-cheng et al., 2014)	Old concrete was cored from an in-situ 600d old pavement. New concrete was made of Portland cement, FA, GGBS, and SF at 0.30, 0.38, 0.60 w/c. New-old samples were prepared in 100 mm diameter moulds with the bottom layer consisting of 25 mm old concrete.	Chloride permeability and chloride diffusivity	The new-to-old concrete interface influences chloride permeability and diffusivity, depending on the composition of new concrete. This is because the interface plays a barrier effect on transport of ion or water.

2.4 Reinforcement spacers

2.4.1 Background

Reinforcement spacers made of mortar or concrete, plastic, or steel wire in various shapes and sizes are the most reliable means of ensuring that reinforcement steel is positioned at the correct distance from the concrete surface (formwork). Spacers are used in both horizontal and vertical elements, in situ or precast, including slabs, beams, columns, and walls. Prior to 1960, any available materials found on site such as stones, bricks, timber pieces, or tiles were commonly used to support the reinforcement. At present, development of standard practice and design guides dictate that such materials should not be used as bar supports.

Formal guidance on the use of reinforcement spacers in concrete is a relatively recent development. The Concrete Society report CS101 "Spacers for reinforced concrete" published in 1989 was one of the first comprehensive guidance on how to achieve specified nominal cover in concrete structures. British Standard Institution (BSI) published the first code-of-practice on spacers in 2001 (BS 7973) preceded by a CIRIA report (King and Dakin, 2001) in the same year, which also discusses the use of spacers. Other similar publications include the American Concrete Institute (ACI 315-99) "Details and detailing of concrete reinforcement" in conjunction with Concrete Reinforcing Steel Institute (CRSI, 2011) "Placing Reinforcing Steel", the Canadian Standards Association (CSA A23.1-14) "Concrete materials and methods of concrete construction" and the Deutsches Institut für Normung (DIN 1045-1) "Structures made of concrete, reinforced concrete and pre-stressed concrete structures – Part 1: Design and construction". At present, it seems there is no standard that recognises the importance of spacers on durability, therefore no guidance is available either on performance testing of the durability of spacers or concrete containing spacers nor for testing the spacer bond to concrete. Also, there is a lack of guidance on the manufacture, shape and material of the spacer. All the standards confirmed that the selection of suitable spacers is the responsibility of the contractors.

Table 2.4 summarises the recommended classification and placement of spacers from these guidance documents. Because all the standards provided almost the same information about the spacers, therefore, in Section 2.4.2, the detailed information presented on spacers will focus on BS 7973 as the reference standard in the UK.

Table 2.4 Summary of various codes of practice on spacer classification and placement.

Standard	Spacer classification	Placing reinforcement spacers
[USA] CRSI-RB4.1:2016 ACI 315-99	Types of bar supports: Steel wire, precast concrete (also known as "dobies"), and plastic bar supports. Steel wire spacers are classified into: Class 1. Epoxy, vinyl or plastic coated for moderate to maximum exposure; Class 2. Stainless steel protected wire bar supports; Class 3. Bright basic wire-provide no corrosion protection Plastic and precast concrete supports can be used for all corrosion resistance classifications.	Spacers to be sufficient in number and strength to support the required reinforcing steel to prevent displacement during construction and to keep the steel at a proper distance from the formwork. Spacers cast in ground to be spaced at 1200 mm in each direction Spacers spacing depends upon the size and placing of the reinforcing bar being supported. The tolerance of spacer dimension to provide the required cover <+/- 3mm. Precast concrete supports shall be submerged in potable water for a minimum of one hour prior to testing. A load of 6.8 kg +/- 2.3 kg shall be applied and allow the support to hold this load.
[Canada] CSA A23.1-14	Spacers shall be made of plastic, plastic coated steel, or prefabricated concrete (precast concrete supports) with compressive strengths equal to or exceeding the placed concrete. The concrete shall be air entrained and chlorine free. Wooden blocks, bricks, stones, pebbles, metal pipe, and plastic shall not be used as bar supports. Bar supports shall be nonconductive and have a geometry and bond characteristics that deter the movement of moisture from the surface to the reinforcement. Bar supports in contact with the soil shall have a base area of less than 10,000 mm². Bar supports and side form spacer	Bar supports shall have sufficient strength and stiffness to carry the loads from the reinforcement, construction crew and concrete pressure without failure, displacement or significant deformation. Drawing shall indicate sizes, spacing, and locations of chairs and spacers. Slab reinforcement to be supported at maximum 1200 mm each way. Wall reinforcing to have side form spacers at minimum 2400 mm vertically and 1200 mm horizontally. Column spirals to have vertical spacers at every turn.
[Germany] DBV Data sheet	Requirement of the spacers: A sufficient capacity and tipping stability, safe enough can be attached to the reinforcing bar, be	Spacers to have sufficient capacity and stability depending on load and

"Spacers" DIN 1045-1:2001	designed so that the spacer is not completely enclosed, have a sufficient resistance to the alkalinity of concrete, made of a material that does not promote the corrosion of the reinforcement. Spacers are classified into two performance class L1 or L2 according to their capacity. L1: No increased demands on capacity and tilt stability; L2: Increased demands on the carrying capacity and rollover stability. Choice of the spacer depends on exposure classes of DIN 1045-1: Increased freeze-thaw resistance, suitably for components that are exposed to temperature stresses, and high resistance to water, chemical, and chloride attacks. Spacer types: Wheel shape, point shape (unattached and attached), line shape (unattached and attached), flat shape (unattached and attached).	temperature exposure. Line spacers to be staggered under the main reinforcement to minimise risk of crack formation in the tension/compression zones. Tolerance: <5mm.

2.4.2 Definitions and categories

The BS 7973-1:2001 defines a spacer as a component of reinforced concrete that is used to support and locate reinforcement in the correct position, so that the nominal cover between the reinforcement and the formwork is maintained before and after concreting. Spacers are made from three basic materials: cementitious material, plastics or steel wire with a number of different shapes and sizes. Cementitious spacers should have a minimum compressive strength of 50 N/mm^2 at 28 days and should be pre-manufactured rather than made in-situ on the construction site. According to (BS EN 13670:2009), cementitious spacers should have at least the same strength and corrosion protection as the concrete in the structure. Plastic spacers should have at least 25% voids within the enclosed perimeter to allow fresh concrete to interweave during compaction, thereby counteracting the thermal expansion of the plastic which is 10 times higher than concrete. When steel wires are used to support reinforcement from an exposed face, the ends of each steel leg shall be encased in a protective tip for a distance of at least 40 mm.

The selection of spacers mainly depends on several factors, which include their applications (horizontal or vertical elements), whether in-situ or precast, and the size and weight of the reinforcement to which they are to be fixed. However, all spacers must have an equivalent durability with the surrounding concrete and not cause any deterioration to the reinforcement or the concrete. BS EN 13670 suggests that the spacers should not lead to enclosure of air, crack

formation, penetration of water or damage of the reinforcement over the design service life of the structure.

There are four categories of spacers and chairs classified according to their application. These are light, normal, heavy, and chairs. The light category refers to spacers that are used to support vertical reinforcement. The normal category refers to spacers that are used to support the reinforcement with bar size of 20 mm or less, while spacers for bar size greater than 20 mm are classified in the heavy category. Chairs is the category of spacers that are used to separate layers of reinforcement and to support the top reinforcement in slabs. Common examples of spacer types classified according to BS 7973-1 are summarised in Figure 2.8.

Spacers may also be classified as point or line spacers as shown in Figure 2.8. Line spacers are used to support horizontal layers of reinforcement, mainly for heavily reinforced foundations. Point spacers are attached to the reinforcement using a tying wire; these are known as wire-on spacers and are usually made of cementitious materials. Point spacers can also be attached to reinforcing steel via a clip action that is an integral part of its design; these are known as clip-on spacers and are usually made of plastic. Clip-on and wire-on spacers are used for most purposes including foundations, columns, beams, slabs, and walls and are designed to be used with conventional formwork and a range of reinforcement sizes. For heavy-duty applications, some clip-on spacers are designed with a base-like tower. Wire-on cementitious spacers are available in single, double, or triple cover format, but the single cover format is often recommended to prevent incorrect positioning of the reinforcing steel. Tie wires can be mild, galvanised or stainless steel. However, in order to avoid disfiguring the formwork surface and giving a poor finish, care must be taken to ensure the wire does not protrude into the outer concrete surface.

Wheel-spacers with a circular cross-section are made with cementitious or plastic materials. Cementitious wheel spacers are used for heavy-duty applications, while plastic wheel spacers are normally designed for light category applications, i.e. for horizontal reinforcement not subject to any foot traffic and for vertical elements such as column, wall, etc. Chairs made of steel wire are grouped into three categories: individual, continuous and circular chairs. The individual chairs are used as single point spacers available in standard heights of between 75 mm and 350 mm. Continuous and circular chairs are used to support grid or mesh reinforcements.

Cementitious spacer	a) Line spacer (N, H)	b) Wire-on spacer (N, H)	c) Wheel spacer (L)
		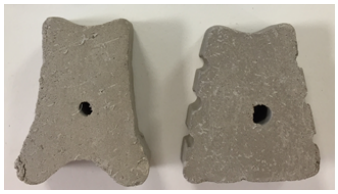	
Plastic spacer	a) Line spacer (N, H)	b) Clip-on spacer (L, N)	c) Wheel spacer (L)
			
Chair	a) Continuous chair (C)	b) Line chair (C)	c) Circular chair (C)
	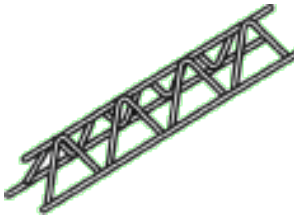	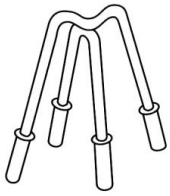	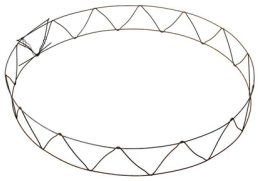

Figure 2.8 Types of spacers as classified according to BS 7973-1. Brackets refer to the load category of the spacer (L = Light; N = Normal; H = Heavy; C = Chairs).

2.4.3 Fixing and applications of spacers

Part 2 of BS 7973 specifies the requirements for the fixing and application of spacers including tying and spacing in elements subjected to normal construction load to achieve and maintain the required concrete cover. A brief summary is provided here.

Slabs

According to BS 7973-2, spacers used to support the bottom reinforcement bars in slabs shall be located at centres not exceeding 50*d*, where *d* is the bar diameter, or 1000 mm and staggered. Welded fabric shall be supported by spacers at centres not exceeding 500 mm in two directions at right angles (Figure 2.9a). For doubly- reinforced sections, continuous chairs are positioned at suitable locations to support the top reinforcement off the bottom reinforcement. In the case where there is no bottom reinforcement, individual chairs shall be located at centres not

exceeding 50*d* in both directions for individual bars, or 500mm for welded fabric (Figure 2.9b). Line spacers (either plastic or cementitious) and wire-on spacers can be used in slabs.

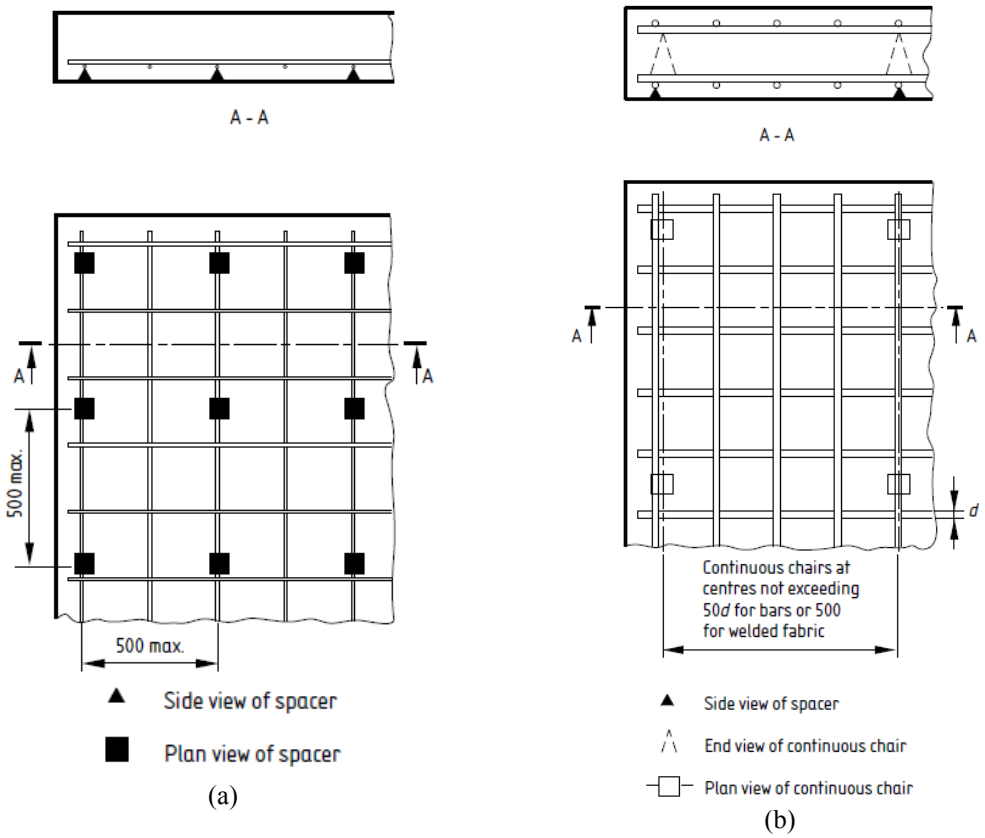

Figure 2.9 Spacers for (a) bottom and (b) top reinforcements in slabs according to BS 7973-2 (dimension in millimetres).

Beams

According to BS 7973-2, all spacers in beams shall be fixed to links or fabrics at centres not exceeding 1000 mm as shown in Figure 2.10. For the bottom face of beams, a number of spacers are required depending on the beam width. For narrow beams with a width of less than 250 mm, one spacer positioned in the middle of the bottom leg of the link is sufficient. For beams with widths of 250 mm to 500 mm, two spacers are required within 50 mm of the ends of the bottom link. For wide beams with widths greater than 500 mm, three spacers shall be positioned within 50 mm of the ends of the bottom link.

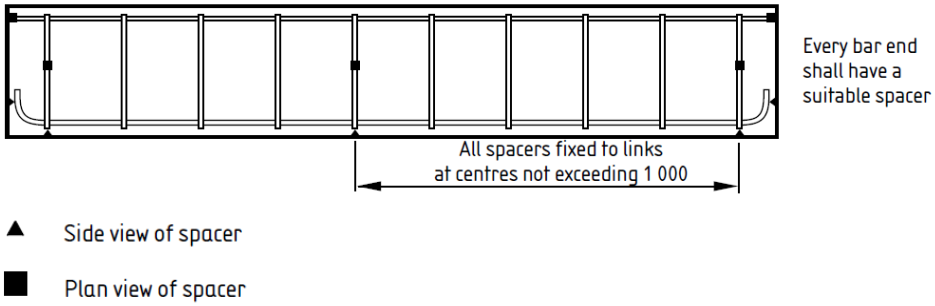

(a) Beam elevation

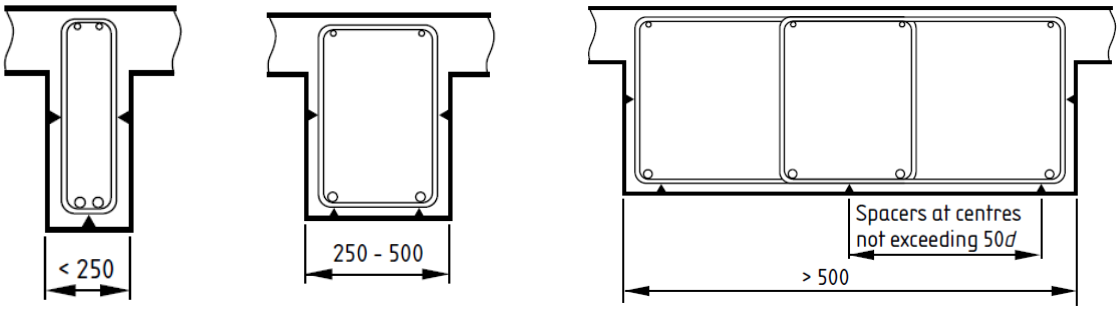

(b) Narrow beam (c) Narrow beam (d) Wide beam

Figure 2.10 Spacers for beams according to BS 7973-2 (dimensions in millimetres).

Columns

Spacers in wide columns (sides exceeding 50*d*) shall be placed on all sides of the same link with the distance between spacers not exceeding 50*d*. For small columns (sides not exceeding 50*d*), spacers shall be positioned in the middle of the link. All spacers fixed to the links shall be at the top, middle and bottom of each lift of concrete and centres not exceeding 100*d* as shown in Figure 2.11.

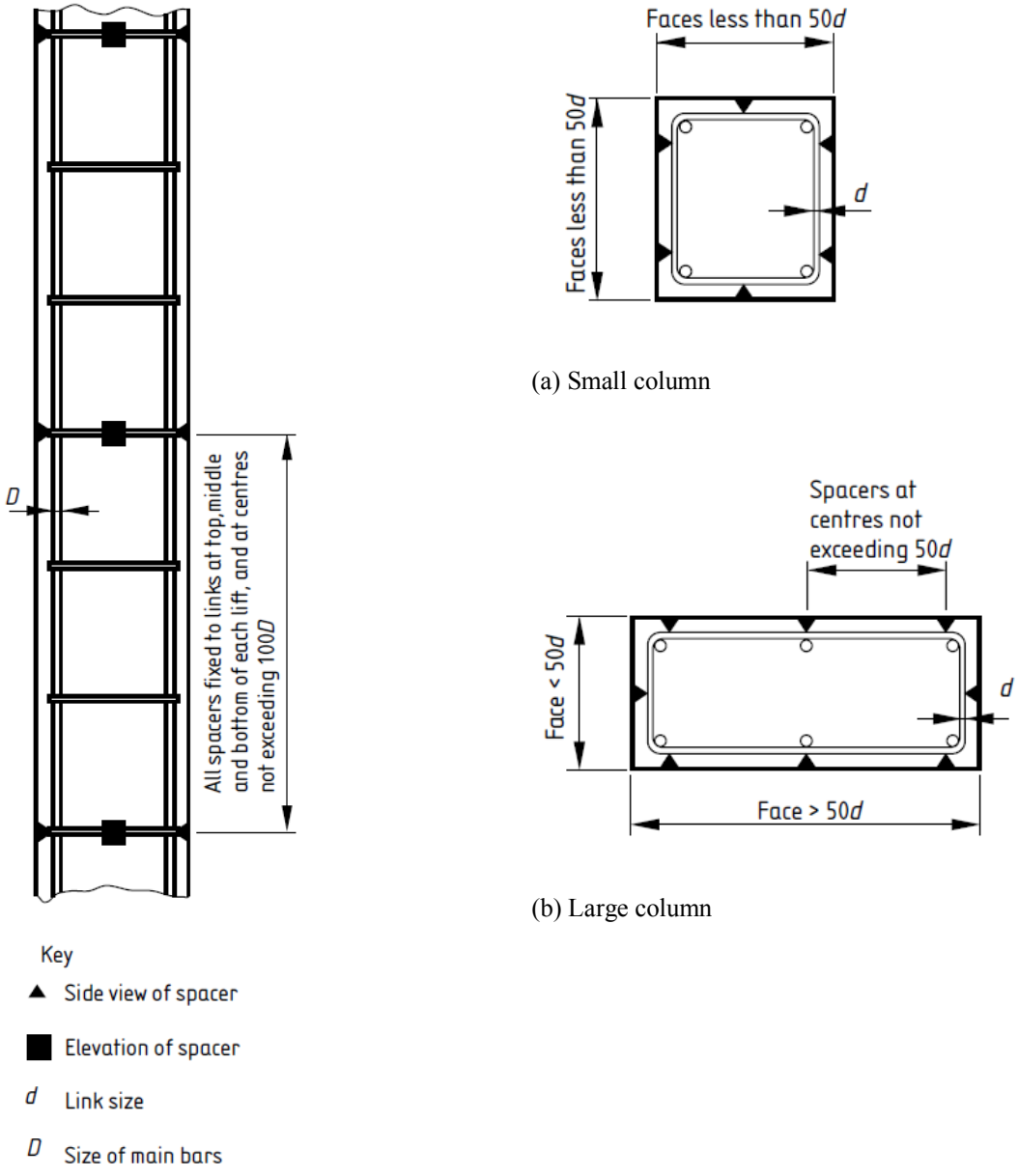

Figure 2.11 Spacers for columns according to BS 7973-2 (dimensions in millimetres).

2.4.4 Effect of spacers on properties of concrete

A small number of studies have reported that the presence of spacers can have important effects on the performance of reinforced concrete. Several investigations on the influence of spacers on the properties of concrete have been carried out on existing field structures or laboratory prepared samples. These are reviewed in chronological order.

Earlier investigations on the effect of spacers have mainly come from qualitative field observations. For example, Levitt and Herbert (1970) investigated the performance of plastic wheel and mortar spacers embedded in concrete beams of dimension 75 mm *x* 75 mm *x* 150 mm prims of a C45-type concrete after ten years of weathering (Figure 2.12). No further explanation regarding the weathering condition was provided. In order to stimulate reinforcement loads, the prisms were loaded for 24 hours. Visual observations indicated slight corrosion at the location of plastic spacer and this was assumed to be due to the presence of voids within the spacer that did not allow the maximum aggregate size to nestle comfortably in these voids. However, considerable local reinforcement corrosion was found at the locations of mortar spacers. This was assumed to be due to the poor quality of the spacer itself or the poor interface between the spacer and concrete. Furthermore, Figure 2.13 shows that surface spalling occurred at the location of plastic spacers. This behaviour occurs not only because the plastic spacer has differential thermal expansion with the surrounding concrete, but also there is no void within the spacer.

The Concrete Society of Southern Africa (Society, 1981) reported the risks of using plastic and precast concrete spacers in an aggressive seawater environment. A series of concrete samples were subjected to cyclic wetting and drying in artificial sea water (4 days in seawater and 3 days drying) in the coastal region of South Africa for over two years. The concrete cover was 25 mm. The concrete spacers were made of high-quality concrete with a compressive strength of 41 MPa. The study reported signs of severe reinforcement corrosion at locations of plastic spacers, but the sample containing concrete spacers appeared not to have corroded as shown in Figure 2.14. However, no explanation was provided for this.

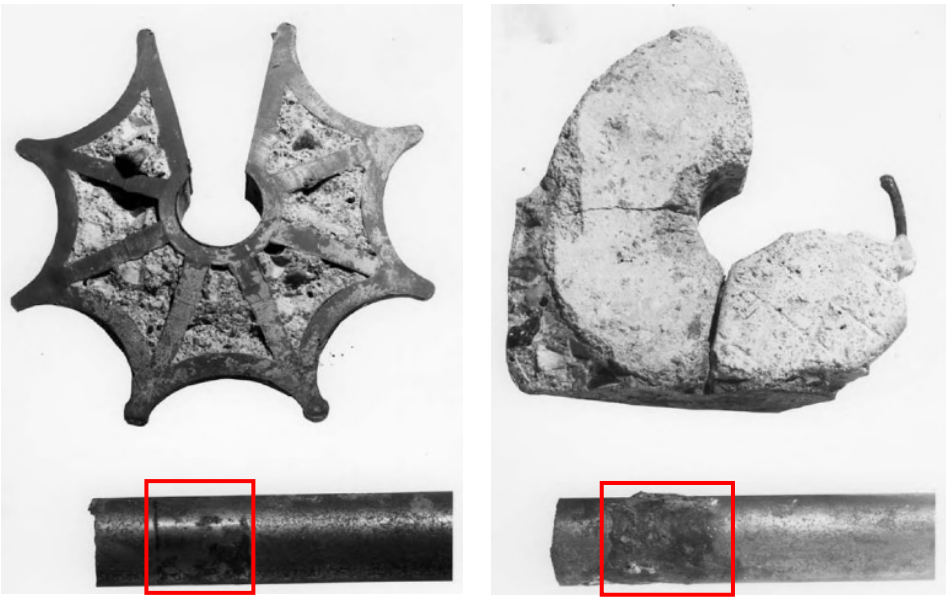

(a) Plastic spacer (b) Mortar spacer

Figure 2.12 Spacer causing corrosion on a reinforcing bar after 10 years weathering (Levitt and Herbert, 1970).

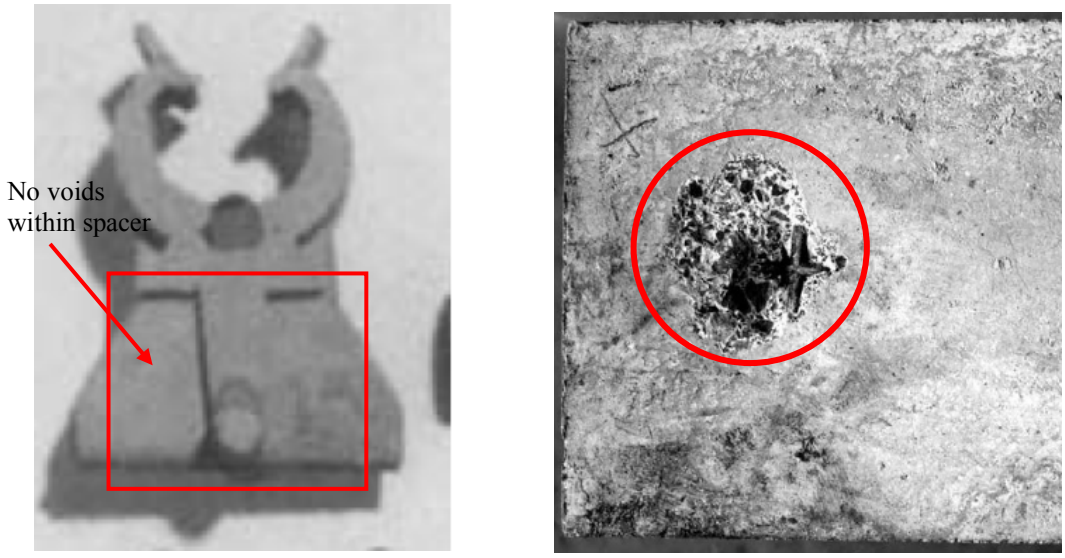

Figure 2.13 Spalling at the location of plastic spacer (Levitt and Herbert, 1970).

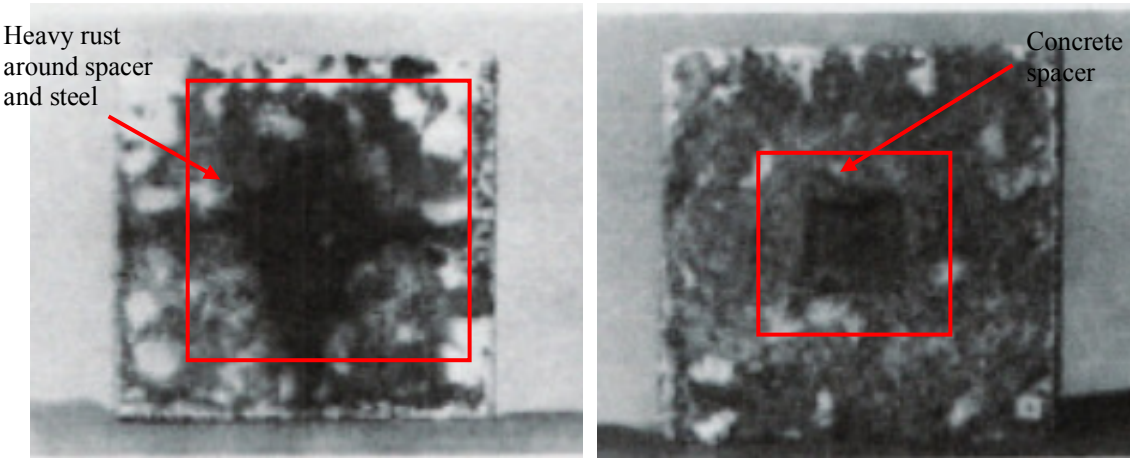

(a) (b)

Figure 2.14 Reinforced concrete cubes containing embedded plastic spacer (a) and concrete block spacer (b) after over two years in an aggressive seawater environment (Society, 1981).

Shaw and Kutti (2003) reported an earlier investigation carried out on the Barseback nuclear power plant that was submerged in seawater. The authors observed some evidence of severe corrosion occurring in the inlet culverts of the concrete structure, causing a 25% reduction in reinforcement in certain locations. Spacers made of cementitious materials (mortar) were believed to be the single most common cause of the problem due to their porous nature. Vik (2002) also stated that the use of spacers made from inferior-quality concrete, plastic, and steel wire, to varying degrees, was likely to encourage corrosion. However, there was no experimental evidence provided to prove this argument.

Kenai and Bahar (2003) also reported on their visual inspection of the Algiers airport building. The spacers were retrieved from the structure, dried and tested for water absorption. They found that the spacers used were made on site and were of inadequate quality containing high open porosity with the water absorption ranging from 10-13% (Figure 2.15). This study proposed that repair works should involve removal of all the apparent spacers and application of a repair mortar on the beam bases to enhance the concrete appearance and durability. It should be noted that site-made mortar spacers are no longer acceptable by current standards.

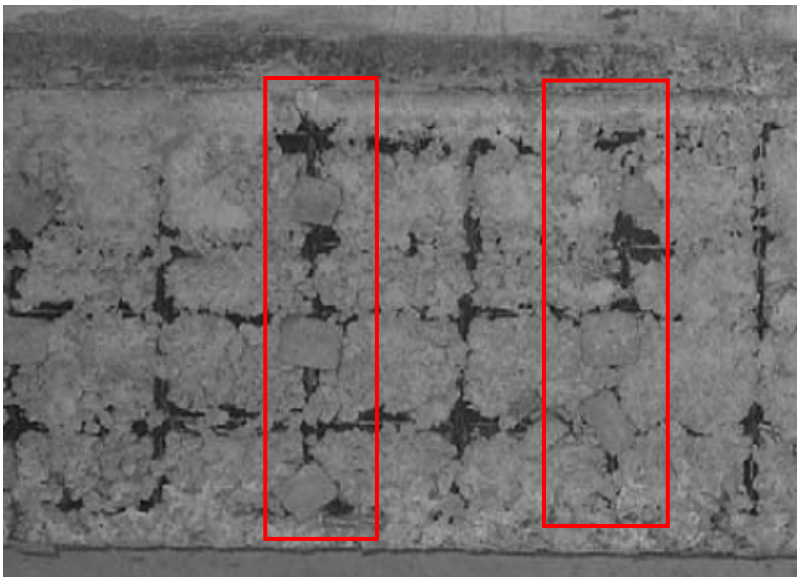

Figure 2.15 Inadequate quality of concrete spacers (Kenai and Bahar, 2003).

Rostam (2005) also found that plastic spacers may facilitate chloride ingress along the spacer-concrete interface to the reinforcement due to differences in thermal expansion as shown in Figure 2.16. Poulsen & Mejlbro (2010) investigated columns of several road bridges exposed to a marine environment. It was also found that plastic spacers provided easy access for the ingress of de-icing salts to migrate along the interface to the reinforcement causing severe local corrosion (Figure 2.17).



Figure 2.16 Corrosion occurring adjacent to plastic spacer (Rostam, 2005).

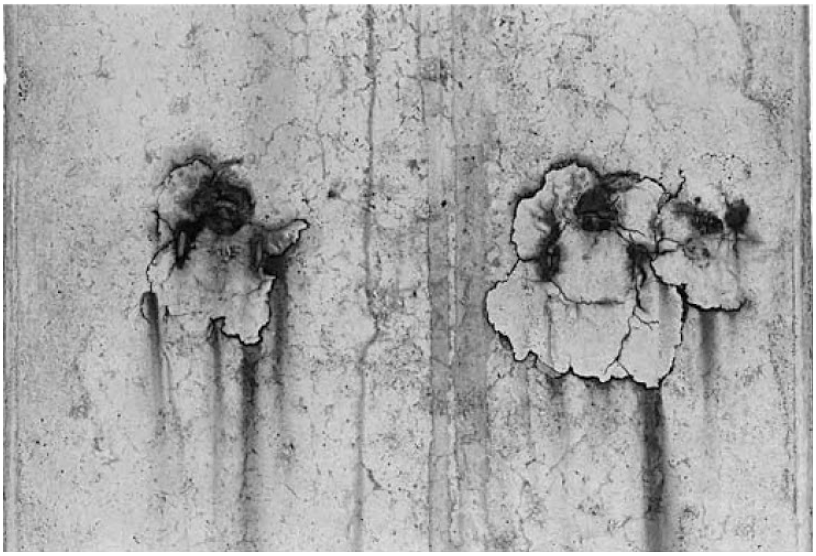

Figure 2.17 Preferential ingress of de-icing salts at the location of plastic spacers causing severe local corrosion in columns of road bridges in a marine environment (Poulsen and Mejlbro, 2010).

However, Shaw (2008) observed that plastic spacers embedded in a 36-year-old multi-storey car park performed well. The spacers were made of medium density polyethylene and the specified concrete cover was 19 mm. When the spacers were retrieved and tested for fixity, stability and load capacity in accordance with BS 7973-1:2001, some of them remained attached to reinforcement as shown in Figure 2.18. The results showed that the spacers passed all the testing. In terms of durability, the author believed that the spacers did not provide a path for water to flow into concrete and reach reinforcing steel because there were no signs of reinforcement corrosion occurring at the position of the spacers.

Tang and Utgenannt (2009) visually inspected several corroded reinforced concrete slabs of w/b ratio 0.3 to 0.4 and air contents of 3% to 6.6% after exposure in a marine environment on the Swedish west coast for 13 years. The concrete cover depths were 10, 15, and 20 mm and the reinforcements were supported by mortar spacers at the edge of the slabs. However, the mix composition of the spacers was not given. It was found that the highest corrosion rate occurred at or near the interface between the mortar spacer and concrete as presented in Figure 2.19. The authors explained that this was attributed to a poor interface between spacer and concrete, which allowed chloride to penetrate easily into the concrete, thus accelerating corrosion initiation.

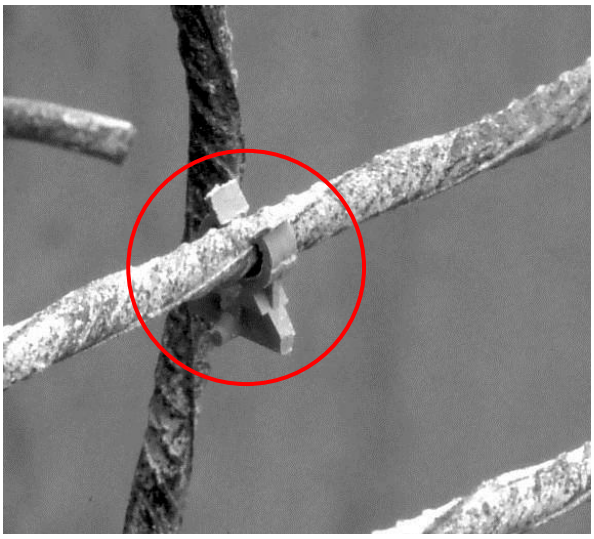

Figure 2.18 Spacer still attached to reinforcement after the concrete had been removed with no sign of corrosion (Shaw, 2008).

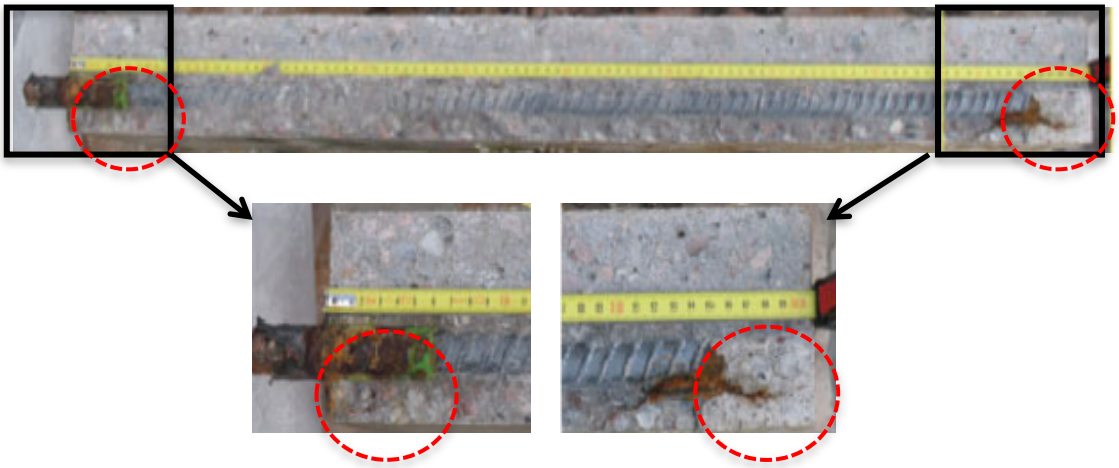

Figure 2.19 Typical example of corrosion occurring at the spacer-concrete interface (Tang and Utgenannt, 2009). Spacer location marked with a red circle.

The first systematic and rigorous research on this issue was probably carried out by Alzyoud (2015) and Alzyoud et al. (2016) in the Concrete Durability Group, Imperial College London, which focused on the effect of spacers on the mass transport and microstructure of concrete. Tests were carried out on 100 mm diameter samples with a centrally placed spacer that is either plastic, cementitious, or a steel wire chair. The concrete cover depth was either 25 or 50 mm and the main binder was Portland CEM I. The samples were cured for 3 and 28 days in a fog room, then conditioned at 20°C/75% RH, 20°C/55% RH, or in a 50°C oven prior to testing. It

was found that spacers have a negative effect on the microstructure of the surrounding concrete, which in turn increases the mass transport properties of concrete. The presence of the spacers produced a micro-cracked and highly porous interface (Figure 2.20), which lowers the resistance of concrete to ingress of aggressive agents causing degradation.

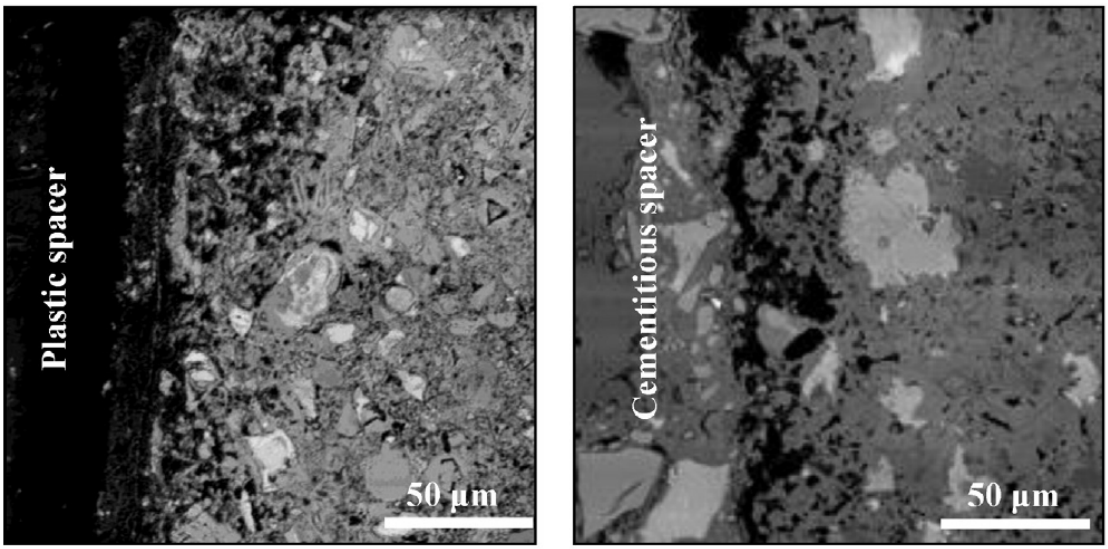

Figure 2.20 Backscattered electron micrographs showing a porous and cracked spacer-concrete interface that facilitates penetration of external aggressive species causing degradation (Alzyoud et al., 2016).

To summarise, the presence of spacers was found to negatively affect the properties of concrete. Possible influences causing deterioration of concrete are numerous including environmental factors, properties and quality of spacer and concrete in which the spacer is embedded, and lower bond strength between spacer and concrete. The BRE carried out a study entitled "The specification and achievement of cover to reinforcement in concrete structures" (King and Dakin, 2001) revealed that there are three potential problematic areas with spacers: 1) low quality control during the manufacture of the spacers; 2) the use of the incorrect spacer type for a given application; and 3) incorrect installation of spacers on site.

2.5 Summary

The interfacial characteristics between aggregate particles and cement paste, steel and concrete, and new and old concrete were reviewed in this chapter. In general, it can be concluded that these interfaces exhibit similar microstructural characteristics and are considered as weak zones in concrete in terms of transport properties and bond strength. Researchers have attempted a number of methods to improve the quality of these interfaces. Such information is important for

understanding the properties of the spacer-concrete interface and how it might influence the long-term performance of concrete structures.

It is evident that there is a lack of systematic and fundamental studies on the effect of spacers on the microstructure and long-term performance of concrete structures. A number of studies have shown that the presence of spacers can cause durability issues, but there is very limited information available on how to improve spacer design and the quality of the spacer-concrete interface in order to mitigate such problems. Understanding the microstructure and bond strength of the spacer-concrete interface will be essential for developing methods to improve spacer design for durable concrete structures.

Chapter 3

Methodology

This chapter presents the materials used in this study, equipment and test methods for transport properties measurements including oxygen diffusion, oxygen permeation, water absorption, electrical conduction, chloride diffusion, and fluorescence epoxy impregnation. The mix proportion and sample preparation procedures were different depending on the purpose of the study, and hence these will be presented separately in the respective results chapters.

3.1 Materials

Portland Cement (CEM I 52.5N) supplied by Hope Construction Materials, complying with the British Standard (BS EN 197-1:2011) was used as the main binder in this study. The cement has a specific gravity of 3.15, and fineness of 291 m^2/kg. The Bogue composition of the CEM I was 53.1% C_3S, 19.1% C_2S, 10.8% C_3A and 7.2% C_4AF and the oxide composition was 63.4% CaO, 20.8% SiO_2, 5.4% Al_2O_3, 2.4% Fe_2O_3, 1.5% MgO, 0.3% Na_2O, 0.7% K_2O, 2.9% SO_3, <0.01% Cl^- and 2.1% loss on ignition.

Thames Valley gravel and sand complying with the British Standard (BS EN 12620:2002+A1:2008) medium grading were used as coarse and fine aggregates respectively. The maximum particle size of aggregate (MSA) for gravel was 10 mm. For sand, the maximum particle size was 5 mm. The physical properties including the specific gravity, moisture content and absorption of the gravel and sand are shown in Table 3.1. Particle size distributions are presented in Figure 3.1. The sieve analysis results show that the gravel and sand complied with BS EN 12620:2002+A1:2008 overall grading. A high-range water reducing admixture MasterGlenium SKY 920 with a specific gravity of 1.08 g/cm^3 complying with the British Standard (BS EN 934-2:2009+A1:2012) was used in selected low w/c ratio mixes to improve workability. Finally, tap water was used as batching water.

Table 3.1 Specific gravity at saturated and surface dry condition (SSD), moisture condition and absorption values of the aggregates used.

Aggregate type	MSA (mm)	Specific gravity (SSD)	Moisture content (%)	24-h moisture absorption (%)
Sand	5	2.51	2.45	0.60
Gavel	10	2.75	0.71	0.62

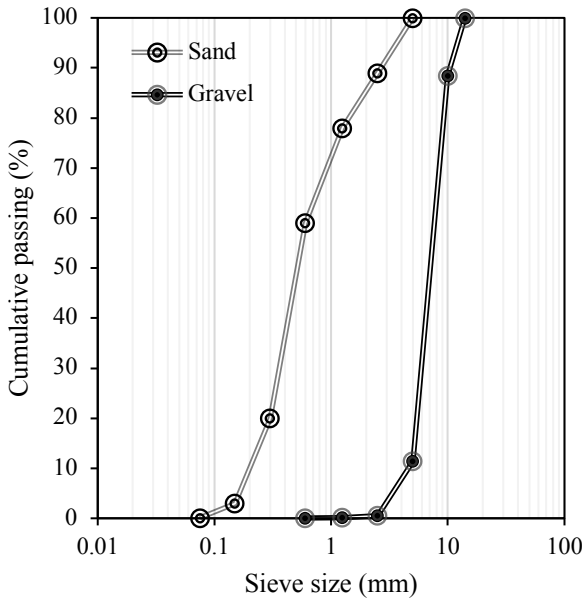

Figure 3.1 Particle size distribution of sand and gravel.

3.2 Spacers

The spacers used in this study are classified into two groups. The first group consists of selected commercially-available spacers (plastic and cementitious) obtained from leading manufacturers and distributors in the UK. These are shown in Figure 3.2. The second group consists of prefabricated modified spacers made in our laboratory. The properties of these spacers will be explained in detail in Chapters 7 and 8. Single cover spacers were selected for this study as they are regarded to be the most commercially demand according to leading spacer distributors in the UK. Furthermore, there are difficulties with testing bar or line spacers because these would require the preparation and testing of very large concrete samples, which would not be practical or possible with some test methods.

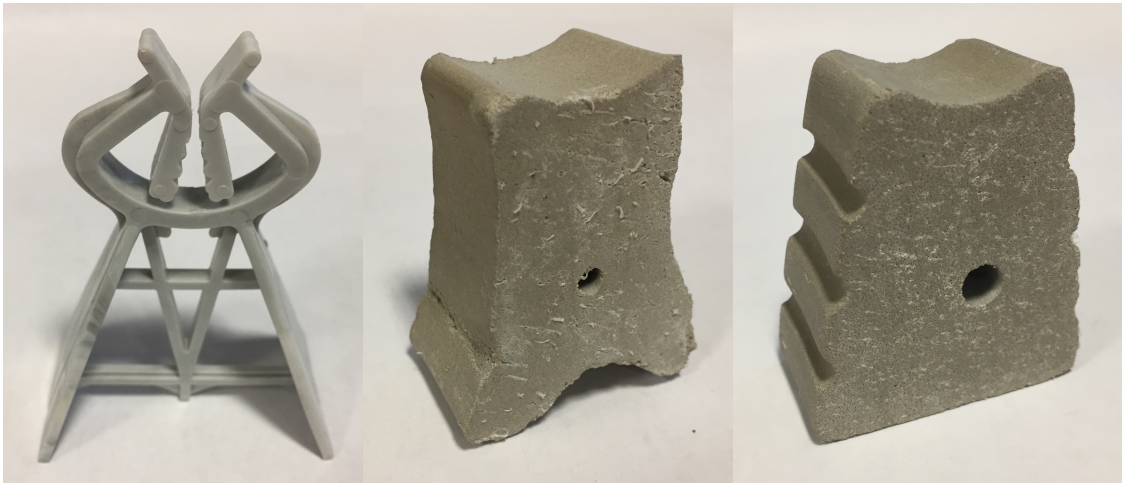

(a) PS (b) CS-1 (c) CS-2

Figure 3.2 Commercially-available spacers used in this study.

The properties of the selected commercial plastic and cementitious spacers are shown in Table 3.2. It includes the volume, surface area and porosity of each spacer. The volume and surface area were calculated from the dimensions and shape of the spacer. The accessible porosity (φ) was determined by measuring the volume of water absorbed by the spacer 60±5%RH, 21ºC to a vacuum saturated surface dry condition (SSD) and dividing it by the sample volume:

$$\varphi = \frac{m_D - m_{SSD}}{\rho_w V} x100\% \qquad \text{Eq. 3.1}$$

Where:

- m_D = mass of sample at preconditioned state (g)
- m_{SSD} = mass of sample at vacuum saturated-surface dry condition (SSD) (g)
- ρ_w = density of water (g/mm^3)
- V = volume of spacer (mm^3)

Prior to use, both plastic and cementitious spacers were cleaned, dried, and stored in the lab under room temperature.

Table 3.2 Properties of commercial spacers used in this study.

Spacer material	Material	Height (mm)	Volume (mm^3)	Surface area (mm^2)	Accessible porosity (%)	Water sorptivity coeff. ($g/m^2mm^{0.5}$)	Thermal expansion coeff. (/°C)
Plastic (PS)	Polyvinyl chloride	50	-	2560	-	-	$80\ x\ 10^{-6}$
Cementitious-1 (CS-1)	Fibre-reinforced mortar made with Portland cement containing 50% ground granulated blast-furnace slag (GGBS) at a water/binder ratio (w/b) of 0.35	50	44640	1860	8.5 (0.86)	35	$(18 – 20)\ x\ 10^{-6}$
Cementitious-2 (CS-2)		50	31920	1330	8.5 (0.45)	35	

Note: standard errors are shown in brackets

3.4 Mass transport properties

Five transport properties were measured in this thesis to study the influence of spacers on different transport mechanisms. These are oxygen diffusivity, oxygen permeability, water sorptivity, electrical conductivity, and chloride diffusivity. Tests were carried out on two to three replicates for each sample type and the results averaged. Diffusivity and permeability were carried out because the ingress of aggressive species such as oxygen and chloride play a vital role in reinforcement corrosion, while water transport is relevant to many degradation processes.

3.3.1 Oxygen diffusion

Diffusion refers to transport phenomena that occur under a concentration gradient. In this study, gaseous oxygen will be used as the transport agent. Diffusion is obtained by applying a concentration gradient across the sample and measuring the flux *F*, which is the flow rate per unit sample cross-sectional area at steady-state conditions. The diffusion coefficient is then calculated from equation 3.2 based on Fick's first law of diffusion.

$$J_A = -D\frac{dC_A}{dx} \qquad \text{Eq. 3.2}$$

Where:

- J_A = oxygen transport rate (kg/m^{2}s) or (moles/m^{2}s)
- D = diffusion coefficient (m^2/s)
- C_A = concentration of oxygen (mol/m^3)
- x = distance (m)

Test procedure

To measure oxygen diffusivity, a cylindrical sample with 100 mm diameter and 50 mm height was placed in a diffusion test cell as shown in Figure 3.3 and schematically illustrated in Figure 3.4. Prior to testing, the sample was pre-conditioned to a constant moisture state by drying either at 75% RH, 21°C or in a 50°C oven. A 15kN load was applied on to the top of the diffusion cell cover using a hydraulic jack. This causes the silicone rubber ring to expand, therefore sealing the sample to prevent side leakage (Wu et al., 2014). Subsequently, the opposite flat surfaces of the sample were exposed to oxygen and nitrogen gases at equal pressure so that the gases counter diffuse in opposite directions through the sample. A stream of nitrogen was applied first by gently turning on the nitrogen valve until the flow measured by the digital

flowmeter reaches approximately 85 m/min. Subsequently, the oxygen stream was applied by gently turning on the oxygen valve until the manometer P_2 shows an insignificant pressure difference between the oxygen and nitrogen streams. Once the flow reaches a steady-state condition, which normally takes about 60 minutes, the oxygen concentration in the outflow stream (measured continuously with a zirconia analyser) was recorded. The diffusion coefficient, D (m^2/s), was calculated according to Fick's first law of diffusion using the following equation:

$$D = \frac{Qd}{A(C_2 - C_1)} \quad \text{Eq. 3.3}$$

Where:

- Q = oxygen diffusion rate at 1 bar (m^3/s) expressed as:

$$Q = \frac{R_1}{60x10^6} x \frac{(G_1 - G_0)}{100} x(P_1 - P_2) \quad \text{Eq. 3.4}$$

- C_1 = mean concentration of oxygen in the nitrogen stream at 1 bar (m^3/m^3) expressed as:

$$C_1 = \frac{(G_1 + G_0)}{2} x \frac{(P_1 - P_2)}{100} \quad \text{Eq. 3.5}$$

- C_2 = concentration of oxygen in the oxygen stream at 1 bar (m^3/m^3) expressed as:

$$C_2 = \left[100 - \left(\frac{R_1}{R_2} x \frac{(G_1 - G_0)}{2} x \frac{\sqrt{32}}{\sqrt{28}}\right)\right] x \frac{P_1}{100} \quad \text{Eq. 3.6}$$

- A = cross-sectional area of sample (m^2)
- d = sample thickness (m)
- R_1 = flow rate of nitrogen stream (mL/min)
- R_2 = flow rate of oxygen stream (mL/min)
- G_0 = percentage of oxygen in the initial nitrogen stream
- G_1 = percentage of oxygen in outflow stream
- P_1 = pressure of oxygen stream (bar)
- P_2 = pressure difference between the oxygen and nitrogen stream (bar)

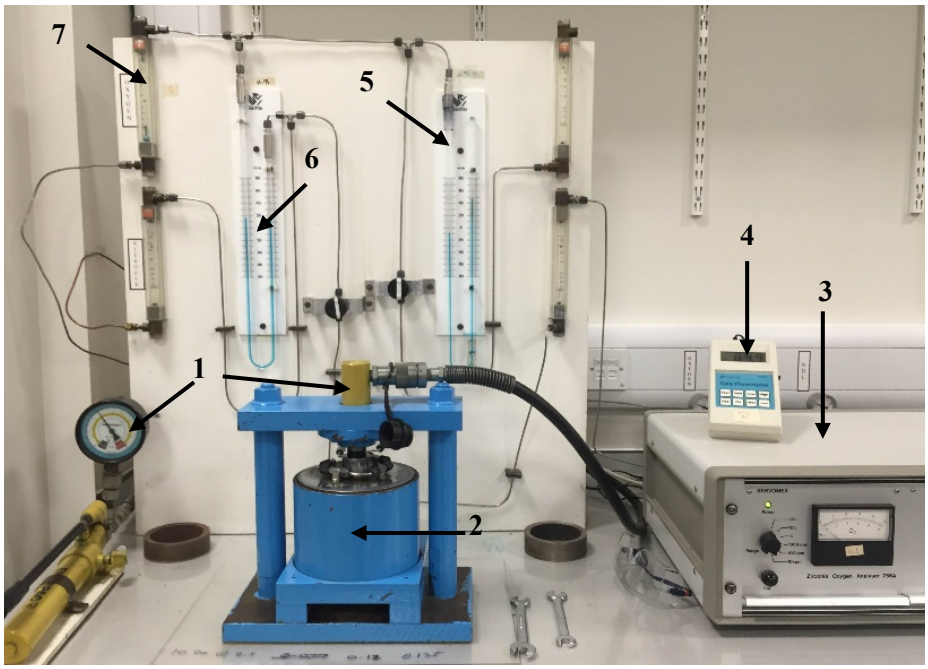

Notation: 1. Hydraulic jack; 2. Diffusion cell; 3. Zirconia oxygen analyser; 4. Digital flow meter (R_1); 5. Manometer (P1); 6. Manometer (P_2); 7. Flow meter (R_2)

Figure 3.3 Diffusion test cell.

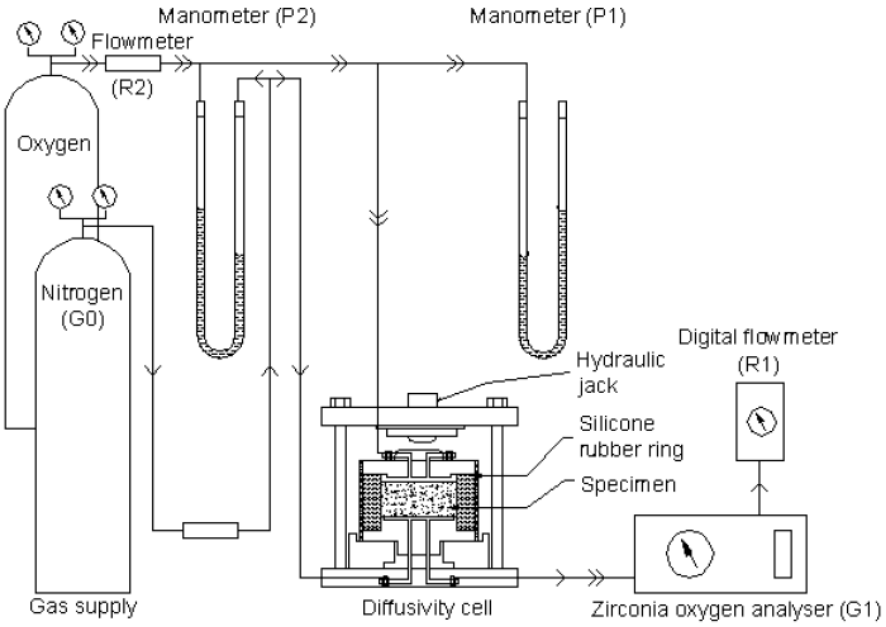

Figure 3.4 Schematic of the oxygen diffusivity test set-up (Wong, 2006, Wong et al., 2006a).

3.3.2 Oxygen permeation

Permeation refers to the transport of fluids through a porous material under an applied pressure gradient. The permeation rate Q^* (m^3/s) can be expressed according to Darcy's law as follows:

$$Q^* = -kA\frac{\Delta P}{\eta d} \quad \text{Eq. 3.7}$$

Where:

- Q^* = oxygen permeation rate (m^3/s)
- k = permeability coefficient (m/s)
- A = cross-sectional area of the sample (m^2)
- ΔP = pressure gradient (N/m^3)
- d = sample thickness (m)

The test fluid used in this study is gaseous oxygen. Since gas is a compressible fluid, its volume and the rate of flow changes from point to point as the pressure decreases, therefore equation 3.7 is not applicable. Instead, we will use a differential form of Darcy's law developed for compressible fluids by considering that the pressure-velocity product is constant throughout the sample at isothermal and steady-state conditions (Klinkenberg, 1941):

$$Q^* = k_g \frac{A}{2\eta_g d}\left(\frac{P_1^{*2} - P_2^{*2}}{P_2^*}\right) \quad \text{Eq. 3.8}$$

where:

- k_g = gas permeability coefficient (m^2)
- η_g = gas viscosity coefficient (for oxygen at 20°C, $\eta_g = 20.2\times10^{-6}$ Ns/m^2)
- P_1^* = absolute pressure on the inlet face (N/m^2)
- P_2^* = absolute pressure on the outlet face (N/m^2)

The permeability coefficient k_g obtained from equation 3.8 is an apparent value that is dependent on the applied pressure. At low pressures or in very fine pores, the mean free path of the gas molecules may approach the dimension of the pore size. Consequently, the frequency of collision between gas molecules and the pore-wall increases compared to the frequency of collision between gas molecules themselves. Consequently, flow will occur via Knudsen diffusion rather than a viscous mechanics. This phenomenon is known as "gas slippage" and it causes the measured gas flow to be higher than expected, thus overestimating the calculated

permeability coeffient (according to equation 3.8). The Klinkenberg method was applied to correct for this effect and to obtain an intrinsic permeability coefficient that is considered to be an independent material property (Klinkenberg, 1941):

$$k_g = k_{int}\left(1 - \frac{\beta}{P_m}\right) \qquad \text{Eq. 3.9}$$

Where:

- k_{int} = intrinsic permeability coefficient (m^2)
- β = constant (N/m^2)
- P_m = mean of the inlet and out pressure calculated as $(P_1^* + P_2^*)/2$ (N/m^2)

To apply the Klinkenberg correction, the measured values of k_g were plotted against the reciprocal of the corresponding P_m values as shown in Figure 3.5. This produces a strong linear relationship, typically with R^2 value greater than 0.99. The obtained best-fit line is then extrapolated to infinite mean pressure ($1/P_m \approx 0$) in order to determine the intrinsic permeability k_{int}.

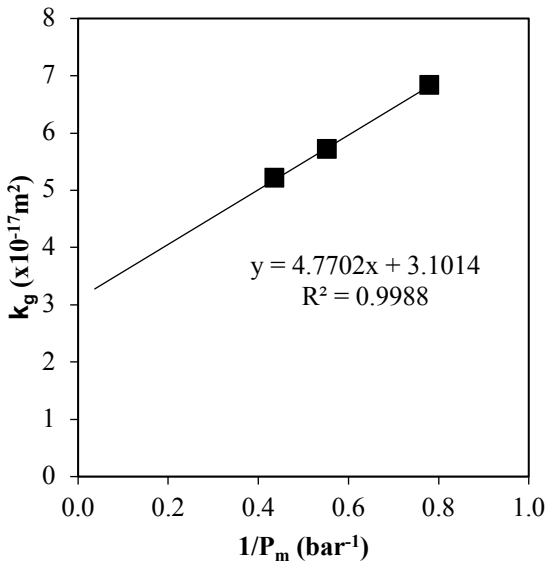

Figure 3.5 A typical k_g vs $1/P_m$ plot for Klinkenberg correction. Sample is concrete at w/c 0.4.

Test procedure

Oxygen permeability was measured by placing the cylindrical sample in a permeation test cell shown in Figure 3.6 and 3.7, which was similar to the one used in the diffusion test. The sample was confined and sealed by applying a 15kN load on to the top cover. The sample was then subjected to gaseous oxygen and the outflow rate was measured under a steady state condition. This was repeated for three input gas pressures of 0.5, 1.5 and 2.5 bars above atmospheric pressure. At each input pressure, it normally takes approximately 60 minutes for the flow to reach the steady-state condition. The outflow rate was determined using a series of soap bubble flowmeters. This was done by measuring the time required for the soap bubble to move through a certain volume, using a digital stopwatch. At least five flow readings were recorded to give an average flow rate. The ratio of the maximum to minimum flow rate between the readings was no more than 1.02.

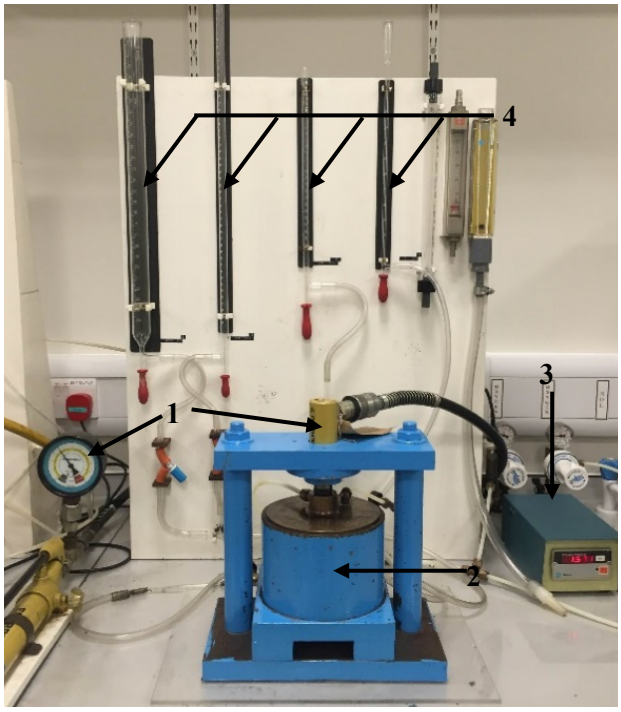

Notation: 1. Hydraulic jack; 2. Permeation cell; 3. Pressure indicator; 4. Soap bubble flowmeters (from left to right: 250 cm^3, 50 cm^3, 10 cm^3, 1 cm^3)

Figure 3.6 Permeation test cell.

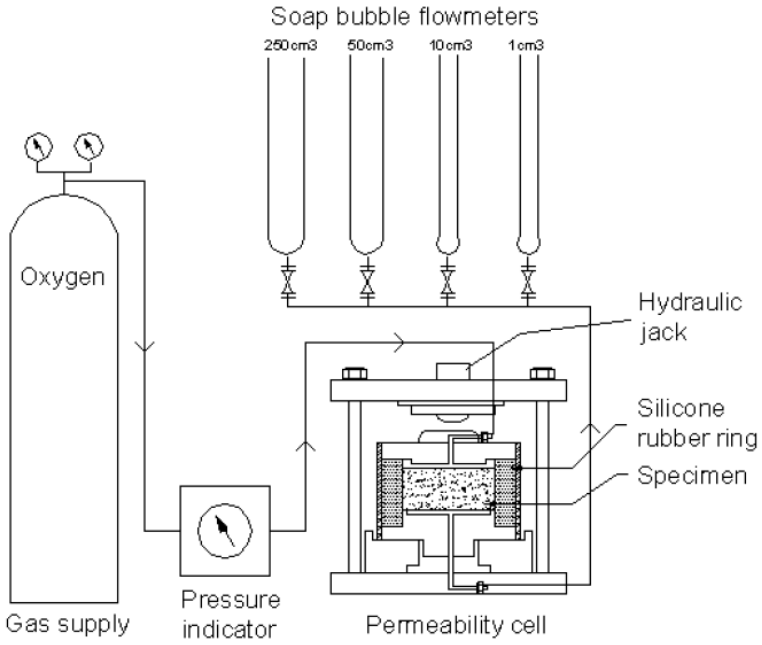

Figure 3.7 Schematic of the oxygen permeability test set-up (Wong, 2006, Wong et al., 2006a).

3.3.3 Water absorption

Water absorption refers to the ability of a porous material to absorb and transmit water under capillary suction (Hall, 1989). The movement of water within concrete via absorption is a partially saturated transport mechanism and it depends on the initial water content and the geometry of the pore structure (Hall and Yau, 1987). According to Sabir et al. (1998), capillary suction in concrete can only be measured in an unsaturated condition. The rate of water absorption is often characterised by measuring a parameter known as the sorptivity coefficient. Considering unidirectional flow under negligible pressure gradient, the cumulative mass of absorbed water per unit area of the inflow surface is linearly proportional to the square root of elapsed time according to classical non-saturated flow theory. This is expressed in the following equation:

$$i = a + S(t)^{0.5} \qquad \text{Eq. 3.10}$$

Where:

- i = cumulative absorbed water per unit area of the inflow face (g/m^2),
- a = fitting constant, due to minor edge and surface effects
- S = sorptivity coefficient (g/m^{2}min$^{0.5}$)
- t = elapsed time (min).

Test procedure

Water sorptivity was measured by immersing the sample in a tray of shallow water to a depth of up to 5 mm above the base of the sample (Hall and Tse, 1986). Plastic strips were placed under the sample to allow free access of water to the sample surface. The quantity of absorbed water was then measured at several intervals by weighing the sample using an electronic balance accurate to 0.01g. Typical time intervals were 5, 10, 15, 30, 60 minutes and every hour for the first 7 hours, followed by daily readings. Prior to weighing, surface water on the sample was removed with a damp cloth or dampened tissue, and the weighing process should be completed as quickly as possible (within 30 seconds). The tray was kept covered with a loosely fitting lid at all the times to prevent loss of absorbed water by evaporation. However, care was taken to ensure that condensation did not form on the inside of the lid and drop on to the sample (Figure 3.8).

The data was then used to plot the cumulative absorption i against $t^{0.5}$ according to the classical unsaturated flow theory, where $i = \frac{\Delta w}{A}$ (in which Δw is the increase in weight and A is the sample

cross-sectional area. A typical plot of cumulative water absorption against the square root of time is shown in Figure 3.9. The sorptivity coefficient S ($g/m^2min^{0.5}$) was determined from the slope of the best-fit linear regression line across the first 16 points. Note that the origin was not included when determining the sorptivity coefficient because of the non-zero y-intercept caused by immediate filling of open surface pores on the inflow face and sides of the sample when immersed in water. The R^2 value of linear fit is typically greater than 0.99.

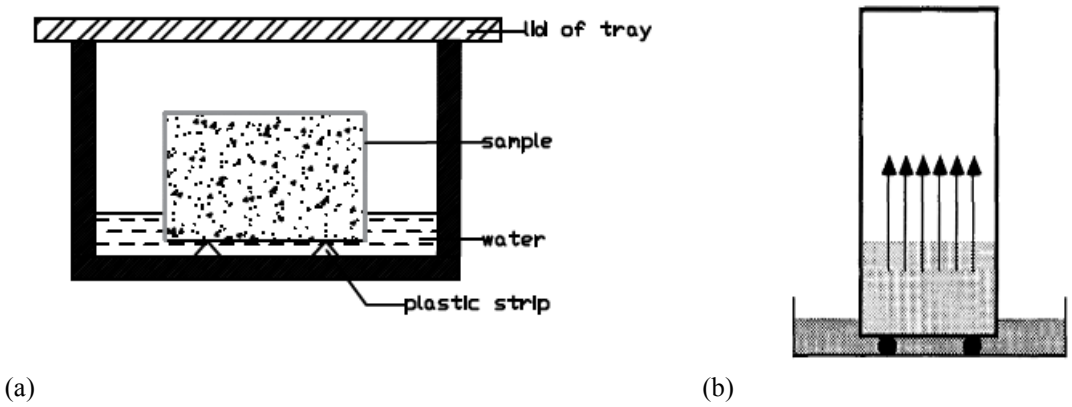

(a) (b)

Figure 3.8 Example of water absorption test set-up; and (b) Schematic diagram of sorptivity test (Hall, 1989).

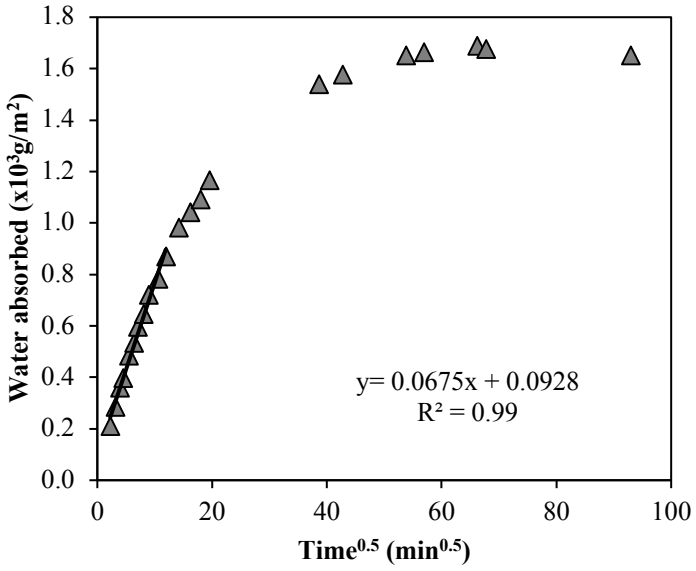

Figure 3.9 Typical plot of cumulative water absorption against square-root of time for concrete.

3.3.5 Accessible porosity

After the first day of testing, the cumulative absorption will gradually deviate from a linear relationship with $t^{0.5}$ and reach a relatively steady value as the sample approaches saturation. After approximately seven days of absorption in the tray, the samples were fully submerged in water and vacuum saturated to determine the accessible porosity. This was estimated by measuring the volume of water absorbed by the sample from the preconditioned state (at 75% RH, 21°C or in a 50ºC oven) to a vacuum saturated-surface dry condition, and dividing it by the sample volume as expressed in the following equation:

$$\varphi = \frac{m_{SSD} - m_D}{\rho_w V} x100\% \qquad \text{Eq. 3.11}$$

Where:

- φ = accessible porosity (%)
- m_{SSD} = mass of the sample at vacuum-saturated-surface-dry condition (g)
- m_D = mass of the sample at preconditioned state (g)
- ρ_w = density of water (for water 20℃ ≈ 1000 kg/m^3)
- V = volume of the sample (m^3).

Test procedure

Figure 3.10 shows the arrangement of the equipment used to perform the vacuum saturation test to measure accessible porosity. The sample was placed in the chamber filled with water and then covered with the vacuum chamber lid with two outlets to connect to the vacuum pump and pressure gauge. The samples in the chamber were fully immersed in water. Then, the vacuum pump, which is capable of reducing the pressure to 1kPa was turned on and allowed to run for approximately 4 hours, or until no significant air bubbles escaped from the sample surface. Finally, the vacuum was released to restore air pressure and the saturated samples were weighed. The accessible porosity was calculated according to equation 3.11. This includes the total volume fraction of pores, cracks, and air voids.



Notation: 1. Vacuum pump; 2. Water trap; 3. Water reservoir; 4. Vacuum chamber; 5. Pressure gauge

Figure 3.10 Vacuum saturation equipment.

3.3.6 Electrical conduction

Electrical conductivity σ_e (S/mm) is the reciprocal of electrical resistivity. This is the property that measures the ability of a material to conduct electrical current (Esbach and Souders, 1975). Electrical current is applied via external electrodes, and it is carried through the concrete pore network by movement of ions in the pore solution. When an electric potential is applied to saturated concrete, ions will be driven to move towards the electrode of the opposite sign, and this produces a measurable electrical current. Therefore, the higher the degree of saturation, the more conductive the material is. Electrical conductivity of concrete is also dependent on the volume and ionic concentration of its pore solution. Electrical conductivity σ_e (S/mm) of the sample is expressed as:

$$\sigma_e = \frac{d}{RA} \qquad \text{Eq. 3.12}$$

Where:

- R = measured electrical resistance (Ω)
- A = sample cross-sectional area (mm^2)
- d = sample thickness (mm)

Test procedure

Electrical resistivity was measured by placing vacuum saturated-surface dry sample between two brass plates, which are connected to an LCR databridge. To ensure a proper electrical

contact between the brass plates and the sample surfaces, a generous amount of a salt-free electrode gel was applied on both surfaces prior to clamping. Five measurements of resistance at 1 kHz were taken per sample. The measurements were recorded within 2 minutes of connection and averaged. The test set-up for electrical conduction and the schematic diagram are shown in Figures 3.11 and 3.12 respectively.

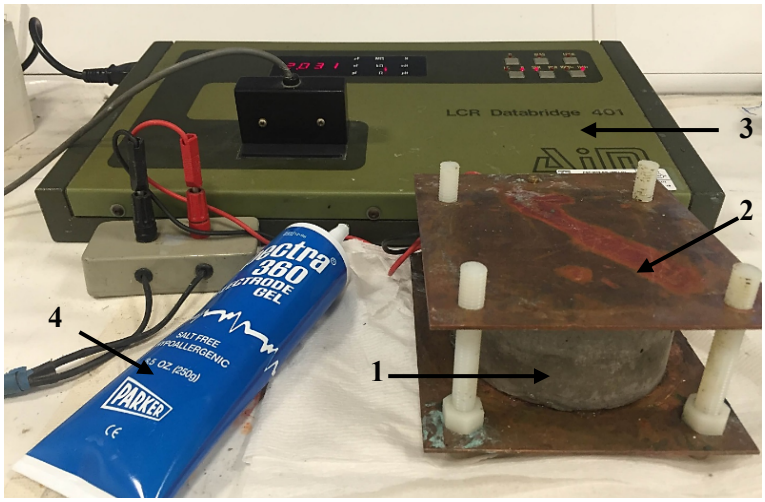

Notation: 1. Sample; 2. Brass plate; 3. LCR databridge; 4. Electrode gel

Figure 3.11 Electrical conductivity test set-up.

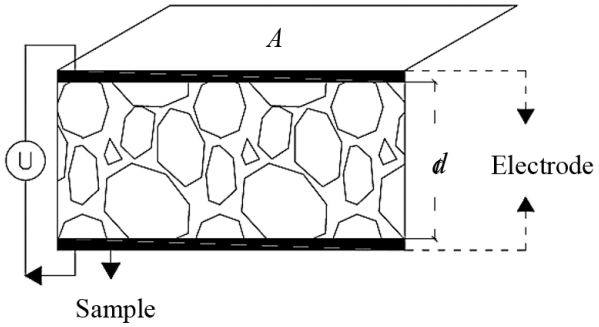

Figure 3.12 Schematic of electrical conduction test set-up.

3.3.7 Chloride penetration

Transport of chlorides into concrete can take place under partly or fully-saturated conditions (Costa and Appleton, 1999). Diffusion, permeation, and absorption are the main transport mechanisms by which chloride ions can penetrate concrete. Of the three mechanisms, in particular for concrete structures exposed to cyclic wetting and drying, the most significant are diffusion and absorption (Hong and Hooton, 1999). Permeation is rarely the dominant transport mechanism unless the structure is deeply submerged in a chloride environment. Pure chloride

diffusion occurs when the concrete is in a fully saturated state and the transport is driven by a concentration gradient of chloride ion. In most cases however, concrete structures are exposed to wetting and drying environment such that the transport occurs via a combination of capillary suction under partially saturated conditions and diffusion in fully saturated conditions.

Chloride penetration is an essential property since the ingress of chloride into concrete structures exposed to de-icing salts or seawater (such as marine structures and other major infrastructures) causes the initiation of the corrosion of steel reinforcement, which then leads to the gradual deterioration of the structure. Similar to oxygen diffusion, chloride diffusion into concrete can be described by Fick's first law of diffusion (Equation 3.3). However, this equation cannot be used for non-steady state conditions (when concentrations are changing). In such conditions, Fick's second law of diffusion, as expressed in Equation 3.13, is commonly applied to quantify the chloride penetration in concrete (Andrade, 1992).

$$C(x,t) = C_s\left[1 - erf\left(\frac{x}{2\sqrt{Dt_{exposure}}}\right)\right] \qquad \text{Eq. 3.13}$$

Where:

- $C(x,t)$ = chloride penetration at a depth x (mm) at time t (seconds)
- C_s = chloride ion concentration of the sample at the surface which is in contact with the chloride solution
- erf = error function which can be found in many mathematical tables
- D = non-steady state apparent diffusion coefficient (m^2/s)
- $t_{exposure}$ = length of exposure to the chloride solution (seconds)

Test procedure

The test was carried out in accordance with the British Standard (BS EN 12390-11:2015). The test set-up for chloride penetration is illustrated in Figure 3.13. Cylindrical samples of the same dimensions to those used in earlier transport testing were used. The samples were preconditioned at 75% RH, 21°C or in a 50°C oven. All faces of the sample except the face to be exposed to the chloride solution were sealed with a waterproof tape prior to testing. The samples were then placed on plastic strips in a tray containing 3% NaCl solution to a depth of about 15 mm from the base of the sample for a specific exposure period ranging from 6 to 12 months. The chloride solution was replaced periodically to maintain its concentration. The tray was covered at all the times to minimise evaporation. At the end of the exposure period, the samples were sectioned with a diamond saw from the centre and freeze-dried immediately to

preserve the chloride profile. Samples were first frozen to -196°C by immersion in liquid nitrogen for approximately 5 minutes. After freezing, the samples were transferred to a Lyotrap freeze-drying chamber (Figure 3.14) maintained at -55°C temperature and high vacuum at 1 Pa pressure to remove ice by sublimation. After drying to constant mass, which typically took around two to six weeks depending on the sample dimension, the samples were stored in a desiccator prior to analysis with a Micro X-ray Fluorescence (μXRF) spectrometer to obtain chloride profiles from the surface exposed to the solution.

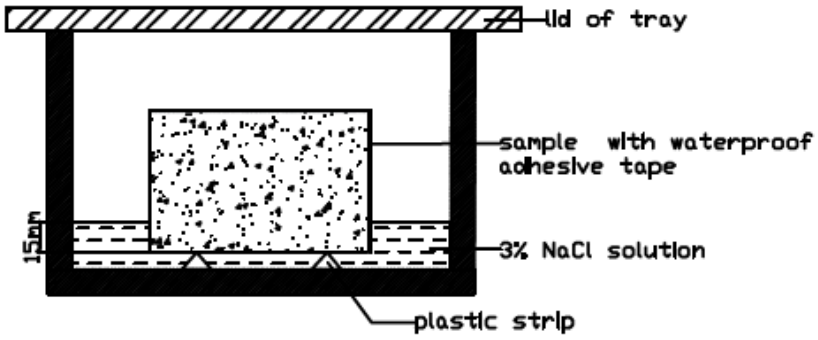

Figure 3.13 Chloride penetration test setup.

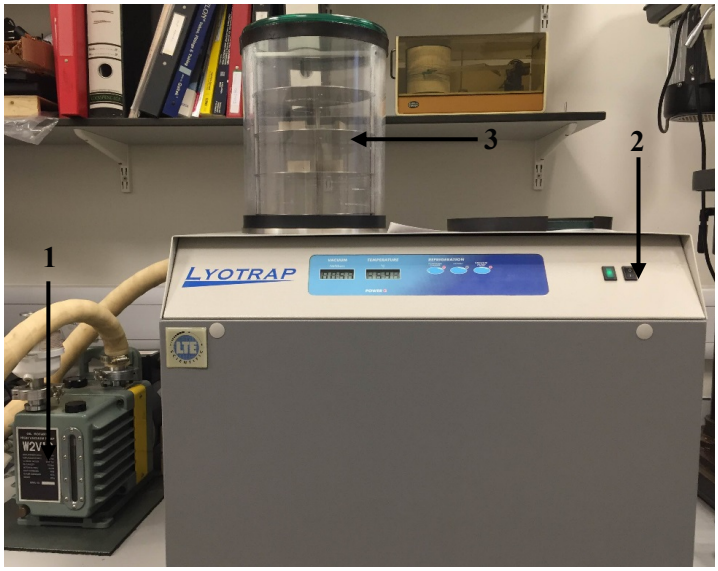

Notation: 1. Vacuum pump; 2. Stainless steel chamber; 3. Trays/shelves for samples

Figure 3.14 Freeze drying chamber.

Micro X-ray Fluorescence (μXRF)

In recent years, μXRF is becoming a popular method for investigating the chloride profiles in cementitious materials (Moradllo et al., 2017, Dehghan et al., 2014, Olsson et al., 2018). μXRF is a technique for analysing the elemental composition of solids. It is capable of detecting elements from sodium Na (Z=11) to uranium U (Z=92), based on the detection of fluorescence X-rays that are emitted from the atoms following X-ray excitation. This generates a spectrum showing the X-ray intensity peaks and their energy. The energy of the characteristic X-ray defines the detected element, and the intensity gives information of its amount in the analysed sample. This information is then used to generate chloride profiles of the sample.

The EDAX Orbis μXRF Spectrometer (Figures 3.15 & 3.16) equipped with a Sapphire^{TM} 80 mm^2 Si(Li) detector and a 30 μm ultra-high intensity poly-capillary optic was used to collect XRF data from the concrete. To acquire a raw XRF spectrum using the Orbis PC, the sample was first placed and secured on the XYZ motorised stage. The sample was then raised by adjusting the Z-axis of the stage until the features appeared in sharp focus under both low magnification camera (10x) and high magnification (75x) camera. The μXRF uses a Rhodium (Rh) x-ray tube to generate high-intensity X-ray photons. The X-ray photons exiting the tube window are then guided by the optics to produce a focused beam on the sample. A 25μm thick Al filter was used to remove the Rh L artefact line to eliminate interference with the Cl K line. Finally, the characteristics of fluorescent X-rays emitted from the sample are detected by a Si(Li) detector and analysed with the ORBIS Vision software. For chloride ingress quantification, the measurements were presented in the form of s spot analysis. About 50 points (at every 1 mm spacing) were manually selected from the cement paste fraction starting at the exposed chloride surface to cover the entire thickness of the sample. After selecting all the points, full spectra data were automatically collected under the optimised operating condition.

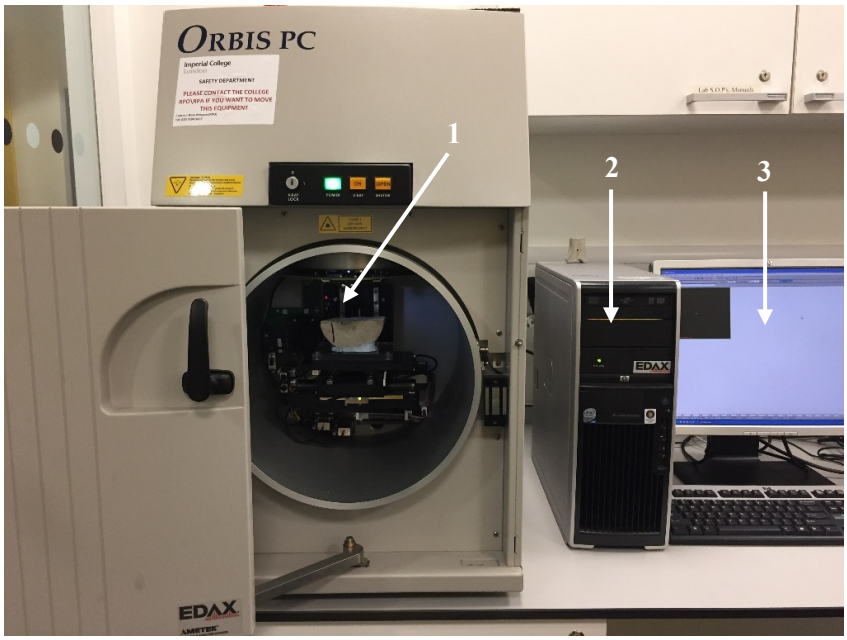

Notation: 1. Orbis PC Spectrometer (sample chamber); 2. PC Workstation G XM2; 3. Monitor

Figure 3.15 Orbis Micro X-ray Fluorescence (µXRF) spectrometer.

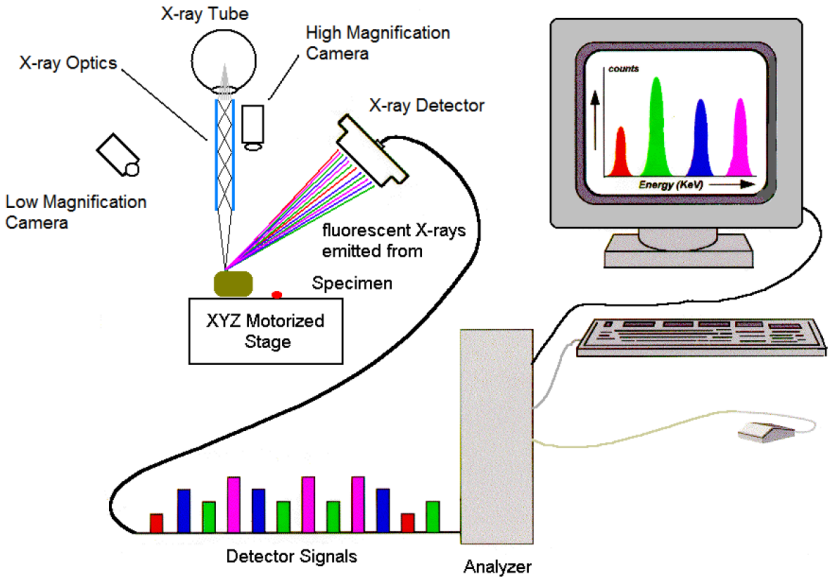

Figure 3.16 Schematic diagram showing the main components of the ORBIS PC micro x-ray fluorescence (µ-XRF) bench-top analyzer (Source: EDAX AMETEK Inc.).

The main operating parameters that influence the collected spectra include the chamber conditions (air or vacuum), shutter filter (no filter, 25µm Al, 25µm Ti, 25µm Ni, 100µm Rh, 127µm Nb, or 250µm Al), beam spot size (30 µm, 1 mm or 2 mm), beam voltage (10 to 50 keV), amplifier time constant (1.6 µs to 102.4 µs), dead time (0 - 50 %), and dwell time (20 to 6000 milliseconds). Table 3.3 summarises the optimised operating conditions for chloride analyses with µXRF used in this study based on the findings by Wahid (2016).

All analyses were carried out in vacuum (< 1.5 Torr). The beam spot size affects the intensity of the characteristic radiation received. The smallest beam spot size (30 µm) was used to achieve the highest density and spatial resolution. An accelerating voltage of 30 keV and amplifier time constant of 12.8 µs were chosen since these are sufficient to allow all heavy elements in cement-based materials to be excited and detected while maintaining a detector dead time to near 40% as recommended by the manufacturer. The amplifier time constant is the length of time in microseconds each emitted photon is processed by detector, while dead time is the percentage of time that the detector rejects an incoming photon because it is still processing the one that has arrived earlier. Finally, dwell time was set to 200ms. Dwell time is the amount of time the X-ray beam spends at a particular point. A higher dwell time increases the detectability of trace elements, but it also increases the total amount of time required to analyse each sample. The selected dwell time of 200ms was considered to be a good compromise. The measured chloride intensity is presented as counts per second (cps).

Table 3.3 Optimal operating conditions of the µXRF for chloride analysis (Wahid, 2016).

Parameter	Optimal condition
Chamber	Vacuum
Shutter filter	25 µm Aluminium
Beam spot size	30 µm
Beam voltage	30 keV
Amplifier time constant	12.8 µs
Dead time	40%
Dwell time	200 ms

3.5 Fluorescent epoxy impregnation

Another method applied in this study to characterise transport property is an impregnation technique using fluorescent epoxy. The technique is based on the principle of applying a low-viscosity fluorescein-dyed epoxy resin to impregnate the concrete sample via its pore structure (capillaries, air voids and cracks) under high-pressure (10 bar) in a cell similar to the one used for measuring oxygen diffusivity and permeability as shown in Figure 3.17. The more porous the sample, the greater the amount of epoxy penetration. Wu et al. (2015) and Wu et al. (2017) have applied this technique to identify micro-cracks in concrete.

Test procedure

The fluorescent epoxy was prepared by mixing Stuers EpoFix resin (refractive index of 1.578) with a fluorescent dye (Struers EpoDye) at 0.05 wt% using a magnetic stirrer for approximately 24 hours and then heated up to 40°C to reduce its viscosity. The fluorescein-dyed epoxy resin was then mixed with hardener at the ratio of 25:3 by mass. Toluene at 5 wt. % of the total mass of resin was added to reduce the viscosity of the resin further. Prior to impregnation, the cylindrical sample was wrapped with two layers of waterproof tape along the curved sides and two layers of clear tape along the perimeter of the bottom surface in order to prevent any leakage of the fluorescent epoxy during the experiment. The sample to be impregnated was then placed in the cell, and the epoxy mix was poured onto the sample surface (Figure 3.18). Once the sample surface was entirely covered by the epoxy, the steel plate lid was placed on the top and then sealed by applying a 15kN load using a hydraulic jack. A 10bar air pressure was then applied and maintained overnight to force the epoxy into the sample. Finally, the impregnated sample was cured at room temperature for two days to allow proper hardening of the epoxy. Figure 3.19 shows an illustration of the impregnation cell. The depth and amount of epoxy impregnation were then measured using image analysis after sectioning the impregnated sample vertically from the prepared surface.

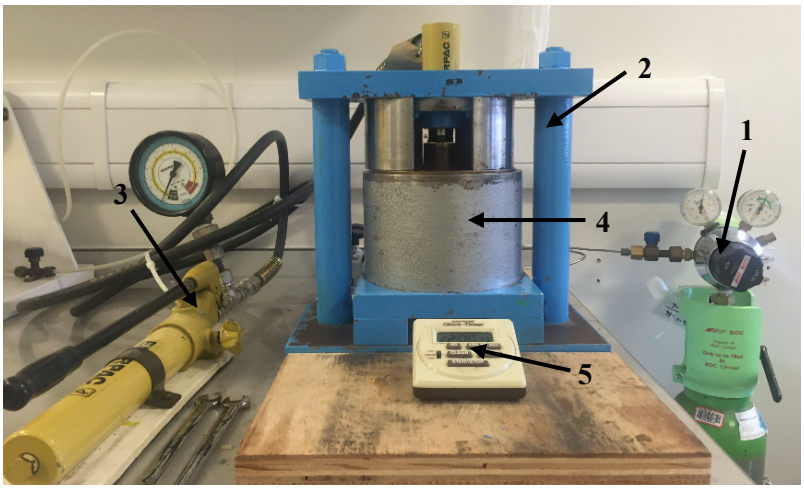

Notation: 1. Air pressure; 2. Loading frame; 3. Hydraulic jack; 4. Impregnation cell; 5. Stopwatch

Figure 3.17 Set-up for fluorescent epoxy impregnation.

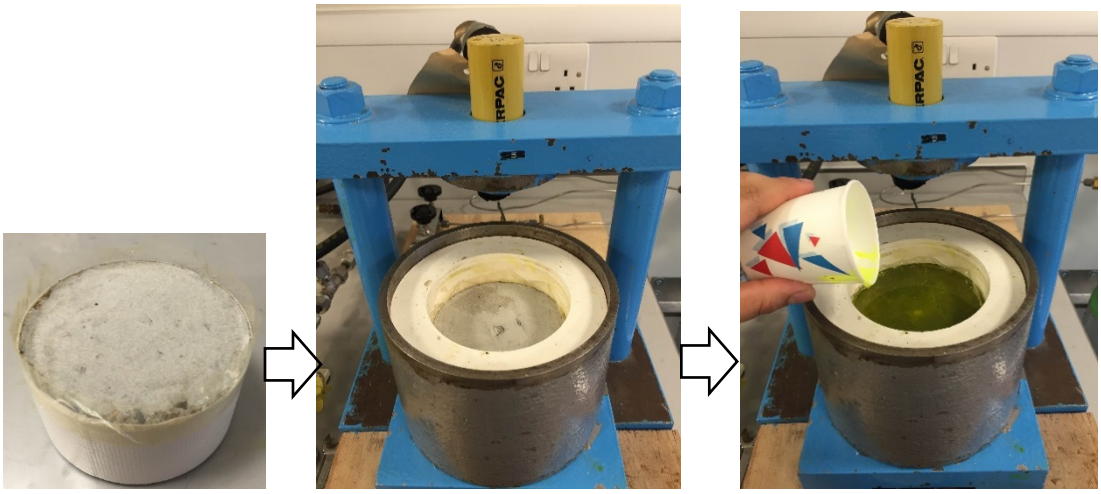

(a) (b) (c)

Figure 3.18 Procedure for epoxy impregnation.

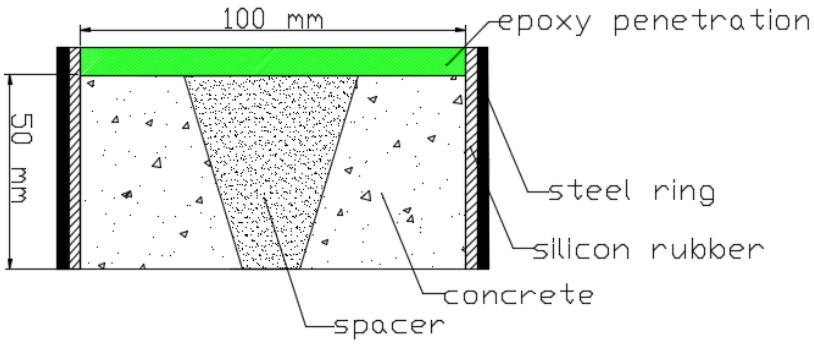

Figure 3.19 Illustration of impregnation cell during experiment.

Fluorescence Imaging

Images were captured using a Sony Alpha NEX-3N mirrorless digital camera equipped with E16 mm focal length and 40.5 mm diameter optical steady shot lens in a dark room. The sample was illuminated under a 15 W ultraviolet lamp operated at ~50 Hz to induce fluorescence (Figure 3.20). There are three critical parameters to optimise the quality of the digital images for image analysis: ISO (International Organisation for Standardisation) value, aperture size and shutter speed. The ISO value determines the sensitivity of the camera sensor, while the aperture size controls how much light passes through the lens during the shot, and shutter speed determines the length of time that light is allowed to hit the sensor. In this study, the camera was set to the lowest ISO setting (ISO 200) to reduce image noise and at the smallest aperture (f/22) to increase depth of field so that the entire sample surface is in focus. A slow shutter speed (8-second exposure) was used to achieve adequate exposure. The sample was placed directly under the camera at a distance of 150 mm between the sample and camera, and a distance of 50 mm between the sample and UV lamp. These parameters are sufficient to obtain a macro view of the sample to measure the penetration depth of the epoxy and so were kept constant throughout the study.

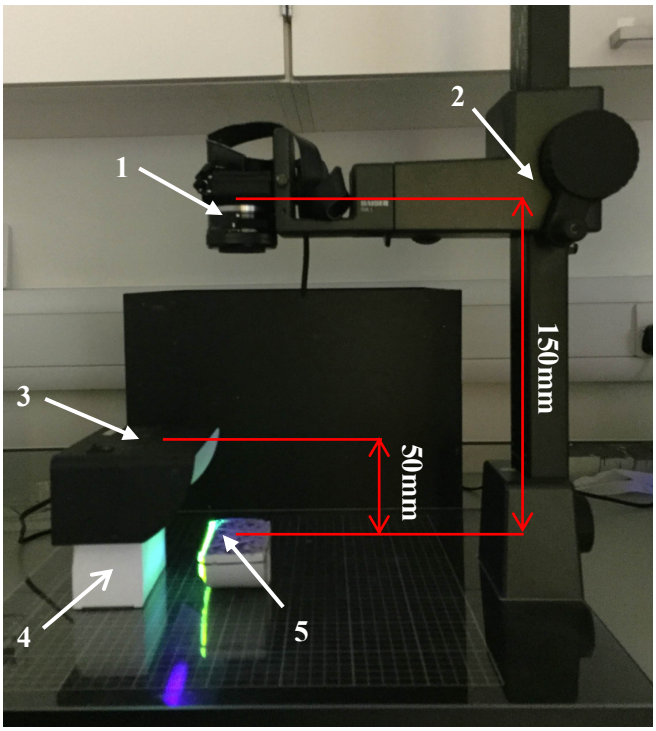

Notation: 1. Digital camera; 2. Camera stand; 3. UV Light; 4. Block to support the UV Light; 5. Cross-section of impregnated sample.

Figure 3.20 Setup for fluorescence imaging. Sample was placed at a distance of 150 mm directly under the camera and 50 mm from the UV lamp.

3.6 Summary

The materials including the selected commercially-available spacers used in this study and details of test methods for transport testing were described in this chapter. The mix proportions and other features of the experimental set-up for sample casting as well as techniques for sample mixing, curing, and conditioning will be presented in the relevant result chapters (Chapters 4 to 8).

Chapter 4

Combined effects of vertical reinforcement spacers and segregation on transport properties of concrete

This chapter investigates the effect of spacers attached to vertical reinforcement and segregation on mass transport properties of concrete. Rectangular column samples were cast in a wooden mould with dimensions of 80 mm length, 90 mm width and 400 mm height. Spacers for cover thickness of 50 mm were attached to the vertical steel bars and placed at near the top and the bottom of the columns. The samples were compacted using a vibrating table and cured in a fog room (100% RH, 21°C) for 28 days, then conditioned to mass equilibrium in a 50°C oven or 75% RH, 21°C before water sorptivity and electrical conductivity tests. Segregation of the concrete was characterised by measuring the volume fraction of aggregate particles on cross-sections along the height of the column using image analyses. The results showed that the top of the column consistently showed lower aggregate content and gave lower resistance to transport compared to the bottom sections. Segregation occurred in all columns despite care taken to avoid over-compaction. The presence of spacers influenced segregation and produced an increase in transport coefficients.

4.1 Introduction

Studies to date have concentrated on the properties of concrete containing spacers that support horizontal reinforcement. However, it is suspected that the use of spacers for vertical reinforcement would induce a greater impact on the concrete microstructure and transport properties. This is due to bleeding and segregation that inevitably occur in fresh concrete when compacted. Segregation is generally defined as the separation of aggregate particles in fresh concrete such that they are no longer uniformly distributed. Bleeding or a water gain is a particular form of segregation where water appears at the upper concrete surface (external bleeding) or under aggregate particles and reinforcing bars (internal bleeding) after compaction. It is suspected that most concrete structures experience some amount of segregation and bleeding, and that these effects have a negative influence on the microstructure, which lowers the resistance of concrete to the ingress of aggressive agents causing degradation (Panesar and Shindman, 2012). However, limited studies have been carried out to quantify this.

Furthermore, it is reasonable to suspect that the presence of spacers may potentially affect the segregation of concrete because it disrupts the distribution of aggregate particles in vertically cast concrete. However, no studies have been carried out on this to-date regarding the combined effect of segregation and vertical reinforcement spacer (type and position) on the transport properties of concrete. These are then the main objectives that this study seeks to redress.

Concrete columns with plastic or cementitious spacers vibrated at two different frequencies and periods were tested for water sorptivity, electrical conductivity, and accessible porosity via water vacuum saturation. The spacers were positioned near the top and bottom of the 400 mm tall samples. Segregation of the concrete was estimated by measuring the area fraction of aggregate on the cross-section at different heights using image analysis. Finally, the measured transport properties were correlated with the segregation profile to comprehensively establish the combined effects of segregation and vertical spacers on the transport properties of concrete.

4.2 Experimental

4.2.1 Materials and mixture proportion

Plastic 'A' clip spacers and single cementitious spacers of 50 mm height as shown in Figure 4.1 were used in this study. The cementitious spacers contain a small hole to allow fixing to steel reinforcement using tie wire. The spacers were obtained from leading manufacturers and distributors in the UK. Prior to application, the spacers were stored in the laboratory environment (60±5% RH, 21°C) to avoid moisture or temperature variations. Details of the spacer properties are given in Chapter 3.2.

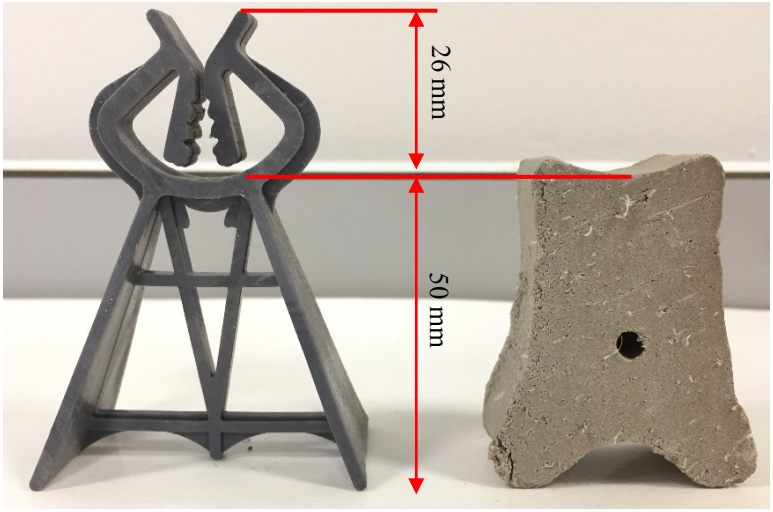

Figure 4.1 Spacers used in this chapter.

The concrete mix used had a free water/cement (w/c) ratio of 0.4 and was designed based on absolute volume method. The mix proportions are given in Table 4.1. Ordinary Portland cement CEM I complying with BS EN 197-1:2011 was used as the main binder. Thames Valley sand (< 5 mm) and gravel (<10) complying with BS EN 12620:2002 medium grading were used as fine and coarse aggregate respectively. The total aggregate volume fraction was fixed at 70% and the sand to total aggregate mass fraction was 0.4.

Table 4.1 Concrete mix proportion used in this chapter.

w/c ratio	Aggregate content (%)	Water (kg/m^3)	CEM I (kg/m^3)	Sand (kg/m^3)	Gravel (kg/m^3)
0.4	70	167	418	728	1092

A standard slump test was performed to assess the workability of the fresh concrete following the British Standard (BS EN 12350-2:2009). As can be seen in Figure 4.2a, the initial mix was very stiff with a recorded slump value of only 10 mm. This could cause difficulties in achieving a good compaction. Therefore, a superplasticiser (MasterGlenium SKY 920) was added at a dosage of 0.75% wt. of cement to improve the workability of the mix. When the superplasticiser was added, the slump of the mix achieved 120 mm as shown in Figure 4.2b. The superplasticiser was then used throughout the study.



(a) Without superplasticiser (b) With superplasticiser 0.75% wt. cement

Figure 4.2 Slump tests showing the improvement in workability of the fresh concrete with added superplasticiser.

4.2.2 Experimental setup

Rectangular column samples were produced by casting concrete in the vertical direction in a specially fabricated wooden mould as shown in Figure 4.3. The wooden moulds were designed to produce two columns with dimensions 80 mm depth, 90 mm width and 400 mm height, per casting. Spacers to achieve 50 mm cover were fixed to high-yield reinforcing steel (Ø12 mm, ribbed) and placed near the top and the bottom of the samples as illustrated in Figure 4.3. Control samples were prepared by casting columns without spacers. External horizontal and vertical steel rods (Figure 4.4) were attached to the sides of the mould and tightly screwed to avoid leakage during concreting and to achieve the required sample dimensions. Prior to casting, a thin layer of oil was applied to all internal sides of the mould as a release agent. However, excessive or insufficient amounts of oil can cause surface defects, i.e. bugholes, and care was taken to avoid this. A top view of the column samples is shown in Figure 4.5. The plastic spacers attached to the top of steel bar were used to ensure that the steel bar do not move during compaction. These spacers were removed when the samples were demoulded.

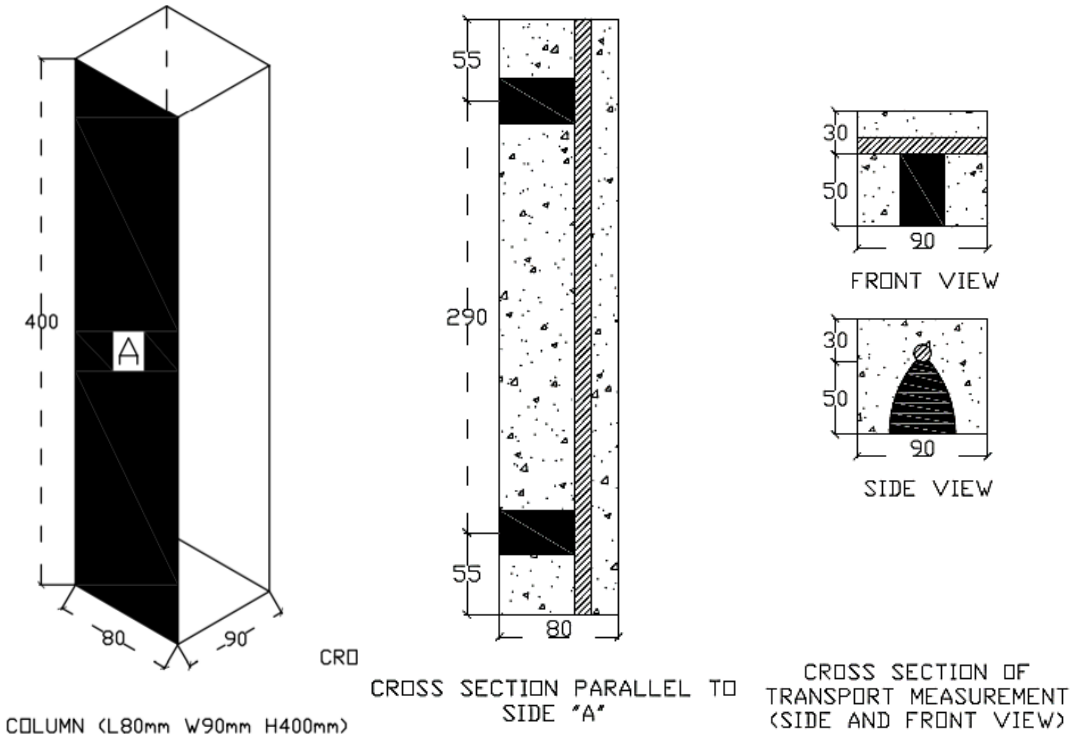

Figure 4.3 Schematic diagrams showing: a) cast column *L80 x W90 x 400H*; b) cross section of column parallel to A-side showing the position of spacers and Ø12mm rebar and; c) samples extracted from column for transport tests (front and side view).

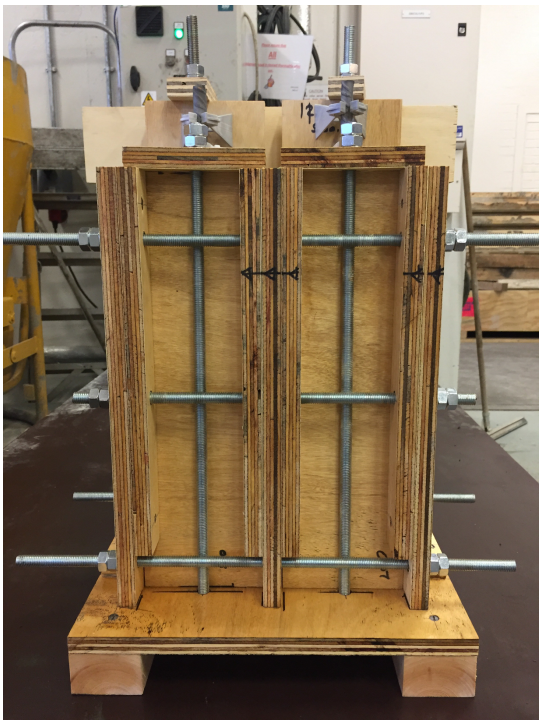

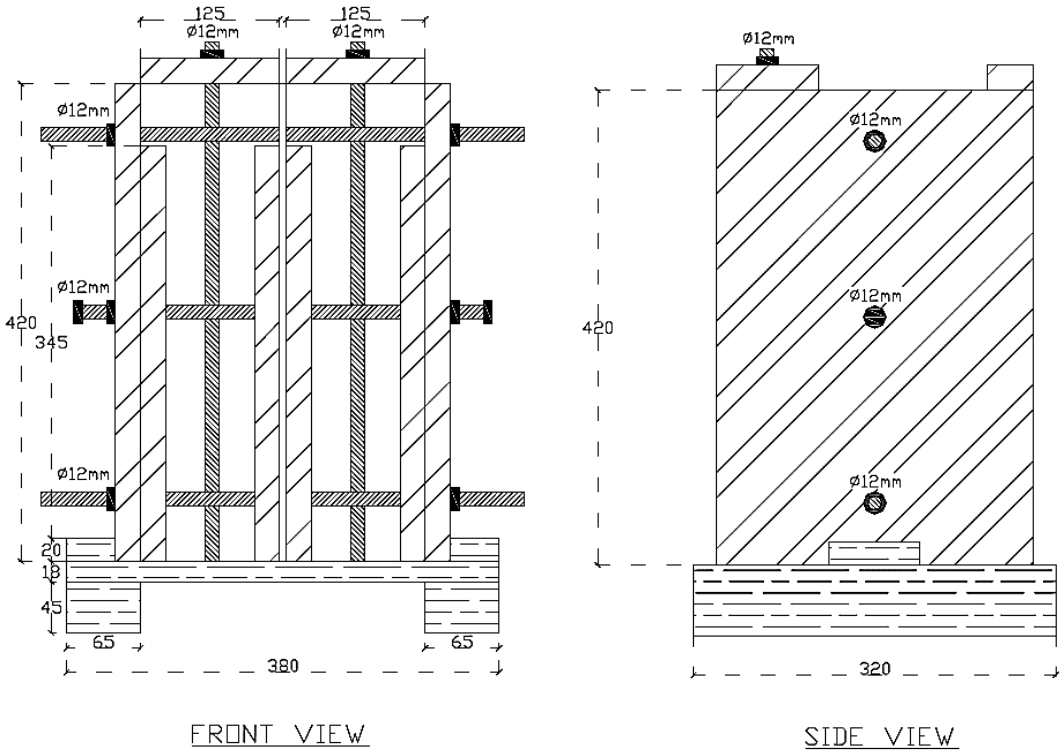

Figure 4.4 Set-up for casting column samples (front and side view of formwork).

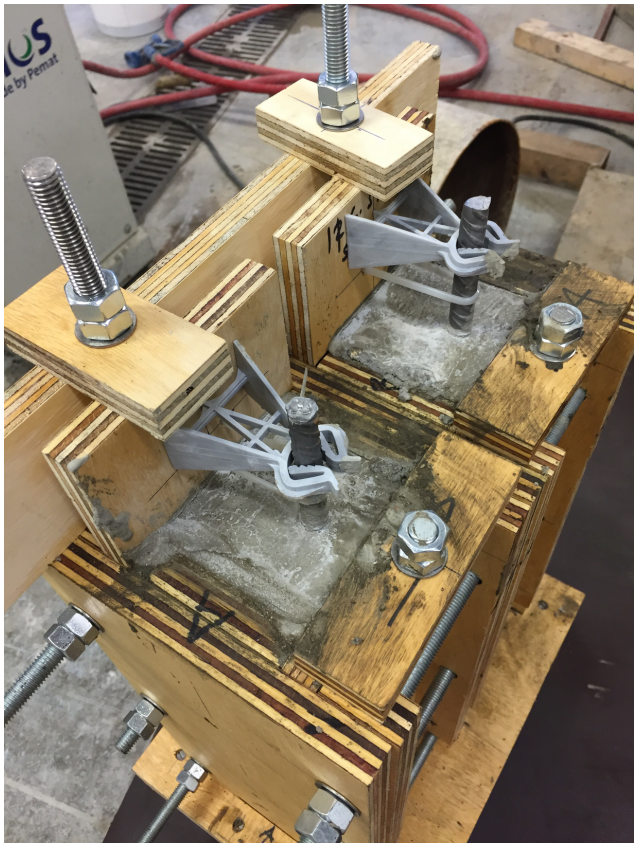

Figure 4.5 Top view of column samples cast in a specially fabricated wooden mould with dimensions 80 mm depth, 90 mm width and 400 mm height. Image taken after 24 hours of curing.

4.2.3 Mixing, curing and conditioning

All ingredients for the concrete mix were batched by weight. Cement, sand and gravel were first dry-mixed in a 50-litre capacity pan mixer for 30 seconds to ensure the dry materials were well mixed before addition of water. Water pre-mixed with the required amount of superplasticiser was then added gently and mixed for a further 3 minutes. Samples were compacted in four uniform layers using a vibrating table VIBTEC 2 x 1 m with variable frequency control as illustrated in Figure 4.6. Figure 4.7 shows the actual sample during the compaction process. The frequency and period of the vibration were adjusted to produce two levels of compaction and segregation degree. Trials were carried out to determine the amount vibration required and the details of the selected vibration frequencies and periods are presented in Table 4.2.

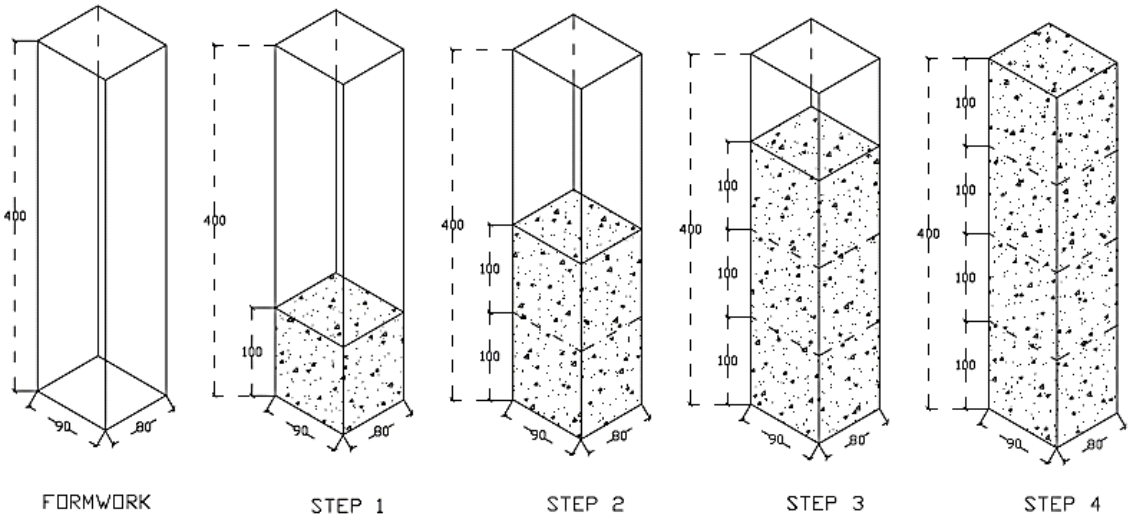

Figure 4.6 **Illustration of the compaction process.**

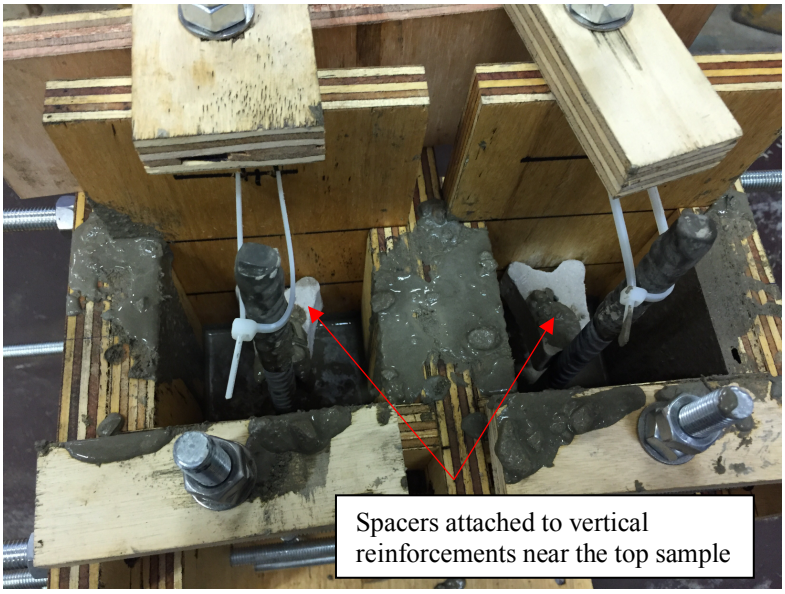

Figure 4.7 **Samples during compaction process. Spacers placed at near the top samples remain in the correct position.**

Table 4.2 Compaction factors

Compaction regime	Frequency (Hz)	Average period for each layer (seconds)	Notes
C1	8.5	90	Over compaction
C2	6.5	40	Adequate compaction

An initial casting was performed to see the effect of the vibration. Samples were cast in cylindrical moulds with diameter of 100 mm and height of 300 mm and vibrated using the values shown in Table 4.2. Once the concrete had hardened, the cylinders were cut using a diamond saw to extract cross-sections for examination. As expected, severe segregation was observed in samples compacted at the higher frequency and longer period of vibration (Figure 4.8).

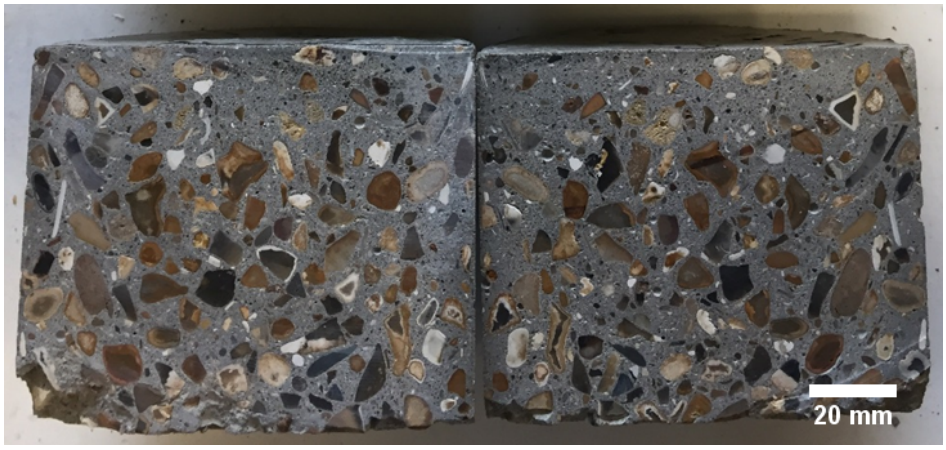

(a) C1

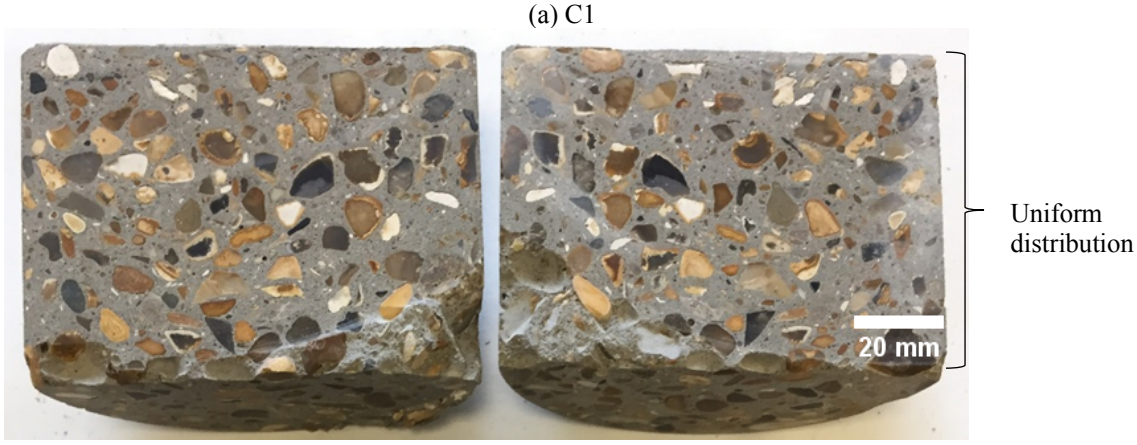

(b) C2

Figure 4.8 Initial trials showing aggregate distribution on the cross-sections of cylindrical samples prepared at different levels of vibration.

As mentioned in Section 4.2.4, a release agent (oil) was applied to all the sides of the wooden mould before placing the concrete. Trials were carried out to determine the amount of oil needed to achieve a smooth surface finish and to avoid surface defects. This is important since surface defects will affect the penetrability of the concrete cover zone (Buenfeld and Okundi, 1998). During the initial casting, severe surface defects in the form of bugholes were found in samples where no oil or too little oil was applied. These can be seen in Figure 4.9a and 4.9b. Samples with surface defects were discarded and only those with a good surface quality (e.g. Figure 4.9c) were used throughout the study.

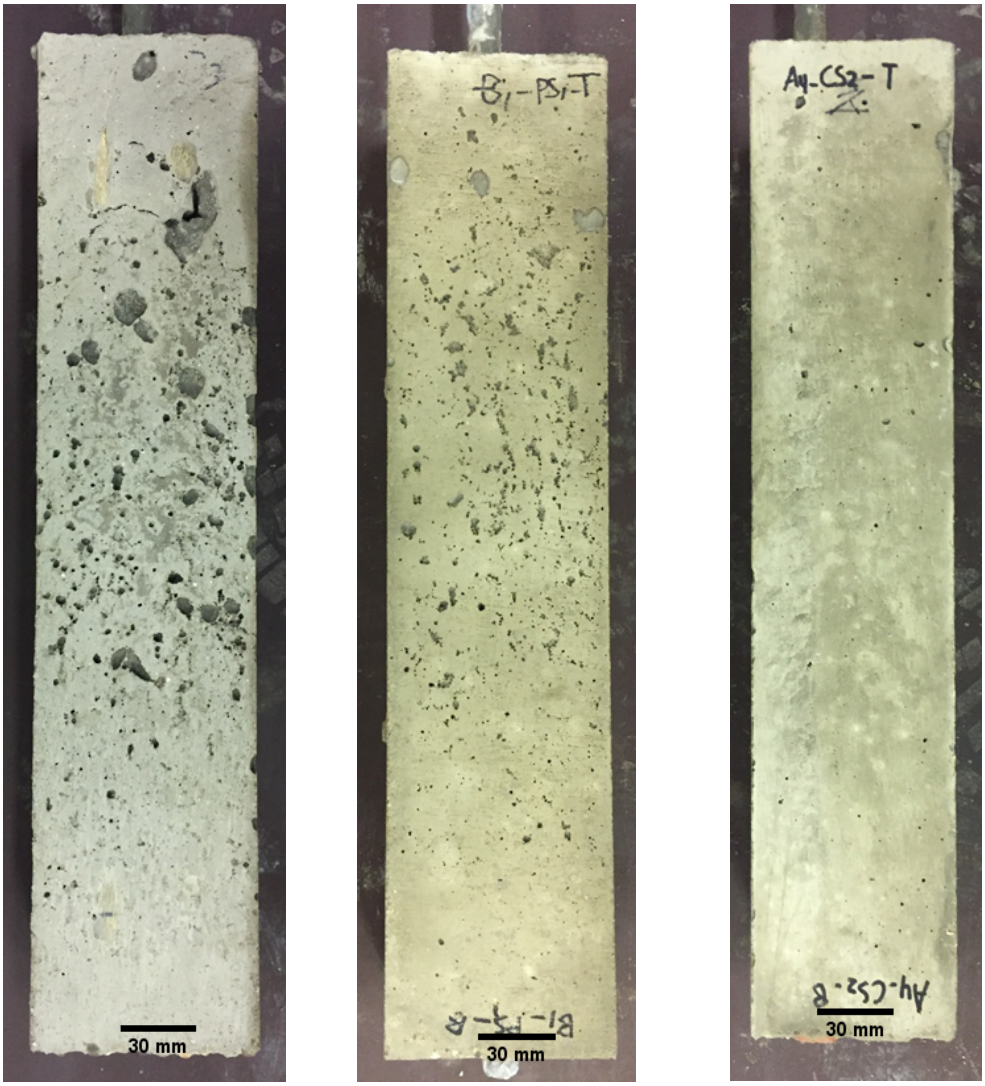

(a) No oil (b) Inadequate oil (c) Sufficient oil

Figure 4.9 Surface defects occurred due to inadequate release agent oil on mould.

The cast samples were covered with wet hessian and a plastic sheet at room temperature for the first 24 hours. The samples were then demoulded and wet cured in a fog room (100% RH, 21°C) for 28 days. Prior to placing the samples in the curing room, the externally exposed rebars on the top of the columns were encased with cement grout (w/c 0.30) to prevent corrosion.

After curing, each column was cut using a diamond blade to extract two rectangular samples of dimensions $L80\ mm$ x $W90\ mm$ x $H100\ mm$ as illustrated in Figure 4.10. The top and bottom samples were used for testing, while the middle section was discarded. Figure 4.11 shows typical cross-sections of top samples containing cementitious and plastic spacers.

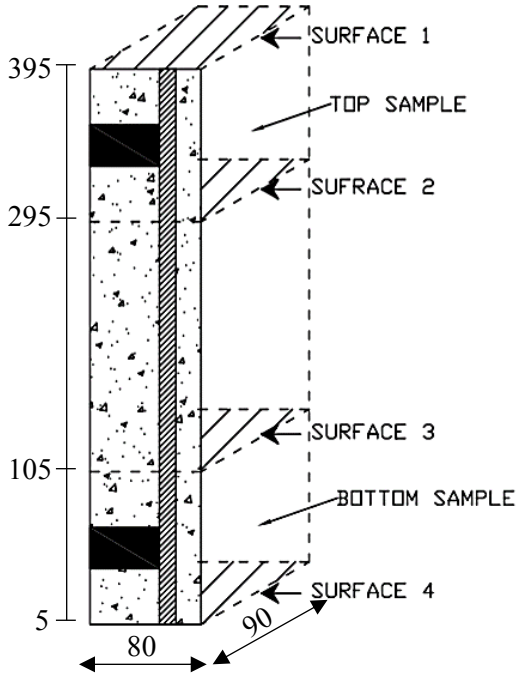

Figure 4.10 Schematic diagram showing the top and bottom samples extracted for transport testing. Dimensions in millimetres.

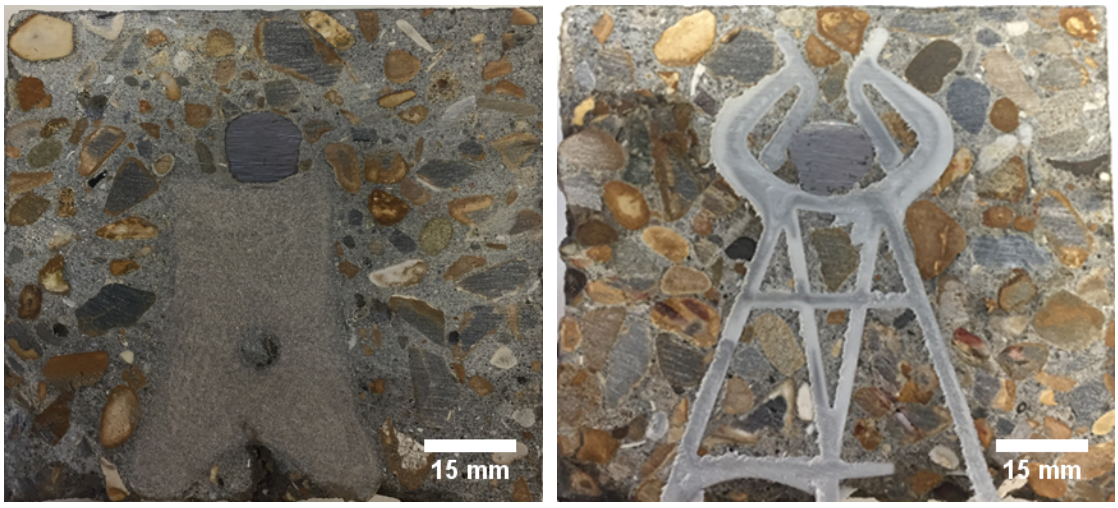

Figure 4.11 Cross-section of rectangular samples extracted from column with cementitious (left) and plastic spacers (right) for transport testing.

The cut samples were subsequently conditioned at 75% RH, 21°C in a chamber containing saturated NaCl to reach an "equilibrium" mass, taken as when the mass loss was less than 0.01% per day. The purpose of conditioning to a constant mass was to ensure that the measured transport properties are not influenced by a variation in moisture content (Wong et al., 2007). This conditioning regime was chosen to represent a relatively mild drying condition when exposed to humid weather conditions. Replicate samples were conditioned in an oven at 50°C to replicate severe drying in hot weather conditions. The conditioning time required for samples dried at 75% RH (21°C) and 50°C to reach the defined constant mass was approximately four and three months respectively.

Throughout this study, samples will be designated using the approach summarised in Figure 4.12.

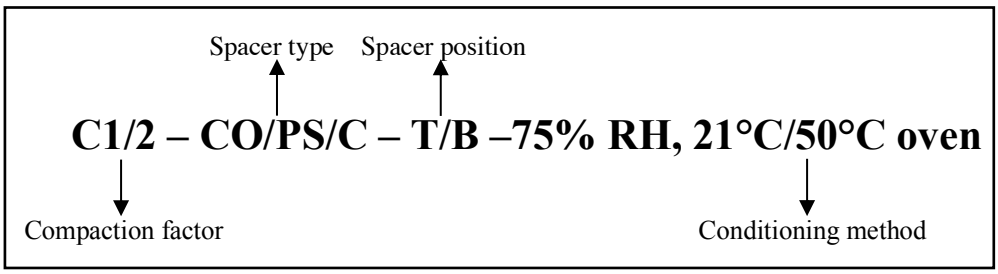

Notations: Compaction factor = 1 (over-vibration) / 2 (adequate vibration); Spacer type = CO (Control without spacer)/CS/PS; Spacer position = Top/bottom; Conditioning method = 75% RH 21°C/50°C oven

Figure 4.12 Sample designation.

4.2.4 Image analysis to estimate segregation

Segregation in the concrete was estimated by measuring the coarse aggregate area fraction on cut surfaces using image analysis carried out with ImageJ/Fiji software. The cut surfaces from the rectangular prisms shown in Figure 4.10 were imaged and analysed. It should be noted that the cutting process was done using a diamond blade operated at a slow feed rate to avoid creating any damage or particle pull-out from the sample. Images were then collected using a digital camera at constant magnification, brightness and contrast settings for repeatability.

Because the aggregate particles were clearly resolved from their shape and colour, no further image processing was needed to enhance contrast. Once recorded, the digital images were analysed using ImageJ/Fiji. The first step was to enlarge the image on the screen so that the aggregate particle boundaries are clearly visible. Next, a fine pixel-wide line was drawn to trace and segment the aggregate particles. Although this seems to be a tedious process and prone to operator judgmental error, the result should be accurate because the boundary marking was done at high magnification. The marked image was compared to the original sample under an optical microscope to check the accuracy of the segmentation. The smallest aggregate size detectable with this approach was 0.4 mm (diameter). Therefore, not all of the fine aggregates were included.

Once all the aggregates were selected and accurately marked, the total area of the aggregate was calculated automatically using ImageJ. The aggregate fraction (%) was calculated by dividing a total area of the aggregates to the total area of the sample surface. Figure 4.13 shows four different surfaces with all the aggregate particles marked with a yellow boundary. Picka et al. (2000), Roussel (2006) and Breul et al. (2008) also applied the same method to measure the solid fraction of concrete in the segregated zone.

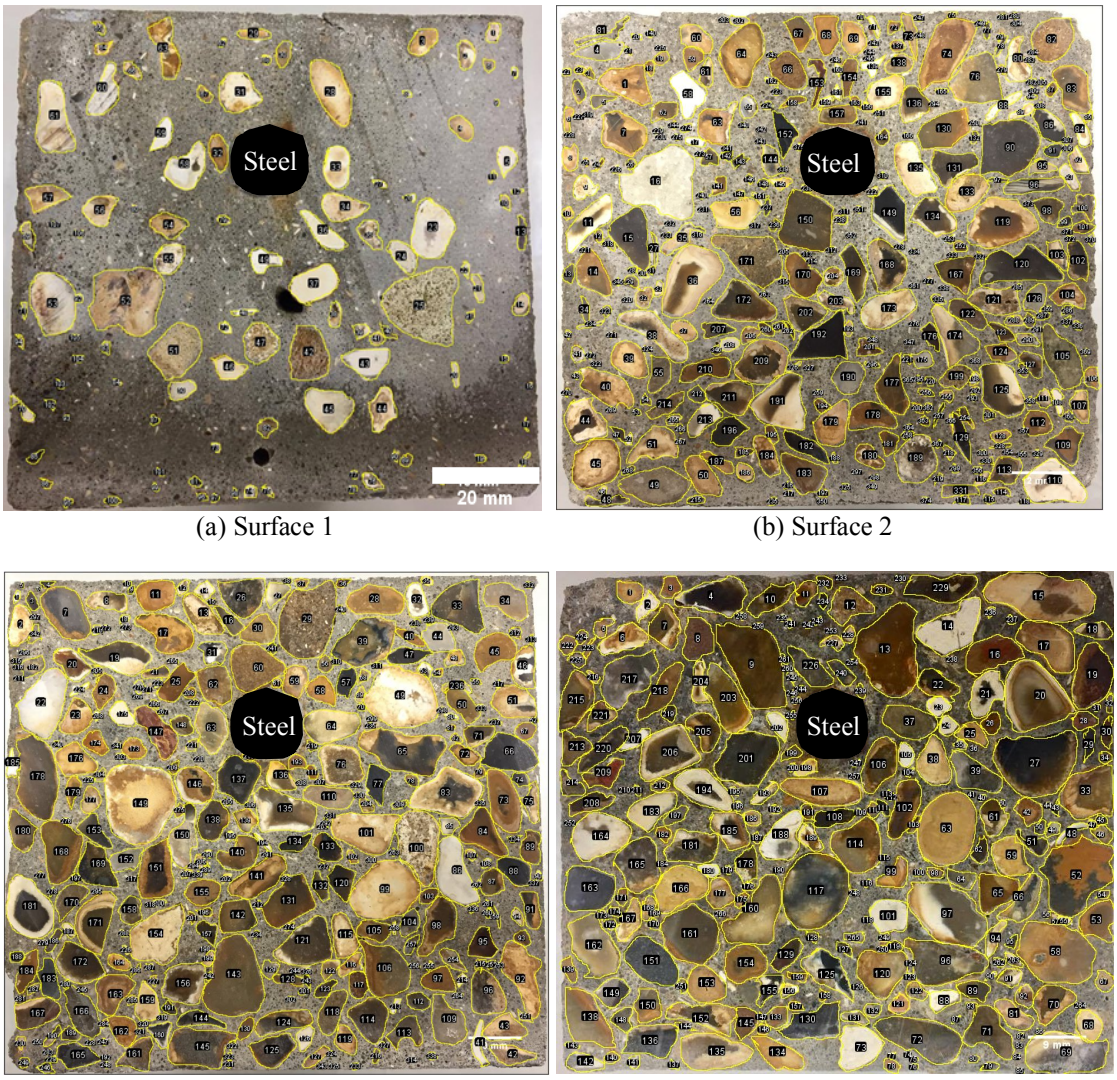

(a) Surface 1 (b) Surface 2

(c) Surface 3 (d) Surface 4

Figure 4.13 Example of image analysis showing segmented coarse aggregate particles on cross-sections taken at different heights (Sample is C2-PS).

4.2.5 Transport properties

The cut samples were tested for water sorptivity and electrical conductivity at two replicates per test. Details of the tests are given in Chapter 3 and summarised here. Water sorptivity was measured by placing the sample in a rectangular tray containing water to a depth of about 3 mm from the bottom surface of the sample as shown in Figure 4.14 and then measuring the mass gain with time until saturation was achieved. The sorptivity coefficient ($g/m^2min^{0.5}$) was determined from the slope of the regression line of absorbed water per unit flow area against the square root of time ($R^2 > 0.99$) according to the classical unsaturated flow theory. The best-fit regression line was drawn across at least ten readings taken during the first seven hours of measurement.

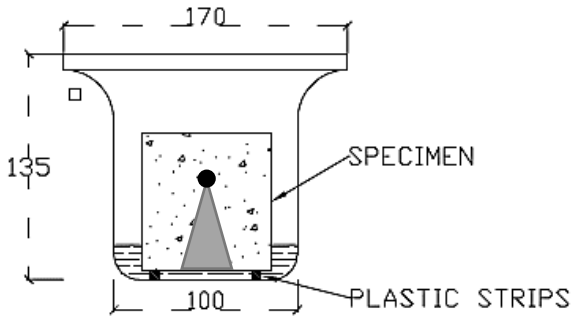

Figure 4.14 Diagram of test set-up for the water absorption test.

Immediately after the water absorption test, the samples were vacuum saturated in water for approximately four hours to determine its accessible porosity. Sample porosity was estimated from the mass difference between the preconditioned state and vacuum saturated-surface dry condition. Samples in a vacuum saturated-surface dry condition were then placed between two brass plates and connected to an LCR databridge in order to determine the electrical conductivity. A generous amount of a salt-free electrode gel was then applied on both surfaces prior to clamping to ensure a proper electric contact between the brass plates and the sample surfaces. The resistance typically stabilises within one minute; three readings were taken and then averaged. Electrical conductivity σ_e (*S/mm*) is the reciprocal of electrical resistivity.

4.3 Results

4.3.1 Segregation profile

Figure 4.15 shows the segregation profiles of samples with and without spacers compacted at frequency of 8.5 Hz for 90 seconds per layer (C1) and at frequency of 6.5 Hz for 45 seconds per layer (C2). The profiles were created by plotting the measured area fraction of coarse aggregate against surface height relative to the cast column. For C1, 5 mm thick material from the top and bottom samples was cut-off to remove uneven surface. Unfortunately, no data were available at 5 and 395 mm for C2 due to a problem with the diamond cutter.

The results clearly show that all columns experienced some amount of segregation. As expected, columns that were compacted at higher intensity and for longer duration (C1) showed a greater amount of segregation. Samples with cementitious spacers showed the highest segregation for both compaction regimes (C1 and C2). Samples containing plastic spacers showed less segregation, for example at C2, the distribution of aggregate content was fairly consistent (~40%) at heights between 100 and 300 mm.

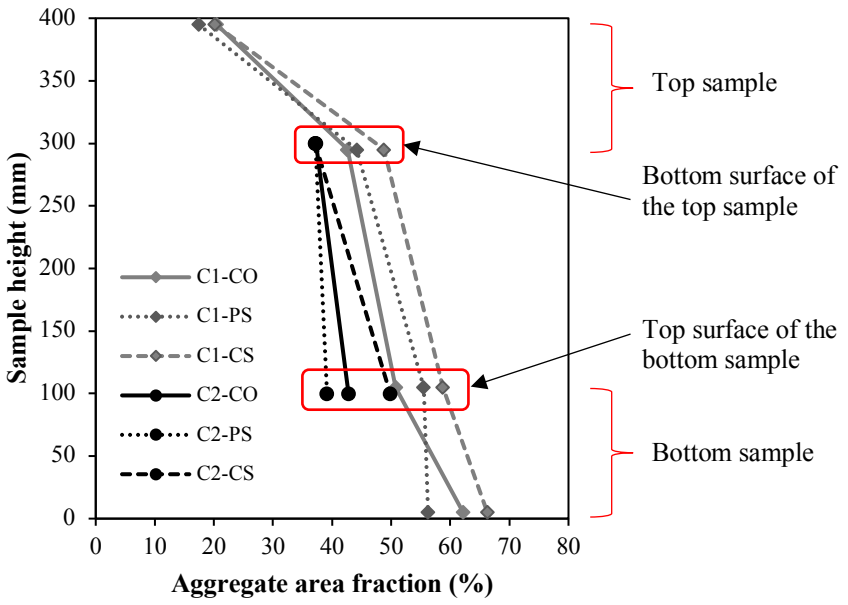

Figure 4.15 Segregation profiles of samples compacted according to regime C1 and C2.

By measuring the aggregate fraction on each cut surface, the data can also be used to produce an area distribution plot as shown in Figure 4.16. The results show that the most aggregate observed on the top sample surfaces (surface 1) has an area in the range of 0.5 – 1 mm^2 (equivalent to a diameter of 0.8 – 1.1 mm) while the bottom surface contained the aggregate particles with area in the range of 1 – 5 mm^2 (equivalent to a diameter of 1.1 – 2.5 mm).

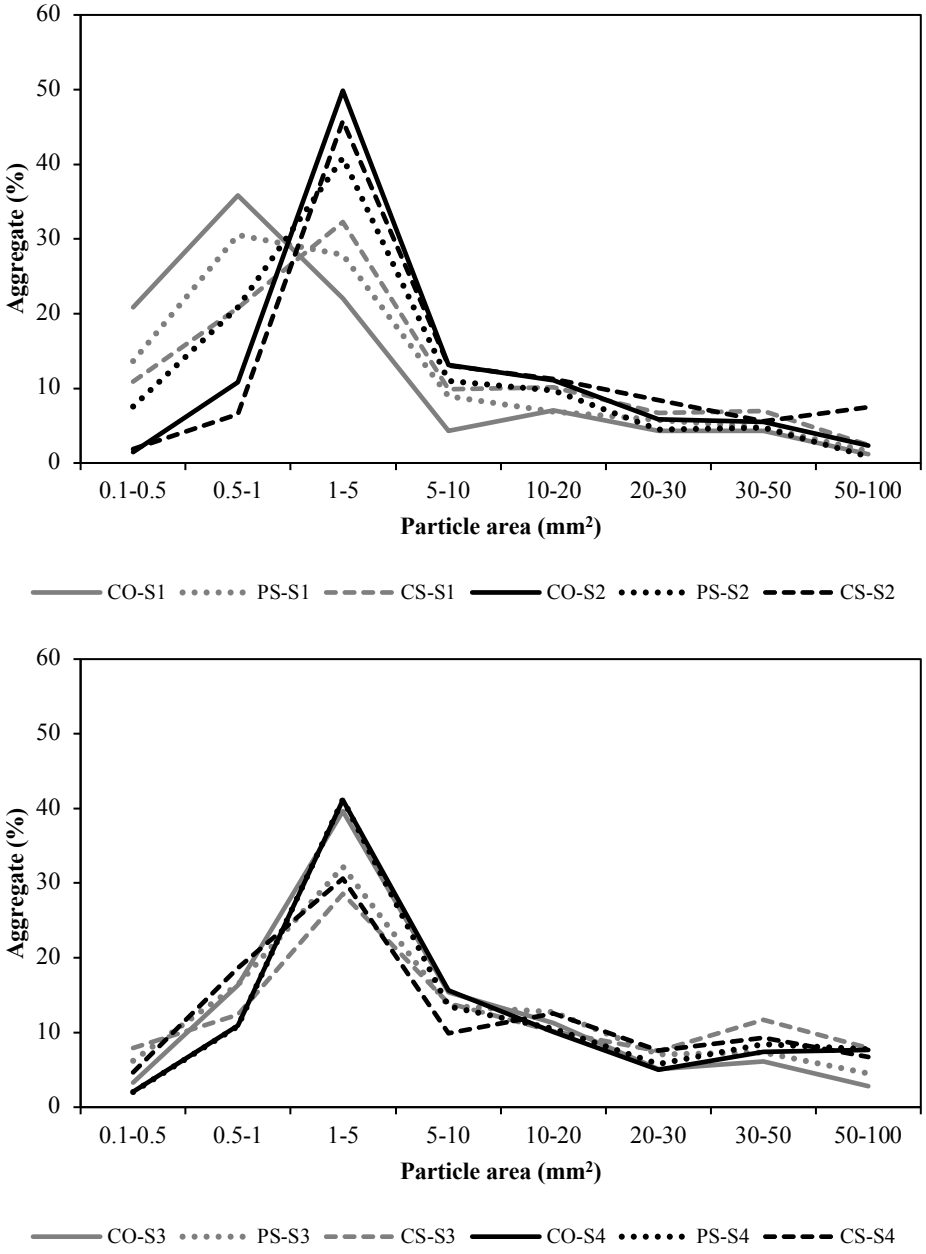

Figure 4.16 Area distribution of aggregate particles measured from cut-surfaces at different heights.

Figure 4.17 shows a comparison between the aggregate size distribution measured using the sieve analysis method and the detected aggregate size on the top and bottom samples measured using the image analysis technique. The results indicate that the bottom surface is mostly covered with the coarse aggregate particles (gravel), while the top surface contains smaller aggregate particle sizes. It is worth noting that the aggregates measured on the bottom surface have a similar particle size distribution to the gravel, while the top surface is similar to the sand.

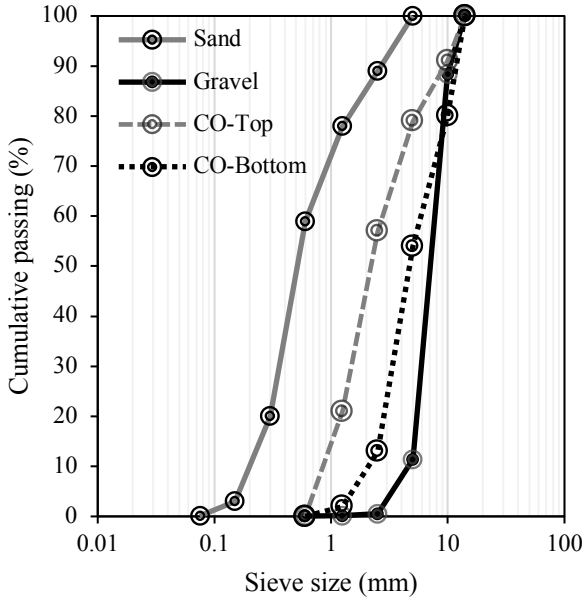

Figure 4.17 Comparison between aggregate size distribution measured using sieve analysis method (solid line) and image analysis technique (dashed line).

4.3.2 Water sorptivity

The measured water sorptivity coefficients are presented in Figure 4.18. Each data point represents the average of two replicate measurements, and error bars indicate the standard error ($\sigma/\sqrt{n}$) of the average where σ is the standard deviation and n is the number of replicates. It is noted that the variability within replicates is relatively small and so meaningful comparisons can be made.

The results show that the top samples consistently produced higher water sorptivity coefficients than that of the bottom samples. However, the samples compacted with a lower frequency and shorter period (C2) gave lower sorptivity coefficients than samples compacted with a high frequency and long period (C1), the largest differences being amongst the top samples. The average differences between the top and bottom samples for C1 and C2 were 10 g/mm^{2}min$^{0.5}$ and 4.8 g/mm^{2}min$^{0.5}$ respectively.

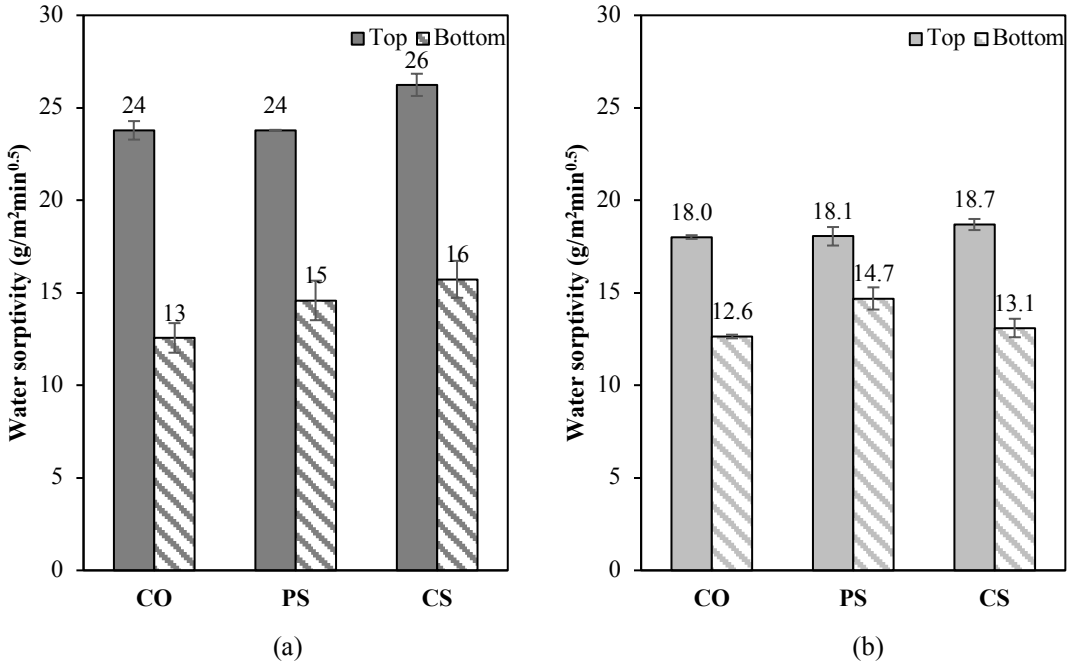

Figure 4.18 Effect of spacer type and position on water sorptivity for compaction regime (a) C1 and (b) C2. Samples were conditioned at 75% RH, 21°C.

Figure 4.19 shows the comparison of water sorptivity after being subjected to drying to 75% RH, 21°C or 50°C. The results clearly show that the sorptivity increases with increasing severity of drying. The measured sorptivity of samples without spacers (CO), with plastic spacers (PS), and cementitious spacers (CS) after drying at 50°C were higher than the corresponding samples dried at 75% RH, 21°C by a factor of 3.3, 5.2 and 3.3 respectively. It is worth noting that the effect of spacers on water sorptivity is greater when samples were severely dried prior to testing. For the C1- and C2- samples dried at 50°C, plastic spacers increased the water sorptivity of the top and bottom samples by about 26% to 58% and 77% to 88% respectively. The corresponding values for cementitious spacers were 17% to 34% and 9% to 58% respectively.

Typical plots of the cumulative water absorption against square root of time are shown in Figure 4.20. The results show that the initial slope of the water absorption profile and the total amount of water absorbed for the top samples were higher than those of the bottom samples for all cases. The 50°C oven-dried samples showed a slightly nonlinear relationship between the square-root of elapsed time and cumulative absorbed water, where the initial mass gain was followed by a more rapid mass gain before achieving saturation, compared to those that were conditioned at 75% RH, 21°C (Figure 4.20a). This nonlinear behavior is probably due to drying-induced microcracking as observed by Wong et al. (2007) and Wu et al. (2018). Also, fine cracks of approximately 5 μm width were observed at the base of samples containing plastic spacers. The cracks appear to be parallel to the spacer position as shown in Figure 4.21. Overall, the presence

of plastic spacers led to higher water sorptivity coefficients that were up to a factor of 1.9 compared to the control samples after drying at 50°C.

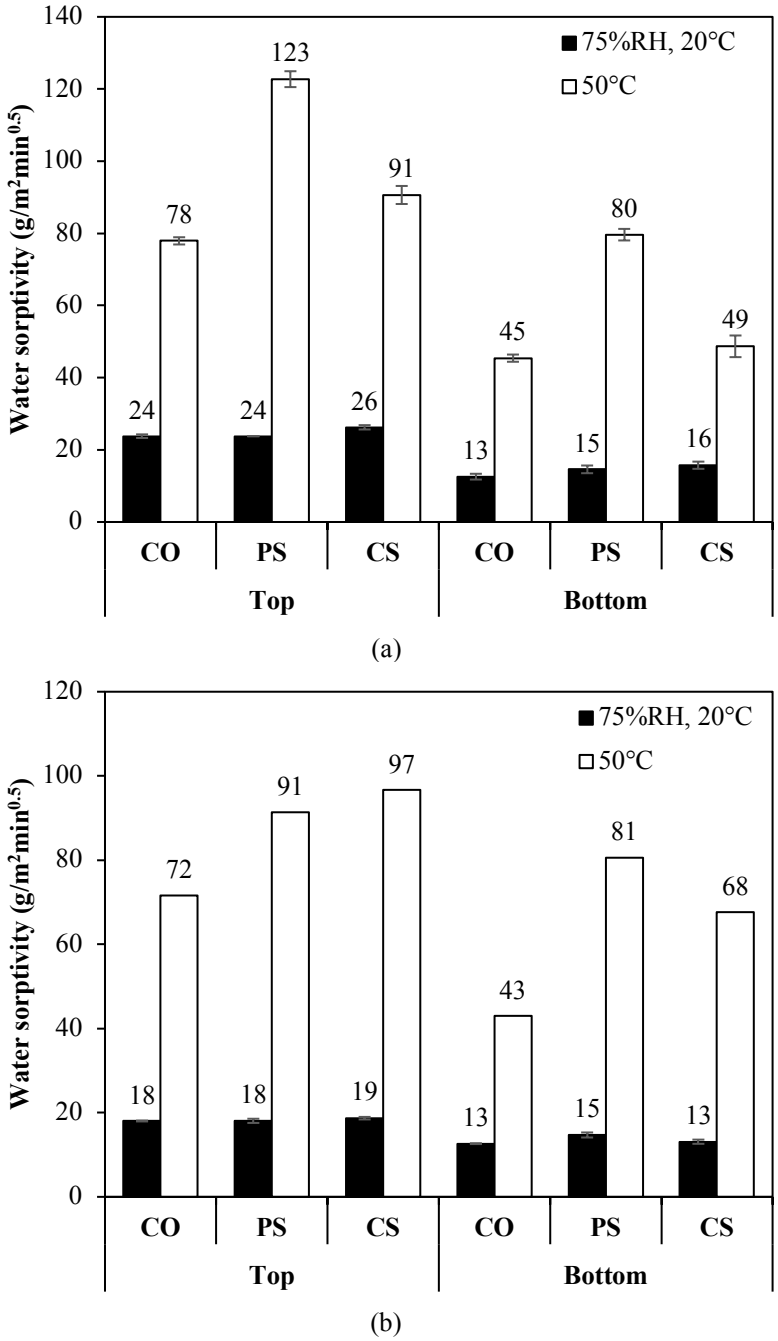

Figure 4.19 Effect of oven-drying at 50°C on the measured water sorptivity for compaction regime (a) C1 and (b) C2.

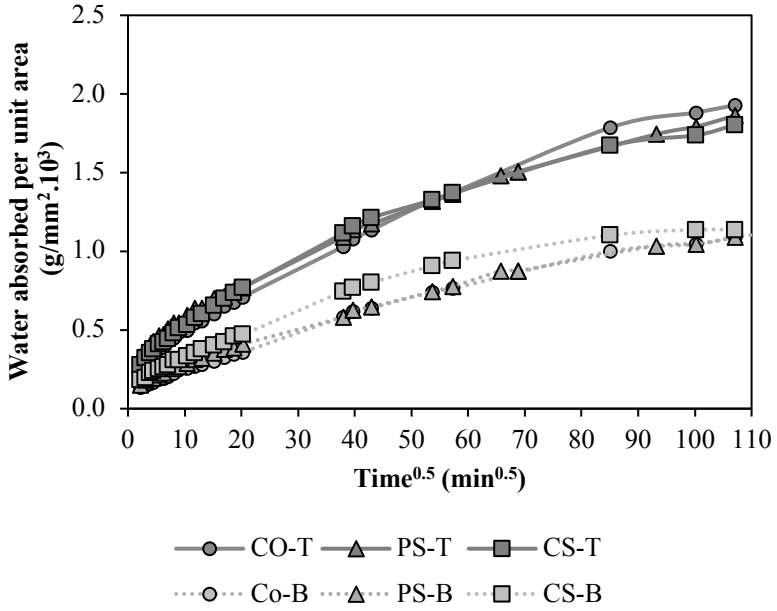

(a)

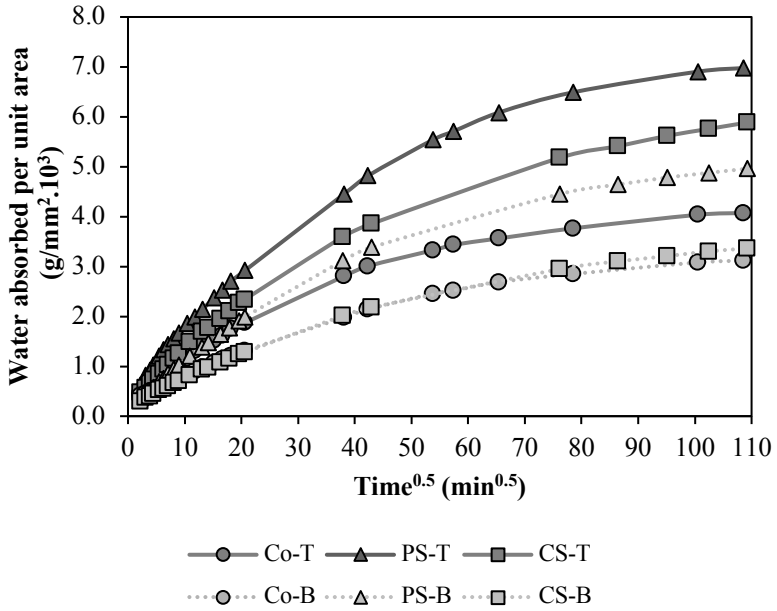

(b)

Figure 4.20 Typical plots of cumulative water absorption against square-root of time after conditioning at: (a) 75% RH, 21°C; (b) 50°C (Compaction regime C1).

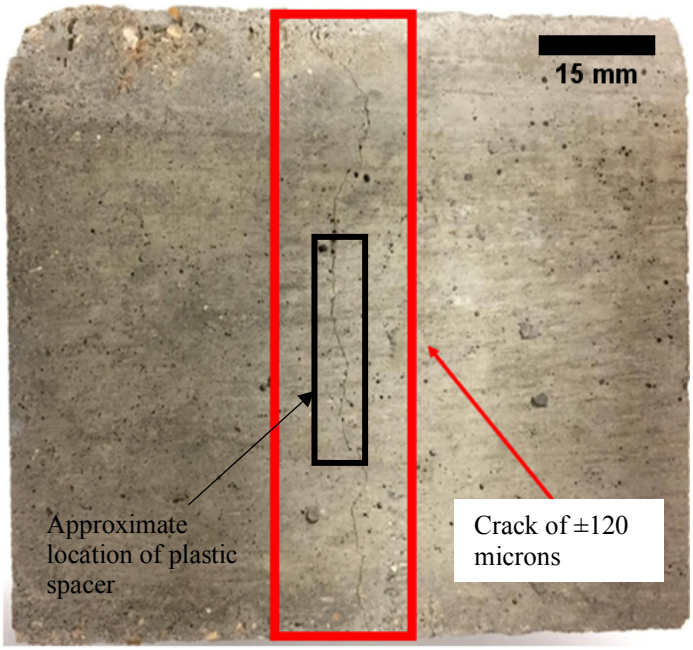

(a)

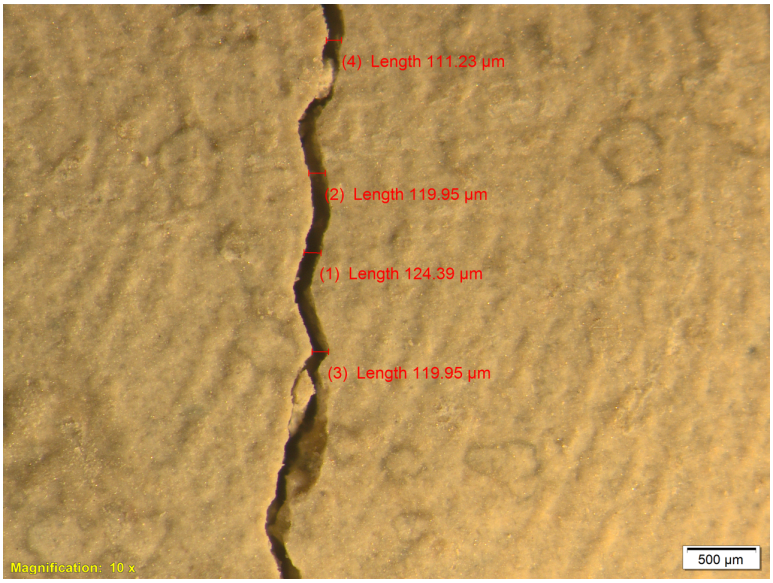

(b)

Figure 4.21 (a) Fine cracks appearing on the base of samples containing plastic spacers conditioned at 50°C. (b) Crack widths were measured using a stereo microscope SZX9.

4.3.3 Electrical conductivity

Figure 4.22 shows the measured electrical conductivity for all samples. The results show that the top samples consistently have higher conductivity compared to the bottom samples for both C1 and C2 compaction regimes. However, the difference between the top and bottom samples decrease with decrease in the amount of compaction and degree of segregation. The effect of spacers can also be detected. On average, the conductivity of the C1- and C2- top samples with spacers were higher than of the control samples by about 6.4% to 11% and 11% to 17 % respectively. For the bottom samples, spacers increased the conductivity by about 10%. The presence of spacers in C2 compacted samples gave a higher increase in electrical conductivity compared to C1. It appears that decreasing the amount of compaction (and hence segregation) produced a larger difference between the conductivity of samples with and without spacers.

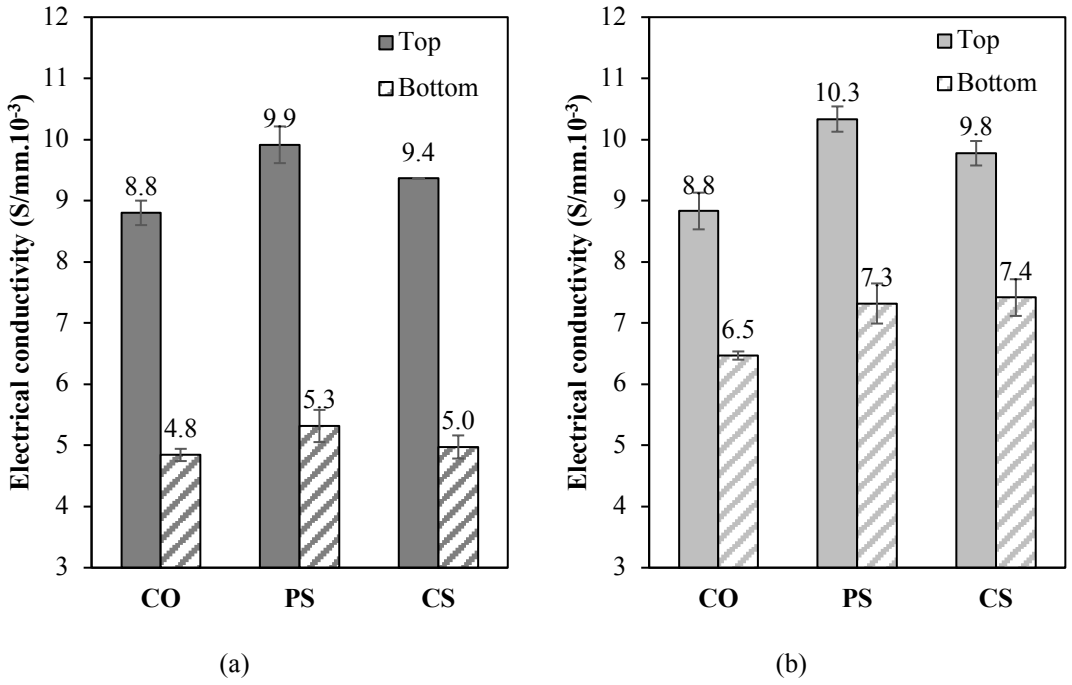

Figure 4.22 Effect of spacer type and position on electrical conductivity for compaction regime (a) C1 and (b) C2. Samples were conditioned at 75% RH, 21ºC then vacuum saturated prior to measurement.

4.3.4 Sample porosity

As explained in Chapter 3.3.4, the sample porosity was estimated by measuring the volume of water absorbed from a preconditioned state (75% RH, 21°C) to a vacuum saturated-surface dry condition and dividing it by the sample volume. Results are shown in Figure 4.23. Similar to the trends from transport property measurements, it can be seen that samples compacted with higher frequency and longer period (C1) produced the highest porosity for all cases. The porosity of the top and bottom samples decreased by up to 50% and 25% respectively when the

compaction factor changed from high frequency of 8.5 Hz to 6.5 Hz. Samples containing spacers consistently gave the highest porosity regardless of the spacer position and compaction regime. The measured sample porosity of C1 and C2 samples with spacers were higher than the control samples by up to a factor of 1.2 and 1.47 respectively.

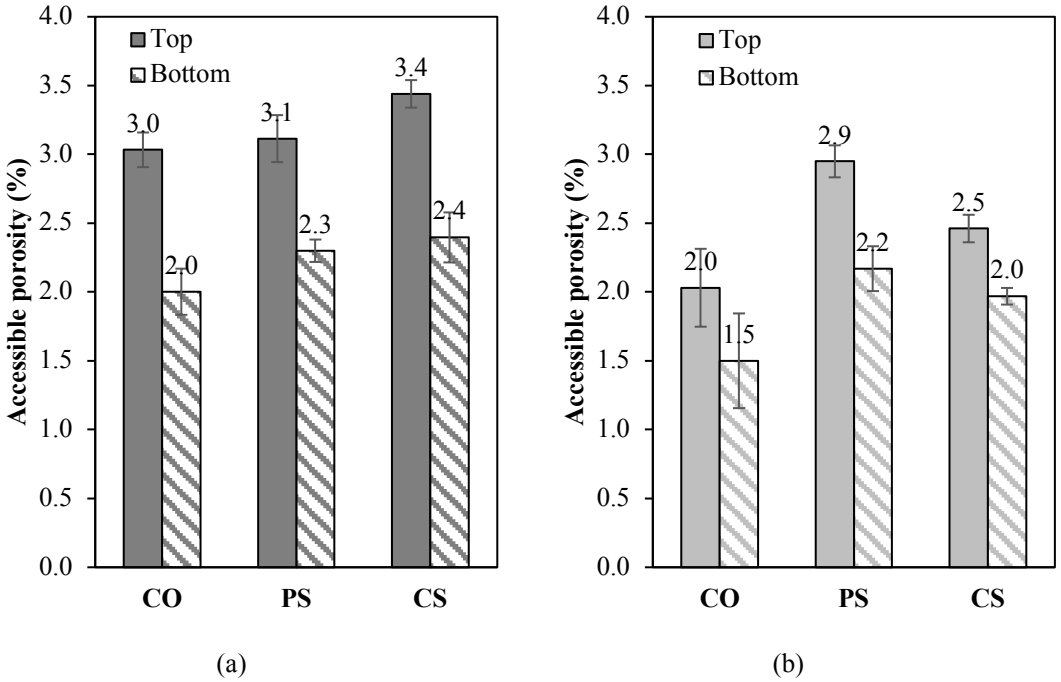

Figure 4.23 Effect of spacer type and position on sample porosity for compaction regime (a) C1 and (b) C2. Samples were conditioned at 75% RH, 21°C then vacuum saturated prior to measurement.

Figure 4.24 shows the comparison of sample porosity after being subjected to drying at 75% RH, 21°C or in a 50°C oven. The results clearly show that the porosity increased with increasing severity of drying by a factor of 2.6 to 4.2. Samples containing a cementitious spacer had the highest increase in all cases. For C1-samples dried at 50°C, the spacers increased the accessible porosity of the top and bottom samples by up to 29% and 21% respectively. The corresponding values for the C2-samples were 38% and 47% respectively. Similar to the results in water sorptivity, the effect of spacers on the accessible porosity is greater when the samples were severely dried. Interestingly, the presence of a plastic spacer did not significantly increase porosity as it did to water sorptivity. This indicates that the drying induced microcracks at the spacer-concrete interface occupy only a small volume and did not produce a significant change in total porosity.

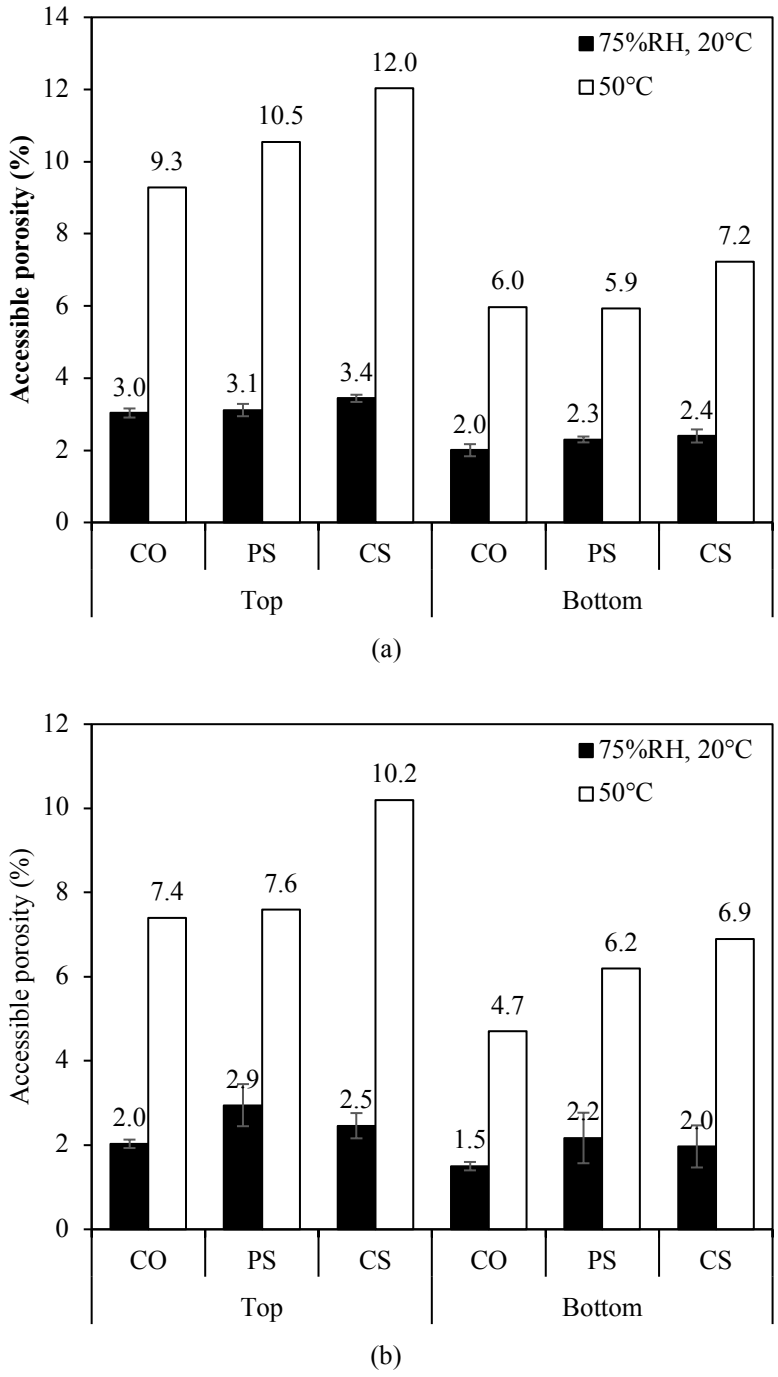

Figure 4.24 Effect of oven-drying at 50°C on sample porosity for compaction regime (a) C1 and (b) C2.

4.3.6 Relationship between aggregate content, spacers and transport properties

The correlations between accessible porosity, water sorptivity and electrical conductivity for samples conditioned at 75% RH, 21ºC are shown in Figure 4.25. Each data point corresponds to one sample. The results show that the transport coefficients are highly dependent on porosity, which is well-known and consistent with the fact that water absorption and electrical conduction only occur through empty pores and cracks.

When the sample porosity is plotted against the aggregate fraction (Figure 4.26), it can be seen that porosity increased with decreasing aggregate fraction. The top samples consistently have higher porosity and a lower aggregate fraction compared to the bottom samples. This is again in line with expected behaviour. As a result of segregation, the top samples contained fewer aggregate particles and a higher amount of cement paste. Bleeding would also increase the effective w/c ratio and porosity of the cement paste. In contrast, the bottom samples contained more aggregate particles and less porous cement, thus decreasing porosity.

Furthermore, an interesting trend is observed when the transport data are plotted against the area fraction of aggregate as shown in Figure 4.27. The figures are produced by normalising the transport results to the lowest value of each test, which is the bottom control sample without spacer (C1-CO-B). The results show that the top samples consistently gave higher transport properties and porosity compared to the bottom samples. The measured water sorptivity of the top samples was twice higher than that of the bottom samples. This trend is similar to the measured electrical conductivity. It is worth noting that the samples containing cementitious spacer had the highest aggregate fraction and water sorptivity.

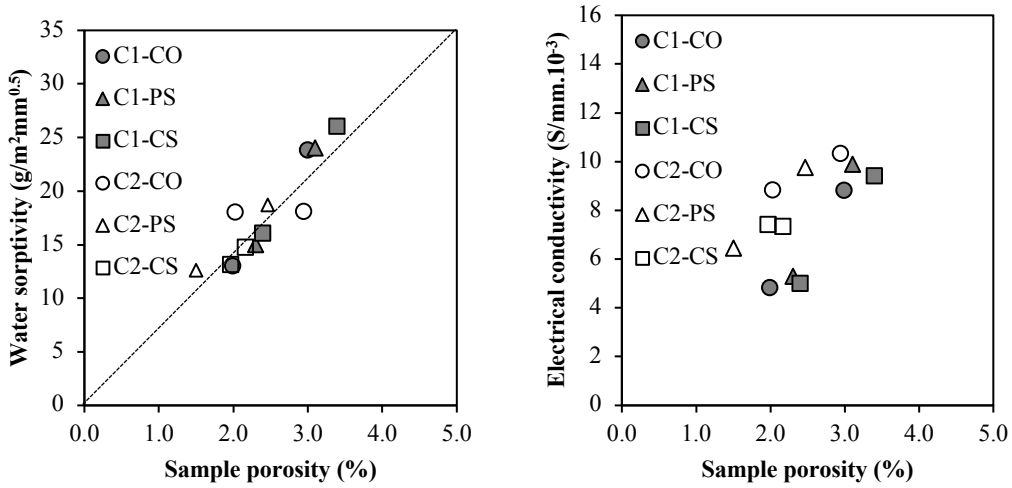

(a) (b)

Figure 4.25 Correlation between sample porosity and transport properties: (a) Water sorptivity; (b) Electrical conductivity.

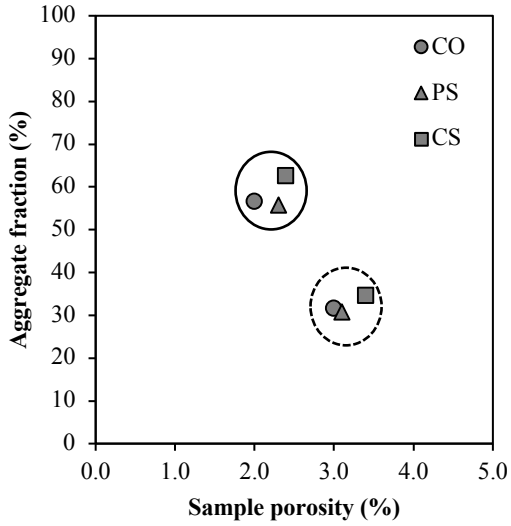

Figure 4.26 Correlation between sample porosity and aggregate fraction showing that porosity increased with decreasing aggregate fraction. Solid and dashed circles indicate the C1- bottom and top samples respectively.

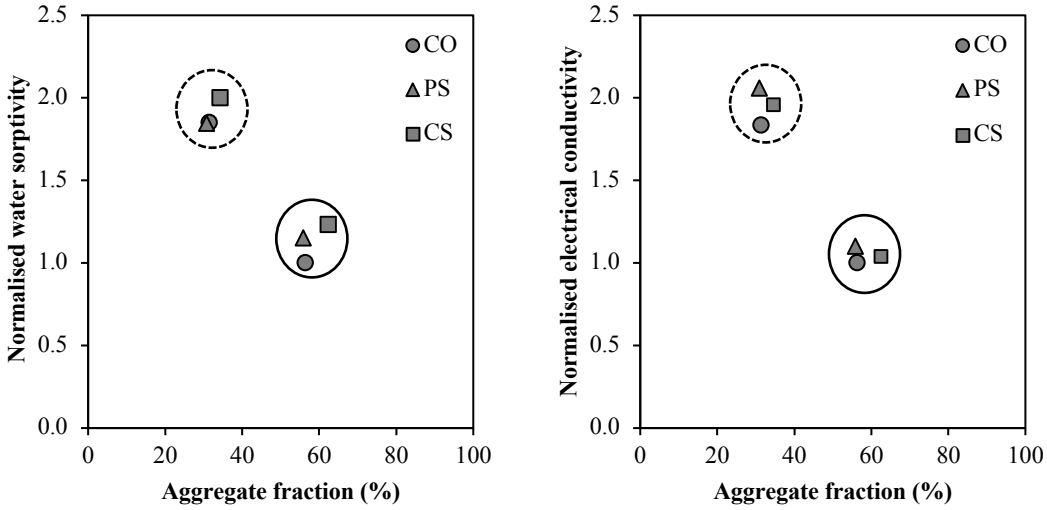

Figure 4.27 Effect of segregation and spacers on transport properties. Solid and dashed circles indicate the C1- bottom and top samples respectively.

4.4 Discussion

Regardless of the amount of segregation, samples containing spacers consistently gave higher water sorptivity, electrical conductivity, and sample porosity compared to the control samples (without a spacer). This occurred whether the spacer was in the top or bottom of the column. The control samples had the lowest transport coefficients in all cases. This is attributable to the fact that in samples containing spacers, the spacer replaces a substantial volume of the concrete and creates interface zones that have higher porosity with the surrounding concrete. As such, the spacers provide additional transport paths either through the spacer itself (in the case of a cementitious spacer) or at the spacer-concrete interface, thus increasing the overall bulk transport properties. A cementitious spacer that is very different to the surrounding concrete will affect the overall transport property. For example, the spacer used in this study has a total porosity of 8.5% and water sorptivity of 35 $g/m^2.mm^{0.5}$. However, it should be noted that the spacer was conditioned at 60±5% RH, 21ºC prior to use, which is different to the drying regimes of the concrete. This finding shows a good agreement with the experimental data reported by Tang and Utgenannt (2009) and Alzyoud et al. (2016).

The results also show that reducing the frequency and period of compaction caused a significant reduction in segregation, which is line with other studies (Safawi et al., 2004). Compaction of the concrete induced by vibration forces excess water to rise and the heavier constituent materials (aggregate and cement particles) to settle due to gravity. The higher the frequency and the longer the compaction time, the greater the tendency for water to move upwards through the capillary network to higher parts of concrete. In contrast, the heavier aggregate particles are

more likely to settle down. This was confirmed in Figures 4.13 and 4.14 showing that the concrete near the top surface had the smallest aggregate content.

Along with the process described above, part of the bleed water is expected to become trapped underneath spacers. This effect will be particularly relevant for spacers supporting vertical reinforcement due to their orientation and location relative to the casting direction. This behavior leads to more porous zones beneath the spacers due to the accumulation of water, thus decreasing the strength and transport properties (Figure 4.28). In contrast, the settlement of aggregates and cement above the spacers could produce the opposite effect on the top spacer-concrete interface. Nevertheless, the results from this study show that the net effect of spacers and segregation on mass transport properties is negative.

As a result of segregation, samples near the bottom of the columns are denser than the top, have lower total porosity, resulting in lower transport coefficients. Although it is well-known that concrete experiences segregation on compaction, very few studies have actually characterized its effect on mass transport. Wong et al. (2009) reported that 250 mm tall cylinders showed gradients in porosity and aggregate content along the height of the cylinder due to segregation. This explained why the samples extracted from the bottom of the cylinders consistently showed lower transport properties than those from the top. Earlier studies by Aldea et al. (1999) also found a significant difference in the transport results of cylindrical samples extracted from different locations (top, middle, or bottom), as an effect of segregation. The top samples always gave higher transport properties.

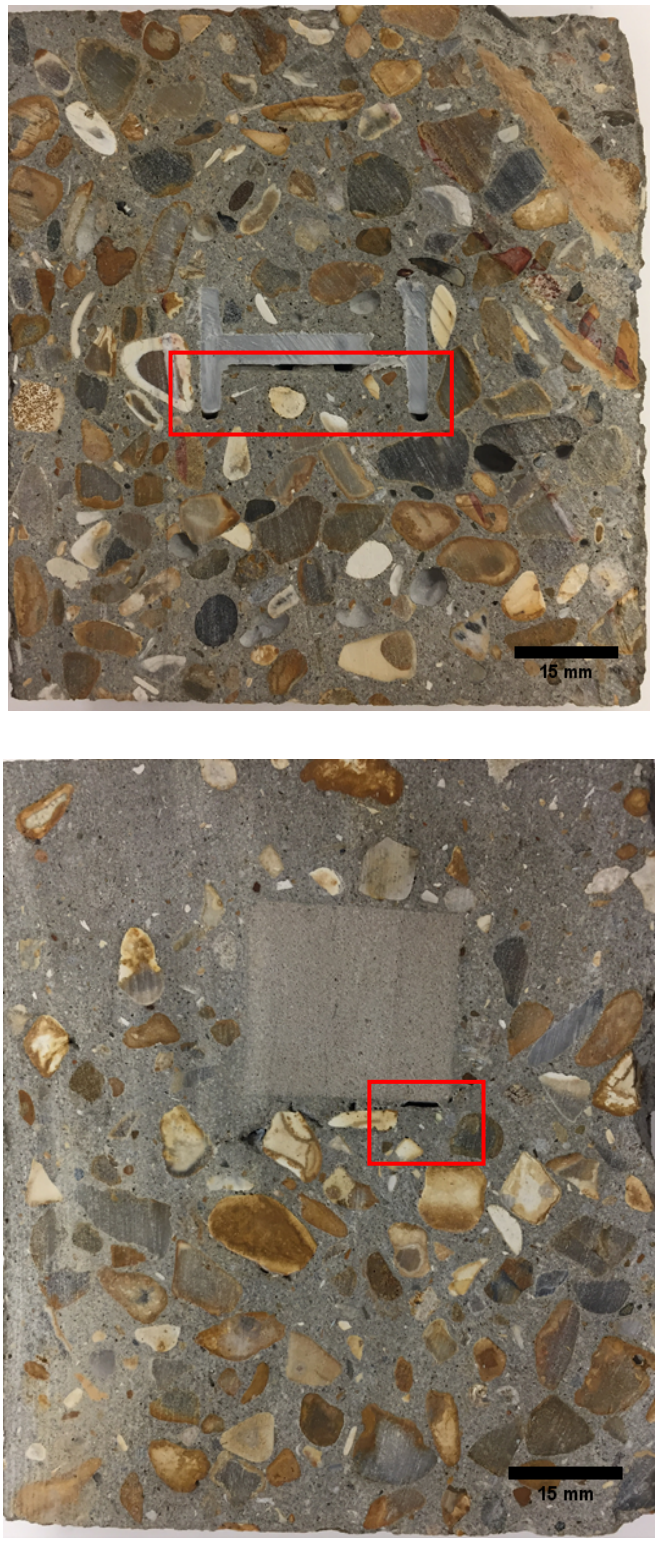

Figure 4.28 **Cross-section of samples extracted from column with plastic (top) and cementitious spacers (bottom) showing a porous interface underneath the spacer due to trapped bleed water.**

It is interesting to note that the presence of plastic spacers reduces the tendency for segregation by about 7.5% relative to the control sample. In contrast, the cementitious spacers increased the segregation by approximately 19% relative to the control sample. This behaviour is probably due to the differences in shape and size between the plastic and cementitious spacer (see Figure 4.1). The plastic spacer has a clip and occupies a larger area such that when attached to the vertical reinforcement, it reduces the cross-sectional area available for aggregates to move during compaction and therefore segregation tendency.

There have been no previous studies on the combined effects of spacers and segregation on the transport properties of vertically cast concrete. However, the effect of spacer position on transport can be compared to the influence of horizontally anchored bars located in upper sections of structural elements (top-bar effect). Studies have shown that the corrosion of concrete increases with increasing the height of concrete section due to the increase of concrete porosity and the decrease of steel-concrete interface quality (Soylev and Francois, 2003, Mohammed et al., 1999). In another study, backscattered electron (BSE) imaging was carried out by Horne et al. (2007) that showed that the steel-concrete interface beneath reinforcing steel had more porosity than that above.

It is interesting to observe that the negative effect of spacers on transport properties for the top samples was more substantial than that for the bottom samples. This again could be linked to bleeding and segregation that modifies the characteristics of the spacer-concrete interface. For example, the accumulation of bleed water near the top produces a more porous interface, while the settlement of aggregate particles at the bottom could induce a densification effect. Moreover, it is clear that the phenomenon of segregation causes not only the reduction of aggregate particles on the top of the samples but also an increase of the cement paste proportion, and therefore the tendency to shrink. The drying shrinkage of cement paste will be restrained by the spacer. This produces radial and tangential stresses, leading to cracks when these exceed the local tensile strength. In contrast, the bottom samples contain less cement paste than those of the top samples; thus, the shrinkage tendency is also less. A similar effect can be seen when the results of C1- and C2- samples were compared. The effects of spacers on the C2-bottom samples are greater than those of the C1-samples. This is because the C2-samples experienced less segregation than the C1-samples, thus having fewer aggregate particles and a higher amount of cement paste. This is in agreement with the numerical observations reported by Grassl et al. (2010) showing that the average lengths and widths of micro-cracks decrease with decreasing aggregate volume fraction.

Finally, it should be noted that the conditioning regime prior to testing has a major influence on the measured transport properties. Oven drying at 50°C produced the highest sorptivity coefficients in all cases. This is in line with previous studies showing that increasing drying severity increases the available transport paths, resulting in higher transport rates (Samaha and Hover, 1992, Wong et al., 2009, Wu et al., 2015). Furthermore, it is interesting to note that oven drying produced a greater increase in transport properties for samples containing spacers. This is because drying shrinkage of the cement paste is restrained not only by the rigid aggregate particles but also by the spacer. Moreover, samples containing plastic spacers were the most sensitive to oven drying. This is believed to be due to the plastic spacer having a thermal expansion coefficient of over 10-15 times than that of the surrounding concrete. This produces a greater stress concentration at the interface on heating. On cooling, large gaps develop at the spacer-concrete interface, facilitating transport processes. This occurred despite the fact that the plastic spacer is already perforated throughout over 25% of the gross plane area to compensate for the thermal differences between the concrete and plastic spacer.

4.5 Conclusions

This chapter presented experimental data on the effect of spacers (type and position) and segregation on the transport properties of vertically cast concrete. Water sorptivity, electrical conductivity, and sample porosity of 400 mm tall concrete columns containing plastic and cementitious spacers positioned near the top and the bottom of the samples and compacted with different frequencies and periods were investigated. The influence of the conditioning regime (75% RH, 21°C; 50°C) on the measured sorptivity was also analysed. Samples were prepared at a constant free w/c ratio of 0.4 and fixed aggregate volume fraction (70%) to enable meaningful comparisons.

Results clearly showed that the segregation and the presence of spacers have a negative effect on mass transport properties. The top samples consistently had the lowest resistance to transport due to higher bleeding and reduction in aggregate content. The inclusion of spacers consistently increased the transport properties relative to the control sample (without spacers). Drying at 50°C prior to testing increases the severity of the effect of spacers on the water sorptivity. This is due to the thermal and shrinkage differences between spacer and concrete, in particular samples with plastic spacers. The effect of oven-drying induced microcracks on other transport properties will be discussed in Chapter 5.

Chapter 5

Influence of SCMs on transport properties of concrete containing spacer

As discussed in Chapter 4, the inclusion of spacers produces a porous interface that affects the microstructure and transport properties of concrete. This chapter presents an exploratory study on mitigating the negative effects of spacers through the use of supplementary cementitious materials (SCMs) such as silica fume, fly ash and ground granulated blast-furnace slag in the concrete mix. It is well-known that SCMs can produce concretes with a denser microstructure and greater resistance to penetration of deleterious agents through pozzolanic reaction and enhancing cement hydration. SCMs improves particle packing and microstructure at interfaces such as the aggregate-paste ITZ. However, the results from this study showed that the beneficial properties of SCMs are insufficient to overcome the negative effects of spacers. The presence of spacers decreases mass transport properties, and this occurred despite the fact that the concrete contained a partial replacement of CEM I with SCMs.

5.1 Introduction

Supplementary cementitious materials (SCMs) have been widely used for many decades to partially replace ordinary Portland cement in concrete as a means to improve performance and sustainability. Most SCMs are by-products (waste materials) from other industries. For example, silica fume (SF) is a by-product from the production of silicon metal or ferrosilicon alloys containing high amorphous silicon dioxide, fly ash (FA) from the combustion of pulverized coal in electric power generating plants, and ground granulated blast-furnace slag (GGBS) from metal industries containing high reactivity calcium silicoaluminate (Neville, 2011). The incorporation of SCMs in concrete contributes several benefits, such as reducing porosity, increasing strength and enhancing long-term durability (Bijen, 1995, Khan and Siddique, 2011, Lothenbach et al., 2011, Ozbay et al., 2016). One of the main reasons is their pozzolanic behaviour, their ability to react and consume calcium hydroxide (portlandite) and form additional calcium silicate hydrate (C-S-H) with low Ca/Si ratio (Lothenbach et al., 2011, Duan et al., 2013). Their fine particle size distribution improves particle packing and induces a filler effect, providing nucleation sites that accelerates cement hydration. In addition, replacing

Portland cement with the SCMs can lower the environmental impact because no additional clinkering process is involved (Bijen, 1995).

To summarise, it is well-known that SCMs can improve and densify the microstructure at interfaces such as the aggregate-paste ITZ (Duan et al., 2013, Gao et al., 2005b, Cohen et al., 1994, Bijen, 1995), resulting in lower mass transport. Therefore, it is reasonable to expect that the same improvement should occur at the spacer-concrete interface. However, this has not been established. To the best of our knowledge, the effect of SCMs on mass transport properties of concrete containing reinforcement spacer and whether or not the usage of SCMs improves the properties of the spacer-concrete interface is unknown. This is the focus of the current chapter. In the next chapter, the effect of SCMs on the microstructure of the spacer-concrete interface will be examined.

5.2 Experimental

5.2.1 Materials and mixture proportions

Single cementitious spacers and plastic 'A' clip spacers for a 50 mm cover as shown in Figure 5.1 were used in this study. The spacers were obtained from leading manufacturer and distributor in the UK. Both spacers have the highest commercial demand according to the distributors. Single cover spacers were investigated for this study because bar or line spacers require the preparation and testing of large concrete specimens, which would be impractical for the properties of interest to this thesis. Prior to casting in concrete, the spacers were stored in the laboratory at 60% RH, 21ºC to avoid any moisture or temperature variations. Details of the spacer properties are given in Chapter 3.

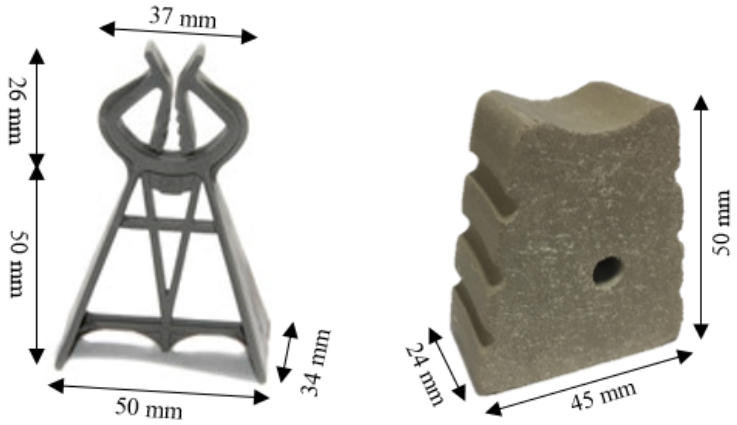

Figure 5.1 Dimensions of the 'A' clip plastic spacer and cementitious spacer used in this chapter.

Three different SCMs, namely silica fume (SF), fly ash (FA), and ground granulated blast-furnace slag (GGBS) were used to produce concrete with water/binder (w/b) ratio of 0.4. SF (Elkem Microsilica) conforms to (BS EN 13263-1:2005), FA (Holcim) conforms to (BS EN 450-1:2012) and GGBS (Holcim) conforms to (BS EN 15167-1:2006). These were used at 8%, 30% and 60% CEM I replacement level respectively. The specific gravity of the CEM I, SF, FA, and GGBS was 3.15, 2.35, 2.35 and 2.90 respectively. The oxide composition and properties of the cementitious materials used are shown in Table 5.1.

The mix proportions for all samples calculated using an absolute volume method are shown in Table 5.2. The Portland cement used (Hope Portland Cement CEM I 52,5N) complies with BS EN 197-1:2011. The aggregates were 10 mm maximum size Thames Valley gravel and sand (< 5 mm) complying with a BS EN 12620:2002 +A1:2008 medium grading. The total aggregate content was 70% vol. and sand to total aggregate mass ratio was 0.4. Superplasticiser Sika ViscoCrete 20RM at a dosage of 0.5% wt. binder was used to improve the workability of the mixes.

Table 5.1 Oxide compositions and properties of cementitious materials used

Binder	Oxide composition									LOI (%)
	CaO	SiO_2	Al_2O_3	Fe_2O_3	MgO	$Na_2O_{(eq)}$	K_2O	SO_3	Cl^-	
CEM I	63.4	20.8	5.4	2.4	1.5	0.3	0.7	2.9	<0.1	2.1
SF	0.2	98.6	0.3	0.0	0.1	0.2	-	0.1	-	N/A
FA	0.1	72.2	24.3	0.4	0.1	0.3	-	0.1	-	N/A
GGBS	40.8	36.5	11.6	1.4	7.5	0.5	-	2.1	-	-0.99

Table 5.2 Mix proportions.

Mix	W/B ratio	CEM I (kg/m^3)	SCMs (kg/m^3)	Sand (kg/m^3)	Gravel (kg/m^3)
CEM I + 8% SF	0.4	380	33	707	1061
CEM I + 30% FA	0.4	289	124	707	1061
CEM I + 60% GGBS	0.4	165	248	707	1061

5.2.2 Experimental setup

Cylindrical samples were prepared in steel moulds of 100 mm diameter and 50 mm height as shown in Figure 5.2. A spacer was placed and secured in the middle of each sample, using rebars (high-yield steel, 12∅ mm) and pieces of wood tightly screwed onto the base plate prior to concreting. This was to ensure that the spacers and rebar did not move during concrete placement and compaction, which would otherwise influence the results. This worked very well,

and checks showed no relative movement between the spacer and mould when the entire assembly was vibrated. In real structures, it is also absolutely critical to ensure that spacers are well secured onto the formwork because displacement of the spacer during concreting will induce negative effects on the microstructure of the hardened concrete or failure to achieve the required concrete cover. The volume fraction of the cylindrical spacer occupied by cementitious and plastic spacer was approximately 14% and 7% respectively.

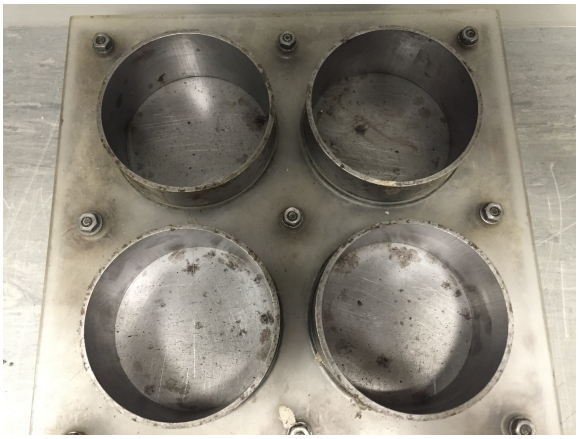

(a) Control sample (no spacer)

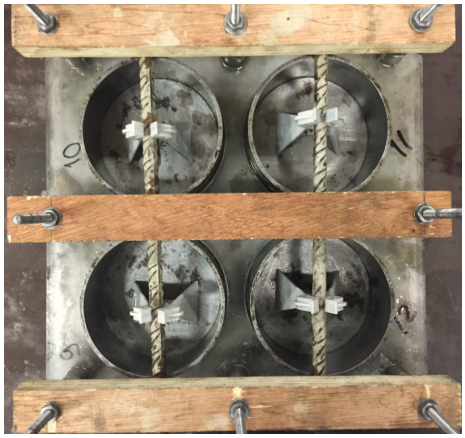

(b) Sample with plastic spacer

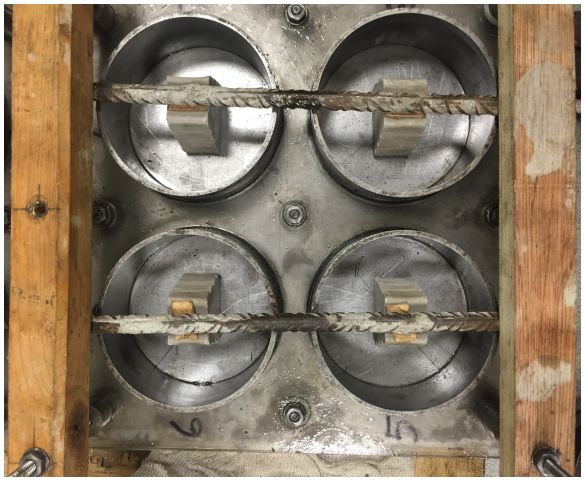

(c) Sample with cementitious spacer

Figure 5.2 Experimental setup for casting cylindrical samples of 100 mm diameter and 50 mm height.

5.2.3 Sample mixing and curing

All materials were batched by weight. The cement, SCMs, sand and gravel as shown in Figure 5.3 were first dry mixed for 30 s in a 30-liter capacity pan mixer. Batch water pre-mixed with superplasticiser was then added and mixed for a further 3 min. The slump values for all mixes were in the range of 90 to 100 mm. Samples were cast in cylindrical steel moulds of 100 mm diameter x 50 mm thickness as explained in Section 5.2.2, compacted in two equal-depth layers until the air bubbles had mostly escaped to the surface. The freshly compacted samples were surrounded by wet hessian and then covered with a plastic sheet at room temperature for the first 24 h (Figure 5.4) to prevent drying and then demoulded. A total of 81 samples were cast for transport testing. The samples were cured for 3, 28, and 120 days. For 3-days of curing, the samples were sealed by wrapping in at least 6 layers of cling film, then sealed in polyethene bags at 21°C. Short curing of 3 days was carried out to replicate typical site practice in addition to the "standard" 28-day curing. For the longer curing periods (28 and 120 days), the samples were placed in a fog room at 100% RH, 21°C.

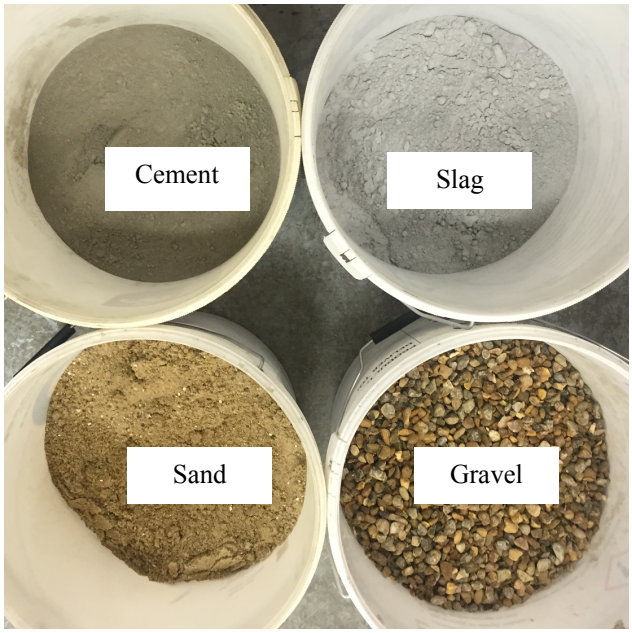

Figure 5.3 Materials used for casting concrete samples.

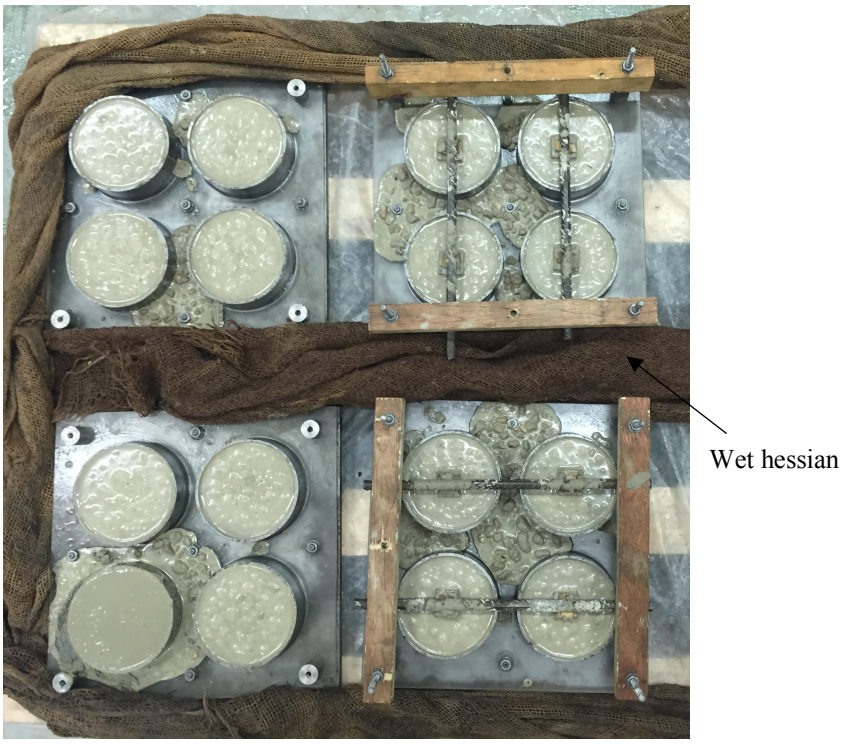

Figure 5.4 Compacted samples surrounded by wet hessian.

The density of the hardened concrete was measured at 24 hours after demoulding by weighing the cylindrical samples in air and dividing it by sample volume in accordance with the British Standard (BS EN 12390-7:2009), as shown in Equation 5.1. The measured density was used to check whether the samples were properly compacted and to ensure that no excessive voidage existed.

$$\rho = \frac{sample\ weight\ (kg)}{sample\ volume\ (m^3)} \qquad \text{Eq. 5.1}$$

The results of the measured density are presented in Table 5.3. Values in brackets represent the standard error ($S.E. = {}^{\sigma}/_{\sqrt{n}}$), where σ and n are the standard deviation and number or replicates respectively.

Table 5.4 Measured density of hardened concrete samples at 24 hours after demoulding.

Mix	Spacer type	Density (kg/m^3)
CEM I + 8%SF	CO	2314 (0.02)
	PS	2307 (0.03)
	CS	2311 (0.03)
CEM I + 30%FA	CO	2319 (0.03)
	PS	2304 (0.03)
	CS	2338 (0.02)
CEM I + 60%GGBS	CO	2314 (0.07)
	PS	2305 (0.07)
	CS	2322 (0.05)

Notes: CO=No spacer; PS=Plastic spacer; CS=Cementitious spacer

The measured density results were then compared with the theoretical density, calculated from the mix design (summing the weight of mix ingredients per 1 m^3 volume) and spacer density. The theoretical density was 2347 kg/m^3. The difference between measured and theoretical density was found to be small and ranged between 0.8% and 2.0%, with an average difference of 1.5%.

5.2.4 Sample conditioning

Prior to transport testing, samples were dried at 21°C in conditioning boxes containing saturated NaCl giving 75±1% RH as shown in Figure 5.5 to an "equilibrium" mass. This was assumed to occur when the mass loss was less than 0.01% per day. The conditioning regime replicates exposure to a humid weather conditions. The boxes contained fans to generate circulating air and soda lime to prevent carbonation. A thermometer/hygrometer was placed in the boxes to monitor temperature and relative humidity of each box. The purpose of conditioning to a constant mass was to ensure that the measured transport properties are not influenced by a variation in the moisture content between samples. The humidity in the conditioning boxes was constantly monitored, and the salt solutions were replaced when necessary.

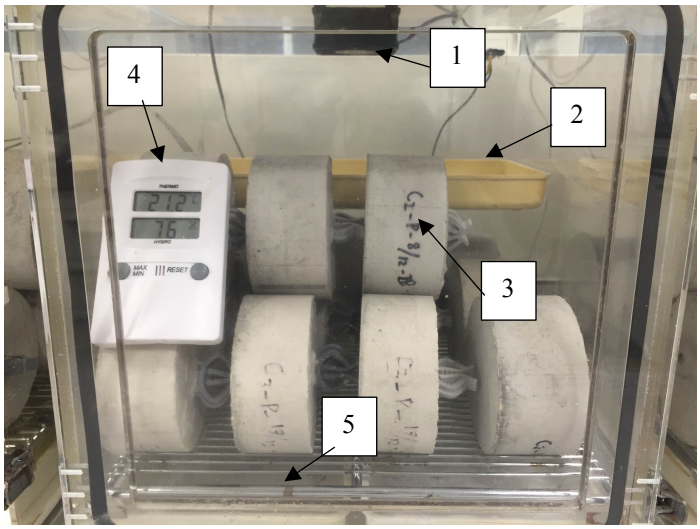

Notation: 1. Fan; 2. Soda lime; 3. Samples; 4. Thermometer/Hygrometer; 5. Salt solution

Figure 5.5 Conditioning box containing saturated NaCl to maintain relative humidity at ~75%.

Figure 5.6 shows some examples of mass loss curves obtained during conditioning. Typically, approximately 3 to 4 months of conditioning time is required to achieve equilibrium. Samples containing FA tend to lose more water on drying compared to GGBS and SF.

Samples were also conditioned at 50°C in the oven to replicate relatively more severe drying under hot weather conditions. The conditioning time required to reach constant mass (< 0.01% mass loss per day) was about 2 to 3 months. Typical mass change curves are presented in Figure 5.7. Before transport testing, the samples were cooled to room temperature in a vacuum desiccator for 24 h to prevent moisture from re-entering the samples during cooling.

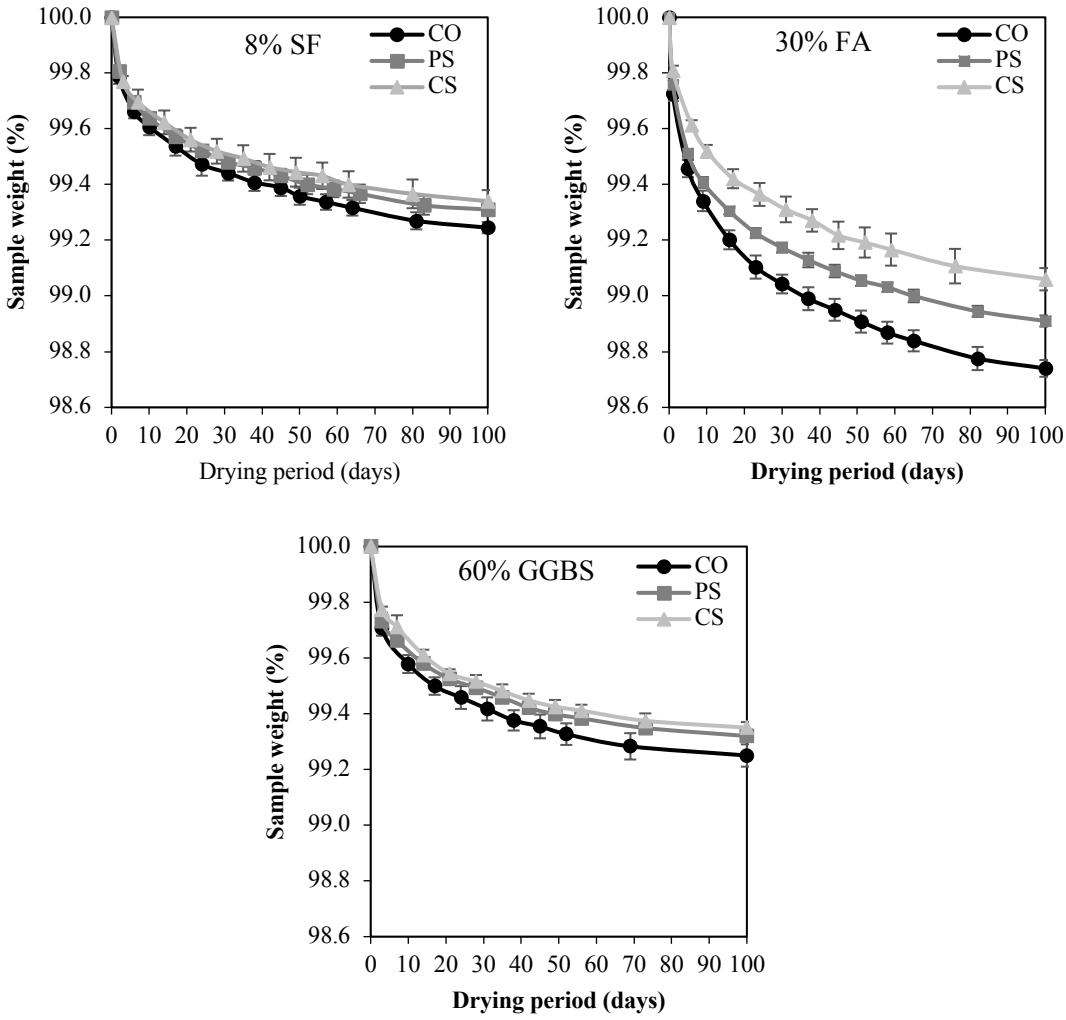

Figure 5.6 Change in mass for 120d-samples subjected to conditioning at 75% RH, 21°C.

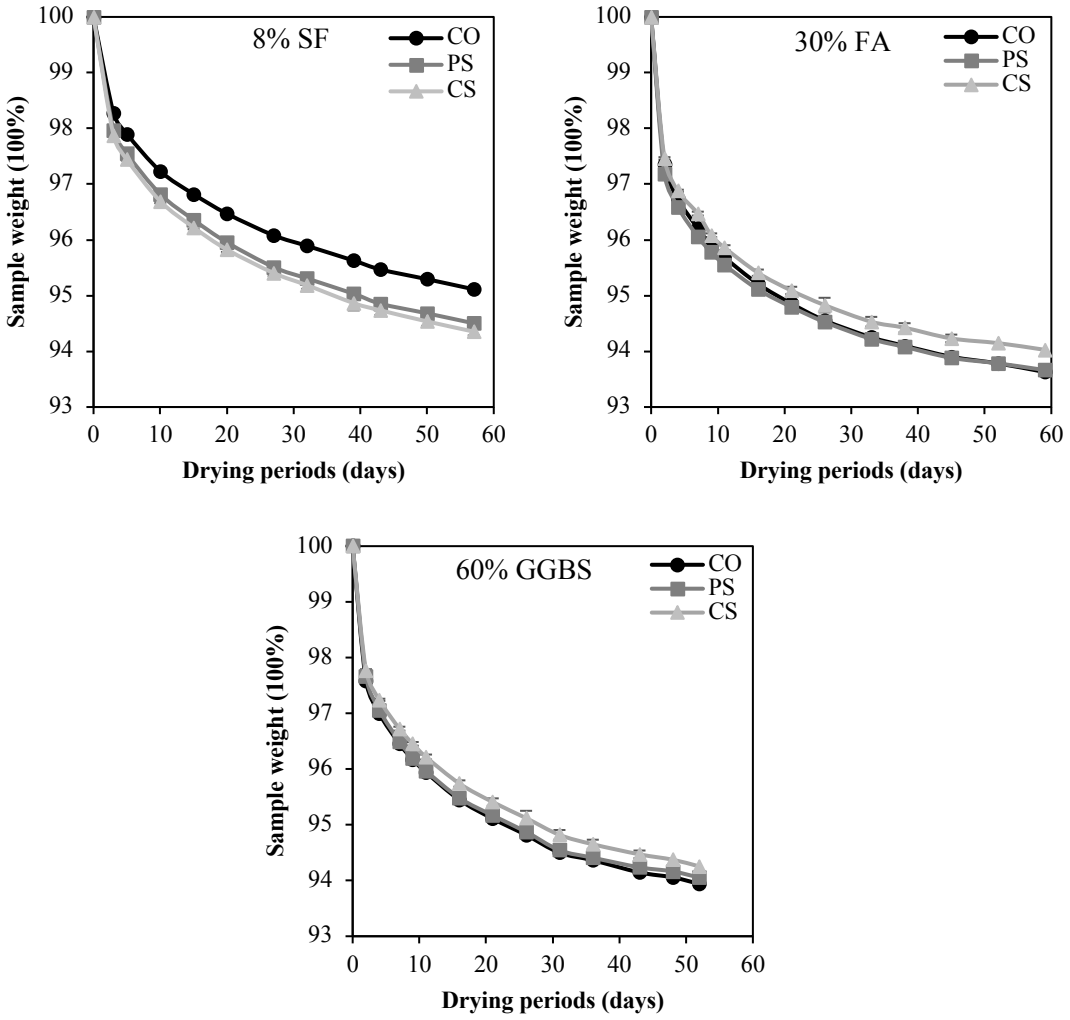

Figure 5.7 Change in mass of samples subjected to conditioning at 50°C oven.

5.2.5 Transport properties measurement

Samples were tested following the sequence of oxygen diffusivity, oxygen permeability, water sorptivity and electrical conductivity. Measurements were made on three replicate samples for each mix. Two cycles of transport testing were carried out; the first after conditioning at 75% RH, 21°C and the second following oven-drying at 50ºC. Details of each transport test are given in Chapter 3 and summarised here.

Oxygen diffusivity and oxygen permeability were measured by placing the sample in a test cell, and applying 15kN compression on the silicone rubber ring to seal the sample. To determine the oxygen diffusivity, the sample was exposed to oxygen and nitrogen gases at the same pressure, which diffuses in opposite directions through the sample. A zirconia analyser was then used to

measure the oxygen concentration in the outflow stream. For permeability, steady-state outflow rates were measured for three input gas pressures of 0.5, 1.5 and 2.5 bar above atmospheric. Permeability at each pressure was calculated by following Darcy's law for compressible fluids, and the intrinsic permeability was determined by applying Klinkenberg's correction for gas slippage. Water sorptivity was measured by placing the sample in a tray containing water to a depth of about 3 mm from the bottom surface of the sample and then measuring the mass gain with time until saturation was achieved. The sorptivity coefficient ($g/m^2min^{0.5}$) was determined from the slope of the regression line of absorbed water per unit flow area against square root of time ($R^2 > 0.99$) according to the classical unsaturated flow theory. The best-fit regression line was drawn across at least 10 readings taken during the first 7 h of measurement. A typical plot of cumulative water absorption against the square root of time is shown in Figure 5.8. In this example, it can be seen that the slope of the water absorption profile and the total amount of water absorbed for the samples containing a cementitious spacer was significantly higher than that of the control sample.

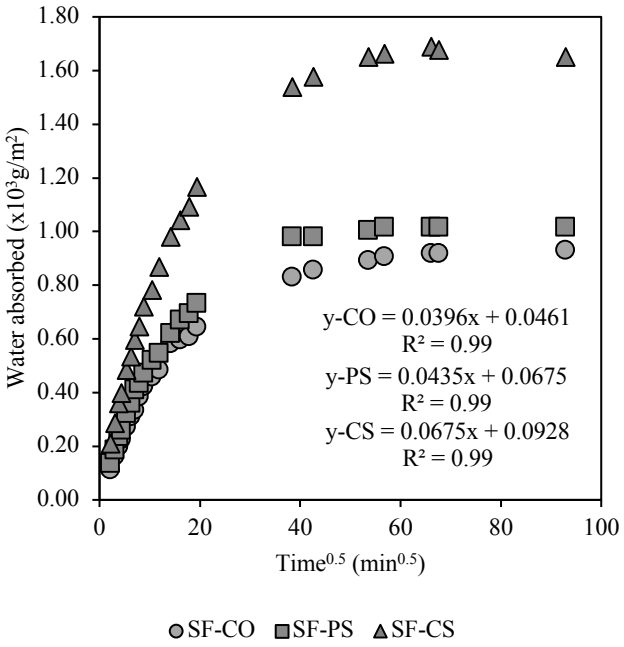

Figure 5.8 Typical plots of cumulative water absorption against square-root of time for 3d-samples containing 8% SF after conditioning at 75% RH, 21ºC.

Immediately after water absorption testing, the samples were vacuum saturated in water for approximately 4 h to determine its accessible porosity. Sample porosity was estimated from the mass difference between the preconditioned state and vacuum saturated-surface dry condition. The vacuum saturated-surface dry samples were then placed between two brass plates and connected to an LCR databridge in order to determine electrical resistivity. To ensure a proper

electric contact between the brass plates and the sample surfaces, a generous amount of a salt-free electrode gel was applied on both surfaces prior to clamping. The resistance typically stabilises within one minute; three readings were taken and then averaged. Electrical conductivity σ_e (*S/mm*) is the reciprocal of electrical resistivity.

5.3 Results

5.3.1 Transport properties after conditioning at 75% RH, 21°C

The results for oxygen permeability, oxygen diffusivity, water sorptivity and electrical conductivity of concrete samples containing different SCMs and spacer types after curing for 3, 28, and 120 days and conditioning until constant mass at 75% RH, 21ºC are presented in Figure 5.9. Error bars indicate standard error ($\sigma/\sqrt{n}$) of the average, where σ is the standard deviation and n is the number of replicates. It should be noted that samples containing cementitious spacers were not tested for electrical conductivity because the spacer protruded above the sample top surface causing an uneven surface.

The results show that increasing the curing age from 3 to 120 days caused a reduction in transport properties in all cases, as expected. The transport properties decreased by up to a factor of 2.5, 3.3, 6.2 for control samples (without spacers) containing SF, FA, and GGBS respectively when comparing the data obtained at 3d curing to that at 120d curing. Samples incorporating SF had the lowest oxygen diffusivity, oxygen permeability, water sorptivity and electrical conductivity compared to samples with FA and GGBS. Samples with FA and GGBS gave about the same magnitude of diffusivity and permeability coefficients at 120 days, but samples incorporating GGBS showed the highest conductivity and the lowest sorptivity.

It is also evident that the spacers have a huge influence on the measured transport properties. There is a clear trend that samples containing spacers have higher transport properties than their respective control samples, in particular, at 3 and 28 days. As a result of spacers, the oxygen diffusivity increased by about 6.5 to 356% for all SCMs used, water sorptivity increased by about 2.6 to 66%, and electrical conductivity increased by about 1.5 to 33%. Spacers led to a significant in increase for oxygen permeability, by about 35 to 1553%. The worst case was in samples containing FA, where the permeability increased by more than 16.6 times compared to the control samples that contained no spacer. The 120d-samples containing GGBS in general, showed the best performance in reducing diffusivity and sorptivity coefficients of the concrete containing spacers by about 21 to 35% compared to samples containing silica fume and fly ash. However, the increase in a given transport property is dependent on spacer type. The presence

of cementitious spacers in concrete induced higher transport properties than plastic spacers, in particular on samples containing SF.

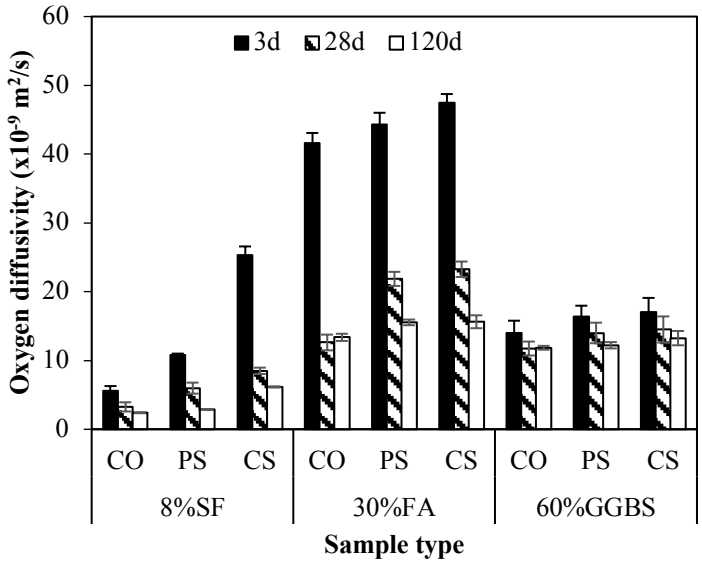

(a)

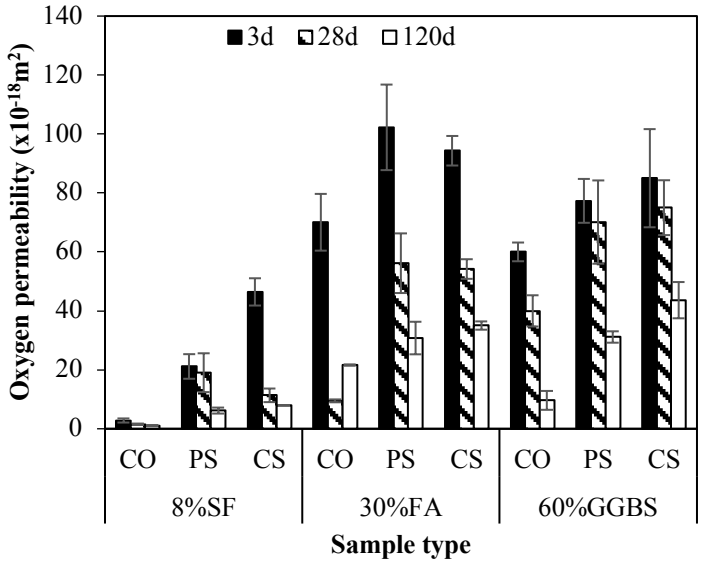

(b)

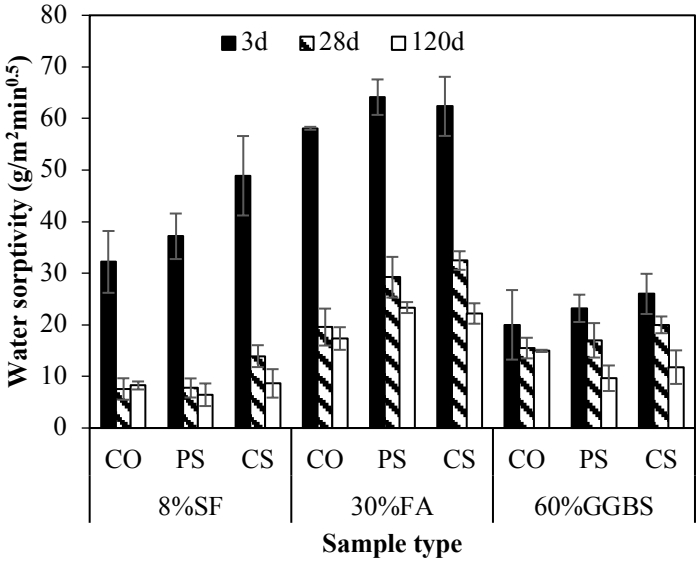

(c)

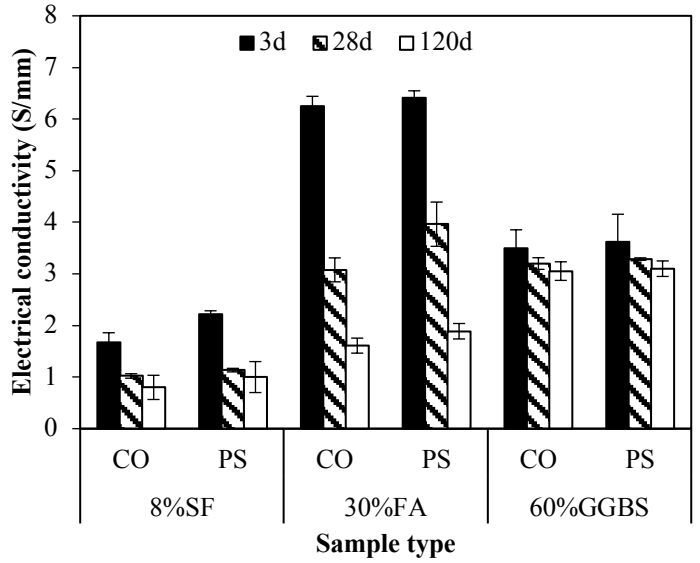

(d)

Figure 5.9 Effect of spacers on a) oxygen diffusivity, b) oxygen permeability, c) water sorptivity, and d) electrical conductivity after conditioning at 75%RH, 21°C.

5.3.2 Accessible porosity from vacuum saturation

Figure 5.10 shows the sample accessible porosity measured by water absorption under vacuum after conditioning at 75% RH, 21°C. Porosity decreased with increasing curing age, as expected. Samples containing SF achieved the lowest porosity at all ages, followed by GGBS and FA. However, the presence of spacers increased the sample porosity by up to 87%, 13.8%, 13.4% for samples incorporating SF, FA, and GGBS respectively. The trend is similar to the results of the water sorptivity as shown in Figure 5.9.

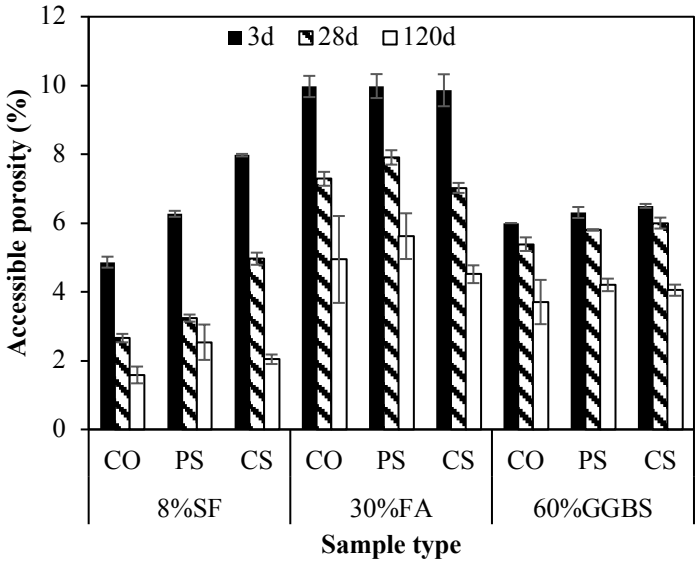

Figure 5.10 Accessible porosity after vacuum saturation.

5.3.3 Transport properties after oven-drying at 50°C

Figure 5.11 shows the measured transport properties after drying in a 50°C oven. It is interesting to note that the conditioning regime before testing has a huge influence on the measured transport properties. Increasing the severity of drying increases the amount of accessible porosity (Figure 5.12). Furthermore, severe drying induces cracking when shrinkage is restrained. Therefore, samples from oven-drying consistently produced much higher measured transport properties for all SCMs and spacers used when compared to the results shown in Figure 5.9. On average, diffusivity, permeability and sorptivity increased by 388%, 5653% and 420% after drying at 50°C relative to 75% RH, 21°C.

For samples conditioned at 50°C, plastic spacers consistently gave the highest permeability and sorptivity coefficients followed by samples with cementitious spacers, then the control samples in all cases. For example, the average increases in permeability and sorptivity for samples containing plastic spacers relative to the control were 3889% and 117% respectively. In contrast,

samples containing cementitious spacers showed lower increases in permeability and sorptivity with the averages being 169% and 12% respectively. However, the measured diffusivity of all samples remained relatively constant, despite the fact that they contained different SCMs and spacers.

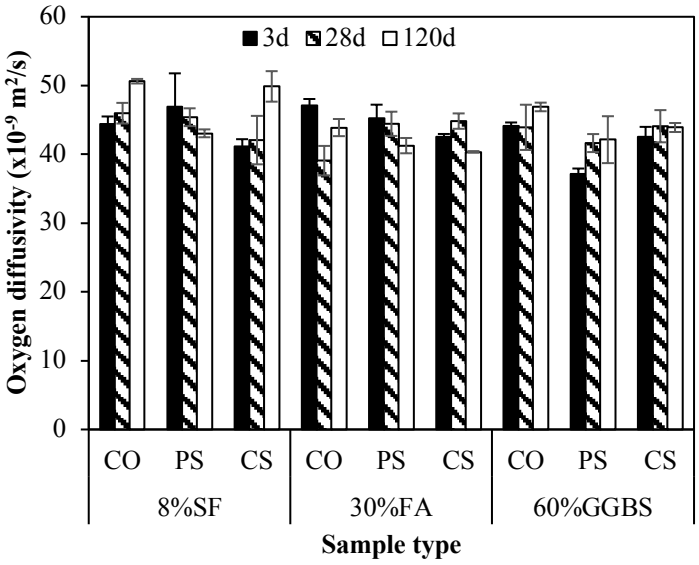

(a)

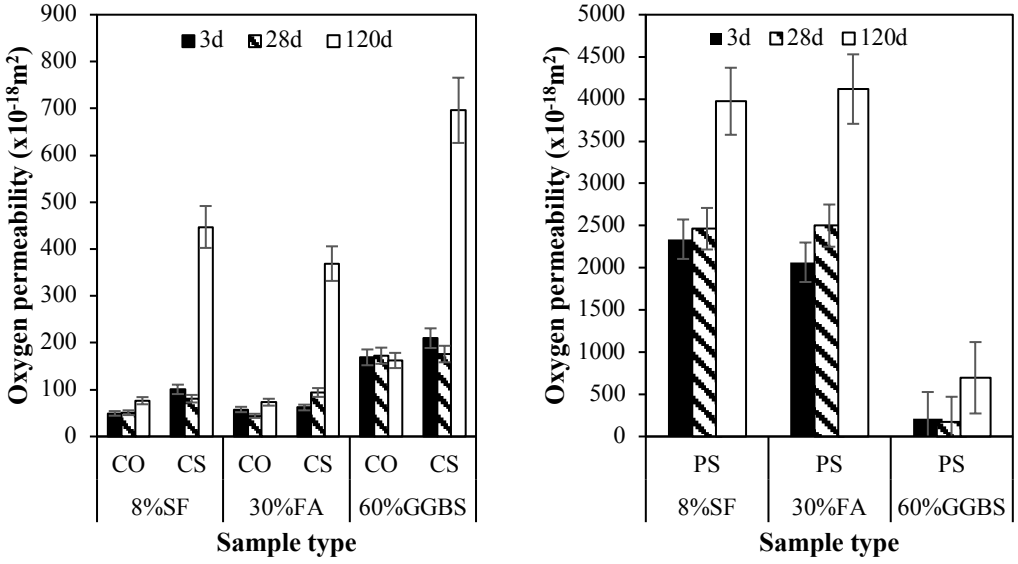

(b)

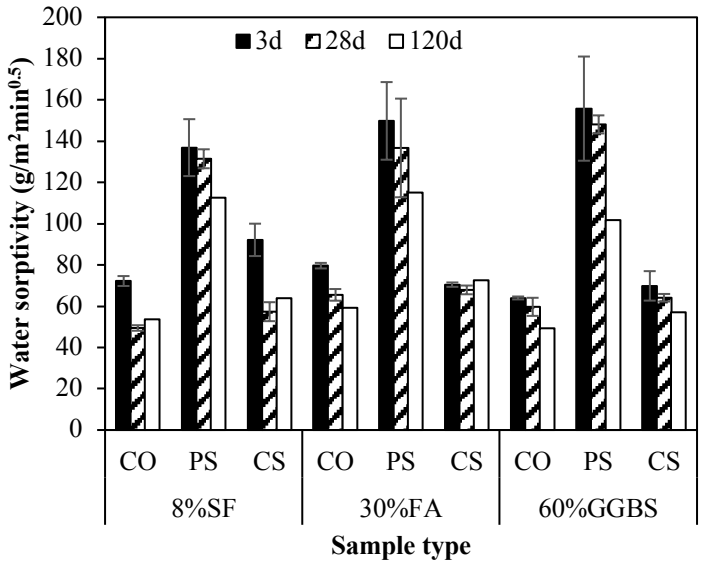

(c)

Figure 5.11 Effect of spacers on (a) oxygen diffusivity, (b) oxygen permeability, and (c) water sorptivity after conditioning in a 50°C oven.

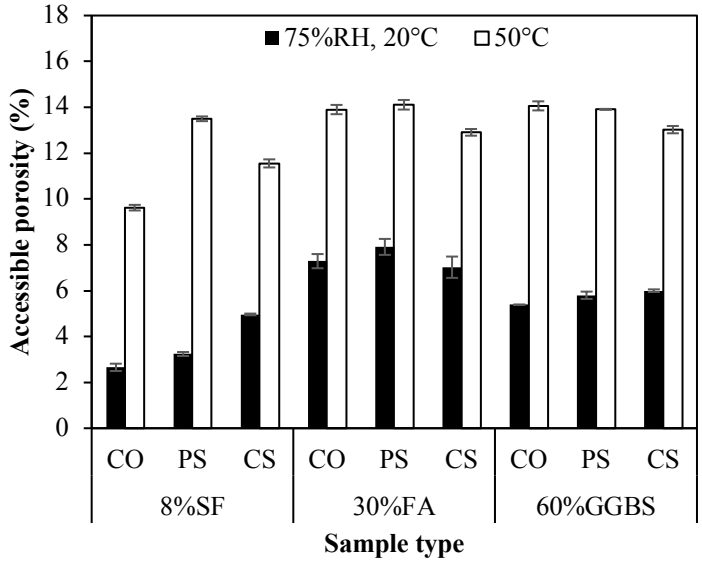

Figure 5.12 Effect of oven drying on sample porosity (28d-samples).

5.4 Discussion

The results presented in this chapter show that the inclusion of spacers in concrete increased the overall transport properties. The spacers facilitate the transport of gas and water regardless of the mechanism, i.e. under pressure gradient, concentration gradient or capillary suction. It occurred despite the fact that the presence of spacers reduces the cross-sectional area available for flow because it occupies and replaces a substantial volume of the concrete, ~14% for samples containing cementitious spacers and ~7% for samples containing plastic spacers. However, the magnitude of increase in the measured transport coefficient depends on the type of SCM used, curing age, spacer type, and transport mechanism. This is consistent with the findings reported by Alzyoud et al. (2016) who showed that the presence of spacers in 28-d concrete (100% CEM I) conditioned at 75% RH, 20ºC increased the oxygen diffusivity, oxygen permeability, and water sorptivity. The magnitude of the increase observed by Alzyoud et al. (2016) is higher than that of samples containing slag but lower than that of samples containing silica fume or fly ash.

When conditioned at 75% RH, 21ºC, cementitious spacers generally produced the most significant increase in transport properties, followed by plastic spacers relative to the control sample. This is probably due to the fact that the cementitious spacer itself has a higher porosity (8.5%) and sorptivity (35 g/m^2mm0^{-5}) than the surrounding concrete. However, it should be noted that the spacer was conditioned at a room temperature or 60±5% RH, 21ºC prior to using, which is different to the drying regimes of the concrete. In contrast, a plastic spacer is non-porous and impermeable. However, the poor bond, coupled by the large differences in thermal expansion and drying shrinkage between plastic and concrete produces microcracking at the interface. This is clearly observed in samples containing plastic spacers particularly when dried at elevated temperatures. This can be verified by examining the porosity distribution, fluorescent epoxy impregnation distribution and chloride penetration profile at the spacer-concrete interface as will be presented in Chapter 6.

The length of curing produced a substantial impact on how spacers and SCMs influence the transport properties when conditioned at 75% RH, 21ºC. At an early age of 3 days, samples containing FA showed the highest transport coefficients for all cases. This is consistent with the fact that FA has a lower reaction rate compared to SF and GGBS. The same observation was reported by Marsh et al. (1995) showing that the use of FA in concrete gave a high permeability at early ages (7 days) due to the substantial amount of large pores. However, a dramatic reduction in permeability occurred beyond 7 days because of the hydration and pozzolanic reactions. At 28 and 120 days, samples incorporating silica fume showed the lowest transport

coefficients, followed by GGBS and FA. This behaviour is consistent with well-established findings that silica fume has a larger pozzolanic reactivity and filler effect compared to GGBS and FA (Lothenbach et al., 2011).

However, it is interesting to observe that the presence of spacers produced the highest increase in oxygen diffusivity, oxygen permeability and electrical conductivity for samples containing silica fume, compared to the samples containing fly ash or slag. This could be attributed to the fact that cracks will induce a larger increase in the transport properties of cementitious materials that are denser compared to those that are relatively more porous. Similar observations have also been reported by Gesoglu et al. (2009) and Gedam et al. (2016), who studied the drying shrinkage of 22 concrete mixes with OPC alone as a binder, OPC with fly ash (10-60%), OPC with silica fume (5-15%) and OPC with slag (15-60%) by mass as binary, ternary and quaternary systems. The results show that the inclusion of fly ash and slag in concrete reduced drying shrinkage, whereas silica fume increased shrinkage. This is because of the refinement of pore size distribution leading to an increase in capillary tension and contraction of the cement paste attributable to hydration in the early age.

Regarding transport mechanisms, permeability was affected the most, with increases up to 1553% observed in 3d-samples containing SF relative to the control. Furthermore, it is worth noting that even with prolonged curing (120 d), the use of SCMs was unable to eliminate the negative effect of spacers on all transport properties as shown in Figures 5.9 and 5.10. However, overall, GGBS was the best performing SCM from the perspective of improving the resistance of concrete containing spacers to the penetration of deleterious species. The average increases of 120d-samples on oxygen diffusivity, oxygen permeability, water sorptivity, electrical conductivity, and accessible porosity were only 7.4%, 81.5%, 0%, 1.5%, 11% respectively.

Finally, it should be noted that the effect of SCMs on the transport properties of concrete showed good agreement with previous studies. Gesoglu et al. (2009) investigated the water sorptivity and electrical conductivity of 22 concrete mixes at w/b of 0.44. The mixes included 100% OPC, OPC with fly ash (20-60%), OPC with silica fume (5-15%) and OPC with slag (20-60%). The samples were cured for 90 days at 70±5% RH, 21±1ºC and conditioned at 50±5% RH for approximately 50 days. The results showed that the maximum electrical resistivity was achieved for the OPC mixed with 45% slag and 15% silica fume, while the lowest water sorptivity was achieved for the OPC mixed with 60% slag followed by 15% silica fume. The lowest transport properties of the concrete with SCMs is attributed to the pore refinement.

Furthermore, the conditioning regime prior to testing has a major influence on the measured transport properties for all the SCMs used. Samples with plastic spacers were the most sensitive to oven-drying in particular for the permeability results. Fine cracks were observed in all samples containing plastic spacers as shown in Figure 5.13 and illustrated in Figure 5.14. The crack widths ranged from 0.1 to 0.5 mm. The presence of cracks is attributed to the fact that plastic spacers have a thermal coefficient of expansion about 10 to 15 times larger than that of concrete, and when subjected to temperature variations, the plastic continues to expand and contract at a higher amount compared to the surrounding concrete. The differential movement between spacer and concrete increases restraint to volumetric changes and therefore cracking.

Overall, drying induced a significant increase in the transport properties due to a number of microstructural changes, and this observation is consistent with the findings from other studies on drying-induced microcracking e.g. Hwang and Young (1984), Bisschop and Mier (2002), Wong et al. (2007), Maruyama and Sasano (2014), Wu et al. (2015). When concrete samples were dried immediately from a saturated state, the largest pores tend to empty first followed by successively smaller pores, hence the volume and connectivity of pores accessible for transport increases. Furthermore, it can be concluded that samples containing SCMs are sensitive to severe drying. This is due to the fact that the presence of SCMs changes the type and amount of hydrates formed, in particular the C-S-H. However, the water within gel pores and C-S-H is removable on severe drying for example drying in a 50ºC oven (Lothenbach et al., 2011). Drying has a greater influence on permeability compared to diffusivity, sorptivity or electrical conductivity. This is because permeability is more sensitive to cracks compared to other transport mechanisms, in line with results by Wong et al. (2007), Wong et al. (2009) and Wu et al. (2015).

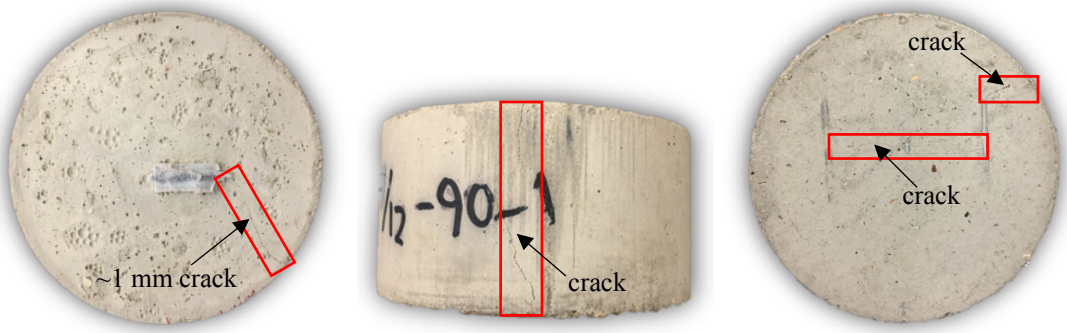

a) Top surface b) Side surface b) Bottom surface

Figure 5.13 Cracks appearing on the surface of samples containing plastic spacer after conditioning at 50°C.

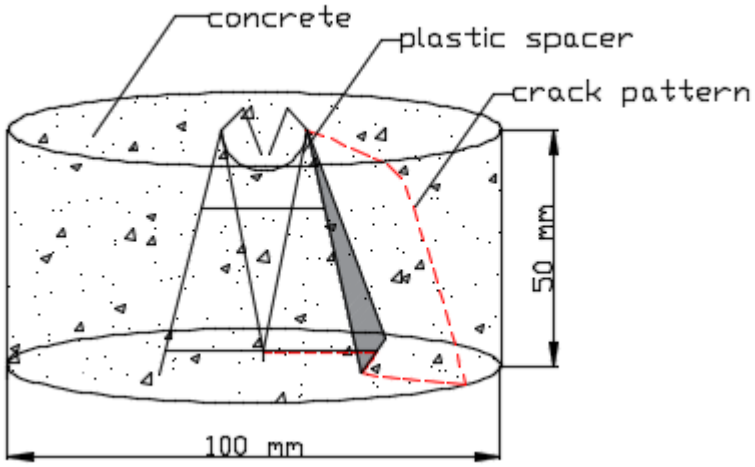

Figure 5.14 Illustration of the location of cracks on samples containing plastic spacer.

5.5 Conclusions

The mass transport properties of concrete incorporating SCM (silica fume, fly ash and ground granulated blast-furnace slag) and spacers (plastic and cementitious) with different curing ages (3, 28, 120 days) and conditioning regimes (75% RH, 21°C; 50°C oven) were investigated. Overall, samples containing silica fume achieved the lowest transport properties. However, samples containing ground granulated blast-furnace slag showed the smallest negative effect on the transport properties due to the presence of a spacer. Nonetheless, this study showed that the use of SCMs was unable to eliminate the negative effects of spacer on the transport properties. The presence of a spacer consistently produced higher transport properties compared to the control sample (without a spacer). The extent of the effect of spacers on oxygen diffusivity, oxygen permeability, water sorptivity, and electrical conductivity depends on the spacer type, SCM used, curing age, and conditioning regime. This suggests that the increase in transport properties of concrete containing spacers is due to drying shrinkage-induced microcracking and a highly porous interface between the spacer and concrete. This will be verified by examining the porosity distribution and chloride penetration profile at the spacer-concrete interface and this is presented in Chapter 6.

Chapter 6

Microstructure and chloride profile of spacer-concrete interface containing SCMs

This chapter follows on from the work presented in Chapter 5 on the properties of the spacer-concrete interface containing supplementary cementitious materials (SCMs). It focuses on investigating the effect of SCMs on the microstructure of the spacer-concrete interface using a fluorescent epoxy impregnation method and laser scanning confocal microscopy (LSCM). Furthermore, this chapter aims to determine the influence of spacers on the transport of chloride ions through the spacer-concrete interface using a micro X-ray fluorescence (μXRF) spectrometer. The results showed that the interface between spacer and concrete consistently had the highest porosity and chloride penetration. This occurred despite the fact that the concrete contained partial replacement of CEM I with SCMs such as silica fume, fly ash and ground granulated blast-furnace slag.

6.1 Introduction

The first detailed study on the microstructure of the spacer-concrete interface was reported by Alzyoud et al. (2016) using quantitative backscattered electron (BSE) microscopy. The study revealed that the presence of a spacer produces a micro-cracked and highly porous interface, which accelerates the ingress of gasses and fluids through the concrete cover. However, the work only focused on concretes containing ordinary Portland cement CEM I as the main binder.

It is well-known that the use of SCMs such as silica fume (SF), fly ash (FA), and ground granulated blast-furnace slag (GGBS) can produce beneficial effects on the properties of concrete. The filler effect and pozzolanic reaction induced by SCMs change the hydrate assemblage, refine the pore size distribution and densify the microstructure of concrete (Gao et al., 2005b, Duan et al., 2013). The blending of CEM I with silica fume that consists mainly of amorphous SiO_2 of very fine particles with relatively high pozzolanic activity is typically the most effective way to improve the microstructure and durability of concrete. The use of GGBS and FA are also viable solutions at higher cement replacement levels. However, to the best of

our knowledge, no studies have been carried out to date to investigate whether this could improve the microstructure of the spacer-concrete interface.

This paper presents a study on the microstructure of the interface between various spacer types and concrete containing SCMs. Samples will be pressure-impregnated with low-viscosity fluorescein-dyed epoxy to examine the distribution and penetration depth of the intruded epoxy. Furthermore, laser scanning confocal microscope (LSCM) and image analysis will be used to characterise the porosity gradient at the spacer-concrete interface. This study will also examine the chloride penetration along the interface using micro X-ray fluorescence (μXRF), which is another method to understand the influence of a spacer on the penetration of deleterious species.

6.2 Experimental

6.2.1 Samples

Details of the materials, experimental setup and mixture proportions are given in Chapter 5 and summarised here. Samples were prepared in cylindrical steel moulds of 100 mm diameter and 50 mm height with three different SCMs (8% silica fume, 30% fly ash, 60% ground-granulated blast furnace slag) and two different spacers (plastic and cementitious spacers) designed for a 50 mm cover. The cylindrical sample is schematically illustrated in Figure 6.1. Ordinary Portland cement CEM I was the main binder used in this study. The water/binder ratio for all mixes was 0.4. The total aggregate volume fraction was 70%, and the sand-to-total aggregate mass ratio was 0.4. The samples were cured for 3, 28, and 120 days.

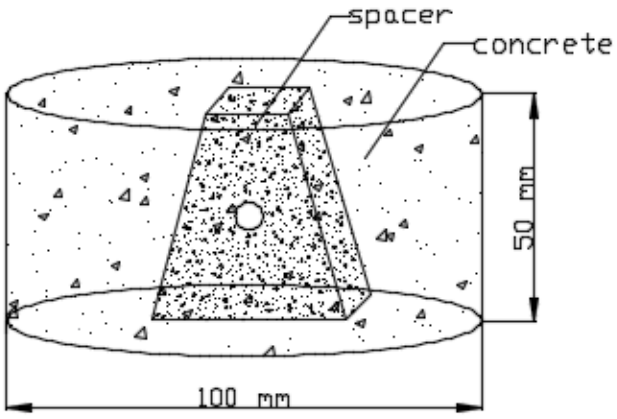

Figure 6.1 Schematic illustration of cylindrical sample containing a cementitious spacer.

A summary of the samples prepared, and the curing and conditioning regimes are as follows:

I. CEM I blended with SCMs at w/b of 0.4, sealed cured for three days and then conditioned at 75% RH, 21°C or in an oven at 50°C. Cylindrical samples containing 50 mm cementitious or plastic spacers were prepared. These were used to study the distribution of epoxy impregnation along the spacer interface.

II. CEM I blended with SCMs at w/b of 0.4, cured in a fog room (100%RH, 21ºC) for 3 and 120 days then conditioned at 75% RH, 21°C. Cylindrical samples containing 50 mm cementitious or plastic spacers were prepared. These were used to study the porosity distribution of the spacer-concrete interface using LSCM. After cutting the samples into small blocks for microscopy, the samples were dried at 40°C until a constant mass was achieved.

III. CEM I blended with silica fume at w/b of 0.4, cured in a fog room for 28 days and then conditioned at 50°C, cooled to room temperature and then immersed in chloride solution. Cylindrical samples containing 50 mm cementitious or plastic spacers were prepared. These were used to study the chloride penetration profile of the spacer-concrete interface. After sectioning, the samples were freeze-dried and analysed using micro XRF.

The sample designation used in this chapter is shown in Figure 6.2.

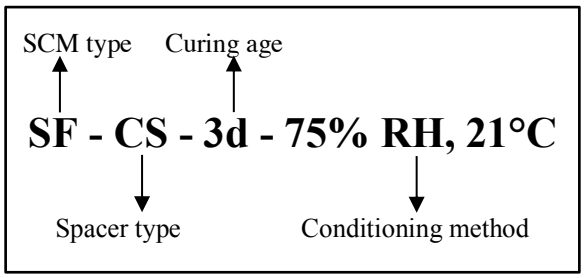

Notations: SCM type = SF/FA/GGBS; Curing age = 3/28/120d; Spacer type = CO(Without spacer)/CS/PS; Conditioning method = 75% RH, 21°C/50°C oven

Figure 6.2 Sample designation.

6.2.2 Fluorescent epoxy impregnation

Selected samples were pressure-impregnated with low-viscosity fluorescein-dyed epoxy as a means to detect cracks and regions of high porosity. Details of the procedure are given in Chapter 3.4 and summarised here. The sample was first placed in a pressure cell. The epoxy mix was poured onto the sample top surface, and a 10bar air pressure was applied and maintained overnight to force the epoxy into the sample. Finally, the impregnated sample was cured at room temperature for two days to allow the proper hardening of the epoxy before sectioning for

imaging to determine the distribution of fluorescent epoxy impregnation along the spacer-concrete interface.

Images were captured using a Sony Alpha NEX-3N mirrorless digital camera kitted with an E16 mm focal length in a dark room under a 15W ultraviolet lamp operating at ~50 Hz to induce fluorescence. The camera was set to the lowest ISO setting (ISO 200) to reduce noise and shot at the smallest aperture (f/22) to increase the depth of field and a slow shutter speed (20-second) was used to achieve a good exposure. These parameters are sufficient to obtain a macro view of the sample to measure the penetration depth of the epoxy. These settings were kept constant throughout the study.

6.2.3 Sample preparation for microscopy

In order to analyse the microstructure of the spacer-concrete interface, samples were prepared following the method described in Wong et al. (2006b), but with some modifications. First, the cylindrical samples (100 mm diameter, 50 mm height) were cut in half and dried at 40°C until a constant mass was reached. The half cylindrical samples were then epoxy-impregnated to preserve and protect the spacer-concrete interface from damage during subsequent preparation stages. The epoxy was Stuers EpoFix resin containing fluorescein dye at 0.05 wt.% (Struers Epodyde) mixed using a magnetic stirrer for at least 24 hours to ensure that the dye was uniformly dispersed in the resin. Then it was mixed with hardener at a ratio of 25:3 by mass and toluene at 5 wt.% and heated to 40°C for several hours to reduce the viscosity of the resin to facilitate impregnation.

The vacuum impregnation process was carried out by placing the sample in a vacuum chamber and gently introducing the resin onto the sample until the entire surface was covered, using the equipment shown in Figure 6.3a. Subsequently, the vacuum was released, the sample was placed in a pressure chamber (Figure 6.3b) and pressurised at 2.5 bar for another two hours to ensure full impregnation. Excessive resin was then removed, and the samples were placed back in the pressure chamber and left overnight for hardening. The impregnated samples were then cured at room temperature for two days to allow for the proper hardening of the epoxy.

The impregnated samples were sectioned using a water-cooled diamond saw to extract a 40 *x* 20 *x* 8 mm^3 block from the central region containing the spacer and concrete (Figure 6.4). The block size was chosen to accommodate the size of the sample holder on the grinding and polishing machine and microscope. Following that, the sample was gently dried in an oven at 40°C until constant mass was achieved. The block was subsequently encased in epoxy resin to

protect all sides for the remaining steps. Once the epoxy has hardened, the impregnated surfaces were dry ground carefully with SiC papers at successively finer grit sizes of 220 (68 µm), 500 (30 µm), 1000 (18 µm), and 2000 (14 µm) to remove excessive resin and then polished using diamond abrasives with grit sizes of 9 µm, 6 µm, 3 µm, 1 µm, and 0.25 µm for 3-4 minutes per direction to achieve a flat and highly reflective surface for high resolution imaging. The grinding and polishing were carried out with a Struers LaboPol-5 (Figure 6.5) at a speed of 50 rpm, with an approximately 7 N force applied to each sample. A Kemet oil was used as a lubricant for polishing. Samples were cleaned with acetone in an ultrasonic bath during grinding and polishing. The blocks were regularly checked with an Olympus BX51 petrographic microscope (Figure 6.6) in normal and ultraviolet light mode to ensure that the sample was well-ground and polished. The polished samples (Figure 6.7) were then kept dry in a desiccator containing silica gel at room temperature until required for imaging.



a) b)

Notation: 1. Pressure gauge; 2. Vacuum pump; 3. Epoxy resin container; 4. Pressure chamber

Figure 6.3 a) Set-up of the vacuum epoxy impregnation kit; b) Pressure chamber.

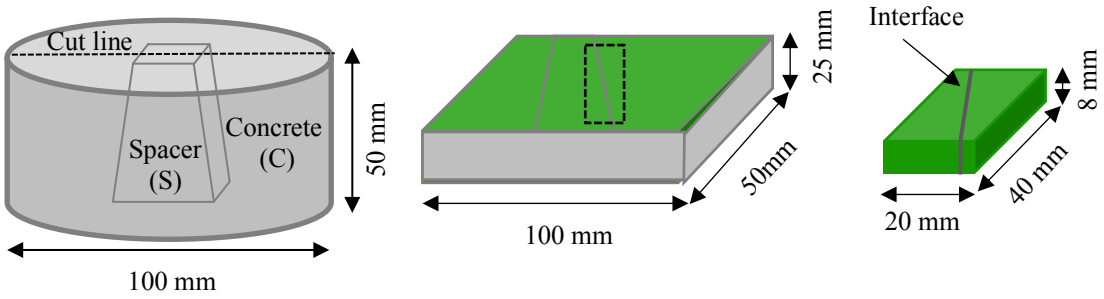

Figure 6.4 Schematic of the extraction of a block sample for imaging. Drawing not to scale.

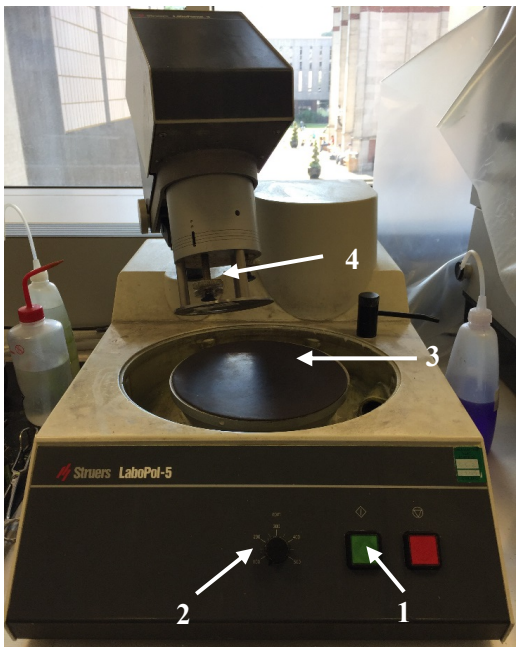

Notation: 1. Start and stop switch; 2. Speed control; 3. Turntable; 4. Sample holder

Figure 6.5 Grinding and polishing machine.

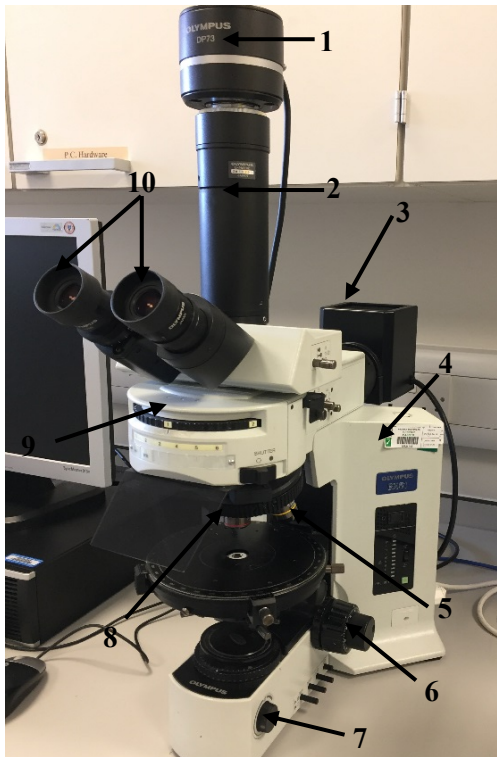

Notation: 1. Olympus DP 73 digital camera; 2. Camera extension tube; 3. Epi-illuminator for reflected polarised investigations; 4. Microscope stand; 5. Strain-free objectives; 6. Focus; 7. Brightness adjustment knob; 8. Circular rotating stage; 9. Fluorescence mirror unit; 10. Eyepieces.

Figure 6.6 Olympus BX-51 petrographic microscope.

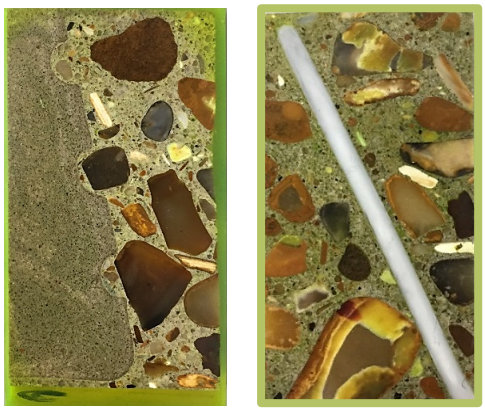

Figure 6.7 Epoxy impregnated and flat polished block samples ready for imaging.

6.2.4 Laser scanning confocal microscopy

Fluorescence images of the spacer-concrete interface were captured with a Leica TCS SP5 laser scanning confocal microscopy (LSCM) shown in Figure 6.8 with HCX PL APO 40x (NA 1.25) oil immersion objective. LSCM is a common imaging technique in biological sciences and its application for examining the pore structure of cement-based materials was first introduced by Head and Buenfeld (2006) and Head et al. (2006). More recently, the work carried out by Yio

et al. (2015) and Yio et al. (2017) demonstrated the potential of LSCM for the three-dimensional imaging of pores and voids in cement-based materials at sub-micron resolution.

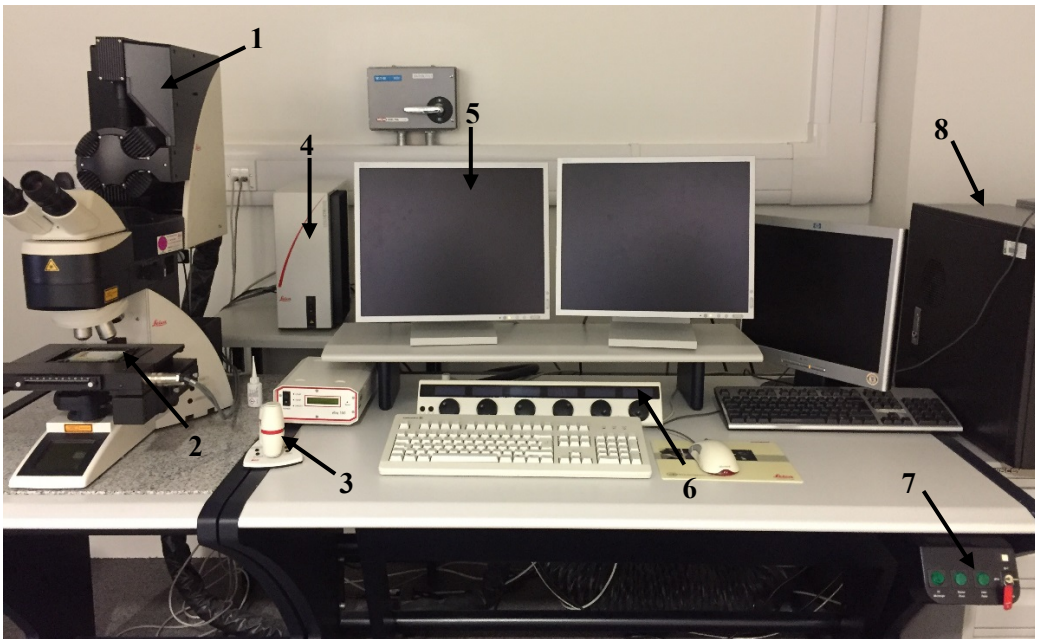

Notation: 1. TCS SP5 scanner; 2. Marzhauser scanning stage; 3. SmartMove stage remote control; 4. CTR6000 electronics box; 5. Monitor; 6. Panel box; 7. Control panel; 8. TCS SP5 workstation

Figure 6.8 Leica TCS SP5 laser scanning confocal microscope.

A schematic showing the main working principle of laser scanning confocal microscope is shown in Figure 6.9. The microscope uses an intense laser beam as a light source. The laser beam is reflected by a dichroic mirror, passes through the selected objective lens of the microscope and is focused onto a small spot on the specimen surface. The laser excites fluorophores in the sample and the emitted fluorescence passes back through the mirror system and through a small pinhole that blocks out-of-focus light. This optical sectioning process increases signal resolution. The collected fluorescence is finally directed into a photomultiplier tube (PMT) detector which records the fluorescence intensity at each point and converts it into an electrical signal. The beam in scanned across the sample and the collected signals are used to form a high-resolution 2D confocal image.

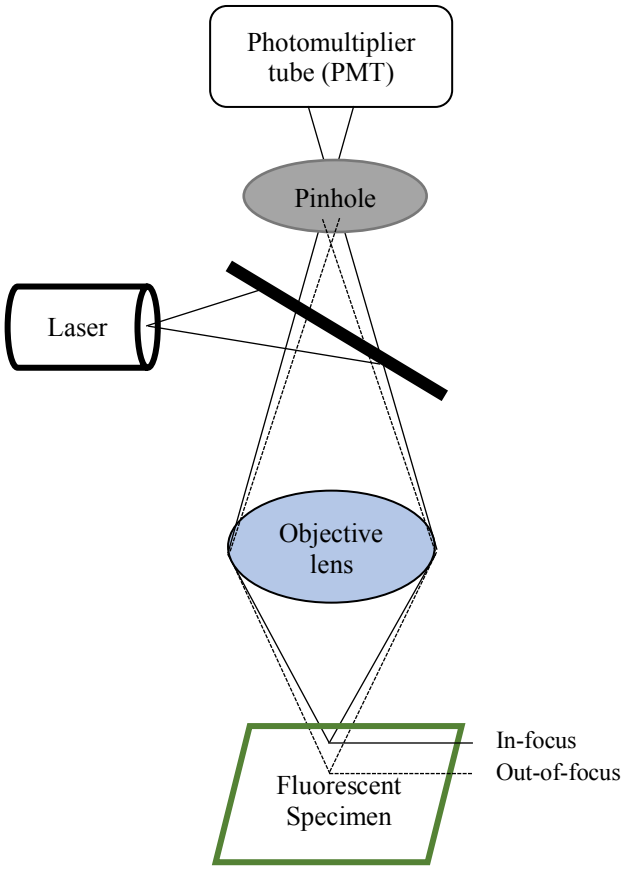

Figure 6.9 Schematic of LSCM.

In this study, the excitation of the fluorescein was performed using an argon laser of 488 nm wavelength operated at a 15% intensity. This was chosen to match the maximum absorption wavelength of Struers EpoDye and fluorescein sodium to ensure optimal fluorescence. The fluorescence emission between 500 and 600 nm were filtered and collected with the PMT detector. The pinhole size was maintained at 1 Airy Unit (AU) and two-times line averaging was applied to reduce noise. Each image was digitised to 2048 x 2048 pixels at a pixel spacing of 0.189 µm, giving a field of view of 387.5 x 387.5 µm. Twenty images were collected per sample. For this study, the brightness and contrast setting of the confocal microscopy were adjusted by trial and error to achieve the optimum image brightness histogram as shown in Figure 6.10. The image processing and analysis were carried out with Fiji/ImageJ software.

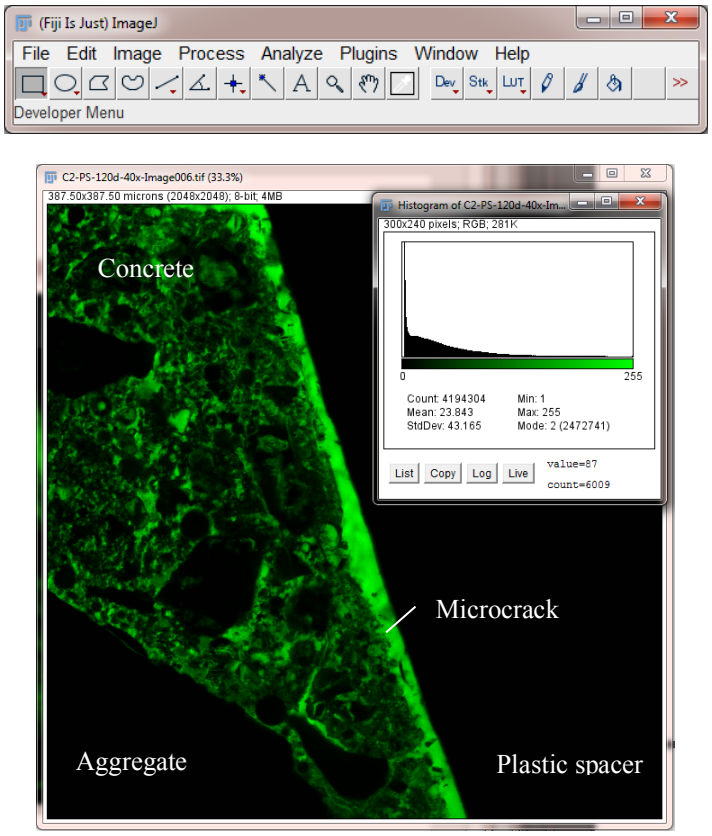

Figure 6.10 Screenshot of Fiji/ImageJ, showing a LSCM image and its corresponding brightness histogram obtained when the brightness and contrast settings was set at optimum. The sample is FA-PS-120d.

6.2.5 Quantitative image analysis

The collected images were analysed to determine the porosity gradient at the spacer-concrete interface. This was done using the Euclidean Distance Mapping (EDM) method proposed by Wong and Buenfeld (2006). The technique uses a distance transformation algorithm to convert a binary image of the spacer-concrete interface into a grey-scale image, from which the porosity gradient is obtained. Figure 6.11 and 6.12 show an example application of the EDM method on an LSCM image of the paste region adjacent to a cementitious spacer.

First, the spacer boundary was carefully traced and segmented using ImageJ/FIJI software. The pores and any cracks were segmented using a moment-preserving method proposed by Tsai (1985). This method was selected after testing all the thresholding methods available in ImageJ software including including Otsu's method, IsoData, maximum entropy and triangle method. It was found that the moment preserving method or known as Moments gave the most satisfactory and best fitting output. This method has been applied to 3D fluorescence LSCM images of a reconstructed silica monolith (Hlushkou et al., 2010) that contains pore sizes

resembling the microstructure of cement-based materials. Recently, Yio (2016) also applied this method to quantify the there-dimensional pore structure of cement paste.

Following pore segmentation, the binary mask of the pore (Figure 6.11b) and the spacer (Figure 6.11c) were then created. Next, an EDM of the concrete (Figure 6.11d) was generated from the binary mask of the pore using an EDM function of the software. Finally, the porosity distribution (Figure 6.12c) was measured by normalising the brightness histogram of the pore EDM (Figure 6.12b) to the paste EDM (Figure 6.12a) and converting the grey values to actual distances by factoring with the pixel spacing value (0.189 μm/pixel).

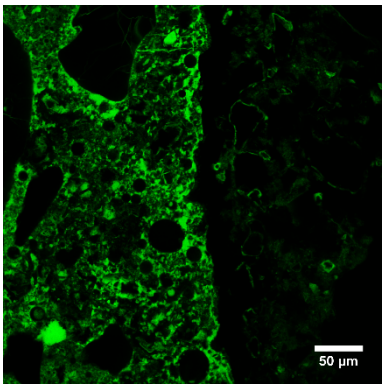

(a) Confocal image of spacer-concrete interface

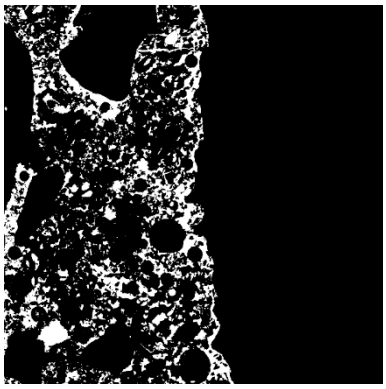

(b) Pore binary mask

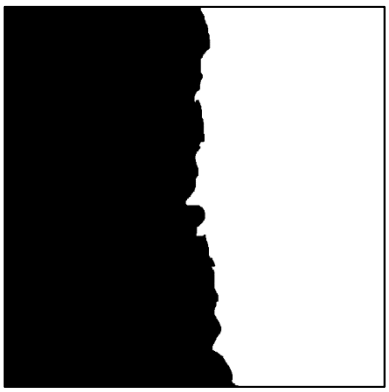

(c) Spacer binary mask

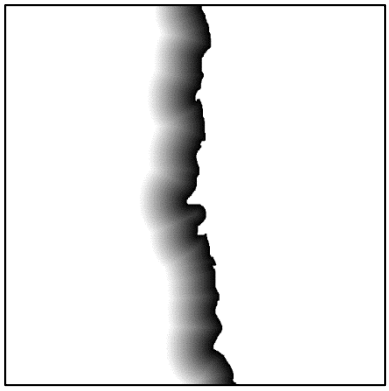

(d) EDM of paste from the spacer boundary

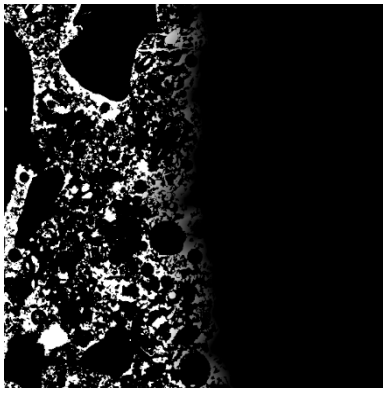

(e) Distance map of pores from the spacer boundary

Figure 6.11 Measuring porosity gradient at spacer-concrete interface using EDM. Sample is FA-CS-3d.

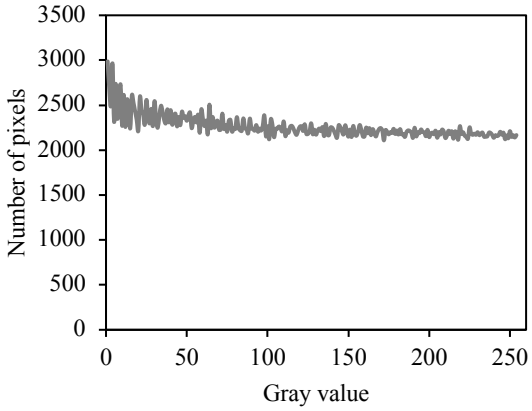

(a) Brightness histogram of Figure 6.11d

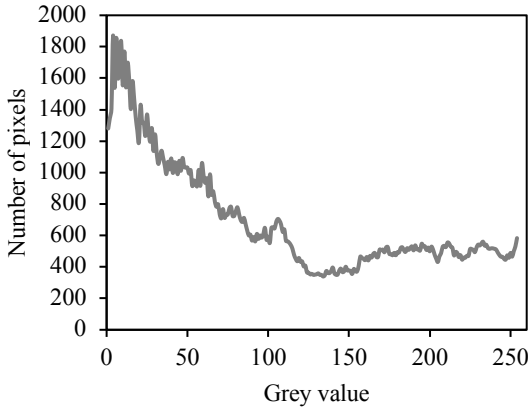

(b) Brightness histogram of Figure 6.11e

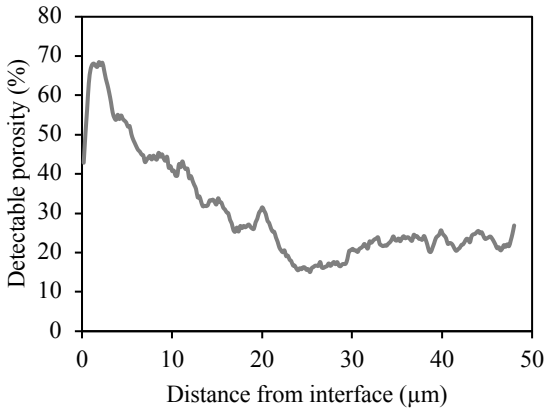

(c) Porosity distribution from spacer-concrete interface at 1 pixel (0.189 μm) strip width

Figure 6.12 Quantifying porosity distribution at the cementitious spacer-concrete interface using brightness histograms of the pore and paste distance maps.

6.2.6 Chloride penetration

As explained in Chapter 3.3.6, chlorides can penetrate concrete via several mechanisms: capillary absorption, diffusion or combination of the two. In this study, samples conditioned at 75% RH, 21°C were vacuum saturated with water prior to exposure to chloride solution. Therefore, the chloride transport mechanism was predominantly diffusion. In contrast, samples conditioned at 50°C were exposed to chloride solution directly. Therefore, the chloride transport mechanism was initially via capillary suction and subsequently via diffusion when the samples achieved saturation.

Prior to placing the samples in chloride solution, all surfaces of the samples except for the surface to be exposed were sealed with two layers of waterproof tape. The purpose of this was to ensure that the chloride ingress into the sample will be unidirectional. The samples were then

placed in a shallow tray containing 3% NaCl solution for four to twelve months at room temperature. The depth of the solution was about 5 mm above the exposed surface. The NaCl solution was periodically replaced with fresh solution to main chloride concentration. The tray was covered with the lid all times to prevent evaporation during the test.

At the end of the exposure period, the samples were sectioned with a diamond saw from the centre and then immediately subjected to freeze-drying to preserve the chloride profiles. Details of the freeze-drying are provided in Chapter 3.3.6. Figure 6.13 shows some examples of sample mass change during freeze drying, which took about three weeks to reach constant mass. After drying, the sample was stored in a desiccator prior to analysis with micro X-ray fluorescence (μXRF) spectrometer to obtain chloride profiles from the exposed surface.

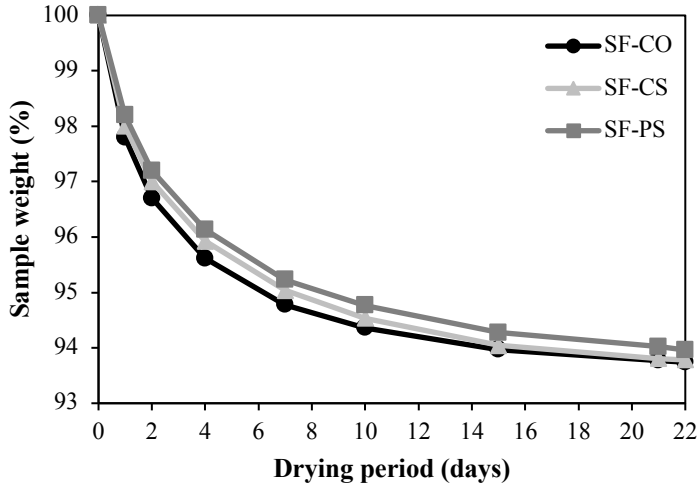

Figure 6.13 Change in mass of samples containing silica fume subjected to freeze drying.

The chloride profiles were measured at three locations: the spacer-concrete interface, the centre of spacer, and at bulk concrete zone away from the interface. This was done by conducting line scans that consist of 30 spot analyses in total per line, as shown in Figure 6.14. The distance between spots was 1 mm increments.

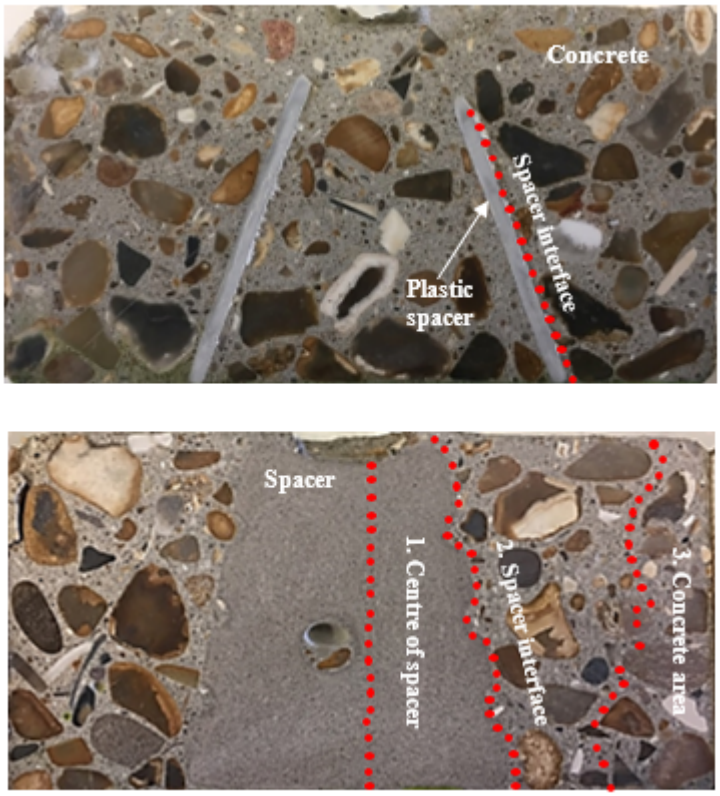

Figure 6.14 Cross-sections of samples with plastic spacer (top) and cementitious spacer (bottom) showing the locations of µXRF spot analysis (red dots) for chloride profiling.

Figure 6.15 shows examples of the analysed spots at the interface between the spacer and concrete. The small red circle on each image indicates the sampling point which is the size of the 30 µm X-ray beam. The analysed spots should be carefully positioned with the help of a high magnification camera (75x) to ensure that the spots avoid large aggregate particles, air voids, and cracks that would cause discontinuities or gaps in the generated chloride profiles. Fine cracks were also observed at the spacer-concrete interface as can be seen in Figure 6.15.

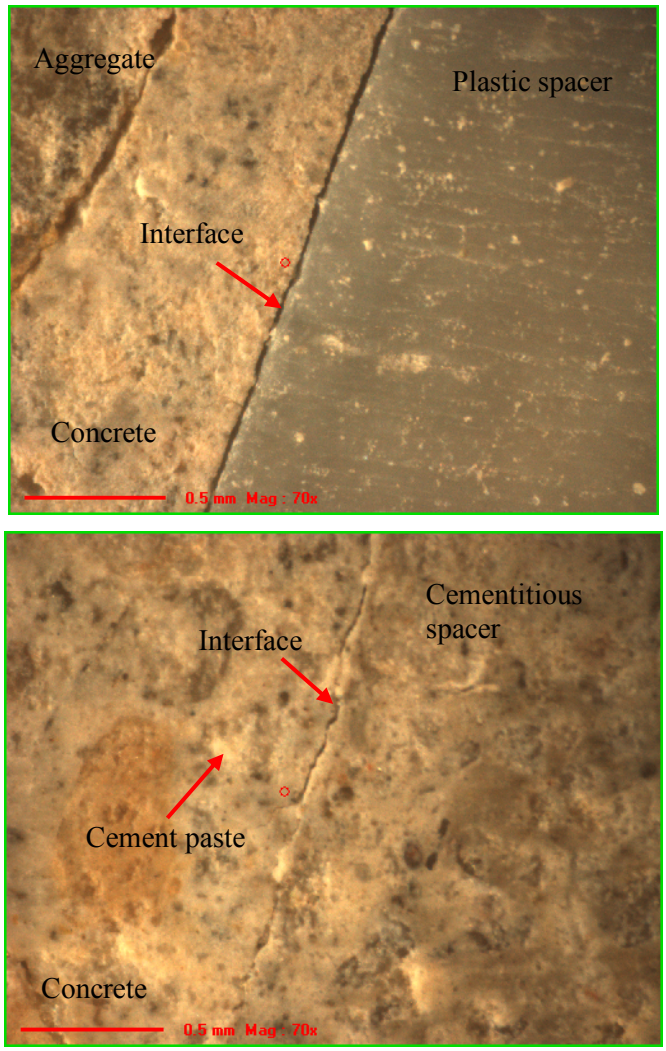

Figure 6.15 Close-up of the spacer-concrete interface showing the analysed µXRF spot (red dot) and fine debonding cracks at the interface.

6.3 Results

6.3.1 Epoxy impregnation depth

Figures 6.16 to 6.18 shows the fluorescence images of sample cross-sections after epoxy impregnation from the bottom exposed surface. Overall, the results show that the presence of spacer in concrete increases the depth of epoxy penetration, particularly along the spacer-concrete interface and within the spacer. Samples containing plastic spacers showed the highest epoxy penetration, followed by samples with cementitious spacers. The control sample (without spacers) had the lowest amount of epoxy penetration in all cases.

It can also be seen that the conditioning regime had a significant effect on the extent of epoxy penetration. As expected, samples conditioned at 50°C oven showed greater amount and depth

of impregnation compared to samples conditioned at 75% RH, 21°C. An interesting observation is that all samples with plastic spacer almost reached the full thickness of the sample (50 mm) when conditioned at 50°C. As shown in Figures 6.16 to 6.18, most of the epoxy intrusion occurred along the interface between spacer and concrete and through the concrete nestled inside the plastic spacer.

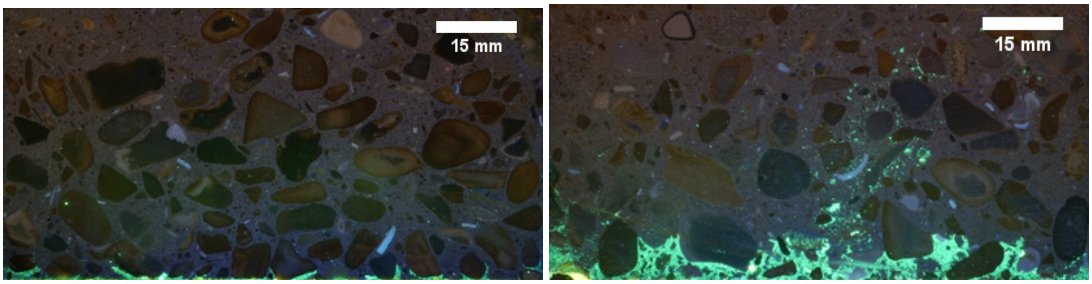

(a) CO

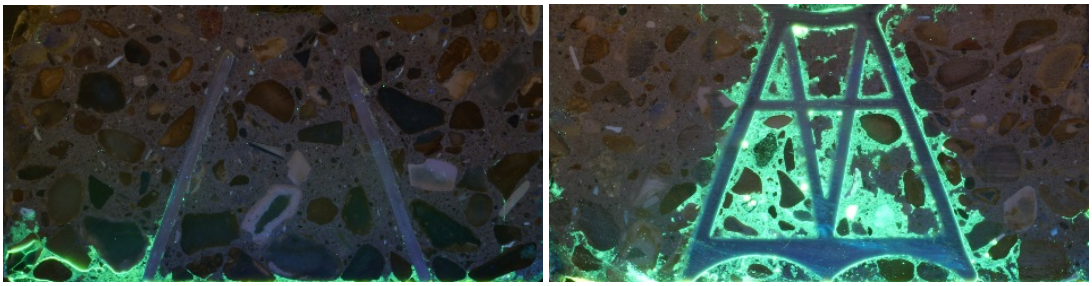

(b) PS

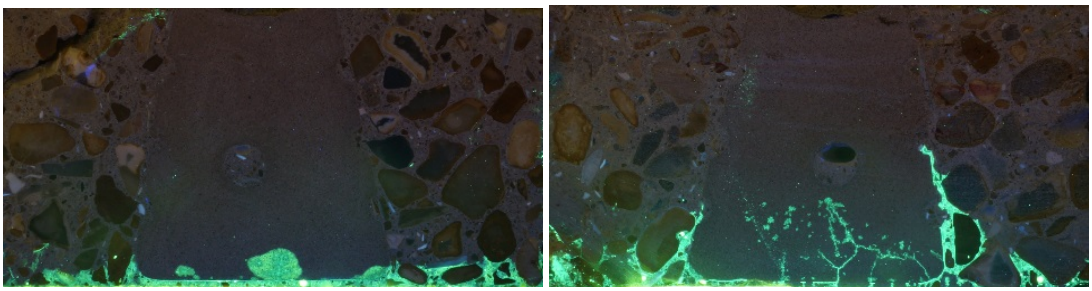

(c) CS

Figure 6.16 Fluorescence images showing the extent of epoxy penetration on 3d-samples containing SF imaged under UV light after conditioning at 75% RH, 21°C (left) and at 50°C (right).

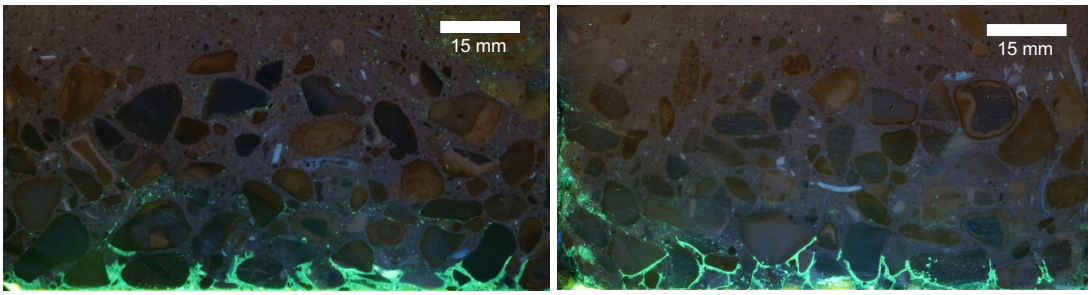

(a) CO

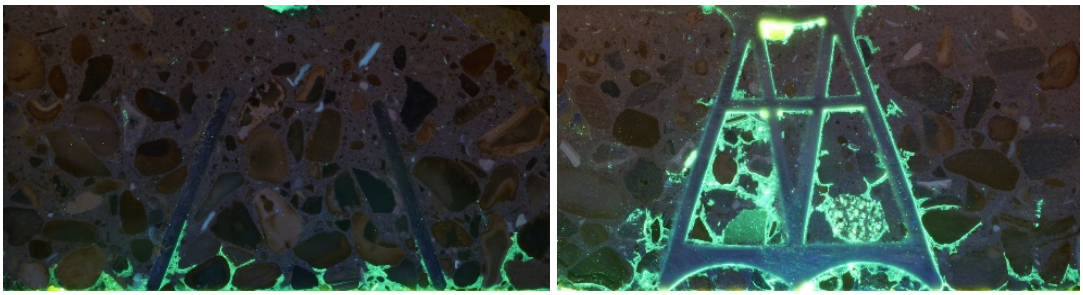

(b) PS

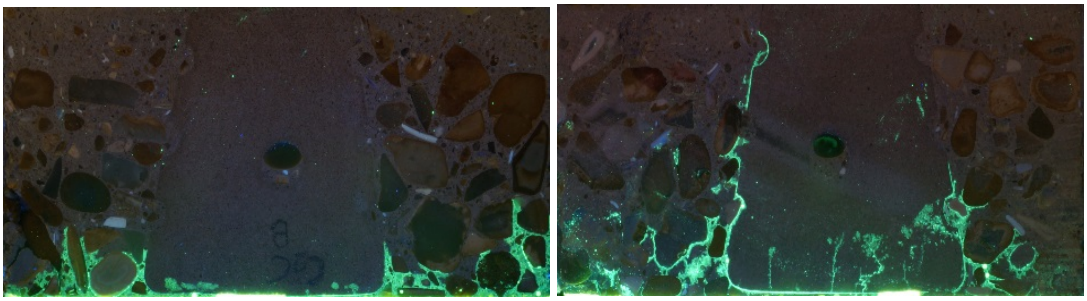

(c) CS

Figure 6.17 Fluorescence images showing the extent of epoxy penetration on 3d-samples containing FA imaged under UV light with different conditioning regime after conditioning at 75% RH, 21°C (left) and at 50°C (right).

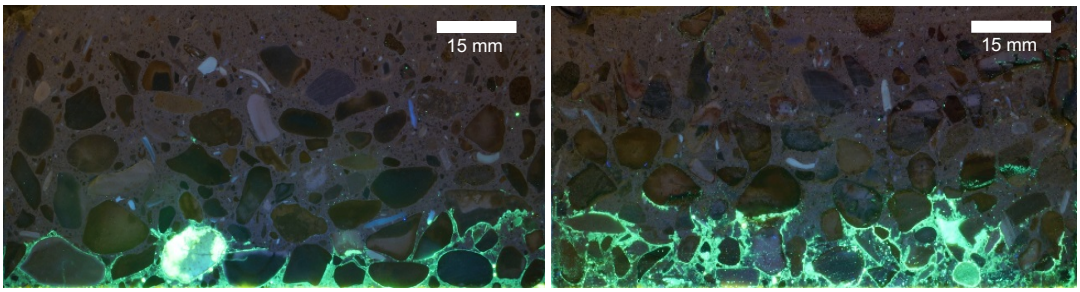

(a) CO

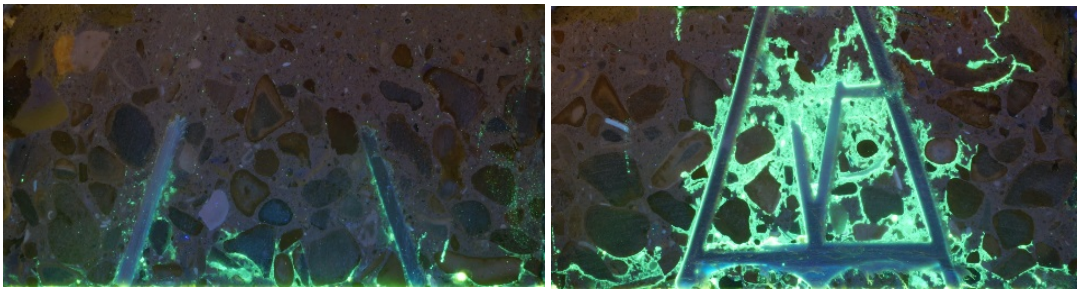

(b) PS

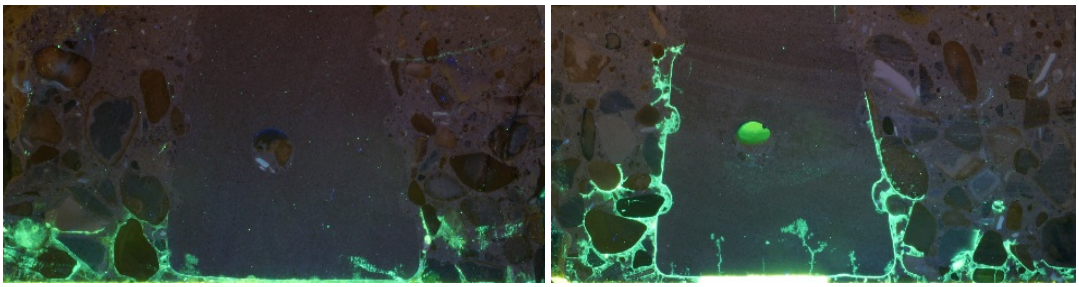

(c) CS

Figure 6.18 Fluorescence images showing the extent of epoxy penetration on 3d-samples containing GGBS imaged under UV light with different conditioning regime after conditioning at 75% RH, 21°C (left) and at 50°C (right).

The maximum depth of fluorescent epoxy penetration for samples with different SCMs, spacers, and conditioning regimes are presented in Figure 6.19. When conditioned at 75% RH, 21°C, samples containing silica fume consistently had the lowest amount of epoxy penetration. This is consistent with the results of oxygen diffusivity, oxygen permeability and water sorptivity observed in Chapter 5. The maximum depth of epoxy impregnation for samples with a cementitious and plastic spacer were higher than those of the control sample by up to a factor of 1.8 and 3.0 respectively. The corresponding values for samples conditioned at 50°C were 4.2 and 5.6 respectively.

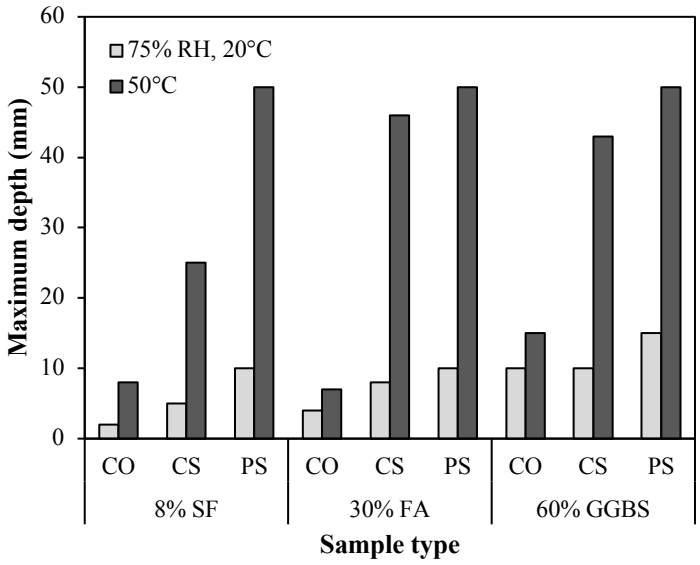

Figure 6.19 Effect of spacers, conditioning regime and SCM on the maximum depth of epoxy impregnation.

6.3.2 Porosity of the spacer-concrete interface

Figure 6.20 shows LSCM images of 3d-samples containing fly ash. These are selected from the set of images used for image analysis and can be considered to be representative of the typical microstructure observed from the image set for the particular sample. The distribution of detectable porosity in samples containing different SCMs and spacer types after curing for 3 and 120 days, measured from the spacer-concrete interface are presented in Figure 6.21. The results are an average of 20 images per sample and expressed as the area percentage of the cement paste.

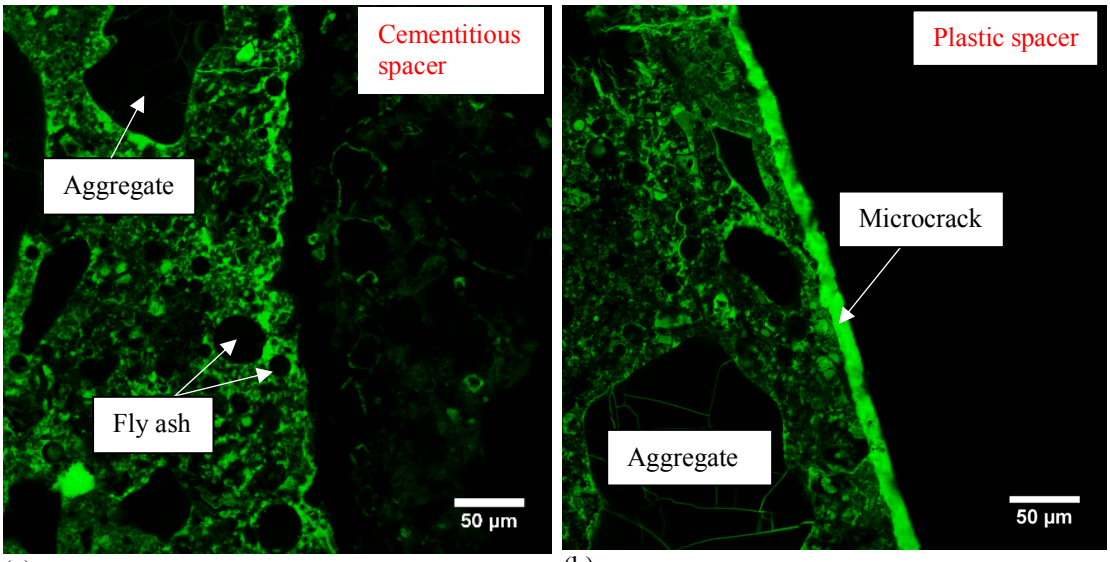

(a) (b)

Figure 6.20 Examples of LSCM images showing (a) cementitious spacer-concrete interface and (b) plastic spacer-concrete interface. Samples are FA – 3d.

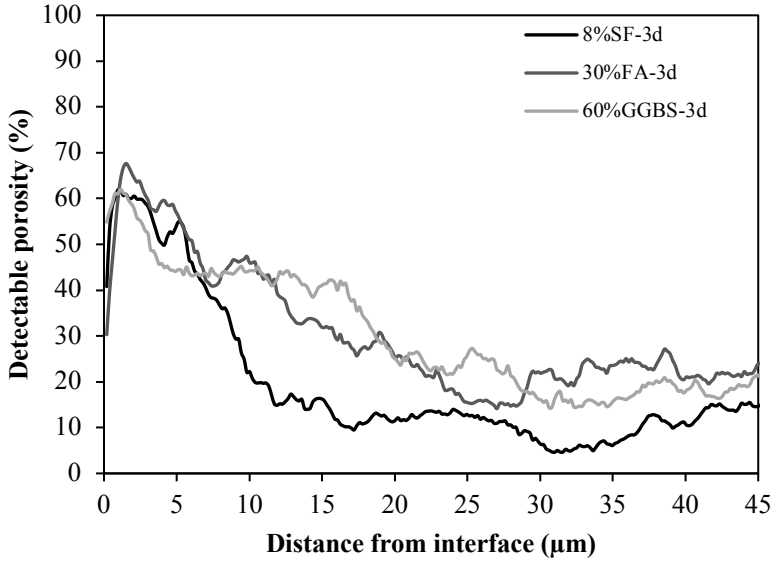

a) Samples containing cementitious spacers

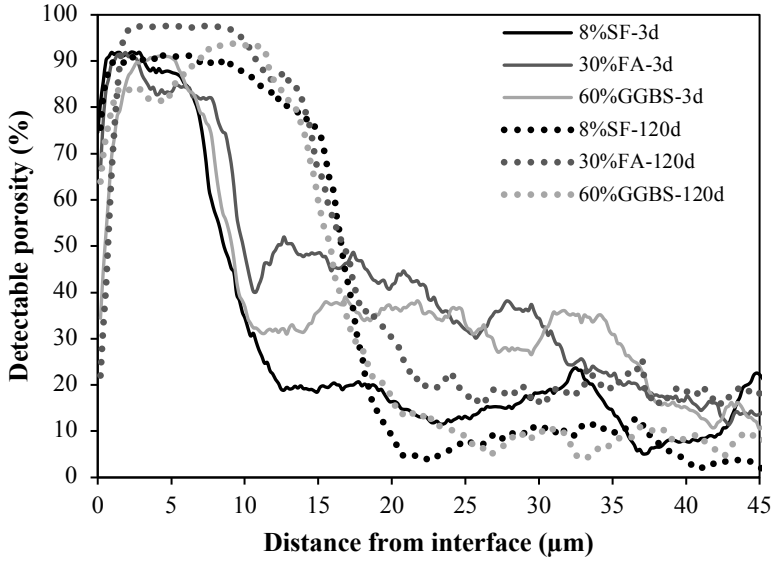

b) Samples containing plastic spacers

Figure 6.21 Average porosity distribution from the spacer-concrete interface for samples containing cementitious and plastic spacers. Samples were dried in a 40ºC oven for seven days prior to impregnation.

The results show a general trend of high porosity at the spacer-concrete interface, decreasing with increasing distance from the spacer boundary. This was observed for all spacer types, SCMs and curing ages. The affected zone occurred within the first 40 microns from the interface. Therefore, the presence of spacer disturbs the microstructure of the surrounding concrete, and this effect remained even in very well cured concretes containing SCMs. The increased porosity is caused primarily by a higher initial water content due to poor particle packing and bleeding along spacer surface, as also observed by Alzyoud et al. (2016). Samples containing silica fume showed the lowest porosity, which is consistent with the understanding that silica fume has greater filler effect and pozzolanic reactivity compared to slag and fly ash. Samples with fly ash and slag gave about the same porosity gradient for both spacer types used. It is interesting to note that the porosity at the plastic spacer-concrete interface is greater than that of the cementitious spacer-concrete interface by a factor of ~1.5. This is due to weak bonding between the plastic and concrete, causing microcracking as shown in Figure 6.10. The width of this bond crack increases with curing age, presumably due to additional shrinkage of the concrete with drying.

Figure 6.22 and 6.23 presents some examples of backscattered electron (BSE) images showing the interface microstructure of samples with a cementitious or plastic spacer respectively. The images were captured at 500x magnification using a field-emission gun scanning electron microscope operated in the BSE mode, giving a field of view of 415 x 553 μm. In Figure 6.22, the microstructure of cementitious spacer can also be seen. The main features that can be seen within the cementitious spacer include hydration products, unreacted cement, sand particles, and unreacted slag. It is clearly observed that the area between the spacer and concrete is more porous than the concrete or cementitious spacer.

The visible bond cracks between the plastic spacer and concrete were formed at two stages. The first crack that is adjacent to the concrete is believed to have been formed during the curing and conditioning regimes and occurred due to drying-induced shrinkage. This crack is impregnated with fluorescence epoxy; Therefore, it is considered as the original feature that would contribute to mass transport. The second (thinner) crack that is adjacent to plastic spacer is not filled with the epoxy and appears darker in the image. This crack is believed to be formed during the grinding or polishing stages. Therefore, it is a preparation artefact and is not considered as part of the original microstructure.

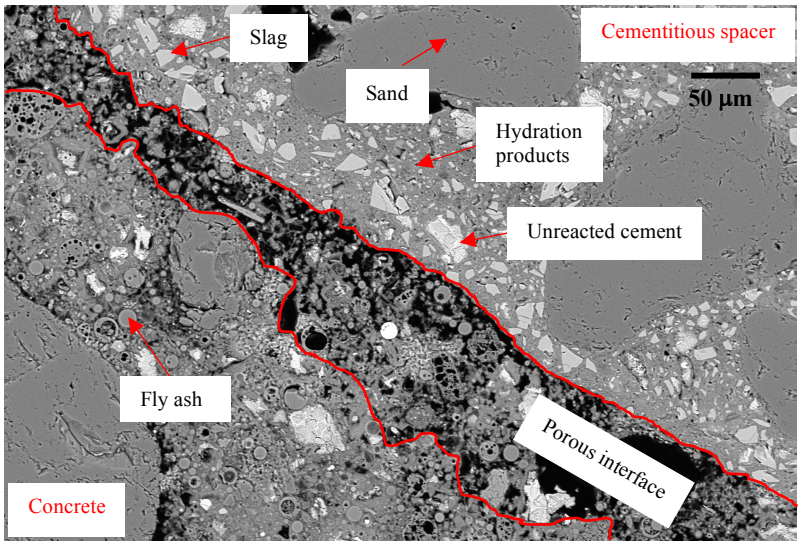

Figure 6.22 BSE image showing microstructure of the cementitious spacer-concrete interface at 500x magnification (field of view 415 x 553 µm). Sample is FA-CS-3d.

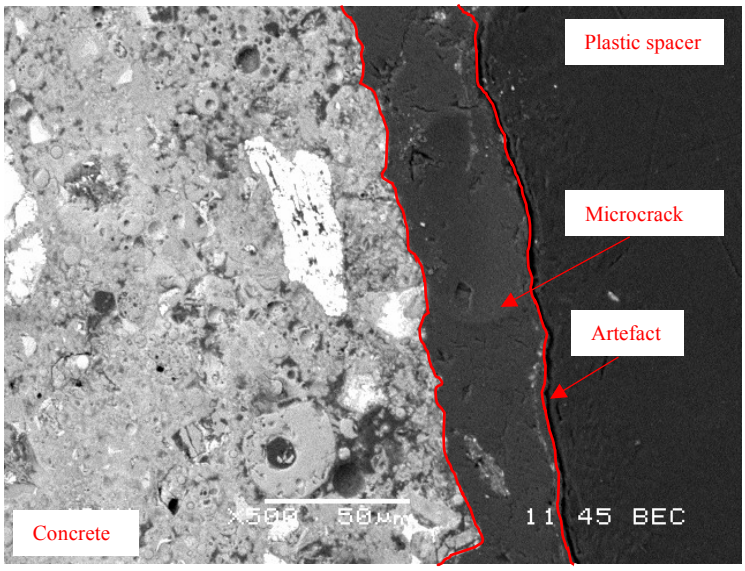

Figure 6.23 BSE image showing microstructure of the plastic spacer-concrete interface at 500x magnification (field of view 415 x 553 µm). Sample is FA-PS-3d.

6.3.3 Chloride penetration profile

The chloride penetration profiles measured at the spacer-concrete interface, at the centre of the cementitious spacer, and bulk concrete zone away from the interface are shown in Figure 6.24. It can be seen that the chloride content was highest near the exposed surface (depth = 0 mm) and decreased with an increase in depth. The depth of concrete affected by chloride ingress ranged from 5 mm to over 50 mm. The spacer-concrete interface showed a greater concentration and depth of chloride penetration compared to the bulk concrete zone. However, the concentration of chlorides through the cementitious spacer was much lower than that of the spacer- concrete interface. These results are generally consistent with the results of the fluorescence epoxy impregnation and microstructure analysis as discussed in Sections 6.3.1 and 6.3.2.

Factors influencing the chloride profiles other than the presence of a spacer include the conditioning regime, chloride transport mechanism, and period of exposure. As expected, severe sample drying prior to exposure had a major influence on the chloride profiles. This is particularly the case for the sample containing a plastic spacer, which showed a substantial increase in chloride ingress along the spacer-concrete interface when conditioned at 50°C compared to that of 75% RH, 21°C.

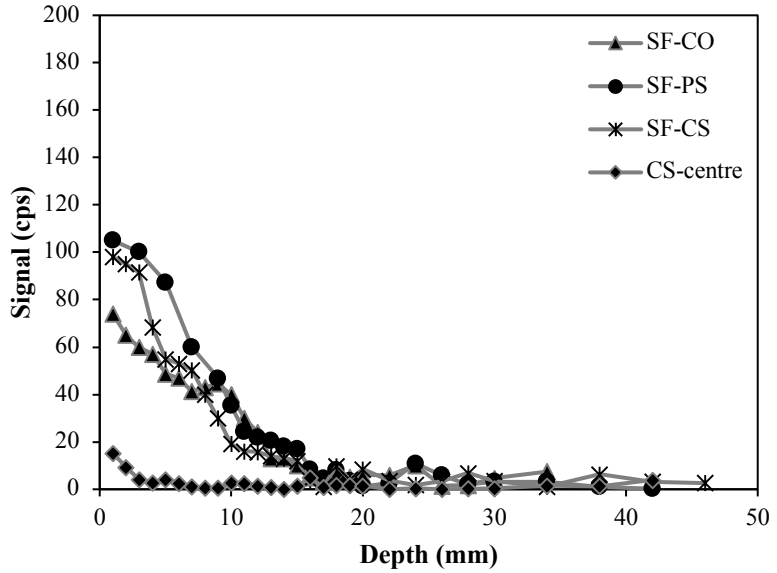

(a)

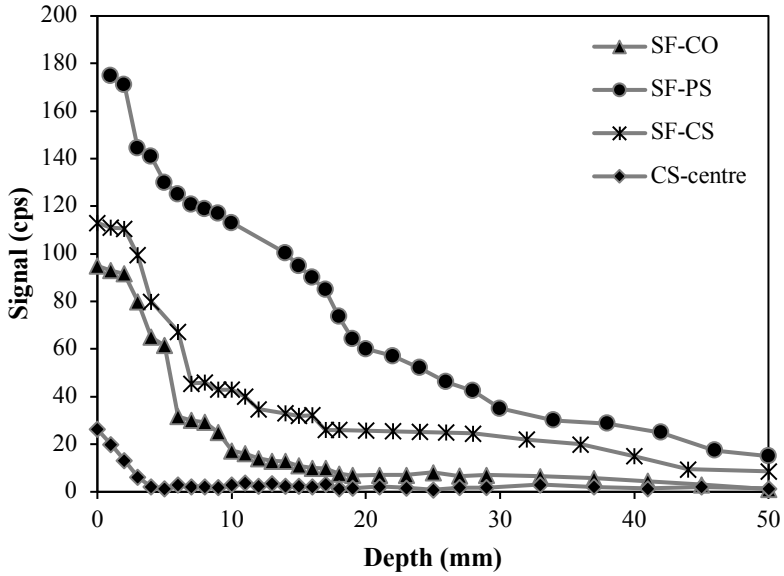

(b)

Figure 6.24 Chloride penetration profiles for 28d-samples containing silica fume: (a) Conditioned at 75%RH, 21°C, vacuum saturated with water and then exposed to salt solution for 12 months; (b) Conditioned at 50°C oven and exposed to salt solution for 4 months.

6.4 Discussion

The spacers used in this study are either impermeable plastic or cementitious (mortar containing slag and fibre at w/b of 0.35) with a lower porosity than the cement paste around it (Figure 6.22). As such, the inclusion of spacers may decrease the transport properties by reducing the cross-sectional area available for flow. However, results in Chapter 5 showed that the samples containing a spacer always had higher transport properties compared to the control samples (without a spacer). Therefore, the substantial increase in the transport properties that occurred in the samples containing spacers can be attributed to the porous interface between the spacer and concrete.

This is confirmed by the results presented in Figures 6.16 to 6.18 showing a preferential transport path of fluorescence epoxy impregnation via the spacer-concrete interface. Figure 6.19 shows that the maximum depth of epoxy occurred at the interface between the spacer and concrete. The results from LSCM and BSE images (Figures 6.20 to 6.23) exhibiting substantially higher porosity at the spacer-concrete interface than the surrounding concrete further substantiate this. The zone of higher porosity is approximately 15 – 50 μm wide away from the spacer-concrete interface. Furthermore, the results from μXRF (Figure 6.24) indicating a preferential transport path along the spacer-concrete interface also confirm that a zone of weakness exists in the concrete near the spacer. The lowest amount of chloride intrusion occurred inside the cementitious spacer. Therefore, the porous interface between the spacer and concrete is firmly believed to have significant influences on the transport results.

The higher porosity at the spacer-concrete interface can be explained by a higher initial water content at the interface due to difficulties in packing cement particles near to the spacer surface, known as "wall effect" and bleeding along the spacer surface or entrapment of bleed water under the horizontal surface of the plastic surface. It is interesting to note that the width of the porous interface zone between spacer and concrete is similar to that of the aggregate-cement paste "interfacial transition zone" (Larbi, 1993, Ollivier et al., 1995, Scrivener et al., 2004) as well as the steel-concrete interface (Glass et al., 2001, Horne et al., 2007).

Furthermore, changing the drying process from a gentle drying at 75% RH, 21°C to a more severe drying at 50°C induced significant effects on the transport properties and microstructure. When a saturated concrete sample is subjected to drying at high temperatures, the excess water is removed rapidly from the concrete and causes it to shrink. The shrinkage is restrained by spacers creating tensile stresses in the concrete which in turn produce drying shrinkage cracking.

In other words, debonding and microcracking occurred at the interface between the spacer and concrete is probably due to differential volumetric changes (drying or thermal shrinkage) or relative movements between the spacer and concrete. The difference in the thermal expansion coefficients of the spacers and concrete is also believed to induce cracking along the interface. It is known that the plastic spacer has a 10 – 15 times larger thermal expansion coefficient than that of the concrete. The effect of drying induced cracking at the spacer-concrete interface can be seen in Figures 6.16 to 6.19. The results showed that the epoxy reached the top surface of samples containing a plastic spacer via the spacer-concrete interface. A similar effect was observed in samples containing a cementitious spacer showing a significant increase in the depth of epoxy impregnation due to the drying process. This shows that the plastic spacers undergo a greater expansion on heating and contraction on cooling compared to the cementitious spacers which has almost similar thermal and shrinkage properties to the surrounding concrete.

Finally, it is worth noting that although the incorporation of silica fume in samples conditioned at 75% RH, 21ºC produced the lowest epoxy intrusion as expected, the presence of a spacer induced a higher increase relative to the control (without a spacer) compared to that of fly ash and slag. The same phenomenon is observed in Figure 6.21 showing that well-cured samples (120 days) had a larger porosity compared to the 3d-samples. This is consistent with the results presented and discussed in detail in Chapter 5.

6.5 Conclusions

Laser scanning confocal microscopy and image analysis using Euclidean distance mapping were applied to investigate the microstructural gradients at the interface of cementitious or plastic spacers with surrounding concrete. The results showed that the spacer-concrete interface has a higher porosity compared to the concrete farther away from the spacer. This is also confirmed by the fluorescent epoxy impregnation results and chloride penetration profiles. The interface between the spacer and concrete has the highest epoxy impregnation and chloride penetration profile. This occurred despite the fact that the concrete contained a partial replacement of CEM I with SCMs such as silica fume, fly ash and ground granulated blast-furnace slag. The increases in the transport properties of the samples containing spacers as presented in Chapter 5 are believed to be due to the highly porous and microcracked spacer-concrete interface. Finally, it can be revealed that the incorporation of SCMs as a partial replacement of CEM I was unable to eliminate the negative effect of spacers on the microstructure of concrete and on the associated transport properties.

Chapter 7

Influence of surface texture on the spacer-concrete bond strength

The previous chapters showed that the presence of reinforcement spacers has a negative effect on mass transport properties and microstructure of concrete. This occurred despite prolonged curing and the use of SCMs such as silica fume, fly ash and ground granulated blast-furnace slag as partial replacement for CEM I. A potentially important factor is the bond strength at the interface between spacer and concrete. This chapter presents the first study to investigate the interface bond strength between a prefabricated spacer and concrete, in particular, to understand the influence of surface texture by performing splitting tensile strength tests on manufactured spacer-concrete composite samples. The results show that the surface texture of the prefabricated spacer plays an important effect on enhancing its interlocking with concrete and this can lead to a significant improvement in bond strength of the prefabricated spacer-concrete interface.

7.1 Introduction

No studies have been carried out to-date regarding the bond strength between a spacer and concrete. However, numerous studies have been reported regarding the bond strength in the field of concrete repair materials and these are briefly reviewed here. It is generally accepted that a number of factors can affect the bond strength between a concrete substrate and repair material. These include substrate surface roughness, substrate moisture content, and the mechanical properties of substrate concrete or repair materials (Courard, 2000, Beushausen and Alexander, 2008, Santos and Julio, 2011, Tayeh et al., 2013). Among these, surface roughness is thought to be the primary factor contributing to bond strength via mechanical interlocking. As such, a number of methods such have been developed and tested to enhance concrete surface roughness, thereby improving mechanical interlocking between the concrete substrate and repair material. These include sand-blasting, grinding, jack-hammering, wire brushing, milling, and hydro-jetting or shot-blasting. However, some of these methods are particularly aggressive and can cause damage to the near-surface concrete layer (Courard, 2000, Garbacz et al., 2004). Table 7.1 summarises the findings of selected key references on studies that have investigated various methods for improving the interface bond strength in field of concrete repairs.

Table 7.1 Selected references on methods for improving interface bond strength for concrete repairs.

Reference	Sample type	Methods for improving bond strength	Bond strength tests	Key findings
Julio et al. (2004)	Concrete and concrete	Steel brushing Partially chipping with a light jackhammer Water saturation for 24h Sandblasting Grinding	Slant shear Pull-off	The highest bond strength was achieved with sandblasting.
Garbacz et al. (2004)	Concrete and repair mortar containing glass microfibers	Sand-blasting Shotblasting Hand-milling Mechanical-milling	Pull-off	The highest pull-off strength was obtained for the samples prepared by shotblasting and sandblasting.
Santos and Julio (2011)	Concrete and concrete	Wire-brushing Sandblasting	Slant shear Pull-off	The sandblasted surface gave the highest values for slant-shear and pull-off strength.
Tayeh et al. (2013)	Normal concrete substrate and ultra-high performance fiber reinforced concrete (UHPFC) as a repair material	Sand-blasting Wire brushing Drill holes Grooving	Slant-shear Splitting tensile	The highest bond strength was achieved for the sand blasted surface.
Munoz et al. (2014)	Ultrahigh-performance concrete (UHPC) and normal-strength concrete (NSC)	Chipping Wire brushing Sand-blasting Grooving Using retarder to obtain a high course aggregate exposure	Slant-shear Pull-off Split tensile	Results from split tensile tests showed that the brushed and chipped surfaces had similar profiles with the smooth (untreated) surface. A highly roughened surface was achieved by using retarder to expose aggregates

The effect of surface texture has been widely investigated in the field of tribology over the last decade because this is an important aspect of surface engineering. Various texturing techniques have been employed to improve the tribological properties of surfaces and some recent studies

are reviewed here. Yu et al. (2010) investigated the effect of surface textural shape (e.g. circle, ellipse and triangle) on the friction of lubricating steel on steel pair. All the shapes have the same depth, area of dimple and area ratio. It was found that the geometric shape has a clear effect on the load-carrying capacity and that ellipses give the highest load capacity. Uddin et al. (2017) presented a numerical study on the effect of surface texturing on the tribological performance of hydrodynamic slider surfaces. The geometric parameters considered were the texture shape, bottom profile, orientation and depth. The investigated shapes included a circle, square, triangle, chevron, ellipse, hexagon and octagon. It was revealed that the shape, geometry and orientation were critical parameters impacting the film thickness and friction coefficient. Square shapes with a single wedge bottom profile offered the best tribological performance. Texture density defined as the ratio of the area covered by the surface texture divided by the total area of the imaginary square cell was found to be more dominant than the texture aspect ratio in affecting tribological performance. An earlier study by Yan et al. (2010) also suggested that the dimple area density was the most important geometrical parameter, followed by depth and diameter. Another study by Hsu et al. (2014) concluded that dimple shape and orientation with respect to the sliding direction significantly affect friction.

Most of the commercially available spacers have surfaces that are smooth. Spacers with simple grooved surfaces are also available (e.g. Figures 3.2 and 5.1), but these are less common. Therefore, a simple method to enhance the prefabricated spacer-concrete interface would be to optimise the surface texture of the prefabricated spacer so that it can bond better with concrete. However, there are a number of issues and research challenges. The purpose of the study is to investigate the effect of surface texture on the interface bond strength between a prefabricated spacer and concrete. Prefabricated cementitious spacers with eight different surface textures and two mix proportions were prepared, cast in concrete, and then tested for splitting tensile strength. Finally, the measured surface properties were correlated with the measured bond strength to establish the effects of surface texture on the prefabricated spacer-concrete interface.

7.2 Experimental

7.2.1 Materials and mixture proportions

The prefabricated spacers used in this study were made of either mortar or concrete (marked as PMS and PCS, respectively). Portland cement CEM 1 52.5N complying with BS EN 197-1:2011 was used as the main binder at water/binder (w/b) ratio of 0.4. 10 mm Thames Valley gravel

(10 mm) and sand (<5 mm) complying with BS EN 12620:2002+A1:2008 medium grading were used.

Mix proportions of the mortar and concrete, calculated using the absolute volume method, are shown in Table 7.2. The total aggregate content for the mortar and concrete were 50% and 70% respectively. A super plasticising admixture (Master Glenium SKY 920) was used at dosage of 0.75% wt. binder to improve the workability of the mixes. Detailed information regarding the materials used are given in Chapter 3. The mixes were chosen after several trials to achieve a satisfactory workability and to ensure that the cast spacers meet the 28-day compressive strength requirement of 50 MPa in accordance to BS 7973-1.

Table 7.2 Mix proportion of the mortar and concrete used in this chapter.

	W/C ratio	CEM I (kg/m^3)	Water (kg/m^3)	Sand (kg/m^3)	Gravel (kg/m^3)
Mortar	0.4	697	279	1375	-
Concrete	0.4	418	167	728	1092

7.2.2 Producing surface texture on prefabricated spacers

A number of methods were trialled to produce the prefabricated spacers with different surface textures. In the initial trials, the prefabricated spacers were produced by casting against aluminium plates with different textures as shown in Figure 7.1. The surface textures were analysed using laser scanning confocal microscopy (LSCM) with the operating conditions presented in Table 7.3. Confocal microscopy is an optical method that has the ability to create a three-dimensional surface topographic map, which is a digital image in which each pixel is assigned a value that represents the z-level (Lange et al., 1993).

Table 7.3 Operating conditions of the LSCM for surface texture analysis.

Parameters	Specifications
Objective lenses	HCX PL Fluotar 5x NA 0.15 Dry
Mode	Reflection
Gas Laser	Argon (458)
Beam splitter	RT 30/70
Pixel format	512x512
Scanning speed	400Hz
Pinhole size	1 AU
Tile size	Varied depends on area of the texture shape

The map is then used to quantify surface characteristics such as area and roughness. Surface area was measured using ImageJ software while the surface roughness parameters were characterised using two plugins within ImageJ, namely extended depth of field (Forster et al., 2004) and SurfCharJ (Chinga et al., 2007). The first plugin generates a composite image by compiling all of the sharpest regions from each focus plane. By using the height map from the first plugin, the surface is then analysed using the SurfCharJ toolbox that provides local and global roughness analysis, gradient analysis, segmentation, surface levelling and directional analysis. Examples of 3D surface plots are presented in Figure 7.2.

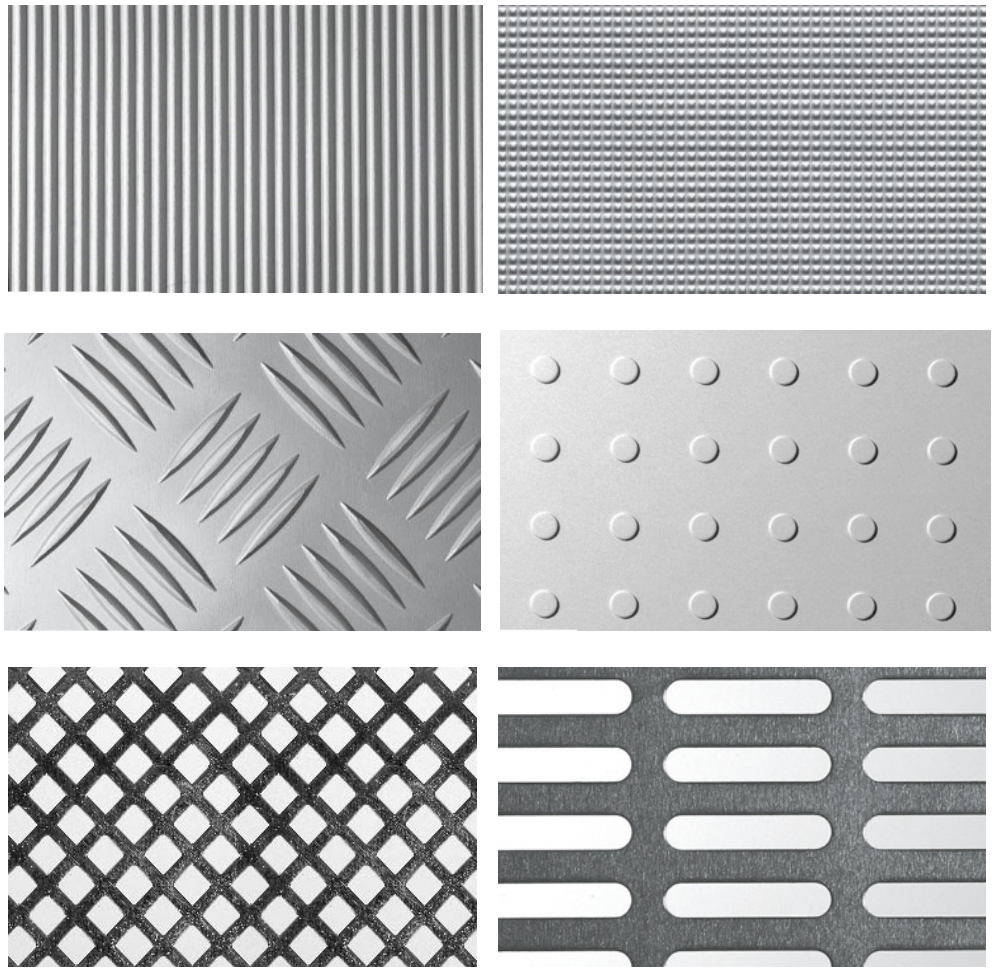

Figure 7.1 Aluminium plates for producing prefabricated spacers with various surface textures.

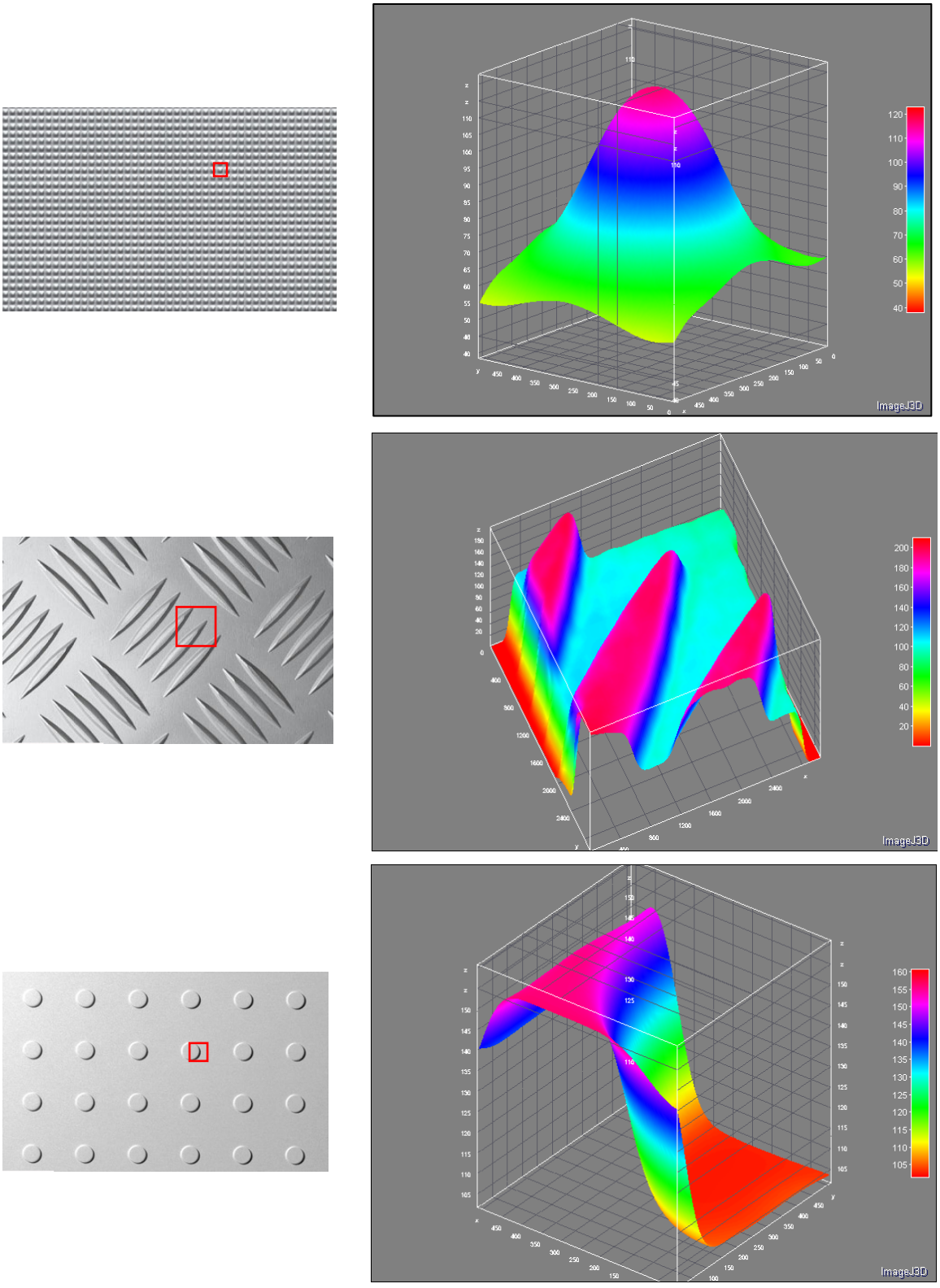

Figure 7.2 Examples of 3D surface texture plots.

However, when cast against fresh concrete, it was observed that the aluminium plate reacted with the alkalis in the Portland cement, producing hydrogen gas. This caused surface defects in the form of bubbles which were found on all surfaces as shown in Figure 7.3. An attempt was made to avoid this problem by painting the aluminium plates with a thin layer of epoxy prior to casting the prefabricated spacers. Although this worked, the resulting texture was not of consistent quality because the epoxy changes the shape of the texture. Hence, the use of aluminium plates was discontinued, and other methods were examined.



Figure 7.3 Poor surface quality due to hydrogen gas released from the reaction between aluminium plate and alkalis from Portland cement.

Of all the methods trialled, an approach using a silicone rubber mould was found to be the most successful and this was used for the rest of the thesis. Seven silicone moulds with different textures were chosen and applied as shown in Figure 7.4. These were made of a high-quality platinum-cure silicone that was obtained from several manufacturers in the UK. The moulds are typically used by military modellers to enable the casting of small-scale building supplies. There are dozens of texture types available and they vary in terms of shape, profile depth and orientation. From these, seven types of textures representing different surface parameters were selected for further testing.

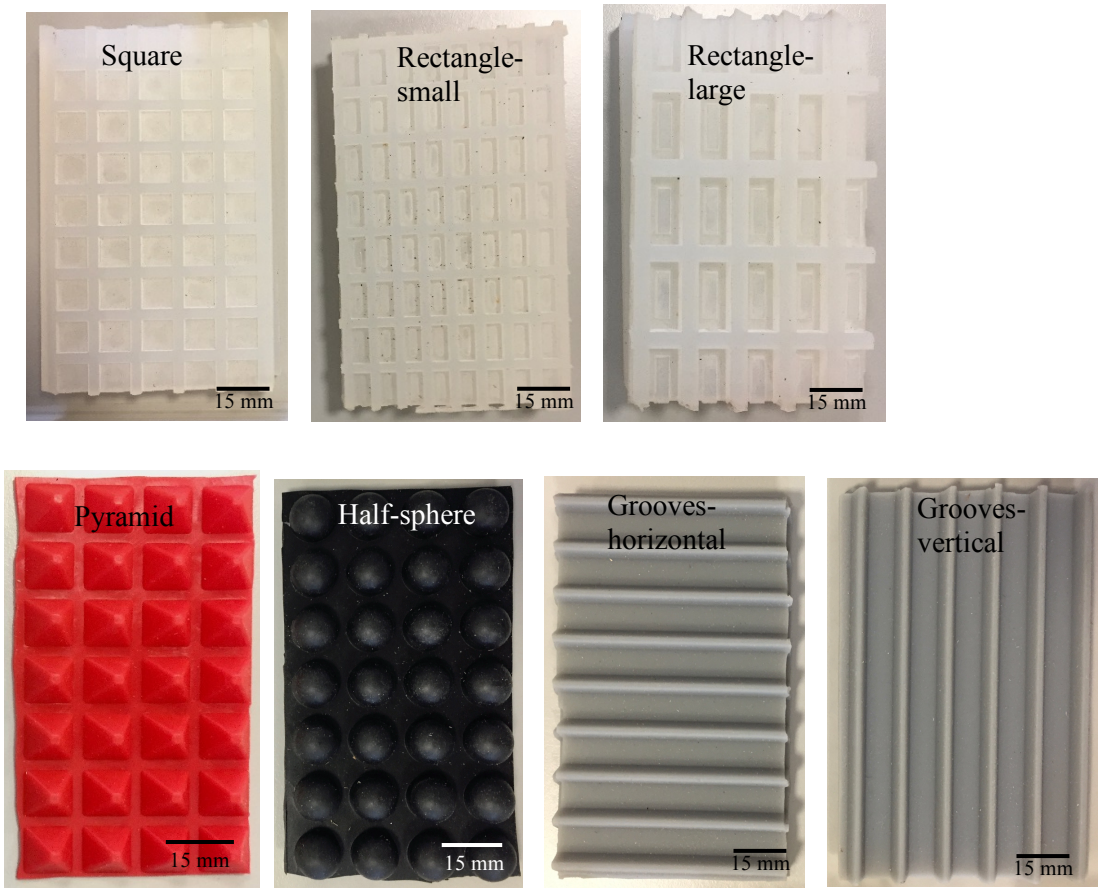

Figure 7.4 Silicone moulds used for producing various surface texture.

Surface texture refers to geometrical irregularities (BS 1134:2010). In this study, the chosen textures are different in terms of shape, profile depth, surface roughness, and texture density. Three of the surface textures are convex or have features that protrude out of the surface (i.e. square, rectangle-small and rectangle-large). The remainder are concave or consist of features that curve inwards (i.e. pyramid, half-sphere, grooves-vertical and grooves-horizontal).

The detailed dimensions of all the textures are shown in Table 7.4. The properties of the investigated surface textures are summarised in Table 7.5. Surface roughness (r) is defined as a ratio between the actual and projected surface areas (BS 1134:2010):

$$r = \frac{A_T}{A_0} \qquad \text{Eq. 7.1}$$

While texture density (T_d) is calculated based on the formula:

$$T_d = \frac{A_t}{A_o} x100\% \qquad \text{Eq. 7.2}$$

Where A_T (mm^2) is the total surface area following the shape of the dimples/bulges (also known as total bonded surface area); A_0 (mm^2) is the projected surface area, $A_0 = L\ x\ W$, where L and W are the length and width of the sample; A_t is the total area covered by the projected surface areas, $A_t = l\ x\ w\ x\ N$, where N is the number of bulge or dimple, l and w are the length and width of each dimple or bulge, as shown in Figure 7.5. The maximum profile depth, h, is defined as the distance between the highest and lowest point of the profile. Both the surface area and profile depth were calculated using elementary geometric formulas.

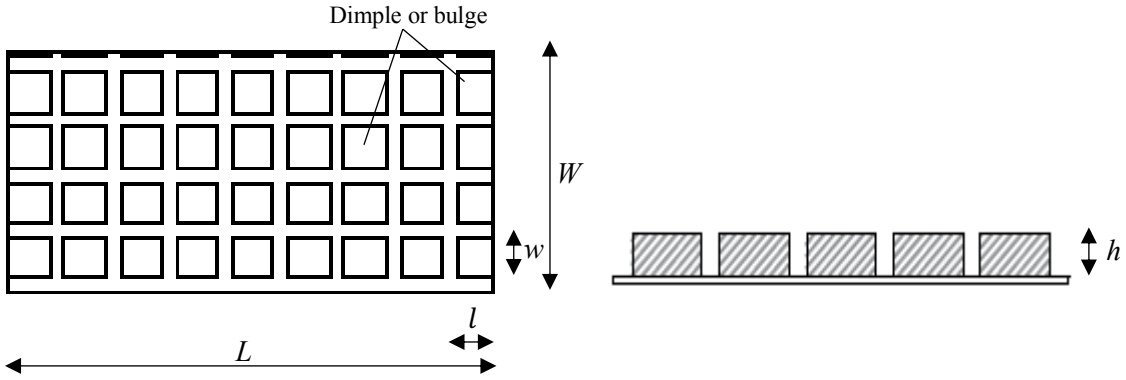

Figure 7.5 Illustration of surface texture parameters used for calculating roughness and texture density

Table 7.4 Dimensions of prefabricated spacer surface texture (units in mm).

CO	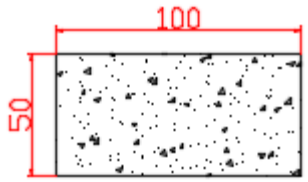	**SQ**	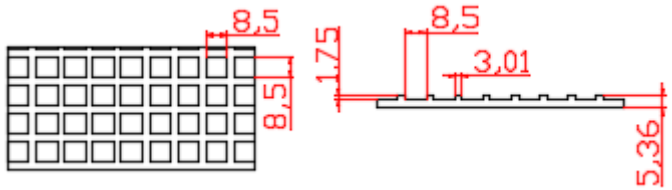
RS	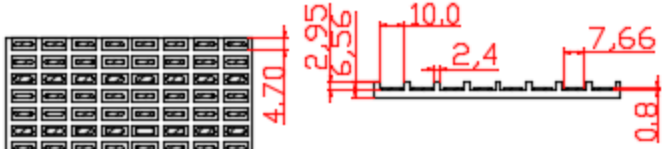	**RL**	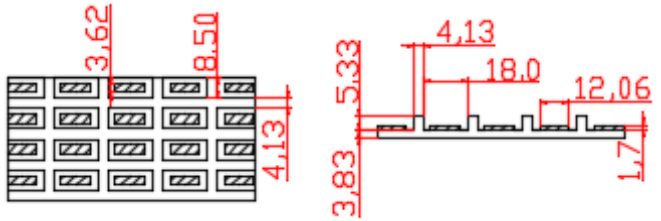
GH	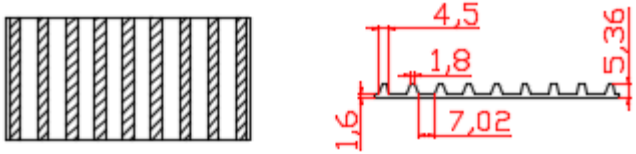	**GV**	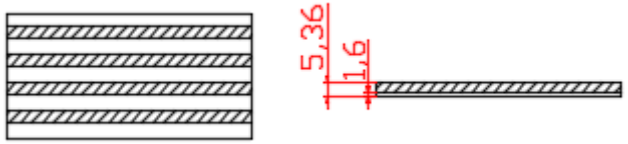
HS	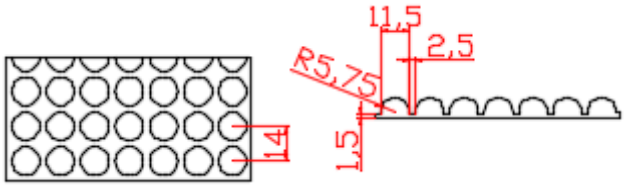	**PY**	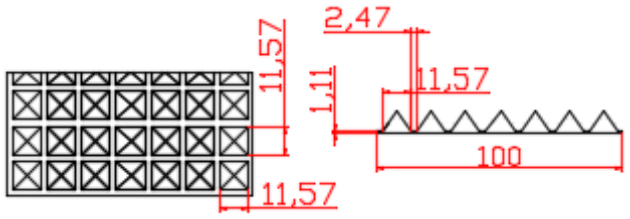

Table 7.5 Shape, profile depth and various of surface texture parameters investigated.

Name	Shape	Max. profile depth (mm)	Surface roughness	Texture density (%)
Control – flat (CO)	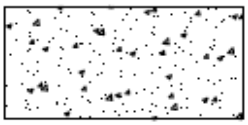	-	1.00	0
Grooves-horizontal (GH)	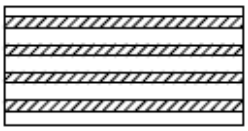	4	1.21	45.0
Grooves-vertical (GV)	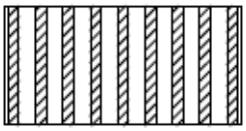	4	1.20	45.0
Square (SQ)	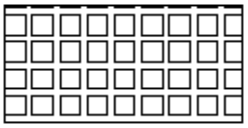	1.75	1.43	52.0
Rectangle-small (RS)	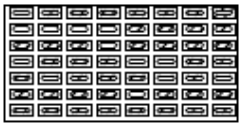	2.96	2.03	52.6
Rectangle-large (RL)		5.33	2.02	55.0
Half-sphere (HS)	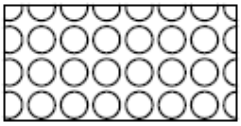	8	1.89	46.6
Pyramid (PY)	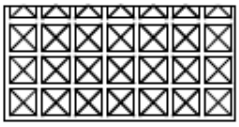	9	1.92	51.0

7.2.3 Sample preparation

Cylindrical samples were prepared in steel moulds of 100 mm diameter and 50 mm height according to the mix proportions shown in Table 7.2. Each sample was cast and cured in two stages. The first half of the cylindrical sample was cast with either the mortar or concrete (Table 7.2) and this was used to represent a prefabricated spacer. The second half of the sample was then cast against the prefabricated spacer using the same concrete mix and cured to different ages. The composite sample was then subjected to splitting tensile test as a means to measure

bond strength of the prefabricated spacer-concrete interface. Figure 7.6 summarises the experimental program for this chapter.

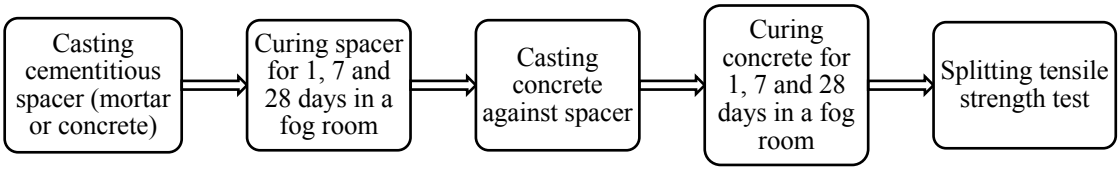

Figure 7.6 Flow chart summarising the sample preparation and testing methodology.

In order to cast the prefabricated spacer, a silicone sheet attached to a wooden block was inserted into the 100 mm diameter steel ring as shown in Figure 7.7. The dimension of the wooden block with silicone sheet was such that it fits the curvature of the steel ring and occupies exactly half of its volume. This is an important aspect of the mould assembly because it ensures that the resulting prefabricated spacer-concrete interface passes through the centre of the cylinder so that it is aligned to the loading direction during tensile splitting strength testing. The surface texture of the prefabricated spacer was varied by varying the texture of the silicone attachment. A range of silicone attachments with different surface textures, as explained in Section 7.2.2, was used. The wooden plate was tightly screwed on to the top of the mould assembly to prevent movements during concrete placement and compaction.

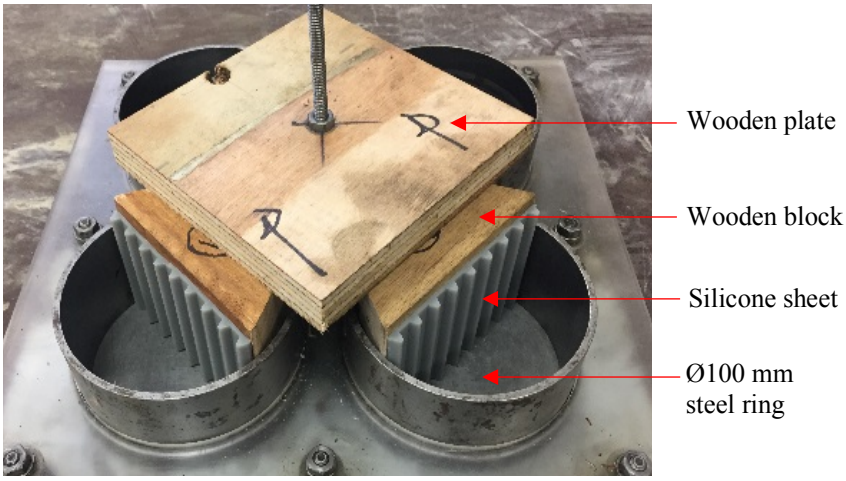

Figure 7.7 Mould assembly for preparing prefabricated spacers with modified surface texture.

The procedures for mixing the mortar and concrete are the same as before and are summarised here. The cement and aggregates were firstly dry mixed for 30 s in a 30-litre capacity pan mixer. The batch water premixed with the required amount of superplasticiser was then added, and wet mixing was carried out for a further 3 min. The fresh mortar and concrete mixes are shown in Figure 7.8.

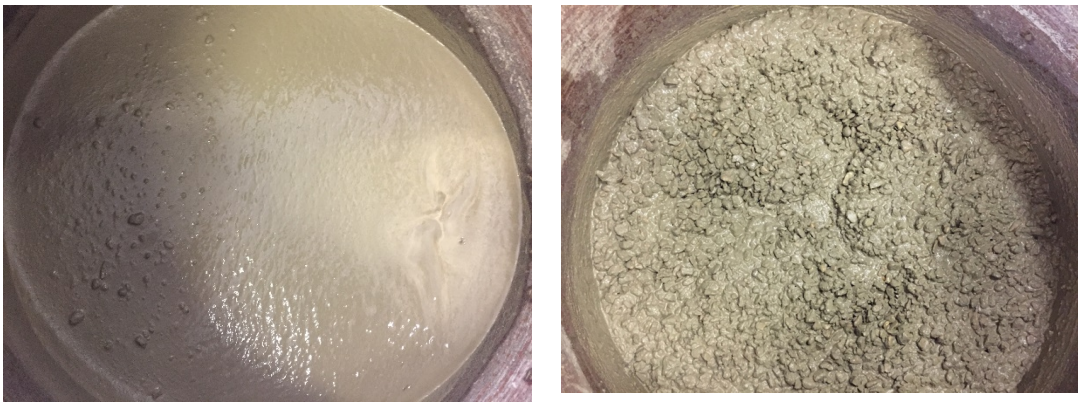

(a) Mortar mix (b) Concrete mix

Figure 7.8 Fresh mortar and concrete mixes.

A vibrating table with adjustable intensity was used for compaction. Samples were compacted in two equal-depth layers until air bubbles no longer rose to the surface. During compaction of the prefabricated spacers, the fresh mix flows over the silicone mould and fills the crevices to produce the desired texture as shown in Figure 7.9. As explained in Section 7.2.2, the textures are classified into two categories: concave or convex. Concave prefabricated spacers include half-sphere, pyramid, grooves-vertical, and grooves-horizontal, while the convex prefabricated spacers include square, rectangle-small, and rectangle-large.

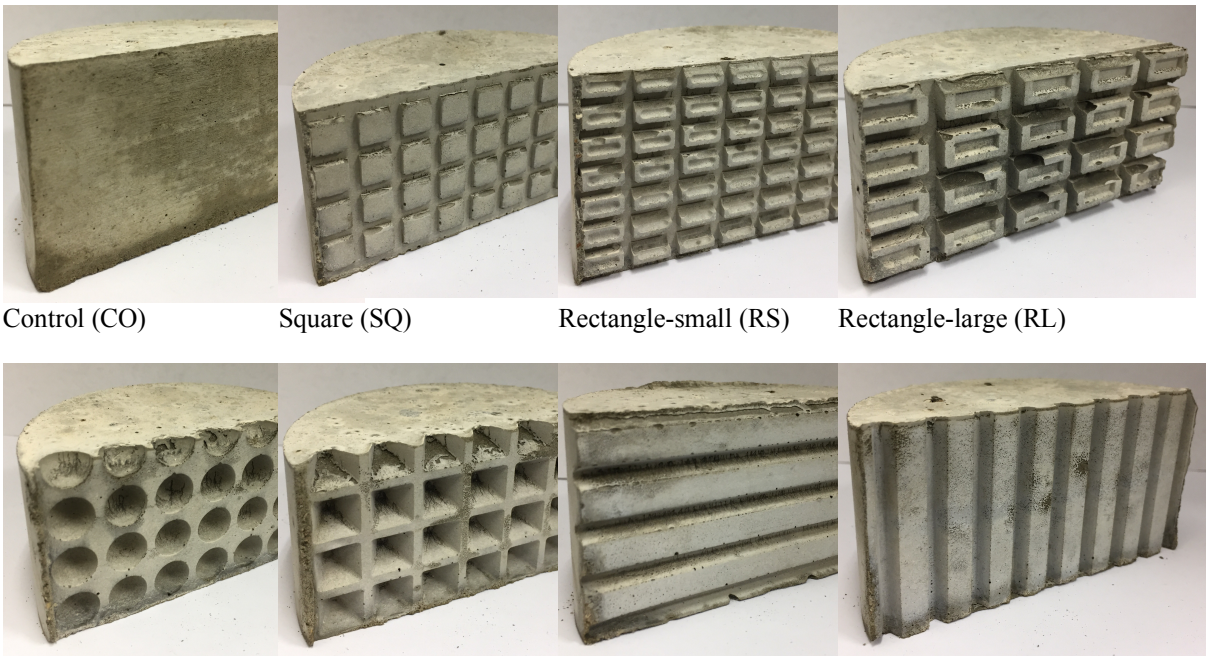

Control (CO) Square (SQ) Rectangle-small (RS) Rectangle-large (RL)

Half-sphere (HS) Pyramid (PY) Grooves-vertical (GV) Grooves-horizontal (GH)

Figure 7.9 Prefabricated cementitious spacers with various surface textures.

The cast spacers were then covered with a polyethylene sheet and wet hessian at room temperature for about 20 to 24 hr to minimise evaporation, then demoulded and transferred to a fog room at 100% RH, 21°C where curing continued for 1, 7 or 28 days. Subsequently, the prefabricated spacers were returned to the steel mould assembly (Figure 7.10a) and fresh concrete was cast against the prefabricated spacers (Figure 7.10b) following the same procedure as before. The composite half spacer-concrete samples were then cured in the fog room (100% RH, 21°C) for either 1, 7 or 28 days. Figure 7.11 show examples of the samples with different spacer-concrete interfacial texture.



(a) Half-spacers in steel mould assembly (b) Casting concrete against prefabricated spacers

Figure 7.10 Set-up for casting concrete against prefabricated spacers.

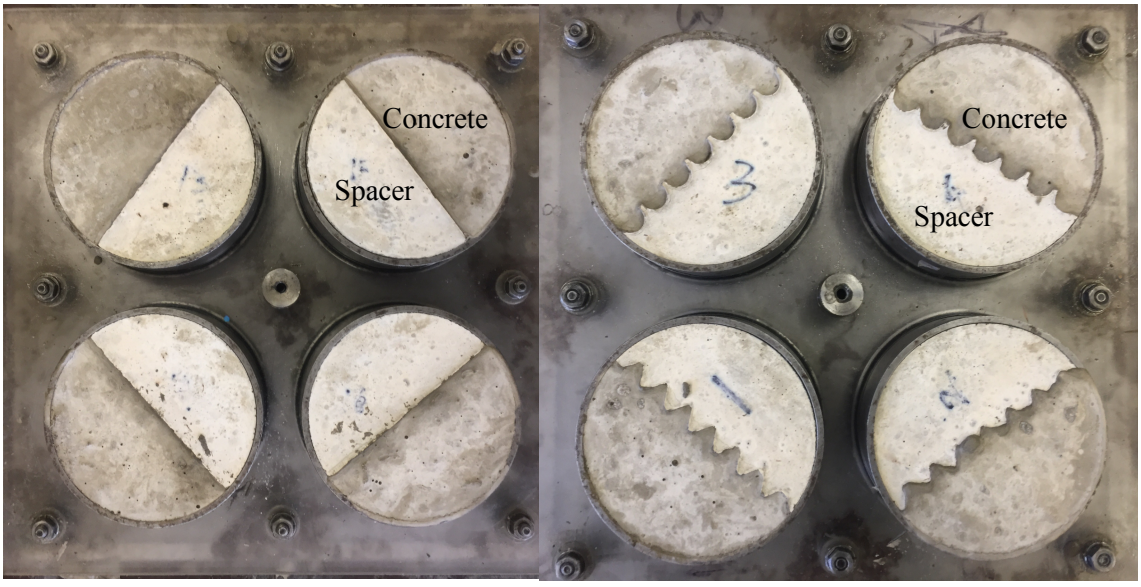

Figure 7.11 Example of prefabricated mortar spacer-concrete sample with different interface characteristics after 24hr of casting (Left: CO; right: HS).

7.2.4 Splitting tensile strength test

The splitting tensile test or indirect tensile test i.e. the Brazilian test conforming to the British Standard (BS EN 12390-6:2009) was carried out to determine the interface bond strength between a prefabricated spacer and concrete. Bond is defined as adhesion between one material against another, which includes chemical adhesion and mechanical interlocking. The tensile bond strength is defined as the unit stress required to separate one material from another material with which it is in contact with where the failure occurring at or near the bonded interface (ICRI, 2015). The splitting test was first proposed in 1943 by Akazawa for measuring the tensile strength of homogeneous cylindrical specimens as reported by Machida (1975). Raphael (1984) showed that the splitting test is easy to apply and gives a reliable estimate of the true tensile strength of concrete, compared to the direct tension and flexural tests. The test has also been applied to evaluate bond strength between cementitious materials. For example, Geissert et al. (1999), Espeche and Leon (2011) and Munoz et al. (2014) applied the splitting test to measure the bond strength of composite specimens consisting of a layer of repair material cast onto a layer of old concrete.

The test method is based on applying a compressive load perpendicularly to the axis of the cylindrical sample in order to induce a uniform tensile stress over the prefabricated spacer-concrete interfacial plane. The test setup is shown in Figures 7.12 and 7.13. Plywood strips (3 *x* 25 *x* 345 mm) were inserted between the specimen and the loading platen in order to avoid local compressive stress concentrations and ensure the sample remains centred when the load is first applied or to hold the two halves of the sample in place after cracking (Machida, 1975). Special care was also taken when positioning the sample so that the prefabricated spacer-concrete interface aligned with the applied load. To ensure the position of the sample, a straight line was drawn along the diameter before placing the sample in the column steel frame. Loading was applied at a constant rate of 0.03 MPa/s until failure as recommended in BS EN 12390-6:2000. Two replicates were tested, and the results were averaged. Tests were also measured on monolithic samples (no interface) of mortars and concretes as control. The mass of each sample was measured prior to testing and the values were used to calculate density.

Assuming a uniform tensile stress across the interfacial plane, the splitting tensile strength f_t can be calculated as:

$$f_t = \frac{2F}{\pi L d} \qquad \text{Eq. 7.3}$$

Where f_t is the tensile splitting strength (MPa), F is the maximum applied load (N), L is the length of the specimen (mm), and d is the diameter of the specimen (mm). The average length (L) and diameter (d) were used in calculating the bond strengths.

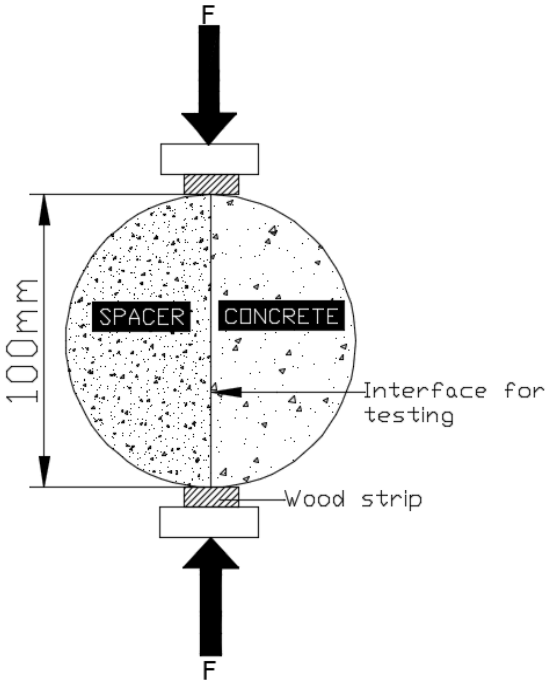

Figure 7.12 Schematic diagram of splitting tensile strength test for prefabricated spacer-concrete interface.

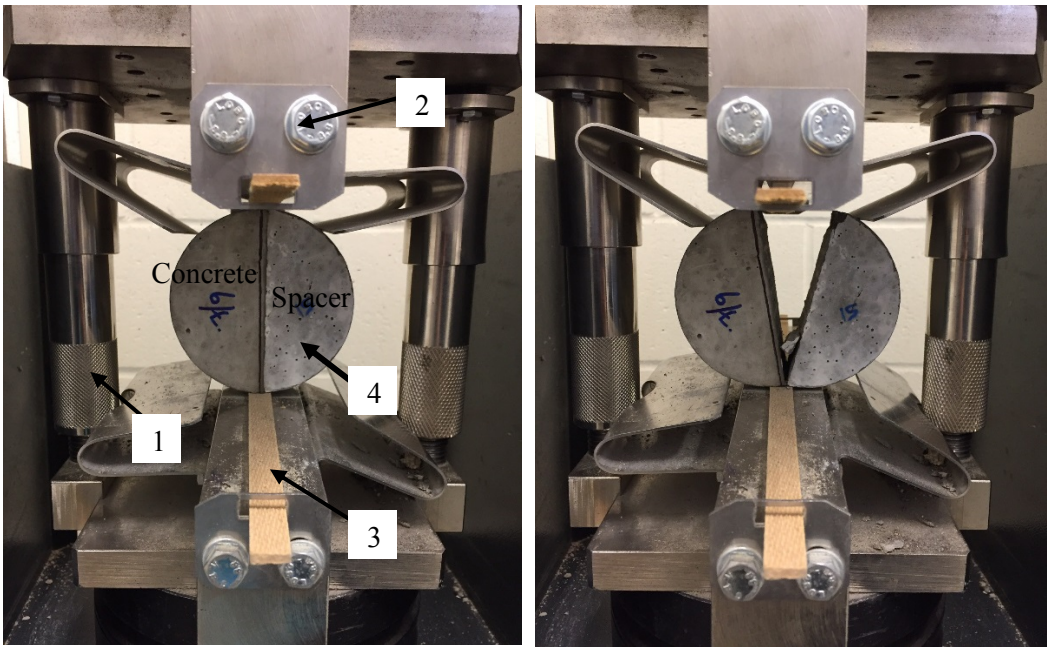

a) Sample under loading b) Split sample at the end of test

Notation: 1. Column steel frame; 2. Load beam; 3. Plywood strip; 4. Specimen.

Figure 7.13 Splitting tensile strength set-up.

7.3 Results

7.3.1 Prefabricated spacer properties

The measured density and 28-day compressive strength of the hardened mortar and concrete are listed in Table 7.6. Each result was obtained as the average value of three tested samples. It can be seen that the 28-day compressive strengths for both mixes are very similar because they have the same w/c ratio. The concrete mix has a slightly lower compressive strength due to the larger aggregate particle size used. Nevertheless, both mixes achieved strengths greater than 50 MPa, which meet the requirement for spacers as specified in BS 7973-1.

The measured density for both mixes is slightly higher than the expected theoretical density. The theoretical density was calculated by summing the weights of the mix ingredients per 1 m^3 volume. The theoretical density of mortar and concrete were 2356 kg/m^3 and 2409 kg/m^3 respectively. The density of each mix was measured and compared against its theoretical density in order to check that the samples were properly compacted.

Table 7.6 Density and compressive strength of prefabricated spacers.

	Density (kg/m^3)	Compressive strength at 28 days (MPa)
Prefabricated mortar spacer	2392 (8.28)	67.2 (1.44)
Prefabricated concrete spacer	2545 (2.06)	66.6 (0.34)

*Standard errors are shown in brackets.

Figure 7.14 shows the development of the splitting tensile strength of monolithic mortar and concrete samples (no interface) with curing age, calculated using Eq. 7.1. The results show that the splitting tensile strength increased with increasing curing age, however most of the strength gain occurred at early ages. Initially, the difference between the tensile strength of the mortar and concrete are significant, but this decreases with curing age. At 28 days, both mixes achieved the same tensile strength, ~ 5 MPa. The ratios of the splitting tensile strength to compressive strength of both mixes at the age of 28 days were also the same at approximately 8%.

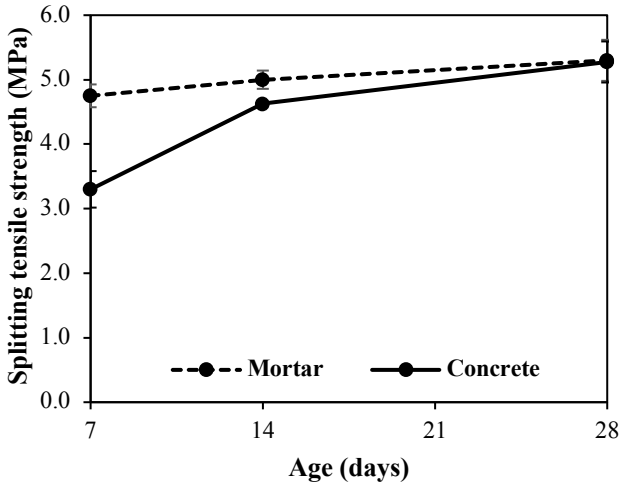

Figure 7.14 Splitting tensile strength of prefabricated mortar and concrete spacers.

7.3.2 Bond strength of spacer-concrete interface

Figure 7.15 and 7.16 illustrates the development of bond strength with curing age for the samples with prefabricated mortar or concrete spacers respectively. The results show that the bond strength increased with curing age as expected. The greatest increase in bond strength for all types of surface textures occurred between 1 and 7 days of curing. Beyond 7 days, the increase in bond strength was relatively small. At all ages, the control sample with a flat spacer consistently achieved the lowest bond strength. The use of textured spacers increased the bond strength relative to a flat spacer by up to 133%. Furthermore, samples with textured spacers showed a greater increase in bond strength with curing age as compared to the control with the average increase ranging between 33% and 88%.

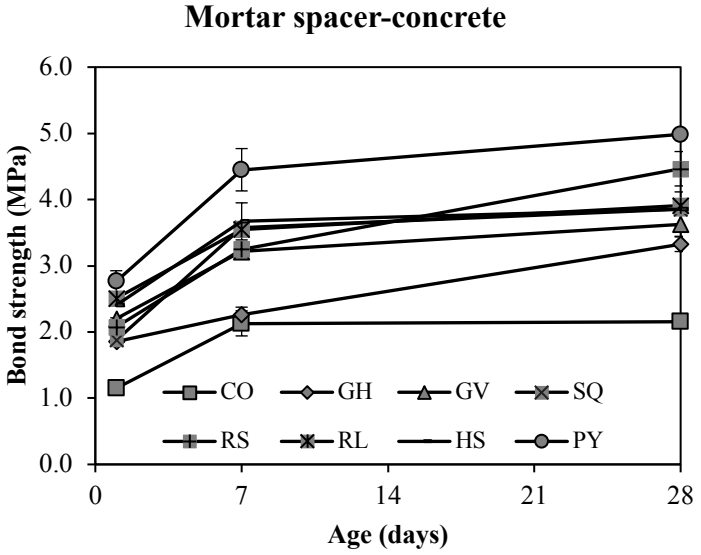

Figure 7.15 Development of prefabricated mortar spacer-concrete bond strength with age for various interface surface textures.

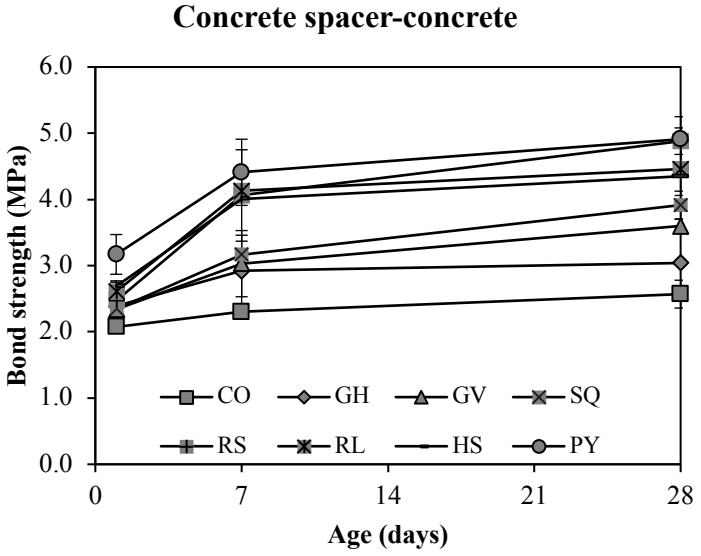

Figure 7.16 Development of prefabricated concrete spacer-concrete bond strength with age for various interface surface textures.

Apart from curing age, the interface bond between prefabricated spacer and concrete is expected to be dependent on the surface geometry and mechanical properties of both the prefabricated spacer and concrete. The results from this study are consistent with this expectation. For example, Figures 7.17 and 7.18 show the relationship between the interface bond strength and the spacer surface roughness and texture density, respectively. The results show that bond strength increased with increasing surface roughness and texture density. However, there were

some exceptions. For example, the rectangle-large (RL) texture has the highest roughness and density, but slightly lower bond strength compared to the sample with pyramid (PY) texture. This behaviour is likely to be due to the presence of air voids at the prefabricated spacer-concrete interface as shown in Figure 7.19. It can be seen that the prefabricated spacer-concrete interface with the RL texture contained more air voids than of the PY texture. This is in line with a well-established understanding that the strength of concrete is fundamentally a function of the volume of voids in it (Neville, 2011). The voids are due to air that is entrapped on the bottom of the convex textures due incomplete filling or compaction. The amount of air voids that occurred at the interface will be presented in Chapter 8.3.

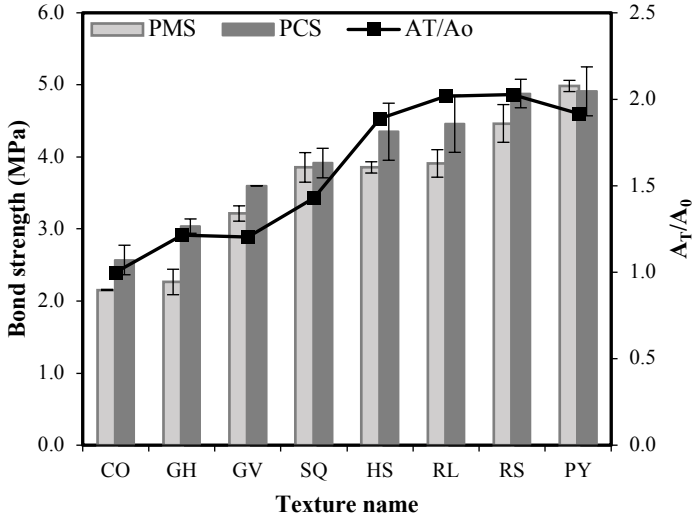

Figure 7.17 Relationship between bond strength and surface roughness (Cured for 28d).

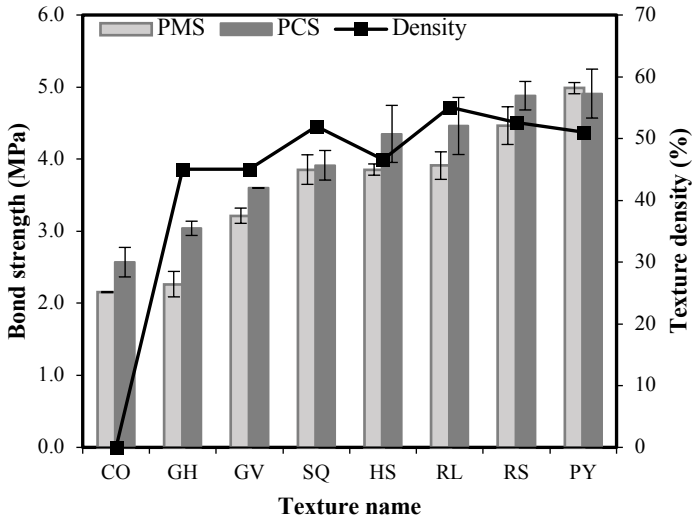

Figure 7.18 Relationship between bond strength and texture density (samples were cured for 28d).



Figure 7.19 Entrapped air voids (circled) at the prefabricated spacer-concrete interface (Top: RL texture; Bottom: PY texture).

Figure 7.20 shows the correlation between the surface profile depth and bond strength. It is interesting to note that in contrast to surface roughness, the surface profile depth does not seem to have a consistent influence on bond strength. For example, the sample with rectangle-small (RS) texture with a depth of only 3 mm showed a similar bond strength to that of the sample with pyramid (PY) texture that has a three times higher profile depth. It is also interesting to note that although the horizontal (GH) and vertical groove (GV) textures have the same surface roughness and profile depth, the latter produced a slightly higher bond strength. This is due to the orientation of the GV-texture being perpendicular to the loading direction as shown in Figure 7.21. It is also worth noting that the GV-texture displayed more fracturing compared to GH-texture (mainly debonding).

Furthermore, Figure 7.20 also shows a comparison of the bond strength between the prefabricated spacer made of mortar (PMS) and concrete (PCS) cured for 28 days. The results indicated that the samples with prefabricated mortar spacers have similar strength levels to samples with prefabricated concrete spacers of the same textures. This is probably due to both

prefabricated mortar and prefabricated concrete spacers having similar compressive strength as shown in Table 7.6. The comparison of the bond strength between prefabricated mortar and prefabricated concrete spacers cured for 1 and 7 days can be seen in Appendix I.

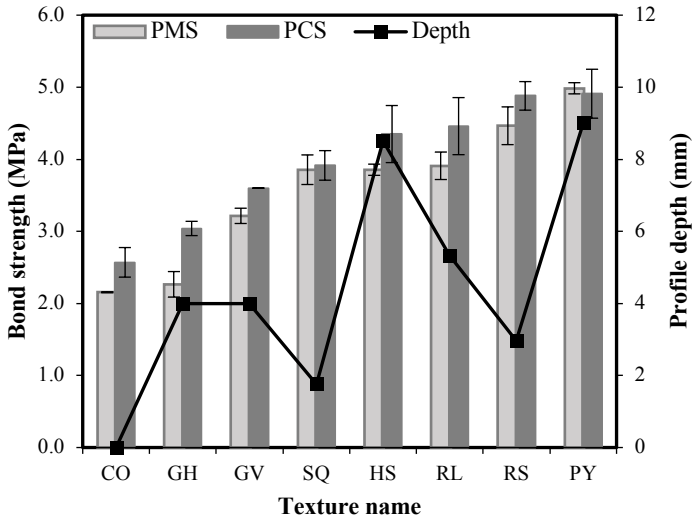

Figure 7.20 Relationship between bond strength and profile depth. (Samples were cured for 28d).

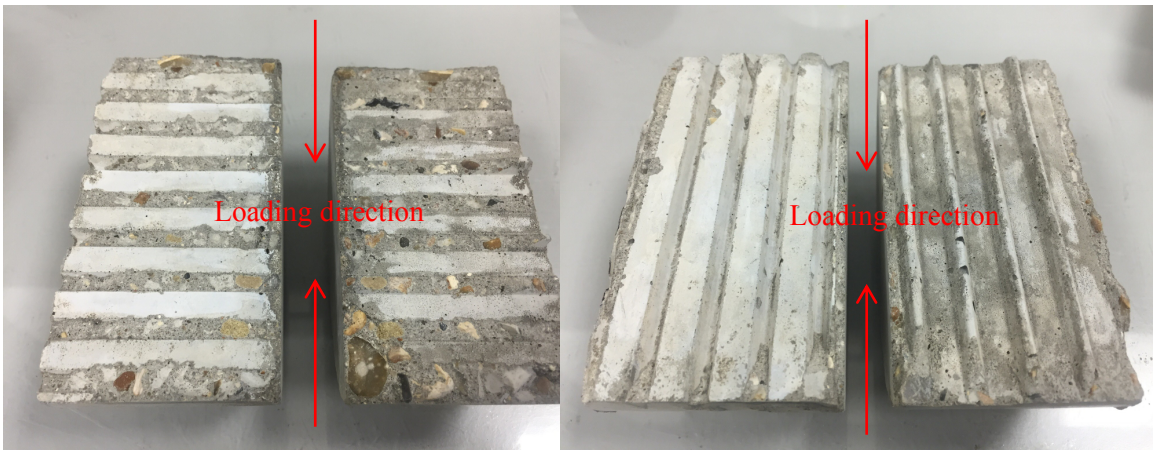

(a) GV texture (b) GH texture

Figure 7.21 The direction of the grooves on the GV and GH textures relative to loading direction has an effect on failure mode and bond strength.

7.3.3 Relationship between curing ages, surface parameters and interface bond strength

An interesting trend is observed when the measured surface parameters are plotted against the measured bond strength with different curing ages. This is shown in Figures 7.22 and 7.23 for surface roughness, texture density and profile depth. All the trends showed a linear relationship between the surface parameters and the bond strength. In general, the results show that increasing the surface roughness, texture density and profile depth of the prefabricated spacer, lead to increases in the bond strength between the prefabricated spacer and concrete. Furthermore, it is worth noting that the effect of surface texture is more substantial when the samples were cured longer.

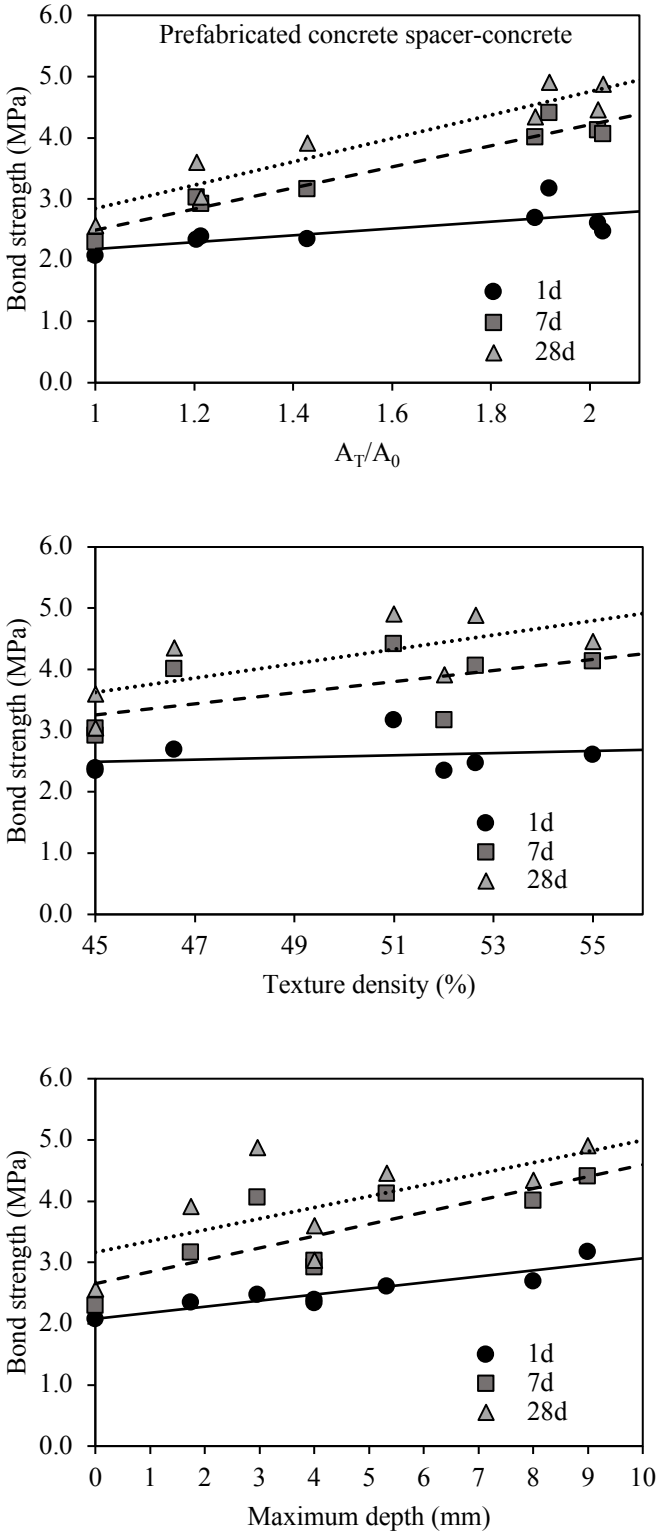

Figure 7.22 Relationship between surface texture parameters, curing ages and interface bond strength of samples with prefabricated concrete spacer.

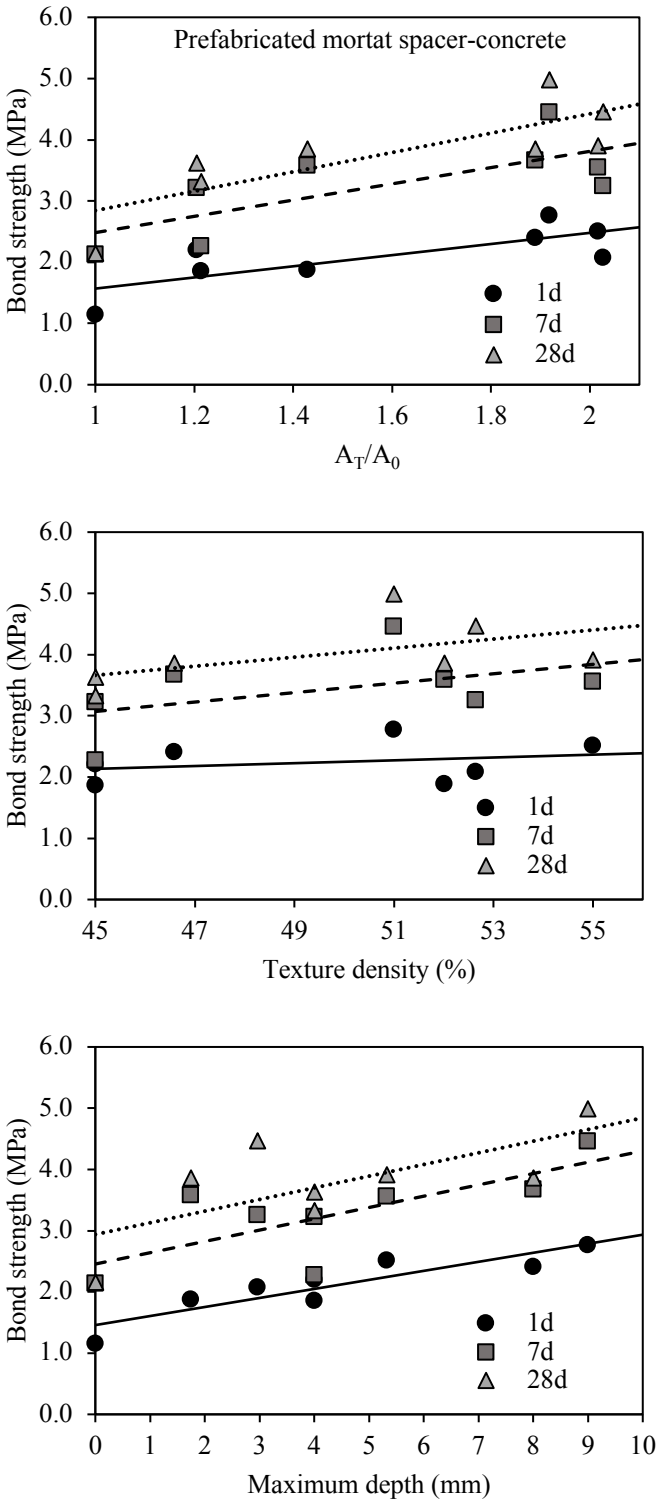

Figure 7.23 Relationship between surface texture parameters, curing ages and interface bond strength of samples with prefabricated mortar spacer.

7.3.4 Failure mode of prefabricated spacer-concrete interface

Three types of failure modes were observed on the samples following tensile splitting testing: interface debonding (ID), a combination of ID and fracturing of the prefabricated spacer (FS) and the combination of ID and fracturing of the concrete (FC) as illustrated in Figure 7.24. Debonding occurs when the prefabricated spacer-concrete interface shows a clean separation without any major damage to either the surface of the prefabricated spacer or concrete. In contrast, failure by fracturing occurs when the interface separates through cracking of the prefabricated spacer or concrete. Most samples fail through a combination of interface debonding and fracturing, as shown in Figure 7.25. The type of failure mode depends on the types of prefabricated spacer texture, concave or convex as described in section 7.2.3. The convex spacers experienced a combination of ID and FS while the concave spacers failed through a combination of ID and FC. It is suspected that the relative amount of debonding or fracturing can be related to interface bond strength.

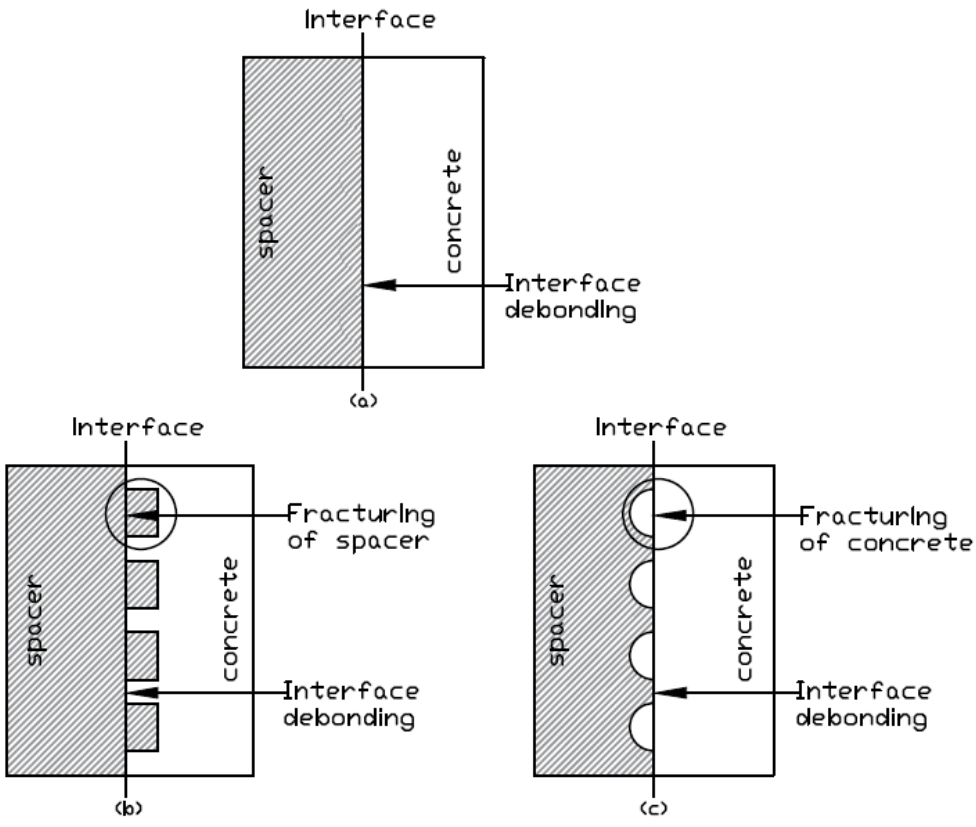

Figure 7.24 Schematic of failure mode at the prefabricated spacer-concrete interface: (a) ID only; (b) ID and FS; (c) ID and FC.

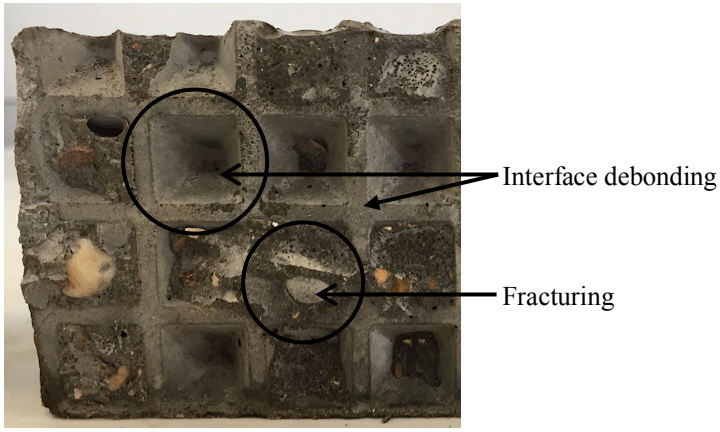

Figure 7.25 Example of a split prefabricated spacer-concrete interface showing failure by combined debonding and fracturing.

Typical interface failures of samples without or with textured spacers are clearly presented in Figures 7.26 to 7.28. Figure 7.26 shows the typical interface failure of the control sample (CO). It is observed that prefabricated spacer-concrete interfaces that are flat failed mainly through debonding. In contrast, samples with textured spacers failed via a combination of interface debonding and fracturing of the prefabricated spacer or concrete. Figure 7.27 shows the differences in the failure modes of the samples containing a prefabricated spacer with square texture (SQ) with increasing curing age. It can be seen that the fraction of debonding failure decreased with increasing curing age from 1 to 28 days, and this correlates with an increase in bond strength. For example, the fraction of debonding failure for samples with SQ texture at 1d, 7d and 28d was 84%, 69% and 49% respectively. This was obtained by measuring the debonding area and dividing it by the total sample cross-sectional area using ImageJ. However, the control samples (flat interface) showed only debonding failures (100%) regardless of the curing age. All failure modes of samples with different surface textures and curing ages are presented in Appendix II.



Figure 7.26 Typical failure (interface debonding) at the prefabricated spacer-concrete interface for the control sample (flat interface).

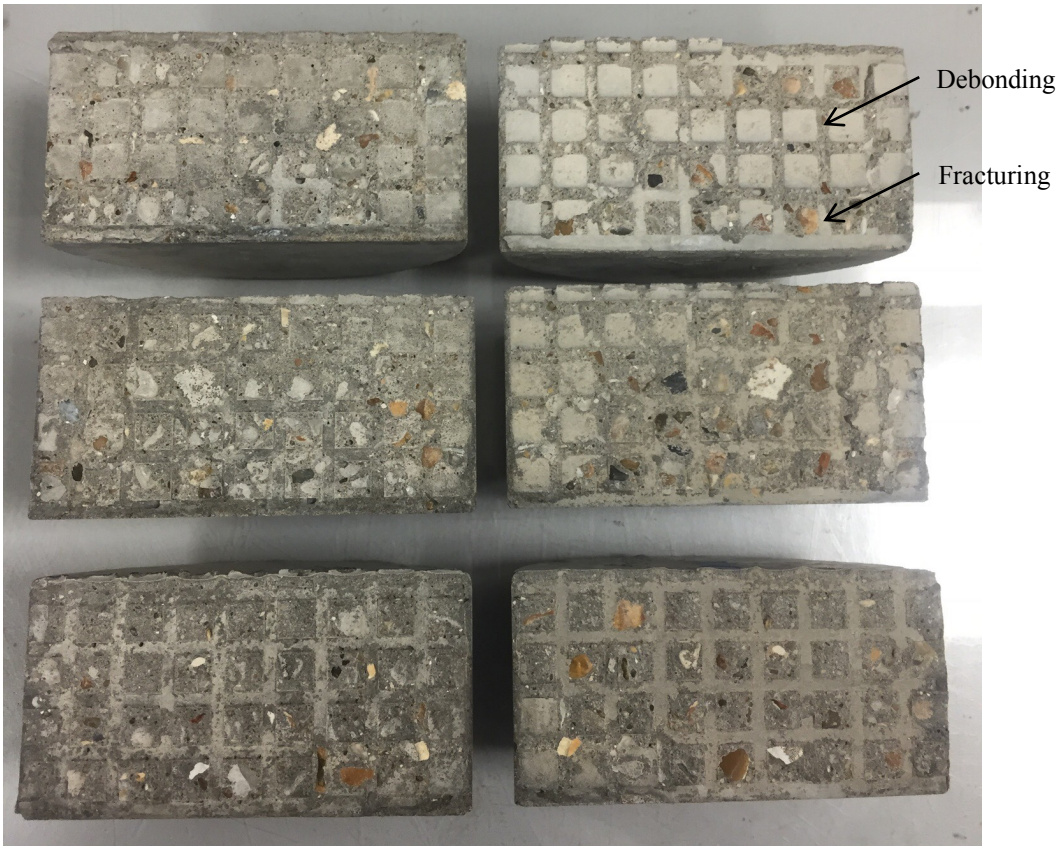

Figure 7.27 Typical failure at the prefabricated spacer-concrete interface after curing for 1d (top), 7d (middle), and 28d (bottom). Sample contains prefabricated spacer with square texture (SQ).

The failure mode and the maximum-recorded load for all samples are presented in Table 7.7. The results show that the failure load for samples with textured spacers increased by up to 140%, 109%, and 133% at 1, 7 and 28 days respectively, compared to those of the flat spacer. In other words, the presence of surface texture can drastically increase the failure load, especially for a

longer curing age, when compared to the control sample without texturing. It is worth noting that there is no difference in the failure mode between the samples with a prefabricated mortar spacer and samples with prefabricated concrete spacer as shown in Figure 7.28. The results suggest that the mix composition of the prefabricated spacer tested in this study did not affect the failure mode.

Table 7.7 Splitting tensile test results.

Texture type (abbreviation)	Prefabricated mortar spacer				Prefabricated concrete spacer			
	Failure mode	Failure load (kN)			Failure mode	Failure load (kN)		
	28d	1d	7d	28d	28d	1d	7d	28d
Control with flat surface (CO)	ID	9.1 (0.03)	16.8 (0.19)	17 (0.01)	ID	16.3 (0.04)	18.1 (0.11)	20.2 (0.21)
Grooves-horizontal (GH)	ID and FC	14.6 (0.06)	26.2 (0.11)	17.8 (0.11)	ID and FC	18.8 (0.17)	22.9 (0.54)	23.9 (0.00)
Grooves-vertical (GV)	ID and FC	17.3 (0.14)	28.5 (0.11)	25.3 (0.18)	ID and FC	18.4 (0.27)	23.8 (0.50)	28.3 (0.10)
Square (SQ)	ID and FS	14.7 (0.11)	28.1 (0.30)	29.1 (0.21)	ID and FC	18.4 (0.04)	24.9 (0.08)	30.8 (0.21)
Half sphere (HS)	ID and FC	18.9 (0.15)	28.8 (0.28)	30.3 (0.08)	ID and FC	21.1 (0.20)	31.5 (0.52)	34.2 (0.40)
Rectangle-large (RL)	ID and FS	19.7 (0.01)	27.9 (0.39)	30.7 (0.13)	ID and FC	20.5 (0.01)	32.5 (0.08)	35.0 (0.40)
Rectangle-small (RS)	ID and FS	16.3 (0.02)	25.5 (0.07)	35.1 (0.26)	ID and FC	19.4 (0.30)	31.9 (0.69)	38.3 (0.20)
Pyramid (PY)	ID and FC	21.7 (0.16)	34.9 (0.32)	38.6 (0.08)	ID and FC	24.9 (0.59)	34.6 (0.50)	38.6 (0.34)

*Brackets shown standard errors



(a)

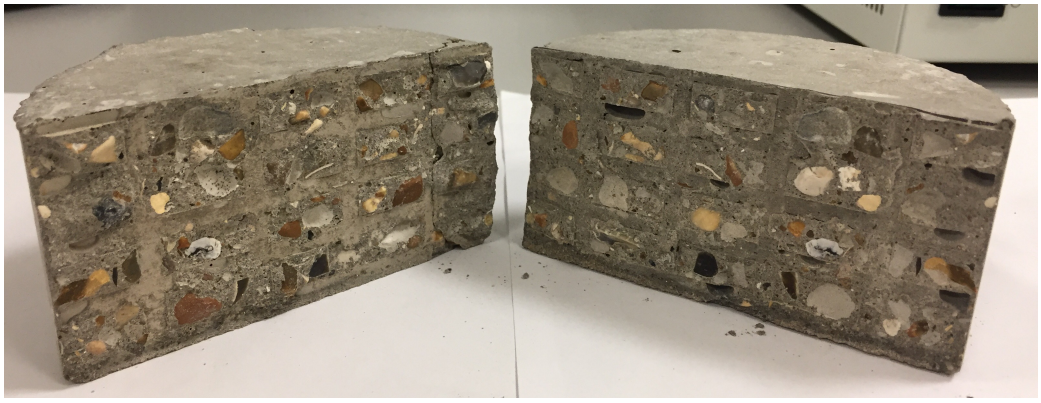

(b)

Figure 7.28 Comparison of failure interface between (a) Prefabricated mortar spacer-concrete and (b) Prefabricated concrete spacer-concrete.

7.4 Discussion

A total of 210 samples were cast to evaluate the interface bond strength and failure mode between the prefabricated spacer and concrete. Overall, the results indicate that the bond strength increased with increasing surface roughness, texture density and profile depth. Observations of the split samples consistently showed that the control samples with flat spacer-concrete interfaces failed through debonding, while samples with textured interfaces experienced a combination of interface debonding and fracturing of the prefabricated spacer or concrete. For samples with textured spacers, the concrete flows into and fills the crevices of the texture. When hardened, this forms a mechanical interlock that enhances bond strength.

It is interesting to observe that the curing age has a substantial effect on both the interface bond strength and failure mode. In other words, the effectiveness of the mechanical interlock increases with curing age as the prefabricated spacer and concrete gains strength. Therefore, the

failure mode at the prefabricated spacer-concrete interface changes from predominantly debonding at early ages to predominantly fracturing at later ages as presented in Figure 7.26. This is accompanied with substantial gains in the measured bond strength as shown in Figures 7.15 and 7.16. The longer the sample is cured, the smaller the debonded area and the higher the interface bond strength. In contrast, such mechanical interlocking does not occur for the case of flat spacer-concrete interfaces. Instead, the bond is transferred mainly through friction or via a small amount of chemical adhesion between the prefabricated spacer and concrete. This is relatively weak and therefore, failure occurs through debonding only resulting in a low measured bond strength. In contrast, the mix proportion of the prefabricated spacer (i.e. mortar or concrete) showed an insignificant contribution to the failure mode or bond strength as can be seen in Figure 7.17 and 7.27, at least for the two mixes investigated in this study. This is probably because both the mortar and concrete have a similar compressive and tensile splitting strength.

The observed beneficial effect of surface texture on the interface bond strength between prefabricated spacer and concrete seems consistent with the findings from some studies in other applications. In the field of structural repair for example, studies have investigated the effect of surface roughness on the bond strength between a substrate and repair concrete. For example, Julio et al. (2004) observed the effect of different surface treatments (wire-brushing, sand-blasting, and chipping with a light jackhammer) on the bond strength between two concrete layers by performing a slant shear test. Parameters such as the mix composition of the concrete substrate and repair concrete, and curing age were kept constant. The results showed that sand-blasting was the best surface treatment for improving the interface bond strength followed by wire brushing and chipping. However, the degree of surface roughness was not quantified. Garbacz et al. (2004) also investigated the effect of surface treatments (e.g. grinding, shotblasting, hand- and mechanical milling) on the bond strength between substrate concrete and repair mortar by performing a pull-off strength test. The results showed that the roughness of concrete substrate influences bond strength. However, they also reported that the treatments (in particular shotblasting and milling) were found to produce voids and microcracks at the surface layer.

Beushausen and Alexander (2008) investigated the failure mode between substrate concrete and overlay concrete. The substrate concrete was cured for 8 months in water at 23°C, while the overlay was moist cured for 7 days. The substrate concrete was notched with a dimension of 40 mm width crest, 30 mm width bottom and 10 mm depth. The results showed that the sample experienced a mixed mode of failure (interface and concrete failures). Santos and Julio (2011) applied four surface treatments (wire-brushing, sandblasting, shotblasting and hand-scrubbing)

to the substrate concrete prior to casting new concrete. The samples were cured for 28, 56 and 84 days. The results showed that shear strength increased with increasing age difference between substrate concrete and the added concrete layer for all different surface treatments.

To conclude, the surface texture of the prefabricated spacers can enhance bond strength and minimise debonding by promoting mechanical interlocking with the concrete. This finding seems to agree with the study reported by Courard (2000), which indicated that mechanical interlocking is the dominant factor for bonding between substrate and repair concrete. Giaccio and Zerbino (1998) also reported that mechanical interlocking between matrix and aggregates is the main parameter affecting bond performance. The overall strength of the prefabricated spacer-concrete interface is dependent on the surface area, shape, and orientation of the spacer surface texture, which is in line with the parameters affecting the tribological performance as reviewed in Section 7.1.

7.5 Conclusions

The study showed that the surface texture of the prefabricated spacer has a clear effect on its interlocking with concrete and this can lead to a significant improvement in the bond strength of the prefabricated spacer-concrete interface. The magnitude of the prefabricated spacer-concrete interface bond strength varies depending on the geometry, shape and orientation of the spacer surface texture. Samples with a higher bond strength showed a greater amount of fracturing and smaller amount of debonding failure at the interface. However, incomplete compaction and the presence of air voids at the prefabricated spacer-concrete interface was found to be slightly detrimental to the interface bond strength.

Chapter 8

Influence of spacer surface texture on transport properties

Chapter 7 showed that a simple modification to the texture of the prefabricated spacer surface can produce a significant change to the failure mode of the prefabricated spacer-concrete interface resulting in substantial gain in bond strength. The stronger spacer-concrete interface should be more resistant to cracking and therefore penetration of aggressive species. However, this needs to be verified. In this chapter, the effects of spacer surface texture on mass transport properties including oxygen diffusivity, oxygen permeability, water sorptivity, and fluorescence epoxy impregnation were investigated. Half spacer-concrete composite samples of various surface textures were prepared and cured for seven days at 100% RH, 21°C and then conditioned at 50°C to reach a constant mass prior to testing. The results showed that certain surface textures decreased mass transport properties while others had a less clear effect. A potential factor affecting the results is the incidence of air voids at the interface between the prefabricated spacer and concrete.

8.1 Introduction

The transport of liquids and gases into concrete are directly related to concrete durability (Neville, 2011), where the main transport mechanisms including diffusion, permeation and absorption. It is well known that interfaces can contribute to increasing the transport properties of concrete (Ping et al., 1991, Breton et al., 1992b, Wong et al., 2009). Most of the research on mass transport properties of cementitious materials have been carried out on plain mortars or concretes without steel reinforcement or spacers embedded. However, as discussed in Chapters 4, 5, and 6, the presence of spacers in reinforced concrete can provide a path for aggressive agents penetrating into concrete thus leading to an increase in transport properties and rate of deterioration.

The main factors that contribute to a porous spacer-concrete interface are the shrinkage of the concrete as a result of drying and the relative volumetric changes that occur between the spacer and concrete when subjected to temperature variations. This produces microcracking along the spacer-concrete interface as explained in the previous chapters when tensile stresses induced relative movement exceed the local strength at the interface. Desnerck et al. (2015) also revealed that the

cracks are inherent in reinforced concrete structures because of their relatively low tensile strength of concrete. Enhancing the prefabricated spacer-concrete bond strength using spacers with textured surfaces as demonstrated in the previous chapter is expected to reduce the risk of microcracking. However, it is not clear to what extent the enhanced bond strength will be able to mitigate this problem. Therefore, an attempt was made to further understand how prefabricated spacers with textured surfaces influence the mass transport of concrete after drying. These are the issues that this chapter seeks to redress.

In this study, both the prefabricated spacer and concrete were made using the same mix proportions at a water-cement ratio of 0.4 following the approach described in Chapter 7 in order to maintain consistent properties and enable comparison. Samples were cured for seven days in a fog room at 100% RH, 21°C and then dried at 50°C to a constant mass prior to testing via oxygen diffusion, oxygen permeation, water absorption, and fluorescence epoxy impregnation. The measured transport properties were then correlated to the surface texture characteristics of the prefabricated spacer and the measured bond strength.

8.2 Experimental

8.2.1 Materials and mixture proportions

The prefabricated cementitious spacer and concrete were prepared with the same materials and mix proportions as in Chapter 7. The mix contained ordinary Portland cement CEM I with a specific gravity of 3.15 at water-cement ratio (w/c) of 0.4, total aggregate content of 70% volume, and sand to total aggregate content ratio of 0.4. The mix achieved a 28-day compressive strength of 66.6 MPa, which conforms to the requirements of BS 7973-1:2001. The Portland cement used complies with BS EN 197-1:2011 CEM I. The aggregates were Thames Valley gravel (<10 mm) and sand (<5 mm) complying with BS EN 12620:2002 medium grading. The mix proportions of the concrete calculated using an absolute volume method is shown in Table 1.

Table 8.1 Mix proportion for the prefabricated spacer and concrete used in this chapter.

W/C ratio	CEM I (kg/m^3)	Water (kg/m^3)	Sand (kg/m^3)	Gravel (kg/m^3)
0.4	418	167	728	1092

8.2.2 Sample preparation

Cylindrical samples were prepared in steel moulds of 100 mm diameter and 50 mm height containing half-spacer and half-concrete. Details of the sample preparation are given in Chapter 7.2 and are summarised here. Casting and curing were carried out in two stages. The first half of the cylindrical sample was cast to represent the prefabricated spacer. Prefabricated spacers with eight different textures were prepared by using textured silicone sheets inserted into the steel moulds before casting the prefabricated spacers (see Figure 7.10). The prefabricated spacers were cured for 7 days in a fog room at 100% RH, 21°C. Subsequently, the second half of the cylindrical sample was then cast against the prefabricated spacer using the same concrete mix to produce a composite sample with a prefabricated spacer-concrete interface. The samples were also cured in a fog room for 7 days. A 7-day curing was selected because this was found to be sufficient to achieve a good level of bond strength (see Figure 7.16).

Finally, the cured sample as shown in Figure 8.1 was conditioned at 50°C, 10% RH to obtain a constant mass prior to transport testing. This relatively severe drying regime was used to simulate hot weather conditions. The sample mass was monitored throughout the conditioning using an electronic balance accurate to 0.01g. Figure 8.2 shows an example of the mass loss curve. Samples were assumed to have reached equilibrium when the mass loss was no more than 0.01% per day and this required about 3.5 months. The purpose of conditioning to equilibrium is to ensure that the measured transport properties are not influenced by a variation in initial moisture content. Dried samples were cooled to room temperature in a vacuum desiccator for 24 h to prevent moisture from re-entering the samples during cooling prior to testing.

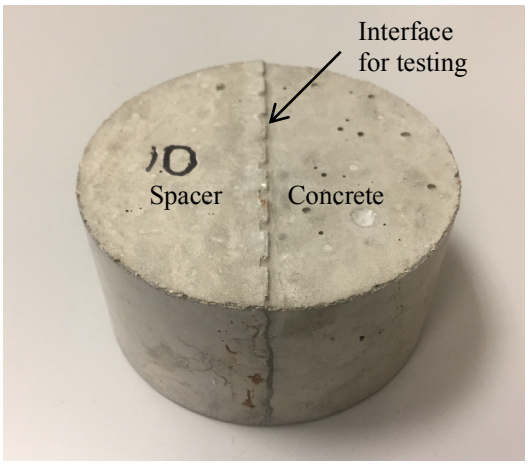

Figure 8.1 Cured cylindrical sample containing half-prefabricated spacer and half-concrete.

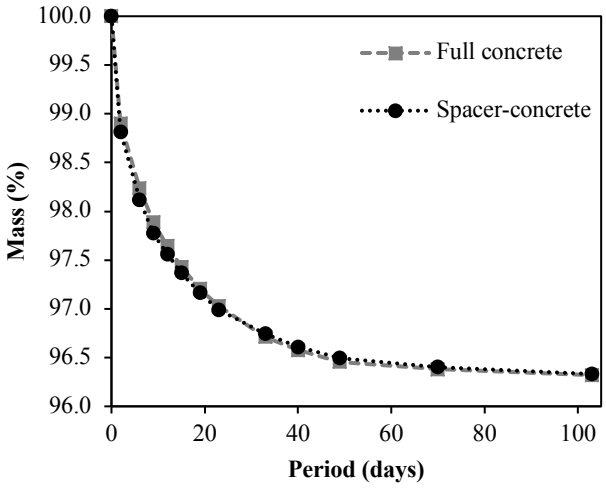

Figure 8.2 Change in mass of samples subjected to 50°C.

8.2.3 Transport measurements

The conditioned samples were tested following the sequence of oxygen diffusivity, oxygen permeability and water sorptivity using two replicates. The same sample can be used for all three tests because the results of each test are not influenced by the previous test. Full details of the tests are given in Chapter 3 and summarised here.

Oxygen diffusivity and oxygen permeability were measured by placing the sample in a test cell and applying 15kN compression to the surrounding silicone rubber ring to seal the sample to prevent side leakage. To determine oxygen diffusivity, opposite faces of the sample were exposed to oxygen and nitrogen gases at the same pressure, which diffused in opposite directions through the sample. A zirconia analyser was used to measure the oxygen concentration in the outflow stream. To determine oxygen permeability, steady-state outflow rates were measured for three input gas pressures of 0.5, 1.5 and 2.5 bars above atmospheric. Permeability at each pressure was calculated by applying Darcy's law for compressible fluids, and the intrinsic permeability was determined by applying Klinkenberg's correction for gas slippage. The recorded mass of the samples before and after both tests showed negligible change. Water sorptivity was measured by placing the sample in tray containing water to a depth of about 3 mm above the bottom surface of the sample, and then measuring the mass gain with time until saturation was achieved. The sorptivity coefficient ($g/m^2min^{0.5}$) was determined from the slope of the regression line of absorbed water per unit flow area against the square root of time ($R^2 > 0.99$) according to classical unsaturated flow theory. The test cell with a prefabricated spacer-concrete sample inside is shown in Figure 8.3.

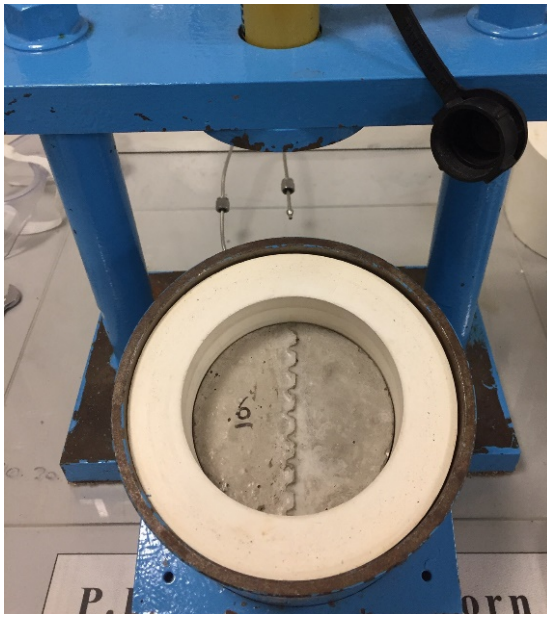

Figure 8.3 Transport test cell showing a sample with textured spacer-concrete interface.

Samples from the sorptivity test were then vacuum saturated in water for 3.5 hours until no significant air bubbles appeared on the surface. Then, the vacuum was released, and the saturated sample was weighed to measure the accessible porosity φ, which is the volume fraction of pores and cracks that have been filled with water. This was estimated from the mass difference between the vacuum saturated stated m_{SSD} and preconditioned state m_D (after conditioning stage at 50ºC), divided by the sample volume V. The density of water ρ_w was taken to be 1 g/cm^3.

Another transport property investigated in this study was fluorescent epoxy impregnation. The sample was pressure-impregnated with low-viscosity fluorescein-dyed epoxy. The cross-section of the sample was then examined to measure the depth of the intruded epoxy. The sample was placed in a cell similar to the one used for oxygen diffusion and permeation testing. The epoxy mix was poured onto the sample top surface and a 10bar air pressure was applied and maintained overnight to force the epoxy into the sample. Finally, the impregnated sample was cured at room temperature for 2 days to allow proper hardening of the epoxy prior to sectioning for imaging to determine the depth of fluorescent epoxy impregnation along the prefabricated spacer-concrete interface. Images were captured using a Sony Alpha NEX-3N mirrorless digital camera kitted with an E16 mm focal length in a dark room under a 15W ultraviolet lamp operating at ~50 Hz to induce fluorescence.

8.3 Results and discussion

8.3.1 Oxygen diffusivity, oxygen permeability, and water sorptivity

The measured oxygen permeability, oxygen diffusivity, and water sorptivity of samples with the different prefabricated spacer-concrete interfaces are presented in Figure 8.4. Each data point represents the average of two replicate samples, and the error bar indicates the standard error $\sigma/\sqrt{n}$, where σ is the standard deviation and n is the number of replicates. The results clearly show that prefabricated spacers with surface texture can substantially reduce the permeability by up to 69% compared to the control. This is likely to be due to an improved interface bond strength between textured spacers with concrete (See Figure 7.16) causing less microcracking to occur when dried. The results showed that permeability was most sensitive to changes to the microstructure at the prefabricated spacer-concrete interface. This is also in line with well-established findings from previous studies showing that permeability is much more sensitive to the presence of microcracking compared to other transport properties such as diffusivity and absorption (Wu et al., 2015, Abyaneh et al., 2016). This is because the permeation depends on the crack width, while diffusion and capillary absorption are more dependent on the total accessible porosity, which is not significantly increased by the microcracks (Aldea et al., 1999).

However, surface texture of prefabricated spacer does not appear to have a consistent influence on other mass transport properties such as diffusion or absorption. In some cases, textured spacers produce lower transport coefficients, while in others, the presence of textured spacers appears to increase transport properties relative to the control. Nevertheless, the difference between textured spacers and the control for these properties are small and insignificant. This can be clearly seen in Figure 8.5 when all the transport data are normalised to the control (flat surface).

It is interesting to note that the sample with pyramid (PY) texture showed the lowest transport coefficients for all transport tests. The measured diffusivity, permeability and sorptivity for the sample with PY texture decreased by about 6.6%, 69% and 4% respectively, compared to the control sample. This result is consistent with the splitting tensile strength result showing the highest bond strength for this particular sample. It is also interesting to note that the vertical grooves (GV) texture consistently produced the highest transport properties, especially for permeability. This behaviour was likely caused by the direction of the grooves being parallel to the flow of gas/water as shown in Figure 8.6.

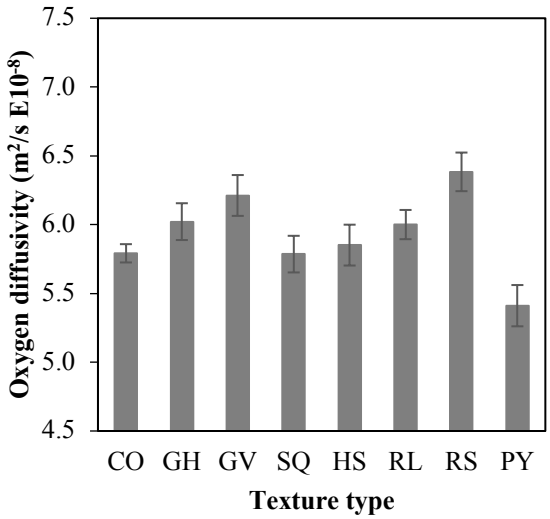

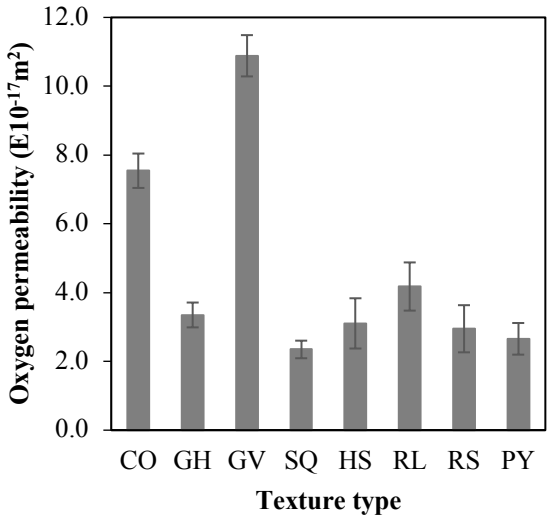

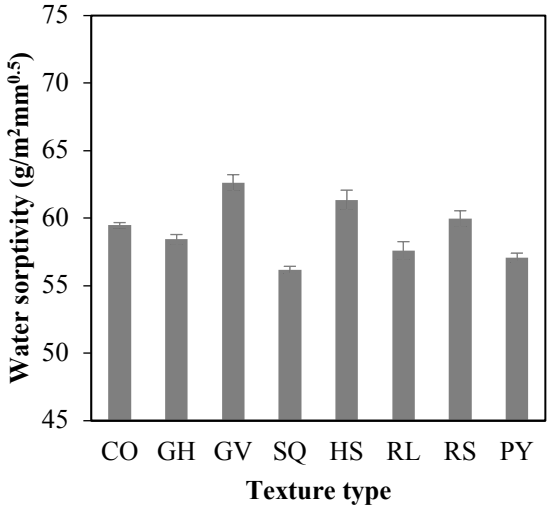

Figure 8.4 Effect of spacer surface texture on mass transport properties of samples after drying at 50°C

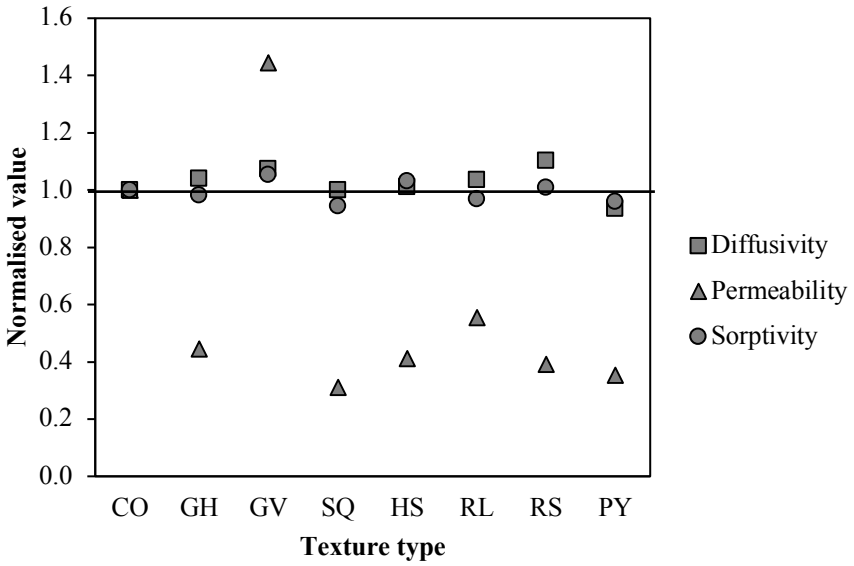

Figure 8.5 **Normalised oxygen diffusivity, oxygen permeability and water sorptivity showing the substantial reduction in permeability for samples with textured spacers.**

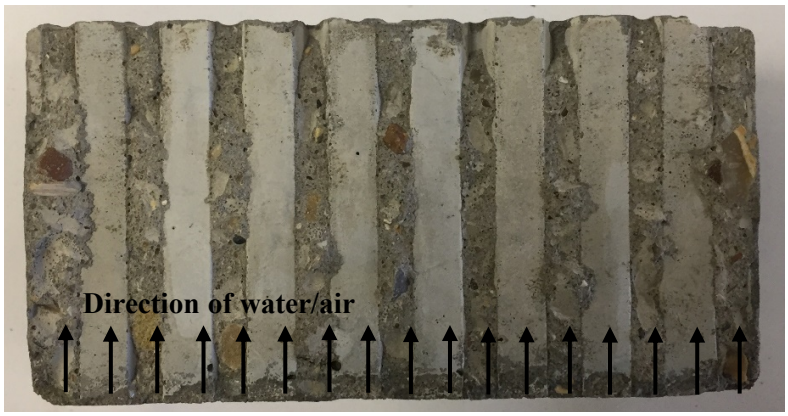

Figure 8.6 **Sample with GV texture showing groves parallel to the flow direction of gas/water during transport testing.**

Furthermore, it was surprising that surface defects in the form of air voids were observed at the prefabricated spacer-concrete interface (Figure 8.7). Most of the voids occurred underneath the texture, where air is most likely to become entrapped during concrete placement and compaction. Therefore, it is believed that these voids were formed during concrete compaction when rising air bubbles along the prefabricated spacer surface become blocked or entrapped beneath the surface texture. The size of the voids ranged from 0.3 to 5.5 mm and they have an elongated shape consistent with the formation mechanism described above. The size of the voids appears to vary depending on the size and shape of the texture, which is also expected.



Control (CO)

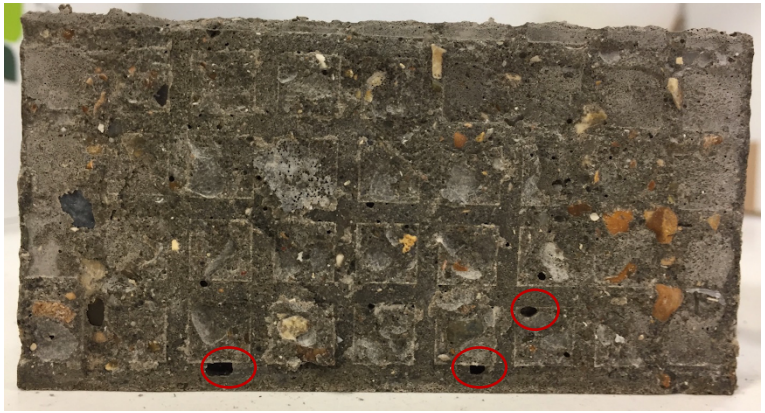

Square (SQ)

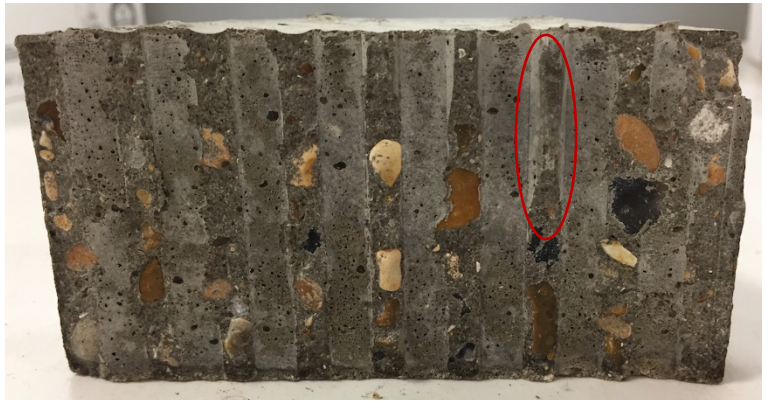

Grooves-vertical (GV)

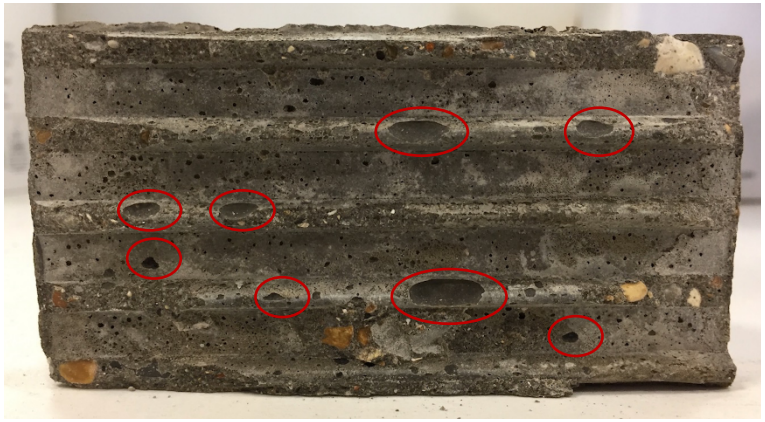

Grooves-horizontal (GH)

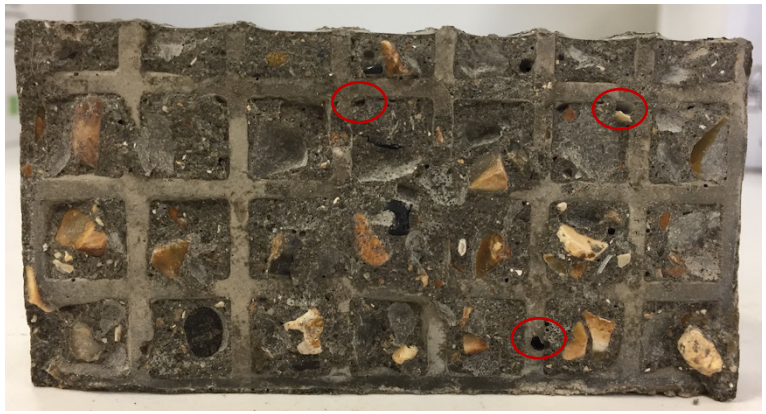

Pyramid (PY)



Half-sphere (HS)

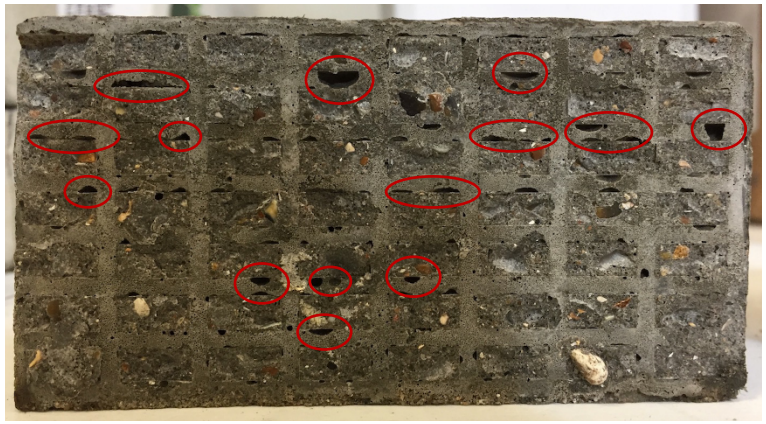

Rectangle-small (RS)



Rectangle-large (RL)

Figure 8.7 Entrapped air voids at the prefabricated spacer-concrete interface.

The fraction of air voids (%) at the prefabricated spacer-concrete interface is presented in Figure 8.8. This was calculated using image analysis carried out with the ImageJ/Fiji software by dividing the total area of the segmented air voids to the total cross-sectional area of the fractured interface. It can be seen that the flat spacer (CO) entrapped the least amount of air, followed by spacers with pyramid (PY) and square (SQ) textures. In contrast, the rectangle-small texture (RS) and grooved-vertical texture (GV) led to the highest amount of entrapped air voids. Such defects are expected to increase transport properties in particular pressure-induced flow as shown in other studies (Wong et al., 2009, Wong et al., 2011). Consequently, this will reduce or negate the beneficial effects of textured spacers.

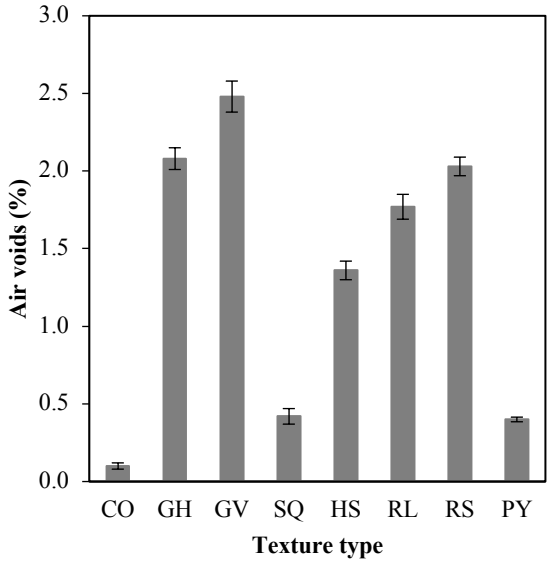

Figure 8.8 Entrapped air content at the prefabricated spacer-concrete interface measured using image analysis.

Figure 8.9 presents the accessible porosity of the prefabricated spacer-concrete samples. The results show that all samples with surface texture have higher accessible porosity compared to the control sample. When the fraction of air voids is plotted against the accessible porosity as presented in Figure 8.10, it is evident that the increase in accessible porosity can be linked to the increase in the amount of entrapped air voids at the prefabricated spacer-concrete interface. The highest porosity was achieved by the sample with rectangle-small (RS) texture with the average increase relative to the control sample of 16%. This observation is again consistent with the fact that the rectangle-small (RS) texture showed a large number of entrapped air voids at the interface (Figure 8.9).

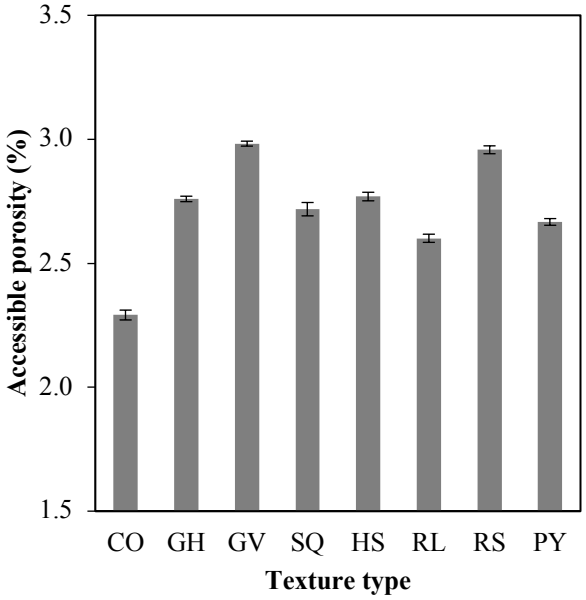

Figure 8.9 Accessible porosity of prefabricated spacer-concrete composite samples of various interface textures.

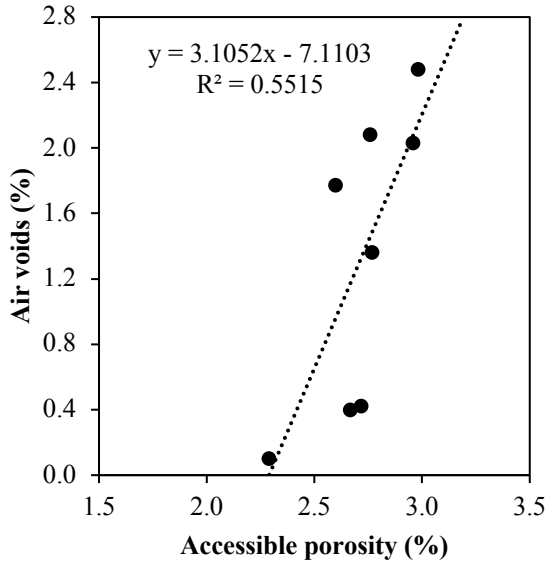

Figure 8.10 Relationship between total accessible porosity and air void fraction measured at prefabricated spacer-concrete interface.

8.3.2 Epoxy impregnation depth

Figures 8.11 and 8.12 show the measured depth of epoxy impregnation respectively and all the fluorescence images of sample cross-sections indicating the extent of epoxy penetration from the bottom-exposed surface along the interface. Overall, the results show that the presence of the surface texture decreased the distribution and depth of epoxy penetration by about 4.5% to 36%, compared to the control sample. As can be seen in Figure 8.12, the sample with the vertical

grooves (GV) texture has the deepest of epoxy penetration at the interface. This is consistent with the earlier results showing the highest diffusion, permeation and absorption coefficients were measured for this sample. This could be linked to the direction of the grooves being parallel to the flow of epoxy.

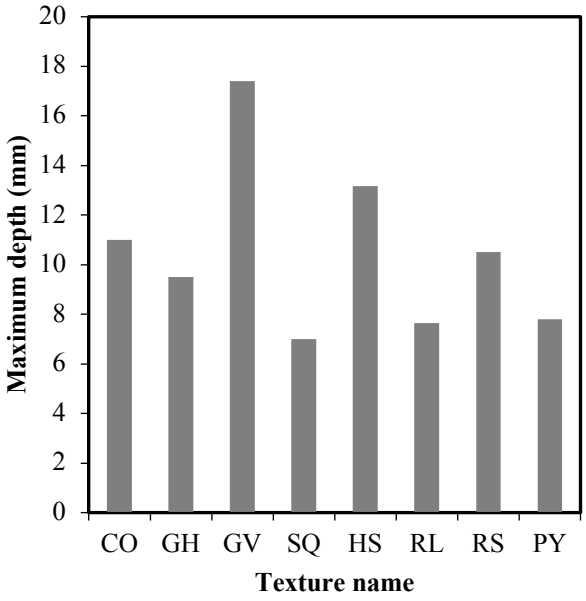

Figure 8.11 Maximum intrusion depth of fluorescent epoxy at the prefabricated spacer-concrete interface.

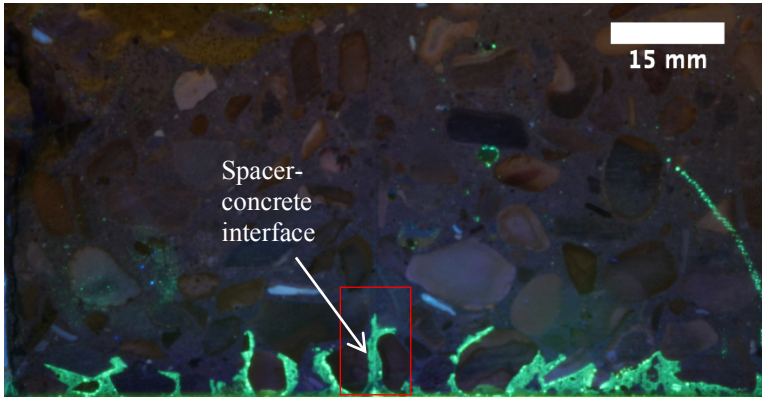

Control (CO)

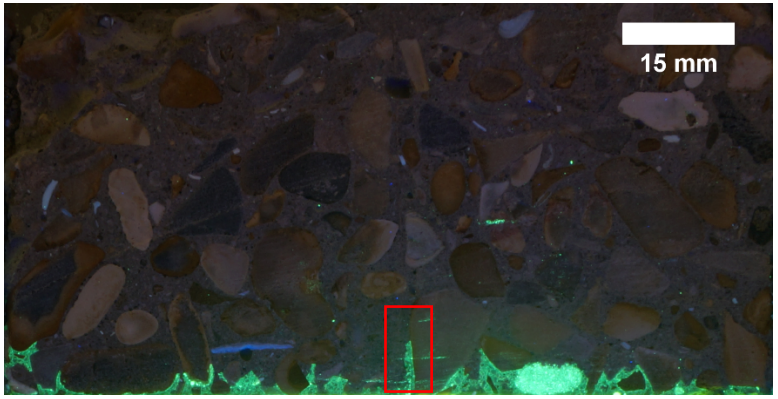

Square (SQ)



Grooves-vertical (GV)

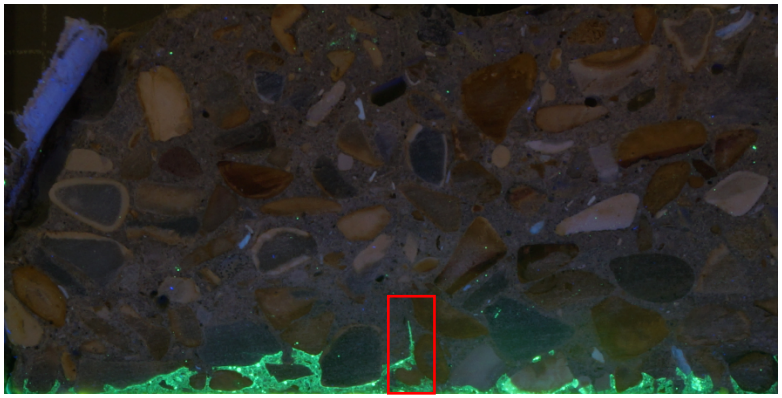

Grooves-horizontal (GH)

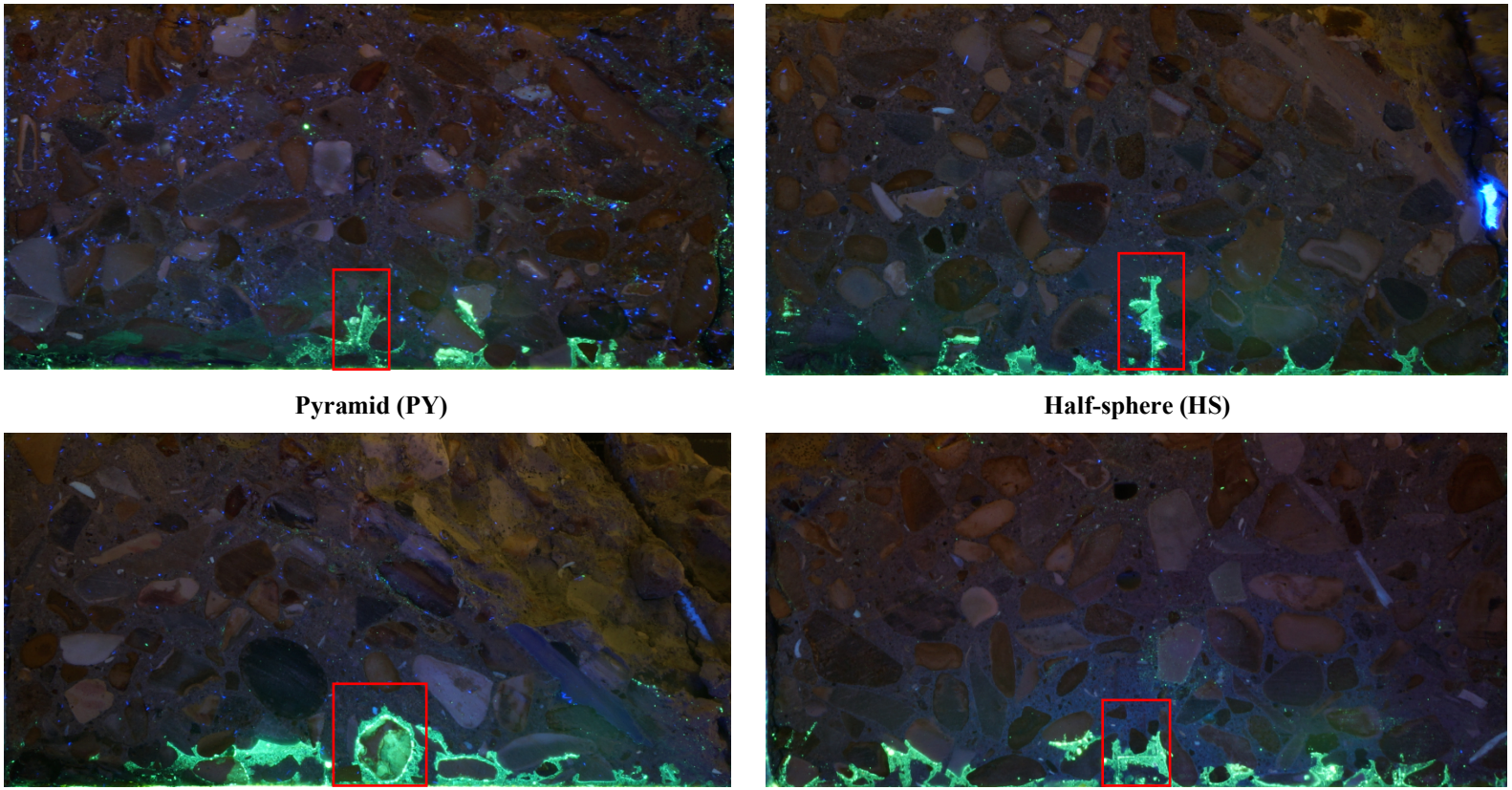

Pyramid (PY) **Half-sphere (HS)**

Rectangle-small (RS) **Rectangle-large (RL)**

Figure 8.12 Cross-sections of fluorescence images showing the extent of epoxy penetration at the prefabricated spacer-concrete interface. All samples contain half-concrete spacer and half-concrete (Red boxes show prefabricated spacer-concrete interface).

8.3.3 Relationship between interface bond strength, surface texture parameters and transport properties

Figure 8.13 shows the correlations between the interface bond strength and the transport properties of the prefabricated spacer-concrete composite samples obtained by plotting the normalised oxygen diffusivity, oxygen permeability, water sorptivity and epoxy penetration depth against normalised bond strength. The normalisation was carried out by dividing the measured values (transport, strength) to the corresponding value for the control sample (without textured spacer). Similarly, the correlation between bond strength and accessible porosity is shown in Figure 8.14.

The results show that there is an inverse relationship with bond strength for permeability and epoxy penetration depth. However, diffusivity, sorptivity and accessible porosity were not substantially influenced by interface bond strength. Samples with higher bond strength do not necessarily have lower transport properties or a lower accessible porosity. Increasing bond strength via the use of textured spacers mainly decreased pressure-induced flow. This behaviour is likely due to the decreased amount of drying-induced microcracking at the prefabricated spacer-concrete interface.

However, transport mechanism such as diffusion and absorption are influenced by total accessible porosity rather than the size of the pores and cracks, as for the case of pressure induced flow. The presence of air voids at the prefabricated spacer-concrete interface caused by incomplete compaction increases overall accessible porosity and this counteracts the benefits of textured spacers in mitigating such transport mechanisms. This can be seen in Figure 8.15 where the surface texture parameters namely surface roughness (A_T/A_0), texture density and profile depth as discussed in Chapter 7.2 are plotted against the normalised transport properties. Therefore, it is expected that the full advantages of textured spacers can only be realised if the surface texture and mix rheology are optimised for compaction, but this requires further research and validation.

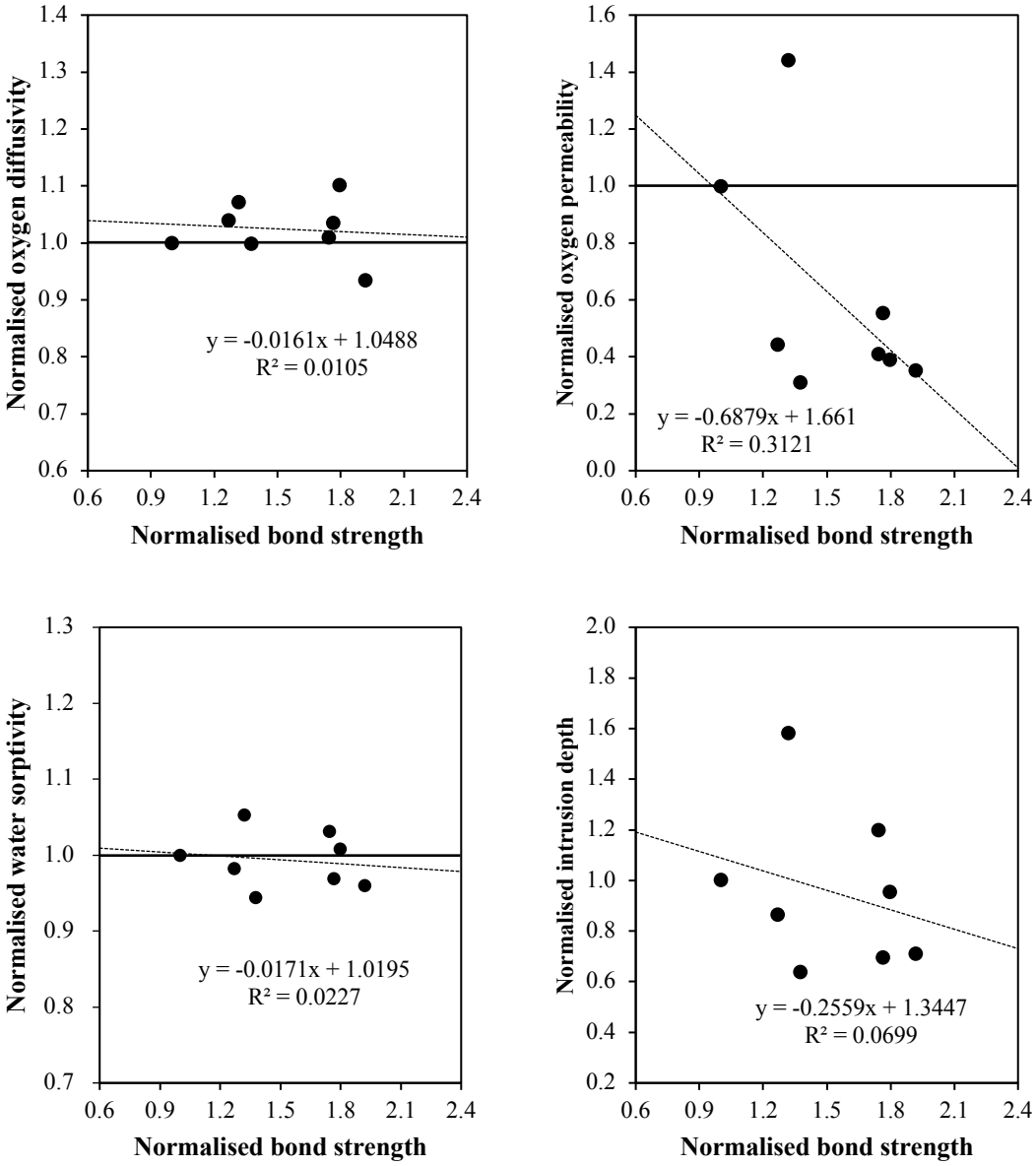

Figure 8.13 Relationship between interface bond strength and transport properties for samples with various textured spacer-concrete interface.

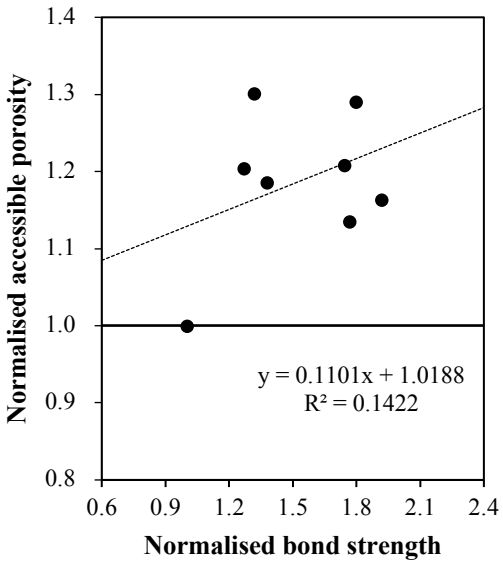

Figure 8.14 Relationship between interface bond strength and accessible porosity for samples with various textured spacer-concrete interface.

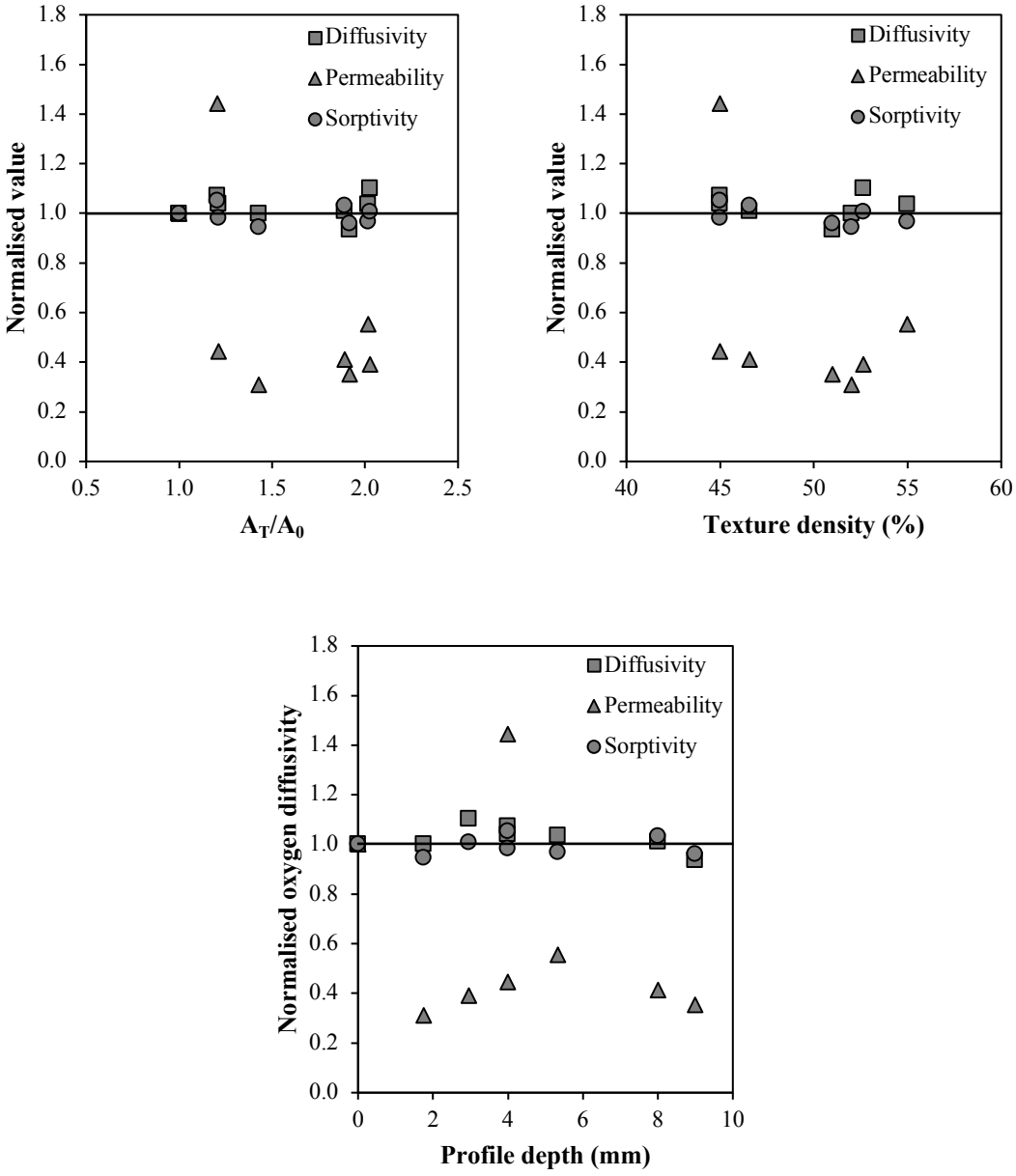

Figure 8.15 Relationship between transport properties and surface texture parameters for samples with various textured spacer-concrete interface.

Unfortunately, it is not possible to compare the results from this chapter with other studies since there are no precedents. However, the effect of air voids on transport properties is in line with the findings reported by Wong et al. (2011) where it was shown that the presence of air voids increases the heterogeneity of the microstructure and provides another path for transport to occur. This is verified in Figure 8.16 which shows that a higher porosity the samples generally leads to higher transport properties. In contrast, the occurrence of air voids at the interface slightly contributes to lower bond strength as discussed in Chapter 7. The presence of air voids has also been found in the vicinity of steel reinforcement. The air voids can be generated by

rising air bubles, bleeding or segregation underneath the embedded steel, perpendicular to the direction of casting. It has been reported that the air voids at the steel-concrete interface accelerates corrosion initiation and that corrosion often starts near the voids (Mohammed et al., 1999, Castel et al., 2006, Soylev and Francois, 2003).

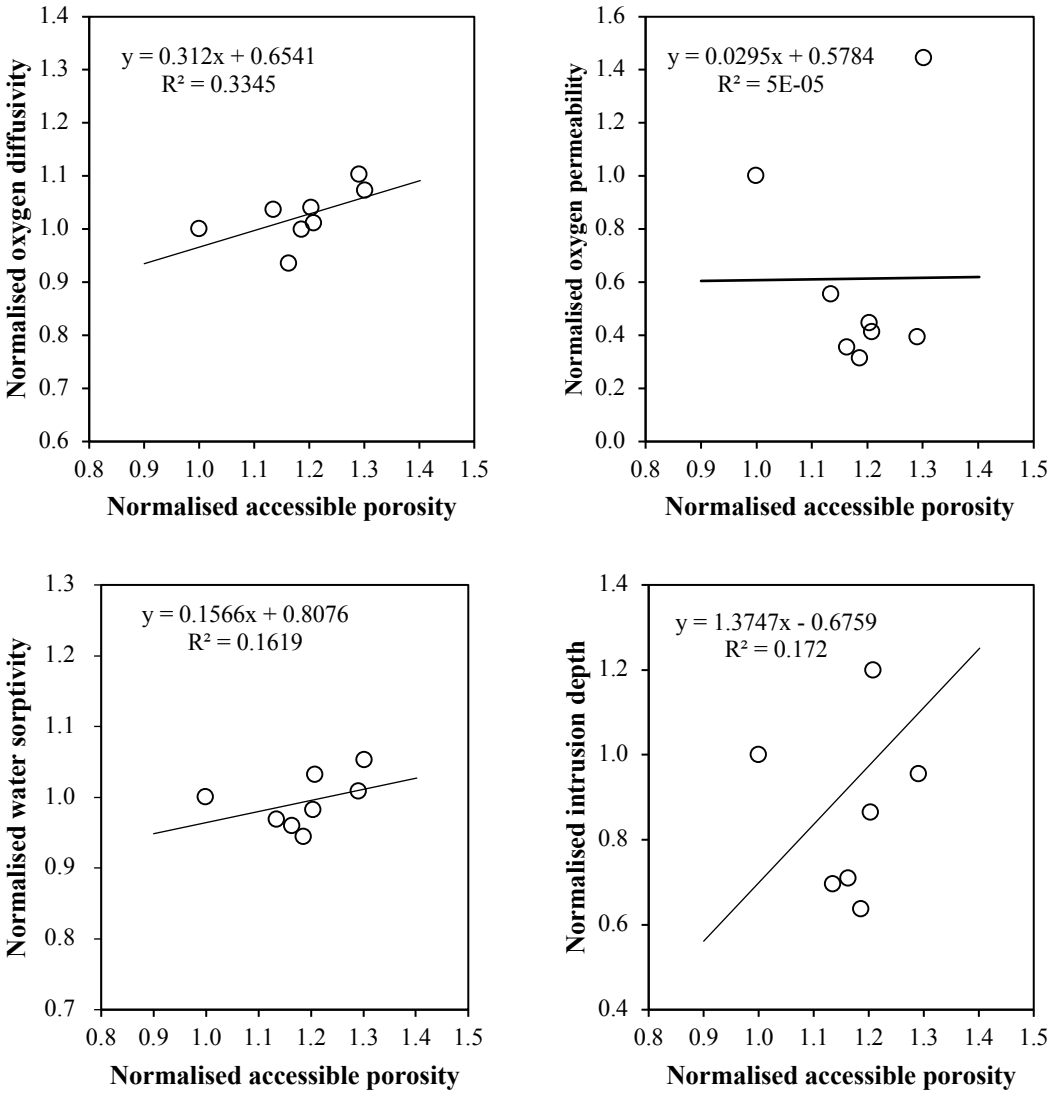

Figure 8.16 Relationship between accessible porosity and transport properties.

8.4 Conclusions

Spacer surface geometry (flat or with texture) plays an important role in ensuring the quality of bonding between prefabricated spacer and concrete as well as the durability of concrete. The results strongly suggest that samples with flat spacers have a greater tendency for cracking compared to samples containing textured spacers, thus leading to a significant increase in pressure induced flow. In contrast, prefabricated spacers with surface textures can substantially reduce overall permeability. However, not all surface textures decreased mass transport properties, and this is attributed to the presence of entrapped air voids at the prefabricated spacer-concrete interface which may reduce or outweighs the benefits of the surface texturing. The effect of surface texture on the transport properties varies depending on its geometry, shape and orientation.

Chapter 9

Conclusions

This study aimed to gain a better understanding of the influence of reinforcement spacers on the transport properties and microstructure of reinforced concrete. This study also had the aim of exploring whether the incorporation of SCMs in concrete and modification of the spacer surface texture could improve the spacer-concrete interface characteristics and decrease the penetration of deleterious species through the concrete cover. Conclusions of this study are established in the context of the three main objectives that were investigated in the five primary results chapters of the study.

Combined effects of vertical reinforcement spacer and segregation on transport properties of concrete

The combined effects of spacer and concrete segregation on the water sorptivity, electrical conductivity, and sample porosity of 400 mm tall vertically cast columns were investigated via an experimental programme involving 84 individual tests. After 28 days of curing in a fog room, top and bottom samples with a dimension of 80 *x* 90 *x* 100 mm containing either a plastic or cementitious spacer were extracted from the columns using a diamond saw. The samples were then conditioned at 75% RH (21°C) or at 50°C prior to testing. The main conclusions of this study are as follows:

a) The presence of a spacer attached to the vertical reinforcement negatively affects the transport properties of concrete. The spacer increases the water sorptivity, electrical conductivity and sample porosity, regardless of whether it was extracted from the top or bottom of the sample. However, the magnitude of the increase in transport properties depends on the type and position of the spacer and transport mechanism.
b) Despite care taken during compaction of fresh concrete, segregation occurred within the 400 mm tall concrete samples and this affected the transport properties. The top samples consistently had the lowest resistance to transport in comparison to the bottom samples.
c) Overall, the top samples showed a higher water sorptivity and electrical conductivity by a factor of 1.2 to 1.8 relative to the bottom samples. The porosity of the top samples was higher by up to a factor of 1.5 relative to the bottom samples.

d) Reducing the frequency and compaction time reduced the amount of segregation, thus decreasing the transport properties of the top samples by up to 28%. However, the water sorptivity and electrical conductivity of the bottom samples remained relatively constant.
e) The maximum increase in water sorptivity and electrical conductivity for the top samples containing spacers compacted at 8.5 Hz frequency for 90 seconds per layer were 23% and 12.5% respectively. The corresponding values for samples compacted at 6.5 Hz for 40 seconds per layer were 17% and 17%
f) For samples conditioned at 50°C, the average increase in water sorptivity for the top samples containing plastic and cementitious spacers relative to the control were 58% and 34% respectively. The corresponding values for the bottom samples were 88% and 58%.
g) The presence of plastic spacers reduces the tendency for segregation by about 7.5% relative to the control sample. In contrast, cementitious spacers increase the segregation by approximately 19% relative to the control sample. This behaviour is probably due to the differences in shape and size between the plastic and cementitious spacer. The plastic spacer has a clip and occupies a larger area such that when attached to the vertical reinforcement, it reduces the cross-sectional area available for aggregates to move during compaction and therefore the segregation tendency.

Influence of SCMs on transport properties and microstructure of concrete containing spacer

Tests were carried out on 100 mm diameter 50 mm height samples containing a centrally positioned spacer that is either plastic or cementitious. A total of 445 individual tests were carried out to study the influence of SCMs on the mass transport properties and microstructure of concrete containing the spacer. Test variables include the SCM type (silica fume, fly ash and ground granulated blast-furnace slag), curing age (3, 28, and 120 days) and conditioning regime (75% RH, 21°C and 50°C oven). The conclusions arising from this study are as follows:

a) The inclusion of spacers increases the penetration of gas, water and chloride ions, regardless of the mechanism, i.e. diffusion, permeation or capillary absorption. This occurred despite the fact that the concrete contained partial replacement of CEM I with SCMs such as silica fume, fly ash and ground granulated blast-furnace slag. The magnitude of the increase in transport depends on the spacer type, SCM type and transport mechanism.
b) The spacer-concrete interface (approximately 15 – 50 μm from the spacer boundary) contains higher porosity compared to the concrete farther away from the spacer. This is

confirmed by fluorescent epoxy impregnation and chloride penetration profiles showing a preferential transport path along the spacer-concrete interface.

c) The negative effects of spacers on the transport properties and microstructure were observed for all SCM types, curing ages and conditioning regimes.
d) The oxygen diffusivity of samples containing spacers were on average higher than the control samples by 85%, 74% and 38% at 3d, 28d and 120d respectively. The corresponding values for oxygen permeation were 392%, 485% and 293% respectively and water sorptivity were 22%, 40% and 2% respectively. Therefore, the negative effect of spacers on the transport properties decreased when concrete was cured for longer periods.
e) The presence of spacers increased the accessible porosity by up to 87%, 13.8% and 13.4% for samples incorporating SF, FA, and GGBS respectively.
f) Overall, samples containing silica fume achieved the lowest transport properties. However, samples containing ground granulated blast-furnace slag showed the least negative effect on transport properties due to the presence of a spacer.
g) For samples conditioned in a 50°C oven, the plastic spacers consistently gave the highest transport properties followed by samples with cementitious spacers, then the control samples in all cases. Permeability was affected the most where increases of up to a factor of 10 were observed for samples containing a plastic spacer. Drying-induced cracks were observed along the interface between the plastic spacer and concrete. These findings are broadly in line with previous research conducted by Alzyoud et al. (2016).

Influence of surface texture on interface bond strength and transport properties between prefabricated spacer and concrete

There have been no studies to-date devoted to interface bond strength between a prefabricated spacer and surrounding concrete. The bond strength between a prefabricated spacer and concrete was measured by performing splitting tensile strength test on composite samples of concrete cast against prefabricated cementitious spacers. The prefabricated spacer-concrete interface was also tested for transport properties including oxygen diffusivity, oxygen permeability, and water sorptivity. A total of 224 samples with 50 mm height were cast and cured for 1, 7 and 28 days. The main variables included the shape and geometry of the spacer surface texture (eight types) and the mix composition of the spacer (mortar or concrete). The main conclusions are as follow:

a) Increasing the surface area of the prefabricated spacer improved its interlocking with concrete and this resulted in an increase of the interface bond strength by up to 133% compared to samples without texturing (i.e. flat interface).

b) At all ages, the control sample with a flat spacer consistently achieved lower bond strength. The interface bond strength for samples with textured spacers increased by up to 140%, 109%, and 133% at 1, 7 and 28 days respectively, compared to those of flat spacers.

c) The overall strength of the prefabricated spacer-concrete interface is dependent on the surface roughness, shape, and orientation of the spacer surface texture. The evidence shows that bond strength increases with increasing surface roughness and texture density. However, the surface profile depth does not have a consistent influence on bond strength.

d) Regarding the failure mode, samples with flat spacer-concrete interface failed through debonding. However, samples with textured spacers failed via a combination of interface debonding and fracturing of the spacer or concrete. This correlates well with the higher bond strength measured for these samples.

e) The mix proportions of the prefabricated spacer had an insignificant contribution to the failure mode and bond strength. This is probably because both the mortar and concrete spacer examined in this study have similar levels of compressive strength.

f) Prefabricated spacers with textured surface were found to substantially reduce overall permeability. In contrast, samples with flat spacers have a greater tendency for cracking when subjected to drying and this led to a significant increase in transport properties, particularly permeability. However, the incidence of voids at the interface due to incomplete compaction may reduce or outweigh the benefits of surface texturing.

g) The effect of surface texture on the transport properties varies depending on the geometry, shape and orientation at the texture. Overall, the lowest transport coefficients were achieved in samples containing prefabricated spacers with a pyramid texture with the average decreases in oxygen diffusivity, oxygen permeability, water sorptivity and epoxy intrusion depth relative to the control samples of 6.6%, 69%, 4% and 29% respectively.

To summarise, this thesis has highlighted several key points including:

- The presence of spacers produced a micro-cracked and highly porous interface in concrete regardless of binder type (with or without SCMs such silica fume, fly ash, and ground granulated blast slag) or their applications (vertical or horizontal elements), which lowers the resistance of concrete to the ingress of aggressive agents causing degradation.
- The transport properties of concrete containing a reinforcement spacer are determined not only by the properties of the concrete and spacer, but it is also strongly dependent on the spacer-concrete interface conditions. Cracking at the interface is linked to incompatibility due to differential volume changes (shrinkage or thermal movements) and poor bonding between the spacer and concrete.
- Increasing the severity of drying prior to testing increases the severity of the influence of spacers on mass transport properties and microstructure of concrete, and this effect was more significant in samples containing plastic spacers. This is due to the fact that the thermal expansion coefficient of plastic is 10 to 15 times higher than that of surrounding concrete.
- Finally, re-engineering the spacer surface properties (e.g. shape and texture) to enhance bonding and mechanical interlocking with concrete have been found to be a promising means to improve the quality of the concrete cover. The presence of surface texture was found to decrease the tendency for cracking at the spacer-concrete interface, leading to a significant decrease in pressure induced flow.

Chapter 10

Implications and recommendations

10.1 Implications

It is well-known that quality and thickness of concrete cover are major factors affecting the transport of aggressive agents into concrete causing degradation, in particular, protecting steel reinforcement embedded in concrete structure against the corrosion. However, the importance of reinforcement spacers within the reinforced concrete structure is considered low and often ignored. This is because spacers seem small and inconsequential, but the findings from this study show that such views are incorrect.

The results from this study suggest that for all reinforced concrete constructions (whether vertical or horizontal elements, containing SCMs or not), the locations where the reinforcements are supported by spacers would experience greater exposure to the ingress of deleterious species. The presence of a spacer provides easy access to aggressive agents such as oxygen, chloride, sulphate, etc. through the spacer itself or its porous interface with the surrounding concrete. This occurred despite the fact that the cementitious spacer selected and used in this study was of a good quality mix with a low w/b ratio containing fibre and slag, and from a well-established manufacturer. Because the properties of spacers used in construction are not well regulated and measured, it is likely that there exist many other spacer types that are inferior to those used in this study. Hence, instead of providing protection, the spacer exposes the reinforcement to a greater risk of premature corrosion deterioration. According to BS 7973-2:2001, a spacer should be located at every meter length of the reinforcement. Therefore, a typical structure would contain many weak points.

However, spacers are a critical component of concrete structures and there is currently no alternative to replace spacers for supporting reinforcement in concrete constructions. Therefore, the quality of spacers is of vital importance and particular care should be made in selecting the appropriate spacers. However, at present, very few studies have looked at or discussed the effects of spacers on the long-term durability of concrete structures. Similarly, very little emphasis on this has been made in codes of practice. For example, the relevant British Standard on spacers focuses on spacer types, their positioning including fixity and stability load-bearing

capacity, without any further information on the selection of spacers for durability. BS 7973-1:2001 and BS EN 13670: 2010 state that spacers shall have an equivalent durability with the surrounding concrete and shall not reduce the durability of the structure, including not causing any deterioration to the reinforcement or the concrete, spalling of concrete cover nor allowing free passage of water to the reinforcement. However, there is no guidance on performance testing to ensure the quality of spacers, the steel reinforcement around spacers or the bond between spacer and concrete. As a result of the lack of information provided in standards, it is not surprising that many contractors and designers select spacers on the basis of cost and ignore aspects of durability. For example, plastic spacers are widely used due to their relatively low cost. However, this study shows that plastic spacers were consistently the worst performing spacer type compared to cementitious spacers when samples were subjected to elevated temperatures.

Moreover, point spacers were used in this study for the sake of convenience because it allowed testing to be conducted on relatively small samples within a manageable time period. However, line spacers made of either plastic or cementitious bars are also commonly used in construction. These line spacers are interesting because they reduce the time for bar installation but create a larger spacer-concrete interface area compared to that of single cover spacers. Thus, line spacers could be more problematic in terms of cracking and its effect on durability. Moreover, in this study, samples were tested under non-loaded conditions and in controlled environments. In fact, real structures are subjected to variations in temperature, moisture and loading. These factors will increase the possibility of cracking and debonding at the spacer-concrete interface, thus exacerbating the effect of spacers on mass transport.

Finally, spacers with surface texture have been found to improve the interface bond strength and this led to decreased cracking and pressure-induced flow as discussed in Chapters 7 and 8. As such, based on the findings from this study, it would be recommended that manufacturers produce cementitious spacers of low porosity with a convex surface texture or features that protrude out of the surface with smooth edges instead of a flat surface. The findings also strongly suggest that plastic spacers should not be used in all reinforced concrete constructions that are exposed to high temperature fluctuations and low humidity.

10.2 Recommendations for future research

The effects of spacers attached to vertical reinforcement on the transport properties of concrete were investigated in Chapter 4. The segregation observed within the 400 mm height samples was found to negatively affect transport properties. On the one hand, columns in real structures are much taller than 400 mm so the segregation could be more severe. On the other hand, compaction of real columns is not carried out on vibrating tables as done in the lab. This merits further investigation. Furthermore, Self-compacting concrete (SCC) has been studied for several years, and it was found that SCC offers a very high level of homogeneity and minimises migration of free water and segregation of fine and coarse aggregate particles (Khayat, 1999). Therefore, it would be interesting to carry out a study to establish whether the use of a spacer in SCC has a similar effect on transport properties. Besides segregation, concrete is also susceptible to bleeding and trapping of bleed water under vertically positioned spacers. Therefore, future work is necessary to investigate the microstructure of interfaces between the spacer and surrounding concrete to better understand the effects of bleeding and to develop methodologies to mitigate this.

Chapters 5 and 6 found that the use of SCMs in concrete could not completely eliminate the negative effects of spacers on the transport properties and microstructure of concrete. Therefore, there is plenty of scope for future research to develop new types of spacers that could bond better to concrete. For example, spacers made of materials with reactive surfaces that interact and bond with concrete would be a very interesting research area. In addition, more studies need to be carried out on the distribution of hydration products at the spacer-concrete interface to gain a better understanding of factors influencing bonding at the microscale or nanoscale.

As presented in Chapters 4 to 6, concretes containing plastic spacers could perform poorly particularly in hot weather and aggressive environments. However, plastic spacers are commonly used in construction due to their low cost. Therefore, understanding the true impact of plastic spacers on the long-term performance of concrete structures and developing methods to mitigate their effects could be another focus area of future research.

Chapters 7 and 8 showed that producing spacers with textured surfaces is simple and a promising approach to enhance the interface bond strength between a spacer and concrete. This led to a decrease in drying induced microcracking and a substantial decrease in pressure-induced flow. However, certain surface textures could lead to air entrapment and incomplete concrete filling or compaction at the spacer-concrete interface. As such, further work can be carried out to optimise the surface texture to avoid this problem. This would further enhance the interfacial

bond strength and also enable the effects of surface texture on transport properties to be better established. Moreover, future work could focus on developing numerical models to understand the effects of surface texture on the spacer-concrete interface bond strength and predict the influence of spacers on the long-term properties of concrete.

Lastly, there is still a lack of standards and guidance on the use of spacers in concrete. The requirements set out in BS 7973 should be regarded as a minimum. Current standards need to provide further guidance on the material, shape, and geometry of spacers to ensure that the presence of spacers do not compromise the durability performance of the structure. The standard should require performance testing on the spacer itself or on concretes containing spacers in order to ensure that the durability requirements are met. The use of plastic spacers should be reviewed and should probably be limited to structures that are exposed to non-aggressive environments only. It is also suggested that the British Standards should follow the approach by ACI 315-99, CRSI's Manual of Standard Practice, CSA A23.1-14, and DIN 1045-1:2001 in providing guidance on specifying spacers according to exposure condition and to require the inclusion of spacer specifications on contract documentation or drawings. To gain a better understanding of the effect of spacers on durability, future work could also be carried out to investigate the effect of spacers on chloride- and carbonation-induced corrosion and transport of other aggressive agents such as sulphates. The effect of spacers on passivating film of steel would also be of interest.

References

ACI 315-99. Details and detailing of concrete reinforcement. American Concrete Institute.

BS 1134:2010. Assessment of surface texture *Guidance and general information.* London: British Standards Institution.

BS 7973-1:2001. Spacers and chairs for steel reinforcement and their specification. *Part 1: Product performance requirements.* London: British Standards Institution.

BS 7973-2:2001. Spacers and chairs for steel reinforcement and their specification. *Fixing and application of spacers and chairs and tying of reinforcement.* London: British Standards Institution.

BS EN 197-1:2011. Cement. *Part 1: Composition, specifications and conformity criteria for common cements.* London: British Standards Institution.

BS EN 450-1:2012. Fly ash for concrete. *Part 1: Definition, specifications and conformity criteria.* London: British Standards Institution.

BS EN 934-2:2009+A1:2012. Admixtures for concrete, mortar and grout. *Part 2: Concrete admixtures - Definitions, requirements, conformity, marking and labelling.* London: British Standards Institution.

BS EN 1504-10:2017. Products and systems for the protection and repair of concrete structures - Definitions, requirements, quality control and evaluation of conformity. *Part 10: Site application of products and system and quality control of the works.* London: British Standards Institution.

BS EN 12350-2:2009. Testing fresh concrete *Part 2: Slump-test.* London: British Standards Institution.

BS EN 12390-6:2009. Testing hardened concrete. *Part 6: Tensile splitting strength of test specimens.* London: British Standards Institution.

BS EN 12390-7:2009. Testing hardened concrete. *Part 7: Density of hardened concrete.* London: British Standards Institution.

BS EN 12390-11:2015. Testing hardened concrete. *Part 11: Determination of the chloride resistance of concrete, unidirectional diffusion.* London: British Standards Institution.

BS EN 12620:2002+A1:2008. Aggregates for concrete. London: British Standards Institution.

BS EN 13263-1:2005. Silica fume for concrete *Part 1: Definitions, requirements and conformity criteria.* London: British Standards Institution.

BS EN 13670:2009. Execution of concrete structures. London: British Standards Institution.

BS EN 15167-1:2006. Ground granulated blast furnace slag for use in concrete, mortar and grout. *Part 1: Definitions, specifications and conformity criteria.* London: British Standards Institution.

CSA A23.1-14. Concrete materials and methods of concrete construction. Canadian Standards Association

DIN 1045-1. Structures made of concrete, reinforced concrete and pre-stressed concrete structures *Part 1: Design and construction.* Deutsches Institut für Normung

ABYANEH, S. D., WONG, H. S. & BUENFELD, N. R. 2016. Simulating the effect of microcracks on the diffusivity and permeability of concrete using a three-dimensional model. *Computational Materials Science,* 119**,** 130-143.

ALDEA, C.-M., SHAH, S. P. & KARR, A. 1999. Effect of cracking on water and chloride permeability of concrete. *Journal of Materials in Civil Engineering,* 11**,** 181-187.

ALZYOUD, S. 2015. *Effect of reinforcement spacers on concrete microstructure and durability.* Doctor of Philosophy, Imperial College London.

ALZYOUD, S., WONG, H. S. & BUENFELD, N. R. 2016. Influence of reinforcement spacers on mass transport properties and durability of concrete structures. *Cement and Concrete Research,* 87**,** 31-44.

ANDRADE, C. 1992. Calculation of chlride diffusion coefficients in concrete from ionic migration measurements. *Cement and Concrete Research,* 23**,** 724-742.

ANGST, U. M., GEIKER, M. R., MICHEL, A., GEHLEN, C. & WONG, H. 2017. The steel-concrete interface *Materials and Structures* 50**,** 1-24.

ASBRIDGE, A. H., CHADBOURN, G. A. & PAGE, C. L. 2001. Effects of metakaolin and the interfacial transition zone on the diffusion of chloride ions through cement mortars. *Cement and Concrete Research,* 31**,** 1567-1572.

BENTUR, A. & COHEN, M. D. 1987. Effect of condensed silica fume on the microstructure of the interfacial zone in portland cement mortars. *J. Am. Ceram. Soc,* 70**,** 738-743.

BENTUR, A. & ODLER, I. 1996. Development and nature of interfacial microstructure. *In:* MASO, J. C. (ed.) *Interfacial transition zone.* London, UK: E & FN SPON.

BENTZ, D. P. & GARBOCZI, E. J. 1991. Simulation studies of the effects of mineral admixtures on the cement paste-aggregate interfacial zone. *ACI Materials Journal,* 88**,** 518-529.

BEUSHAUSEN, H. & ALEXANDER, M. G. 2008. Bond strength development between concretes of different ages. *Magazine of Concrete Research,* 60**,** 65-74.

BIJEN, J. 1995. Benefits of slag and fly ash. *Construction and Building Materials,* 95**,** 309-314.

BISSCHOP, J. & MIER, J. G. M. V. 2002. Effect of aggregates on drying shrinkage microcracking in cement-based composites. *Materials and Structures,* 35**,** 453-461.

BRETON, D., CARLES-GIBERGUES, A., BALLIVY, G. & GRANDED, J. 1992a. Contribution to the formation mechanism of the transition zone between rock-cement paste. *Cement and Concrete Research,* 23**,** 335-346.

BRETON, D., OLLIVIER, J. P. & BALLIVY, G. 1992b. Diffusivity of chloride ions in the transition zone between cement paste and granite. *In:* MASO, J. C. (ed.) *Interfaces in Cementitous Composites.* London: E & FN Spon.

BREUL, P., GEOFFRAY, J.-M. & HADDAM, Y. 2008. On-site concrete segregation estimation using image analysis. *Journal of Advanced Concrete Technology,* 6**,** 171-180.

BSI BS EN 1992-1-1:2004+A1:2014. Eurocode 2: Design of concrete structures. *Part 1-1: General rules and rules for buildings.* London: British Standards Institution.

BUENFELD, N. R. & OKUNDI, E. 1998. Effect of cement content on transport in concrete. *Magazine of Concrete Research,* 50**,** 339-351.

CARLES-GIBERGUES, A., SAUCIER, F., GRANDET, J. & PIGEON, M. 1993a. New-to-old concrete bonding: Influence of sulfate type of new concrete on interface microstructure. *Cement and Concrete Research,* 23**,** 431-441.

CARLES-GIBERGUES, A., SAUCIER, F., GRANDET, J. & PIGEON, M. 1993b. New-to-old concrete bonding: Influence of sulfates type of new concrete on interface microstructure. *Cement and Concrete Research,* 23**,** 431-441.

CASTEL, A., VIDAL, T., VIRIYAMETANONT, K. & FRANÇOIS, R. 2006. Effect of Reinforcing Bar Orientation and Location on Bond with Self-Consolidating Concrete. *ACI Structural Journal* 103**,** 559-567.

CHENG-YI, H. & FELDMAN, R. F. 1985. Influence of silica fume on the microstructural development in cement mortars. *Cement and Concrete Research,* 15**,** 285-294.

CHINGA, G., JOHNSEN, P. O., DOUGHERTY, R., BERLI, E. L. & WALTER, J. 2007. Quantification of the 3D microstructure of SC surfaces. *Journal of Microscopy,* 227**,** 254-265.

CHUNG, D. D. L. 2001. Interface engineering for cement-matrix composites. *Composite interfaces,* 8**,** 67-81.

COHEN, M. D., GOLDMAN, A. & CHEN, W.-F. 1994. The role of silica fume in mortar: Transition zone versus bulk paste modification. *Cement and Concrete Research,* 24**,** 95-98.

COSTA, A. & APPLETON, J. 1999. Chloride penetration into concrete in marine environment - Part I : Main parameters affecting chloride penetration. *Materials and Structures,* 32**,** 252-259.

COURARD, L. 2000. Parametric study for the creation of the interface between concrete and repair products. *Materials and Structures,* 33**,** 65-72.

CRSI 2011. *Placing reinforcing bars,* Illinois, Concrete Reinforcing Steel Institute.

DEHGHAN, A., PETERSON, K., RIEHM, G. & BROMERCHENKEL, L. H. 2014. Application of X-ray microfluorescence for the determination of chloride diffusion coefficients in concrete chloride penetration experiments. *Construction and Building Materials,* 148**,** 85-89.

DELAGRAVE, A., BIGAS, J. P., OLLIVIER, J. P., MARCHAND, J. & PIGEON, M. 1997. Influence of the interfacial zone on the chloride diffusivity of mortars. *Adv Cem Bas Mat,* 5**,** 86-92.

DESNERCK, P., LEES, J. M. & MORLEY, C. T. 2015. Bond behaviour of reinforcing bars in cracked concrete. *Construction and Building Materials,* 94.

DIAMOND, S. 2004. The microstructure of cement paste and concrete - a visual primer. *Cement & Concrete Composites,* 26**,** 919-933.

DIAMOND, S. & HUANG, J. 2001. The ITZ in concrete - a different view based on image analysis and SEM observations. *Cement & Concrete Composites,* 23**,** 179-188.

DUAN, P., SHUI, Z., CHEN, W. & SHEN, C. 2013. Effects of metakaolin, silica fume and slag on pore structure, interfacial transition zone and compressive strength of concrete. *Construction and Building Materials,* 44.

EMBERSON, N. K. & MAYS, G. C. 1990. Significance of property mismatch in the patch repair of structural concrete - Part 1: Properties of repair systems. *Magazine of Concrete Research,* 42**,** 147-160.

EMMONS, P. H. & VAYSBURD, A. M. 1994. Factors affrecting the durability of concrete repair: the contractor's viewpoint. *Construction and Building Materials,* 8**,** 5-16.

ESBACH, O. E. & SOUDERS, M. 1975. *Handbook of Engineering Fundamentals,* New York, John Wiley & Sons.

ESPECHE, A. D. & LEON, J. 2011. Estimation of bond strength envelopes for old-to-new concrete interfaces based on a cylinder splitting test. *Construction and Building Materials,* 25**,** 1222-1235.

FARRAN, J. 1996. Introduction: The transition zone - discovery and development. *In:* MASO, J. C. (ed.) *Interfacial transition zone in concrete.* London, UK: E & FN SPON.

FLATT, R. J., ROUSSEL, N. & CHEESEMAN, C. R. 2012. Concrete: An eco material that needs to be improved. *Journal of the Eropean Ceramic Society,* 32**,** 2787-2798.

FORSTER, B., VILLE, D. V. D., BERENT, J., SAGE, D. & UNSER, M. 2004. Complex wavelets for Extended Depth-of-Field: A new method for the fusion of mutichannel microscopy images. *Microscopy research and technique,* 65**,** 33-42.

GAO, J. M., QIAN, C. X., LIU, H. F. & B. WANG, L. L. 2005a. ITZ microstructure of concrete containing GGBS. *Cement and Concrete Research,* 35**,** 1299-1304.

GAO, J. M., QIAN, C. X., LIU, H. F., WANG, B. & LI, L. 2005b. ITZ microstructure of concrete containing GGBS. *Cement and Concrete Research,* 35.

GARBACZ, A., GORKA, M. & COURARD, L. 2004. Effect of concrete surface treatment on adhesion in repair system *Magazine of Concrete Research,* 56**,** 1-12.

GARBOCZI, E. J. & BENTZ, D. P. 1991. Digital simulation of the aggregate-cement paste interfacial zone in concrete. *J. Mater. Res.,* 6**,** 196-201.

GEDAM, B. A., BHANDARI, N. M. & UPADHYAY, A. 2016. Influence of supplementary cementitious materials on shrinkage, creep, and durability of high-performance concrete. *Journal of Materials in Civil Engineering,* 28**,** 04015173-1.

GEISSERT, D. G., LI, S. E., FRANTZ, G. C. & STEPHENS, J. E. 1999. Splitting prism test method to evaluate concrete to concrete bond strength. *ACI Materials Journal,* 96**,** 359-366.

GESOGLU, M., GUNEYISI, E. & OZBAY, E. 2009. Properties of self-compacting concretes made with binary, ternanry, and quaternary cementitious blends of fly ash, blast furnace slag, and silica fume. *Construction and Building Materials,* 23**,** 1847-1854.

GJORV, O. E., MONTEIRO, J. M. & MEHTA, P. K. 1990. Effect of condensed silica fume on the steel-concrete bond. *ACI Materials Journal,* 87**,** 573-580.

GLASS, G. K., YANG, R., DICKHAUS, T. & BUENFELD, N. R. 2001. Backscattered electron imaging of the steel-concrete interface. *Corrosion Science,* 43.

GRASSL, P., WONG, H. S. & BUENFELD, N. R. 2010. Influence of aggregate size and volume fraction on shrinkage induced micro-cracking of concrete and mortar. *Cement and Concrete Research,* 40**,** 85-93.

GUANG-CHENG, L., XIE, Y.-J., DING, W.-W. & OMRAN, A. 2014. Ion-transport characteristics of new-old concrete composite system. *Journal of Central South University,* 21**,** 790-798.

HALL, C. 1989. Water sorptivity of mortars and concretes: a review. *Magazine of Concrete Research,* 41**,** 51-61.

HALL, C. & TSE, T. K.-M. 1986. Water movement in porous building materials - VII. The sorptivity of mortars. *Building and Environment,* 21**,** 113-118.

HALL, C. & YAU, M. H. R. 1987. Water movement in porous building materials - IX. The water absorption and sorptivity of concretes. *Building and Environment,* 22**,** 77-82.

HASSAN, K. E., BROOKS, J. J. & AL-ALAWI, L. 2001. Compatibility of repair mortars with concrete in a hot-dry environment *Cement & Concrete Composites,* 23**,** 93-101.

HEAD, M. K. & BUENFELD, N. R. 2006. Confocal imaging of porosity in hardened concrete. *Cement and Concrete Research,* 36**,** 896-911.

HEAD, M. K., WONG, H. S. & BUENFELD, N. R. 2006. Characterisation of 'Hadley' grains by confocal microscopy. *Cement and Concrete Research,* 36(8), 1483-1489.

HLUSHKOU, D., BRUNS, S. & TALLAREK, U. 2010. High-performance computing of flow and transport in physically reconstructed silica monoliths. *Journal of Chromatography A,* 1217**,** 3674-3682.

HONG, K. & HOOTON, R. D. 1999. Effects of cylic chloride exposure on penetration of concrete cover. *Cement and Concrete Research,* 29**,** 1379-1386.

HORNE, A. T., RICHARDSON, I. G. & BRYDSON, R. M. D. 2007. Quantitative analysis of the microstructure of interfaces in steel reinforced concrete *Cement and Concrete Research,* 37**,** 1613-1623.

HOSHINO, M. 1989. Relationship between bleeding, coarse aggregate, and specimen height of concrete. *ACI Materials Journal,* 86**,** 185-190.

HSU, S. M., JING, Y., HUA, D. & ZHANG, H. 2014. Friction reduction using discrete surface textures: principle and design. *Journal of Physics D: Applied Physics,* 47.

HSU, T. T. C. & SLATE, F. O. 1963. Tensile bond strength between aggregate and cement paste or mortar. *Journal of the American concrete institure,* 60**,** 465-486.

HWANG, C.-L. & YOUNG, J. F. 1984. Drying shrinkage of portland cement pastes I. Microcracking during drying. *Cement and Concrete Research,* 14**,** 585-594.

ICRI 2015. Concrete repair terminology. *In:* INSTITUTE, I. C. R. (ed.). Saun Paul, USA.

JIANG, Z., HUANG, Q., XI, Y., GU, X. & ZHANG, W. 2016. Experimental study of diffusivity of the interfacial transition zone between cement paste and aggregate. *J. Mater. Civ. Eng. ,* 28.

JULIO, E. N. B. S., BRANCO, F. A. B. & SILVA, V. D. 2004. Concrete-to-concrete bond strength. Influence of the roughness of the substrate surface *Construction and Building Materials,* 18.

JULIO, E. N. B. S., BRANCO, F. A. B., SILVA, V. D. & F.LOURENCO, J. 2006. Influence of added concrete compressive strength on adhesion to an existing concrete substrate. *Building and Environment,* 41**,** 1934-1939.

KENAI, S. & BAHAR, R. 2003. Evaluation and repair of Algiers new airport building. *Cement & Concrete Composites,* 25**,** 633-641.

KHALAF, M. N. A. & PAGE, C. L. 1979. Steel/mortar interfaces: Microstructural features and mode of failure. *Cement and Concrete Research,* 9**,** 197-208.

KHAN, M. I. & SIDDIQUE, R. 2011. Utilization of silica fume in concrete: Review of durability properties *Resources, Conservation and Recycling,* 57**,** 30-35.

KHAYAT, K. H. 1998. Use of viscosity-modifying admixture to reduce top-bar effect of anchored bars cast with fluid concrete. *ACI Materials Journal,* 95**,** 158-167.

KHAYAT, K. H. 1999. Workability, testing, and performance of self-consolidating concrete. *ACI Materials Journal,* 96**,** 346-353.

KING, E. S. & DAKIN, J. M. 2001. Specifying, detailing and achieving cover to reinforcement. London: CIRIA.

KJELLSEN, K. O., WALLEVIK, O. H. & FJALLBERG, L. 1998. Microstructure and microchemistry of the paste-aggregate interfacial transition zone of high performance concrete. *Advances in Cement Research* 10**,** 33-40.

KLINKENBERG, L. J. 1941. *The permeability of porous media to liquids and gasses, drilling and production practice,* New York, American Petroleum Instititue.

LANGE, D. A., JENNINGS, H. M. & SHAH, S. P. 1993. Relationship between fracture surface roughness and fracture behaviour of cement paste and mortar. *Journal of the American Concrete Society,* 76**,** 589-597.

LARBI, J. A. 1993. Microstructure of the interfacial zone around aggregate particles in concrete. *In:* VROUWENVELDER, A. C. W. M. (ed.). The Netherlands.

LEVITT, M. & HERBERT, M. R. M. 1970. Performance of spacers in reinforced concrete. *Civil Engineering.*

LI, G., XIE, H. & XIONG, G. 2001. Transition zone studies of new-to-old concrete with different binders. *Cement & Concrete Composites,* 23**,** 381-387.

LI, Z., XU, M. & CHUI, N. C. 1998. Enhancement of rebar (smooth surface) - concrete bond properties by matrix modification and surface coatings. *Magazine of Concrete Research,* 50**,** 49-57.

LOTHENBACH, B., SCRIVENER, K. & HOOTON, R. D. 2011. Supplementary cementitious materials. *Cement and Concrete Research,* 41**,** 1244-1256.

LUKOVIC, M., SAVIJA, B., DONG, H., SCHLANGEN, E. & YE, G. 2014. Micromechanical study of interface properties in concrete repair system *Journal of Advanced Concrete Technology,* 12**,** 320-339.

MACHIDA, A. 1975. Studies on test for splitting tensile strength of concrete. *Proc. of JSCE***,** 115-124.

MARSH, B. K., DAY, R. L. & BONNER, D. G. 1995. Pore structure characteristics affecting the permeability of cement paste containing fly ash. *Cement and Concrete Research,* 15**,** 1027-1038.

MARUYAMA, I. & SASANO, H. 2014. Strain and crack distribution in concrete during drying. *Materials and Structures,* 47**,** 517-532.

MISRA, A., CLELAND, D. J. & BASHEER, P. A. M. 2001. Effect of different substrate and overlay concretes on bond strength and interfacial permeability. *Concrete Science and Engineering,* 3**,** 73-77.

MOHAMMED, T. U., OTSUKI, N. & HISADA, M. 1999. Corrosion of steel bars with respect to orientation in concrete. *ACI Materials Journal,* 96**,** 154-159.

MOMAYEZ, A., RAMEZANIANPOUR, A. A., RAJAIE, H. & EHSANI, M. R. 2004. Bi-surface shear test for evaluating bond between existing and new concrete *ACI Materials Journal,* 101**,** 99-106.

MONDAL, P., SHAH, S. P. & MARKS, L. D. 2008. Nanoscale Characterization of Cementitious Materials. *ACI Materials Journal,* 105**,** 174-179.

MONTEIRO, P. J. M., GJORV, O. E. & MEHTA, P. K. 1985a. Microstructure of the steel-cement paste interface. *Cement and Concrete Research,* 15**,** 781-784.

MONTEIRO, P. J. M., MASO, J. C. & OLLIVIER, J. P. 1985b. The aggregate-mortar interface. *Cement and Concrete Research,* 15**,** 953-958.

MORADLLO, M. K., SUDBRINK, B., HU, Q., ABOUSTAIT, M., TABB, B., LEY, M. T. & DAVIS, J. M. 2017. Using micro X-ray fluorescence to image chloride profiles in concrete. *Cement anf Concrete Research,* 92**,** 128-141.

MORGAN, D. R. 1996. Compatibility of concrete repair materials and systems. *Construction and Building Materials,* 10**,** 57-67.

MUNOZ, M. A. C., HARRIS, D. K., AHLBORN, T. M. & FROSTER, D. C. 2014. Bond performance between ultrahigh-performance concrete and normal-strength concrete. *J. Mater. Civ. Eng.,* 26**,** 04014031.

NASSER, A., CLEMENT, A., LAURENS, S. & CASTEL, A. 2010. Influence of steel-concrete interface condition on galvanic corrosion currents in carbonated concrete. *Corrosion Science,* 52**,** 2878-2890.

NAUCLER, T. & ENKVIST, P.-A. 2009. *Pathways to a low-carbon economy: Version 2 of the global greenhouse gas abatement cost curve*, McKinsey&Company.

NEVILLE, A. M. 2011. *Properties of Concrete,* England, Pearson Education Limited.

OLLIVIER, J. P., MASO, J. C. & BOURDETTE, B. 1995. Interfacial transition zone in concrete. *Adv. Cem. Cem. Bas Mat,* 2**,** 30-38.

OLSSON, N., WAHID F. A., NILSSON, L. O., THIEL, C., WONG, H. S. & BAROGHEL-BOUNY, V. 2018. Wick action in mature mortars with binary cements containing slag or silica fume - The relation between chloride and moisture transport properties under non-saturated conditions. *Cement and Concrete Research,* 111, 94-103.

OTSUKI, N., HISADA, M., DIOLA, N. B. & MD, T. U. 1998. Experimental study on interfacial transition zones in reinforced concrete. *J. Materials, Conc. Struct. Pavements, JSCE,* 39**,** 155-167.

OZBAY, E., ERDEMIR, M. & DURMUS, H. I. 2016. Utilization and efficiency of ground granulated blast furnace slag on concrete properties – A review. *Construction and Building Materials,* 105**,** 423-434.

PANESAR, D. K. & SHINDMAN, B. 2012. The effect of segregation on transport and durability properties of self consolidating concrete. *Cement and Concrete Research,* 42**,** 252-264.

PICKA, J. D., JAISWAL, S. S., IGUSA, T., KARR, A. F. & SHAH, S. P. 2000. Quantitative description of coarse aggregate volume fraction gradients. *Cement, concrete, and aggregate, CCAGDP,* 22**,** 133-141.

PIGEON, M. & SAUCIER, F. Durability of repaired concrete structures. International Symposium on Advances in Concrete Technology, 1992 Athen. 741-773.

PING, X., BEAUDOIN, J. J. & BROUSSEAU, R. 1991. Flat aggregate-portland cement paste interfaces, I. Electrical conductivity models. *Cement and Concrete Research,* 21**,** 515-522.

PINK, X. & BEAUDOIN, J. J. 1993. Effect of transition zone microstructure on bond strength of aggregate-portland cement paste interfaces.

POULSEN, E. & MEJLBRO, L. 2010. Diffusion of chloride in concrete: Theory and application. Taylor & Francis.

PRINCIGALLO, A., BREUGEL, K. V. & LEVITA, G. 2003. Influence of the aggregate on the electrical conductivity of Portland cement concretes. *Cement and Concrete Research,* 33**,** 1755-1763.

RAPHAEL, J. M. 1984. Tensile strength of concrete. *ACI Journal,* 81**,** 158-165.

ROSTAM, S. 1996. High performance concrete cover - Why it is needed, and how to achieve it in practice. *Construction and Building Materials,* 10**,** 407-421.

ROSTAM, S. 2005. Service life design of concrete structures - A Challenge to designers as well as to owners. *Asian Journal of Civil Engineering (Building and Housing),* 6**,** 423-445.

ROUSSEL, N. 2006. A theoretical frame to study stability of fresh concrete. *Materials and Structures,* 39**,** 81-91.

SABIR, B. B., WILD, S. & O'FARRELL, M. 1998. A water sorptivity test for mortar and concrete. *Materials and Structures,* 31**,** 568-574.

SAFAWI, M. I., IWAKI, I. & MIURA, T. 2004. The segregation tendency in the vibration of high fluidity concrete. *Cement and Concrete Research,* 34**,** 219-226.

SAMAHA, H. R. & HOVER, K. C. 1992. Influence of microcracking on the mass transport properties of concrete. *ACI Materials Journal,* 89**,** 416-424.

SANTOS, P. M. D. & JULIO, E. N. B. S. 2011. Factors affecting bond between new and old concrete. *ACI Materials Journal,* 108**,** 449-456.

SCRIVENER, K. L., BENTUR, A. & PRATT, P. L. 1988. Quantitative characterization of the transition zone in high strength concretes. *Advances in Cement Research,* 1**,** 230-237.

SCRIVENER, K. L., CRUMBIE, A. K. & LAUGESEN, P. 2004. The interfacial transition zone (ITZ) between cement paste and aggregate in concrete *Interface Science,* 12**,** 411-421.

SHANE, J. D., MASON, T. O., JENNINGS, H. M., GARBOCZI, E. J. & BENTZ, D. P. 2000. Effect of the interfacial transition zone on the conductivity of Portland cement mortars. *J. Am. Ceram. Soc,* 83**,** 1137-1144.

SHAW, C. The long term durability of plastic spacers in reinforced concrete: A case study. 7th International Congress on Concrete, 8 - 10 July 2008 2008 University of Dundee, Scotland, UK. IHS BRE Press.

SHAW, P. & KUTTI, T. 2003. Field measurements and experience of chloride induced corrosion of reinforcement in submerged structures. Goteborg, Sweden.

SNYDER, K. A., WINSLOW, D. N., BENTZ, D. P. & GARBOCZI, E. J. Interfacian zone percolation in cement-aggregate composites. *In:* MASO, J. C., ed. Interfaces in Cementitious Composites, 1992 Toulouse. E&FN Spon, 259-268.

SOCIETY, C. 1981. Choosing the right bar supports in aggresive environments. *Concrete Technology Today.*

SOYLEV, T. A. & FRANCOIS, R. 2003. Quality of steel–concrete interface and corrosion of reinforcing steel. *Cement and Concrete Research,* 33**,** 1407-1415.

SUBRAMANIAN, N. & GEETHA, K. 1997. Concrete cover for durable RC structures. *The Indian Concrete Journal,* 71**,** 197-201.

SUMMERBELL, D. L., BARLOW, C. Y. & CULLEN, J. M. 2016. Potential reduction of carbon emissions by performance improvement: A cement industry case study. *Journal of Cleaner Production,* 135**,** 1327-1339.

TANAKA, N. & STIGSON, B. 2009. *Cement technology roadmap 2009,* France, OECD/IEA and World Business Council for Sustainable Development.

TANG, L. & UTGENANNT, P. 2009. A field study of critical chloride content in reinforced concrete with blended binder. *Materials and corrosion,* 60.

TASONG, W. A., LYNSDALE, C. J. & CRIPPS, J. C. 1999. Aggregate-cement paste interface: Part I. Influence of aggregate geochemistry. *Cement and Concrete Research,* 29**,** 1019-1025.

TAYEH, B. A., BAKAR, B. H. A. & JOHARI, M. A. M. 2013. Characterization of the interfacial bond between old concrete substrate and ulta high performance fiber concrete repair composite. *Materials and Structures,* 46**,** 743-753.

TAYEH, B. A., BAKAR, B. H. A., JOHARI, M. A. M. & VOO, Y. L. 2012. Mechanical and permeability properties of the interface between normal concrete substrate and ultra high performance fiber concrete overlay. *Construction and Building Materials,* 35**,** 538-548.

TSAI, W.-H. 1985. Moment-preserving thresholding: A new approach. . *Computer Vision, Graphics, and Image Processing,* 29**,** 377-393.

UDDIN, M. S., IBATAN, T. & SHANKAR, S. 2017. Influence of surface texture, shape, geometry and orientation on hydronamic lubrication performance of plane-to-plane slider surfaces. *Lubrication science,* 29**,** 153-181.

VIK, T. K. The role of bar supports in combating corrosion in reinforced concrete. *In:* P.H. BRETT, N. B. A. P. J. B., ed. Sixth International Conference on Short and Medium Span Bridges, 2002 Vancouver, Canada.

WAHID, F. A. 2016. *Characterising concrete using micro X-ray fluorescence (μXRF).* Imperial College London.

WALL, J. S. & SHRIVE, N. G. 1988. Factors affecting bond between new and old concrete. *ACI Materials Journal,* 85-M15**,** 117-125.

WONG, H. S. 2006. *Quantifying the pore structure of cement-based materials using backscattered electron microscopy*. Doctor of Philosophy, Imperial College London.

WONG, H. S. & BUENFELD, N. R. 2006. Euclidean Distance Mapping for computing microstructural gradients at interfaces in composite materials. *Cement and Concrete Research,* 36**,** 1091-1097.

WONG, H. S., BUENFELD, N. R. & HEAD, M. K. 2006a. Estimating transport properties of mortars using image analysis on backscattered electron images *Cement and Concrete Research,* 36**,** 1556-1566.

WONG, H. S., BUENFELD, N. R., HILL, J. & HARRIS, A. W. 2007. Mass transport properties of mature wasterform grouts. *Advances in cement research* 19**,** 35-46.

WONG, H. S., HEAD, M. K. & BUENFELD, N. R. 2006b. Pore segmentantion of cement-based materials from backscattered electron images. *Cement and Concrete Research,* 36**,** 1083-1090.

WONG, H. S., PAPPAS, A. M., ZIMMERMAN, R. W. & BUENFELD, N. R. 2011. Effect of entrained air voids on the microstructure and mass transport properties of concrete. *Cement and Concrete Research,* 41**,** 1067-1077.

WONG, H. S., ZOBEL, M., BUENFELD, N. R. & ZIMMERMAN, R. W. 2009. Influence of the interfacial transition zone and microcracking on the diffusivity, permeability and sorptivity of cement-based materials after drying. *Magazine of concrete research,* 61**,** 571-589.

WORRELL, E., PRICE, L., MARTIN, N., HENDRIKS, C. & MEIDA, L. O. 2001. Carbon dioxide emissions from the global cement industry. *Annu. Rev. Energy Environ.,* 26**,** 303-329.

WU, Z., WONG, H. S. & BUENFELD, N. R. 2014. Effect of confining pressure and microcracks on mass transport properties of concrete. *Advances in Applied Ceramics,* 113(8), 485-495.

WU, Z., WONG, H. S. & BUENFELD, N. R. 2015. Influence of drying-induced microcracking and related size effects on mass transport properties of concrete. *Cement and Concrete Research,* 68**,** 35-48.

WU, Z., WONG, H. S. & BUENFELD, N. R. 2017. Transport properties of concrete after drying-wetting regimes to elucidate the effects of moisture content, hysteresis and microcracking. *Cement and Concrete Research,* 98, 136-154.

WU, Z., WONG, H. S. & BUENFELD, N. R. 2018. Anomalous water absorption in cement-based materials caused by drying shrinkage induced microcracks. *Cement and Concrete Research*, In press.

XIE, H., LI, G. & XIONG, G. 2002. Microstructure model of the interface zone between fresh and old concrete *Journal of Wuhan University of Technology,* 17.

YAN, D., QU, N., LI, H. & WANG, X. 2010. Significance of dimple parameters on the friction of sliding surfaces investigated by ortoghonal experiments. *Tribology Transactions,* 53**,** 703-712.

YIO, M. H. N. 2016. *Characterising pore structure of cement-based materials using laser scanning confocal microscopy.* Doctor of Philosophy, Imperial College London.

YIO, M. H. N., MAC, M. J., WONG, H. S. & BUENFELD, N. R. 2015. 3D imaging of cement-based materials at submicron resolution by combining laser scanning confocal microscopy with serial sectioning. *Journal of Microscopy,* 258**,** 151-169.

YIO, M. H. N., WONG, H. S. & BUENFELD, N. R. 2017. Representative elementary volume (REV) of cementitious materials from three-dimensional pore structure analysis. *Cement and Concrete Research,* 102, 187-202.

YU, H., WANG, X. & ZHOU, F. 2010. Geomteric shape effects of surface texture on the generation of hydrodynamic pressure between conformal contacting surfaces. *Tribology Letters,* 37**,** 123-130.

YUE, L. & SHUGUANG, H. 2001. The microstructure of the intefacial transition zone between steel and cement paste *Cement and Concrete Research,* 31**,** 385-388.

ZAMPINI, D., JENNINGS, H. M. & SHAH, S. P. 1995. Characterization of the paste-aggregate interfacial transition zone surface roughness and its relationship to the fracture toughness of concrete. *Journal of Materials Sciecen,* 30**,** 3149-3154.

ZHANG, R., CASTEL, A. & FRANCOIS, R. 2011. Influence of steel-concrete interface defects owing to the top-bar effect on the chloride-induced corrosoion of reinforcement. *Magazine of Concrete Research,* 63**,** 773-781.

ZIMBELMANN, R. 1985. A contribution to the problem of cement-aggregate bond. *Cement and Concrete Research,* 15**,** 801-808.

ZIMBELMANN, R. 1987. A method for strengthening the bond between cement stone and aggregates. *Cement and Concrete Research,* 17**,** 651-660.

Appendices

Appendix I - Interface bond strength between spacer and concrete cured for 1 and 7 days

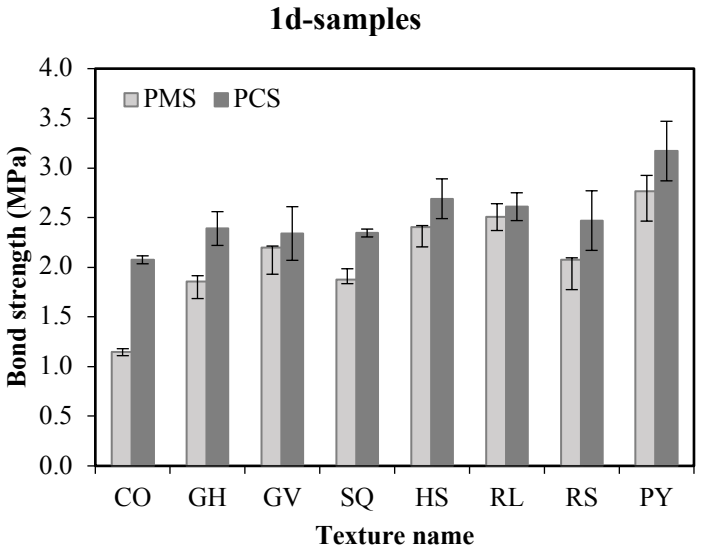

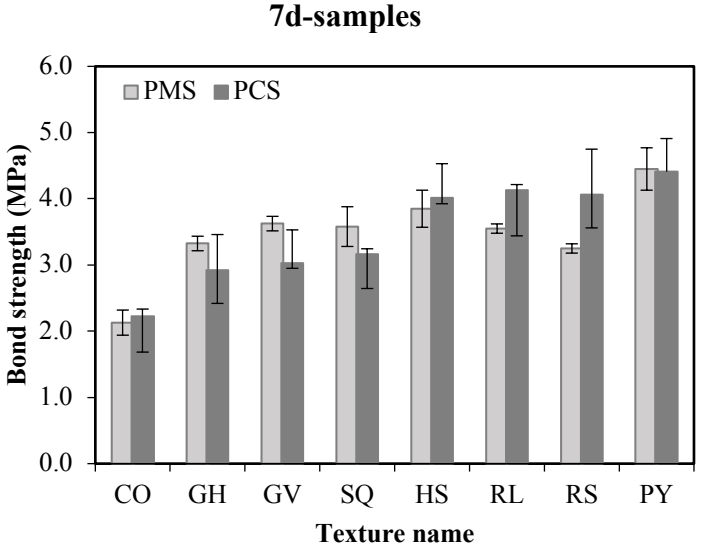

Appendix II - Failure mode of spacer-concrete interface

A. Spacer – concrete cured for 1 day

Mortar spacer - concrete



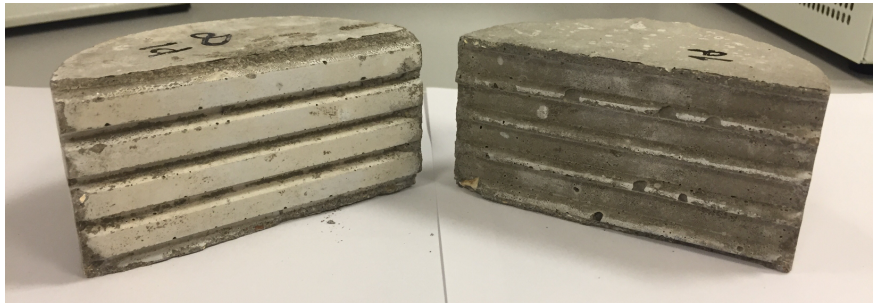

Concrete spacer - concrete

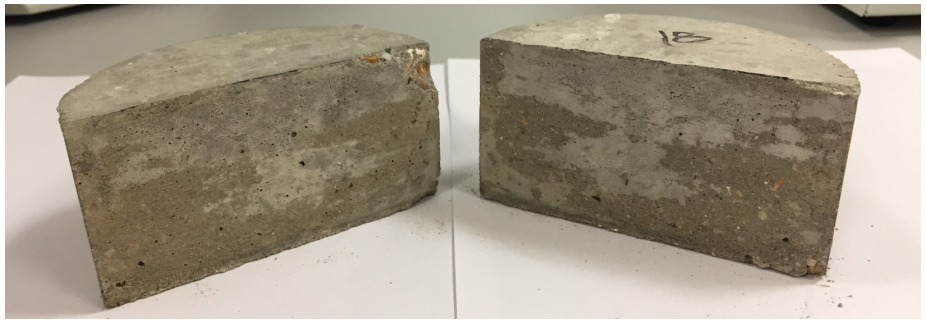



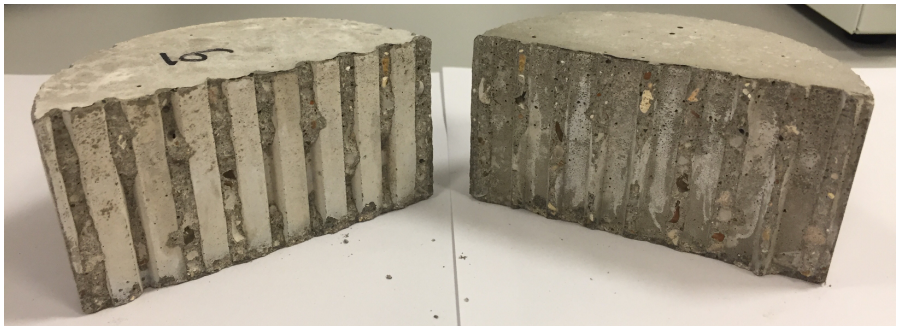




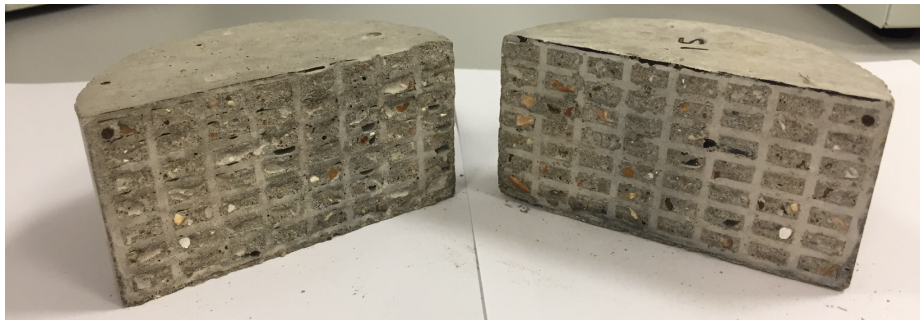

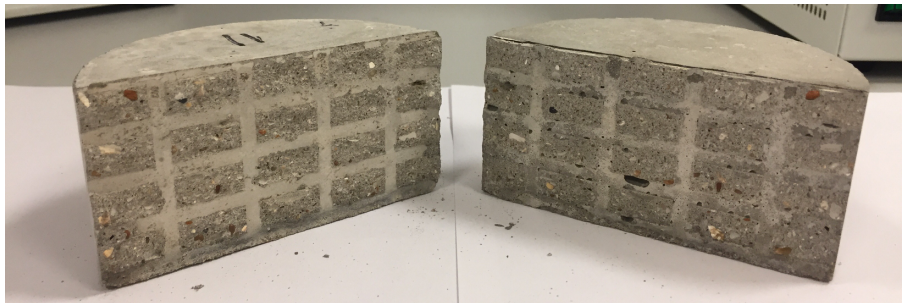







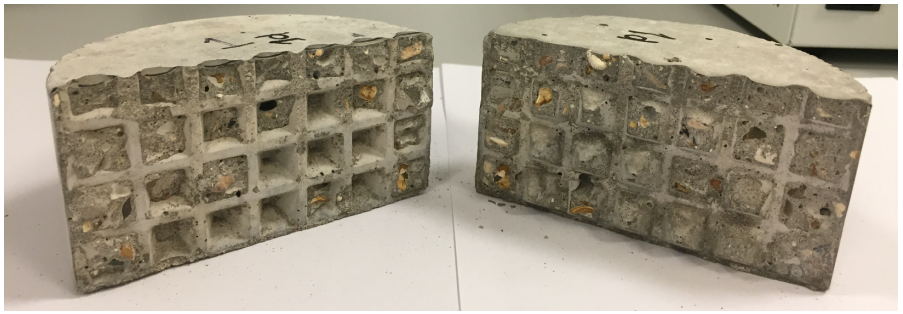

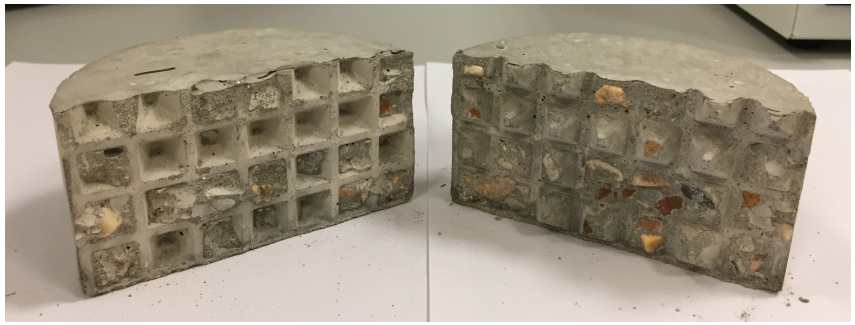

B. Spacer - concrete cured for 7 days

Mortar spacer - concrete

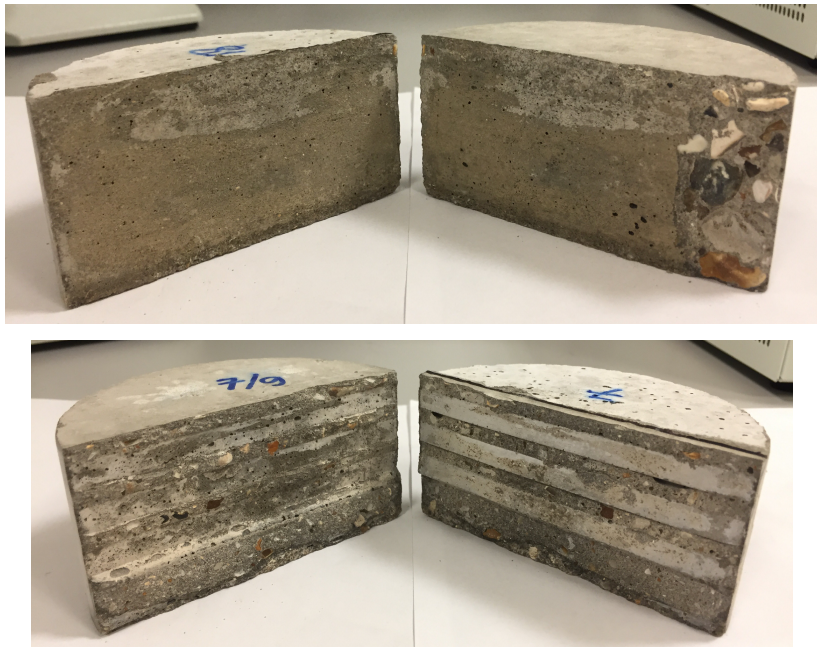

Concrete spacer - concrete

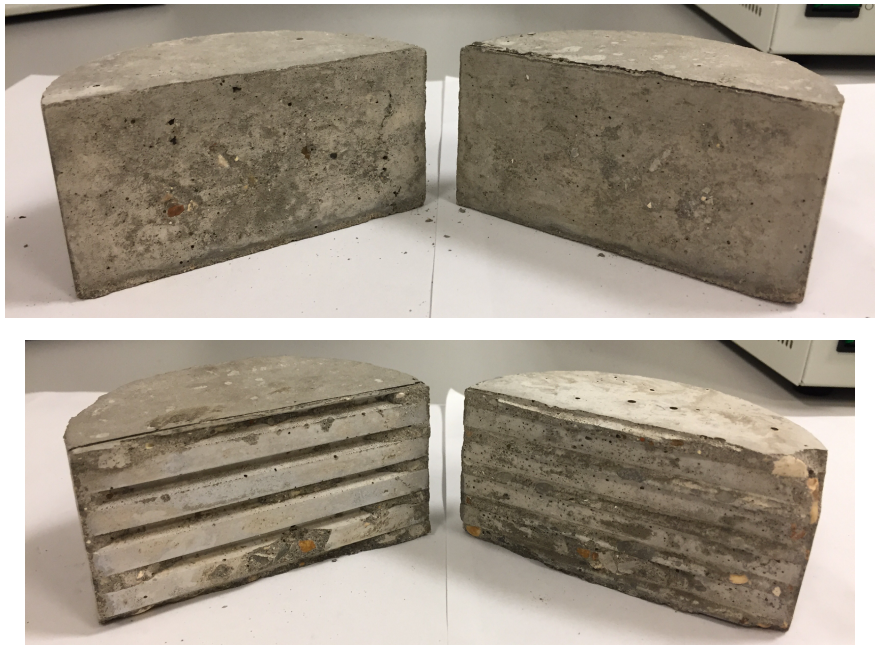

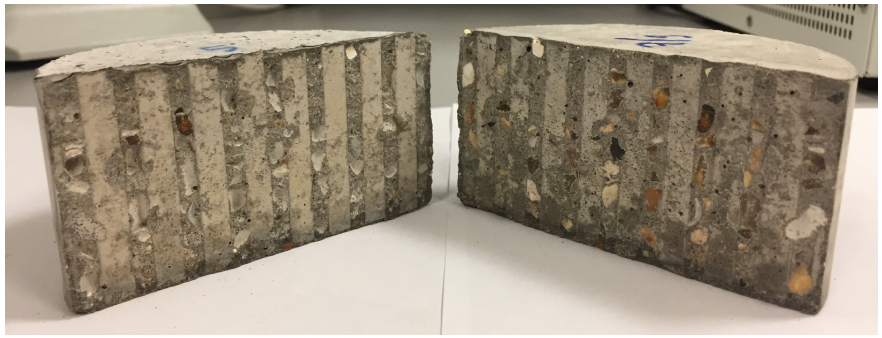













Appendix III - Publications arising from this research

Conference proceedings

1. MUSLIM, F., WONG, H. S. & BUENFELD, N. R. 2018. Improving the spacer-concrete interface for bond strength and durability. *Sixth International Conference on the Durability of Concrete Structure, 18 – 20 July 2018, Leeds, UK*.

2. MUSLIM, F., WONG, H. S. & BUENFELD, N. R. 2018. The interface bond strength between reinforcement spacer and concrete. *Young Researchers' Forum IV, 9th April 2018, Newcastle upon Tyne, UK*.

3. MUSLIM, F., WONG, H. S. & BUENFELD, N. R. 2017. Microstructure of interface between reinforcement spacer and concrete incorporating supplementary cementitious materials. *16th Euroseminar on Microscopy Applied to Building Materials, 14 – 17 May 2017, Les Diablerets, Switzerland*.

4. MUSLIM, F., WONG, H. S. & BUENFELD, N. R. 2016. Effect of reinforcement spacers on mass transport properties of concrete containing supplementary cementitious materials. *36th Cement and Concrete Science Conference, 5 – 6 September 2016, Cardiff, UK*.

Journal papers

1. MUSLIM, F., WONG, H. S. & BUENFELD, N. R. 2018. Combined effects of vertical reinforcement spacers and segregation on transport properties of concrete. (In preparation).

2. MUSLIM, F., WONG, H. S. & BUENFELD, N. R. 2018. Influence of supplementary cementitious materials on transport properties and microstructure of concrete containing spacer. (In preparation).

3. MUSLIM, F., WONG, H. S. & BUENFELD, N. R. 2018. Influence of surface texture on the spacer-concrete bond strength and transport properties. (In preparation).